MODELING AND DESIGN OF PHOTONIC CRYSTAL WAVEGUIDES AND FIBERS

By

LINPING SHEN
B.Sc., M. Eng.

A Thesis
Submitted to the school of Graduate studies
in Partial Fulfillment of the Requirements
for the Degree
Doctor of Philosophy

McMaster University

MODELING AND DESIGN OF
PHOTONIC CRYSTAL WAVEGUIDES AND FIBERS

DOCTOR OF PHILOSOPHY (2003) MCMASTER UNIVERSITY

(Electrical and Computer Engineering) Hamilton, Ontario

TITLE: **Modeling and Design of Photonic Crystal Waveguides and Fibers**

AUTHOR: Linping Shen

B. Sc. (Nanjing University of Science and Technology)

M. Eng. (Nanjing University of Science and Technology)

SUPERVISOR: Dr. W. -P. Huang

Professor, Department of Electrical and Computer Engineering

NUMBER OF PAGES: xviii, 176

ABSTRACT

Photonic crystal waveguides and fibers are emerging waveguides that are formed based on relatively large-scale periodic dielectric materials, also known as the photonic band-gap materials. Modeling and simulation of such waveguide structures will help to gain understanding for the modal and transmission characteristics and their dependence on the key design and operation parameters. In this dissertation, the multilayer slab and circular photonic crystal waveguides are investigated theoretically with emphasis on their modal characteristics and transmission properties relevant to broad-band telecommunication systems and networks. Key performance parameters (e.g., the modal field, the modal effective index, the group-velocity dispersion, the confinement loss, the mode effective area, as well as the confinement factor, etc.) are simulated and analyzed by using both analytical and numerical methods.

For the sake of completeness, a comprehensive review of the different mathematical methods for simulation and analysis of optical waveguides in general and photonic crystal waveguides in particular is presented. The theoretical frameworks for rigorous methods such as the finite difference method and the plane wave expansion method and for approximate methods such as the effective index method and the envelope approximate method are discussed, and their merits and shortcomings in modeling and analysis of photonic crystal waveguides and fibers are examined in great detail.

The one-dimensional (1D) slab photonic crystal waveguides (PCWs) are the simplest to model and analyze, yet can offer deep insight into the salient features of photonic crystal waveguides and fibers. A somewhat exhaustive study for the modal properties of 1D PCWs is carried out with the help of the rigorous transfer matrix method. Four different guiding regimes due to the total internal reflection (TIR) and the photonic band-gap (PBG) are recognized, and their unique features are revealed and discussed. Further, scope of validity and level of accuracy for two insightful approximate methods (i.e., the effective index method and the envelope approximation method) are

examined in detail by comparison with the exact solutions. Furthermore, new results about the effects of the number of unit cells (i.e., layer-pairs), the layer size-to-pitch ratio, and the core thickness on the modal properties are obtained and discussed.

The two-dimensional (2D) photonic crystal waveguides such as the air-hole-filled photonic crystal fibers (PCFs) find more practical applications and also much more difficult to model and analyze. In this context, the modal analyses with different theoretical frameworks such as the scalar, semi-vector, and full-vector formulations are presented and discussed with the help of the finite difference method. It is demonstrated that the vector nature of the guided modes of the PCFs needs to be considered in analyzing the modal characteristics such as the dispersion. Based on the band structure of 2D photonic crystals, modal characteristics of the PBG-PCFs and TIR-PCFs are obtained and their physical behaviors are easy to explain. Also one new parameter is proposed to judge the single-mode operation of the PCFs, and the bending loss of the PCFs is calculated by the numerical method for the first time. Furthermore, the effects of finite number of air holes and size of interstitial holes on modal properties of the PCFs are investigated. Some scaling transformations of modal properties related to the design parameters of the waveguide structures are derived.

Based on the rigorous analysis model and scaling transformations for the modal properties, a general procedure for design and optimization of the PCFs with desired modal properties is proposed. In comparison with the conventional design method, the new design procedure is more efficient and can be readily automated for the purpose of design optimization. Several applications of the design procedure (e.g., the design optimization for the dispersion shifted fibers, the dispersion flattened fibers, and the dispersion compensation fibers) are demonstrated.

Acknowledgements

I would like to express my sincere thanks and deep appreciation to my supervisor, Dr. Wei-Ping Huang, for his guidance, support, and encouragement throughout this work. I benefited from his diverse insights and interests in every aspect of this work. I would also thank to Dr. Xun Li, Dr. M. Jamal Deen, and Dr. S. Safavi - Naeini, the members of my supervisory committee, for their kind assistance and helpful comments.

Sincere thanks are due to Dr. Chenglin Xu of Apollo Inc. for his help in numerical methods related to modal computations in this work. The use of the photonic CAD software from Apollo Inc. was also acknowledged with deep gratitude.

I would like to deeply appreciate the members of the Photonic Research Group at the Department of Electrical and Computer Engineering for their help and friendship. I would also like to thank the staff of the Department of Electrical and Computer Engineering for their support and collaboration.

Finally, I would like to thank my wife, Hua Wang and our lovely daughters, Julia and Jenny, for their continued love, inspiration, and support.

Contents

List of Figures

List of Tables

Chapter 1

Introduction

Photonic crystal waveguides (PCWs), also referred to in literature as the photonic Bragg waveguides (PBWs) in the one-dimensional (1D) form or the photonic crystal fibers (PCFs) in the two-dimensional (2D) form, constitute a new class of optical waveguide structures formed by introducing certain lattice defects (e.g., dots, lines, or wells) over the photonic crystals (PCs) within the transverse cross-section of the waveguides. Due to the band-gap effect of the PCs, the modal properties of the PCWs may exhibit an array of new features that are distinct from and not readily achievable by the conventional optical waveguides. Because the modal characteristics of the PCWs are essential knowledge for design and analysis of practical optical waveguides, it is very important to understand the operation principles and the unique features of the PCWs. Built on the knowledge obtained from the PCWs, we may further explore potential applications of the guided-wave photonic and opto-electronic devices that are based on the photonic crystal concept in integrated optics and fiber optics.

1.1 Optical Waveguides

Since the low-loss glass fibers developed successfully in the early 1970's [1], optical waveguides have attracted much attention for a wide range of applications such as fiber-optic communications, sensors, optical signal processing and computing, etc. For practical purposes, an optical waveguide may be defined as a longitudinal invariant structure, in which light is confined in a guiding region surrounded by the cladding region and propagates along the longitudinal direction. In general, there are two basic guiding mechanisms for an optical waveguide [2]-[4]: the total internal reflection (TIR) and the anti-resonant reflection (ARR), both of which have been used for realizing the low-loss optical transmission through a waveguide structure.

Conventional optical waveguides (WGs) are composed of a guiding core and a cladding region, in which the refractive index of the core is higher than that of the cladding. The optic field is confined in the core owing to the TIR effect at the core-cladding interface. Currently, the photonic integrated circuits (PICs) and the single-mode fibers, which belong to the conventional optical waveguides, are widely used in integrated optics and fiber optics. On the other hand, if the waveguide structures are properly designed and engineered, the optic field can also be well guided by a core with the lower index via the ARR effect. In general, albeit optical waveguides due to the ARR effect (e.g., the anti-resonant reflecting optical waveguides, or ARROWs) are leaky, the leakage loss can be kept in a very low level. This, in turn, leads to achieve the highly efficient optical transmission through the optical waveguides. Actually, the ARR effect is a special case of the photonic band-gap effect, which is one of main topics in this thesis, and can be easily understood through the band structure of the corresponding optical waveguide structures.

1.2 Photonic Crystals

Since the pioneering works by E. Yablnovitch [5] and S. John [6], the photonic crystals (PCs, also called the photonic band-gap materials, or PBGs) have received considerable interest and inspired much theoretical and experimental works around the world [7]-[12]. In general, the PCs are artificial composite structures whose refractive indices vary periodically along one or more directions. Such a structure resembles the electronic solid-state crystal in which the band structure offers a wide range of the wave characteristics. It is indeed the similarity between the photonic and electronic crystals [13] that captures the imagination of people who desire to explore the plethora of potentials the former may offer. They represent a new class of optical materials that are capable of uniquely controlling or manipulating the electromagnetic radiation within certain frequency bands. Generally, the PCs are characterized by the photonic band structure according to their dielectric periodicity. Figure 1.1 shows simple examples of one-dimensional (1D), two-dimensional (2D) and three-dimensional (3D) PCs [7]. The different colors represent materials with different refractive indices.

Due to the multiple Bragg scattering, analogous to the electronic band structure in semiconductor, the PCs possess a variety of unique features [7] such as the band-gaps (or stop-bands) for the electromagnetic (EM) waves over a certain range of frequencies, the localization of the EM fields near defects, the wave tunnelling, and the scaling transformation of the physical dimension, the refractive index, and the operation frequency. For instance, a 3D PC with the diamond lattice of air spheres has a complete photonic band-gap (PBG) for the EM waves from any directions [7]. It is worth mentioning that 1D PCs (traditionally called the periodic multilayer or thin film structures), which are created by simply stacking planar layers with the proper refractive index and thickness, have been known since the 19th century and are widely used in many areas such as omni-reflection mirrors, DFB lasers, DBR lasers, and interference filters [14], [15].

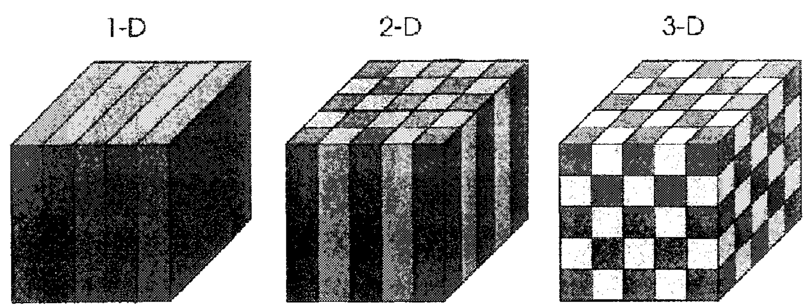

Figure 1.1 Simple examples of 1D, 2D, and 3D photonic crystals

In search for new technologies to tap into the tremendous optical bandwidth available in optical fibers, new optical physical transmission structures and devices are needed to achieve some desirable performances (e.g., compact bend, completely lossless, and controllable dispersion) that current transmission media and devices cannot support. In comparison with the conventional media and devices as shown in Figure 1.2, the PC-based media and devices add more degrees of freedom in controlling the light guiding. They have many potential applications as basic building blocks in the current optical communication systems that contain a large number of individual elements such as laser diodes, modulators, multiplexers/demultiplexers, filters, amplifiers, switches and detectors. Among the various building blocks in integrated optics and fiber optics, as shown in Figure 1.2, PC-based waveguides (e.g., PCWs and PCFs) and devices are expected to play an important role as a promising new enabling technology.

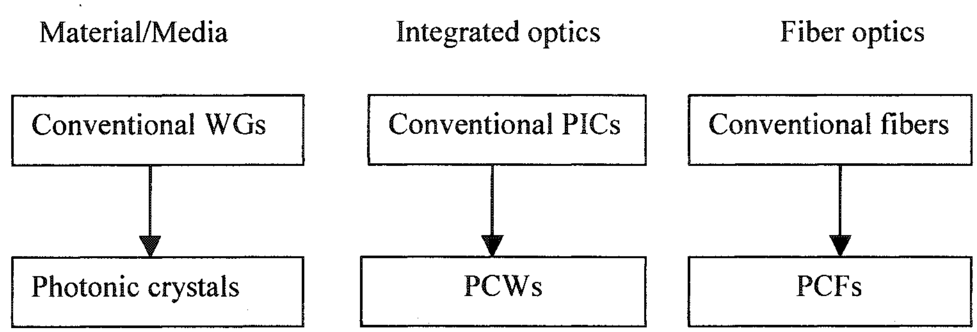

Figure 1.2 Simple applications of the PC-based devices

1.3 Photonic Crystal Waveguides and Fibers

Photonic crystal waveguides (PCWs) are a new class of the optical waveguides and have many unique features that conventional optical waveguides may not possess or are difficult to achieve. By introducing some lattice defects (e.g., dot, line, or well) in the PCs with the proper sizes, localizations of fields (or modes) near defects are created and corresponding photonic crystal devices [including photonic crystal waveguides (PCWs) and photonic crystal cavities (PCCs)] are formed. The surface modes, which are created by the half-infinite PCs, are the special case of the defect-induced modes of PC-based devices. Figure 1.3 shows the simple classifications of the PC-based devices. The only difference between waveguides and cavities is the propagation constant k_z along the propagation axis: $k_z = 0$ for cavities and $k_z \neq 0$ for waveguides.

Judging from the fact if the periodic axis is in the same direction with the propagation direction or not, the PCWs and PCCs can be further divided into two groups:

in-plane and off-plane propagation (or resonance), which have the corresponding field localizations (e.g., 1D, 2D, or 3D) with respect to the dimension of photonic dielectric lattices. In other words, defects in 1D, 2D, and 3D PCs can localize the fields along in 1D, 2D, and 3D dimensions, respectively. As can be seen from Figure 1.3, the so-called photonic crystal fibers (PCFs) belong to the 2D PCWs with off-plane propagation, which are formed in the 2D PCs with dot defects. And the familiar photonic crystal slab waveguides belong to the 2D PCWs with in-plane propagation, which are formed in the 2D PCs with line defects. For the well-known Bragg gratings or the distributed feedback (DFB) structures, they belong to the 1D photonic crystal cavities (PCCs). In this thesis, we mainly focus on the PCWs with off-plane propagation, as underlined in Figure 1.3, which consist of the simplest type of the PCs with the two-material (or a single material with air) system.

- PC - based devices
  - Waveguides
    - In - plane propagation
      - 2D PCWs
        - Infinite 2D PCWs
        - Slab 2D PCWs
      - 3D PCWs
    - <u>Off - plane propagation</u>
      - 1D PCWs
      - 2D PCWs
  - Cavities
    - In - plane resonance
      - 1D PCCs
      - 2D PCCs
      - 3DPCCs
    - Off - plane resonance
      - 1D PCCs
      - 2D PCCs

Figure 1.3 Simple classifications of the PC-based devices

Further, according to the guiding mechanisms, the PCWs are divided into two general categories, namely, the photonic band-gap PCWs (PBG-PCWs) and the total internal reflection PCWs (TIR-PCWs). The PBG-PCWs are made by a reduced index core (e.g., the air-hole defect) within the PCs. Because the effective index of the cladding is always higher than that of the core, the guidance of light in the PBG-PCFs is due to the

PBG effect of the periodic material, as no analogues in conventional index guiding. One of interesting features, partly due to the absence of radiation modes, is the lossless transmission in the sharp bends. Because light travels through air, the PBG-PCWs have the potential to minimize the material absorption effect, the nonlinear effect, and the material dispersion. In general, because the guiding region of the PBG-PCWs is within the stop band of the PCs, it is essential to use the PCs with a larger band-gap to form the PCWs. It is worth to note that, unlike some other PC applications that need the complete band-gap, the partial band-gap is perhaps sufficient to realize the PBG guiding. On the other hand, the TIR-PCWs are made by an increased index core (e.g., pure silica). Because the effective refractive index in the surrounding region is lower than that of the core, light is guided in the core region due to the TIR effect, as analogues in conventional index guiding. Unlike the conventional optical waveguides with the fixed cladding index, the effective cladding index of the TIR-PCWs is a strong function of wavelength and the modes supported by the waveguides are essentially more dispersive. For this reason, the TIR-PCWs have some promised properties (e.g., endlessly single mode operation, highly controllable mode effective area, and highly tunable dispersion) that cannot be readily achieved in the conventional optical fibers. Hence, the PCWs are a new class of the optical waveguides that need to be further researched and developed systematically.

Although some photonic devices based on the 1D PCs have been used for several decades, the photonic devices based on the 2D or 3D PCs for some applications (e.g., the forbidden spontaneous emission) have been researched just over ten years. Because the 3D PCs are very complicated and difficult to fabricate with required precision (e.g., the desired index and dimension), the corresponding 3D PC defects (or disorders) are extremely hard to achieve in the visible or infrared regime. On the other hand, due to ease of fabrication (e.g., advanced planar lithography and mature nanofabrication technology) and compatibility with conventional optical waveguides, the 2D PCs and PCWs have been intensively researched, especially for the silicon-based 2D PCWs with in-plane propagation (i.e., PC slab waveguides) and the silica-based 2D PCWs with off-plane propagation (i.e., PCFs). Owing to the unique ability to guide light around sharp corners (or split beams) and the unique features of the single-mode operation and tunable modal properties (e.g., dispersion and mode effective area), the 2D PCWs show great potential to provide extremely miniature planar circuits (e.g., splitters and couplers) and special optical fibers (e.g., dispersion-shifted fibers). In general, the former can form a variety of elements such as bent, branching, and crossing waveguides and the later can realize various applications (e.g., supercontinuum generation, soliton transmission, and high power transmission). Thanks to the recent advance in various fiber fabrication techniques (e.g., capillary stacking for perform pulling), for example, the silica-based PCFs have shown significant improvements (e.g., the reported losses are steadily dropping from 50 dB/km in 1999 to 0.37 dB/km in 2003 for TIR-PCFs [16] and from 1000 dB/km in 2001 to 13 dB/km in 2002 for PBG-PCFs [17] at the wavelength of 1.55 μm) and are expected to be used in the future optical communication systems.

1.4 Motivation of the Research

Modeling and simulation play important roles in design and engineering of complex optical waveguide structures such as the photonic crystal waveguides (PCWs). By using theoretical models, modal characteristics of the PCWs (e.g., the dispersion, the mode field pattern, the field confinement loss, etc.) can be simulated under different design and operation conditions. A comprehensive analysis will shed light on some of the salient features of the waveguides and lead to new and improved designs for a wide range of applications. Further, the design guideline and optimization procedure for given applications can be developed based on the modeling and simulation techniques. For these reasons, because of the new and unique properties as well as the huge potential applications, a deep understanding of the modal characteristics of the PCWs through comprehensive modeling and simulation is highly desirable.

The PCWs can be modeled and simulated by a number of methods based on scalar and vector formulations, from simple and intuitive analytical approaches (e.g., the effective index method) to time-intensive rigorous numerical approaches (e.g., the finite element method). Despite the seemingly plethora of methods for the modal analysis, the level of accuracy and scope of validity for the scalar and the vector formulations with respect to calculation of the mode dispersion of the PCWs have not been studied in a systematic fashion. Due to the high sensitivity of some modal properties (e.g., the dispersion) on the accuracy of the modal analysis, there has been a significant discrepancy among different published results as pointed out in Ref [18]. Further, the significant contrast in mathematical complexity and computation intensity for the numerical models based on the different formulations also calls for a systematic and comprehensive investigation of the level of accuracy and the scope of validity for these approaches. In this thesis, such a study is performed with the help of the rigorous and versatile mode solvers such as the finite difference method (FDM) [20].

For the propagation applications of the PC-based waveguides, currently there are intensive researches on the 2D PCWs with in-plane (e.g., the photonic crystal slab waveguides) and off-plane propagation (e.g., the PCFs) for the practical purpose. For the 2D PCWs, due to the above-mentioned reasons, accurate and versatile numerical methods, which provide little physical insight into the operation of the PCWs, are employed. The analytical or approximate approaches, although they gain some physical insight into PCW techniques, may not be accurate and only for some specific structures. On the other hand, albeit the 1D PCWs have been researched for several decades and some analytical approaches (e.g., the transfer matrix method) for the 1D PCWs are exact, the 1D PCWs still are a research topic [19]. Also, to the best of our knowledge, the comprehensive analysis on their guiding mechanisms and modal characteristics of the 1D PCWs hasn't been done yet. In this thesis, modal properties of the 1D PCWs are completely investigated with considering some effects (e.g., limited number of the PC pairs) through some rigorous and approximate methods (e.g., the transfer matrix method, the effective index method, and the envelop approximation method), and the physical insight of the 1D PCWs can be understood completely.

In order to utilize some of unique modal characteristics of the PCWs for the design of novel photonic devices with desired modal properties, the conventional design procedure based on some numerical methods is employed. Generally it is a time-consuming and most-likely trial-and-error manual procedure. In order to avoid this shortcoming, a general and automatic procedure for design of the PCWs with desirable properties is proposed. The design model is based on the combination of a rigorous vector mode solver and a scaling transformation for the dispersion properties of the PCWs. In comparison with the conventional design method, the new design procedure is more efficient and can be readily automated for the purpose of design optimization.

1.5 Organization of the Thesis

Chapter 1, entitled *Introduction*, provides a general review of some problems and concepts related to the photonic crystal waveguides (PCWs). Also the scope, focus and objective of the thesis are stated.

Chapter 2, entitled *Modeling Techniques for Photonic Crystal Waveguides and Fibers*, gives a general overview of the modeling and simulation techniques used in the thesis for the modal characteristics of the PCWs, which are essential for understanding the operating principle of the PCWs.

Chapter 3, entitled *One-Dimensional Photonic Crystal Waveguides*, shows the basic optical properties of the 1D PCWs. Due to their simplicity, the deep physical insight can be gained in a highly intuitive way for some of the salient features of the PCWs. With the help of the band-gap structure of the 1D PCs, it is recognized that there are four guiding regimes in the 1D PCWs that depend on the index of the core and the modal characteristics for each regime behave differently from the point of view of guiding mechanism. Furthermore, the modal characteristics analyzed by some approximation methods are also presented.

Chapter 4, entitled *Photonic Crystal Fibers*, presents the modal characteristics of the PCFs through the analytical and numerical modeling tools. It is demonstrated that the vector nature of the guided modes on the PCFs must be considered in analyzing the modal properties. We show that the simple and efficient semi-vector analysis is highly accurate for dispersion of the PCFs and can be utilized in place of the rigorous, yet more complex and costly full-vector mode solvers. The effects on modal characteristics of the PCFs with size of interstitial holes and a finite number of air holes are also investigated, and the scaling transformations of modal properties are obtained.

Chapter 5, entitled *Design of Dispersion Component Elements*, proposes the general procedure to design the dispersion component elements based on the PCFs. In comparison with the conventional design method, the new design procedure is more efficient and can be readily automated for the purpose of design optimization. Several applications of the design procedure (e.g., the dispersion shifted fibers, the dispersion flattened fibers, and the dispersion compensation fibers) are demonstrated and the typical examples are given.

Chapter 6, entitled *Conclusions and Suggestions for Further Research*, summaries the major contributions made in the thesis and lists suggestions for further research.

Appendix A, B, and C, entitled *Performance Parameters of Optical Waveguides*, *Optical Properties of Optical Waveguide Modes*, and *Optical Properties of PC Bloch Modes* give the definitions of performance parameters of optical waveguides and the optical properties related to optical waveguide modes and the PC Bloch modes, respectively.

Chapter 2

Modeling Techniques for Photonic Crystal Waveguides and Fibers

A general overview of the modeling and simulation techniques, which are the basic tools used for the research work in this thesis, is made in this chapter. These modeling techniques are for the solutions of the governing equations for the modal characteristics of the photonic crystal waveguides (PCWs) under certain assumptions and implemented by using different discretizations or base functions. Merits and shortcomings of these methods are discussed in the context of analysis and design of the PCWs with some desired modal properties.

2.1 Introduction

The photonic crystal waveguides (PCWs) can be simulated and analyzed by an array of modeling techniques similar to those used for the modal analysis of the general optical waveguides [21]-[23], especially for the numerical methods such as the finite difference method (FDM) [24]-[26], the finite element method (FEM) [27]-[30], the beam propagation method (BPM) [31]-[34], and the finite difference time domain method (FDTD) [35]-[37]. By incorporating proper numerical boundary conditions such as the perfectly matched layer (PML) boundary conditions [38], all these numerical methods can be used to calculate the optical modes within a relative small spatial domain. These methods are particularly attractive as they solve the governing equations exactly without any approximations. Further, versatile discretization schemes used in these numerical techniques make them applicable for waveguide structures of arbitrary index profiles and/or geometric shapes. The shortcomings of the numerical methods are the demand for heavy computation resources and the lack of intuitive physical insight. In this respect, the analytical and semi-analytical approaches that take into consideration the unique features of the PCWs offer deep insight and often more efficient for a specific structure of the PCWs. Some of these semi-analytical methods (i.e., the mode expansion methods) such as sinusoidal expansion methods (e.g., plane wave method, PWM [39]-[42]), Hermite-Gaussian expansion methods (e.g., localized function method, LFM [43]-[45]), and cylindrical expansion methods (e.g., multipole expansion method, MEM [46]-[48]) can be considered to be exact if a set of sufficiently large base functions in the solutions is employed. Other analytical methods such as the effective index method (EIM) [49] and the envelope approximate method (EAM) [50]-[52] rely on approximations that are only valid under certain conditions. In some sense, they are simple, efficient, and can provide some deep physical insight on the operation principle of the PCWs (e.g., single-mode operation). In this chapter, we will describe these modeling techniques (i.e., FDM, PWE, EIM, and EAM) in great detail, which are used to investigate modal properties of the PCWs, calculate the band structure of the PCs, and verify the simulation results.

2.2 Theoretical Formulations

Without loss of generality, we start our modeling formulations for the PCWs with following assumptions:

(i) Region we are interested in is the absence of sources (e.g., free charges or currents).

(ii) Material we consider is linear and isotropic. The permittivity of material is equal to $n^2(r)\varepsilon_0$, where $n(r)$ is the refractive index of material and ε_0 is the permittivity of free space.

(iii) Material we use has a magnetic permeability μ that closes to the permeability μ_0 of free space.

(iv) Electromagnetic fields are time-harmonic fields: $\vec{H}(r,t) = \mathrm{Re}\{\vec{H}(r)e^{j\omega t}\}$ and $\vec{E}(r,t) = \mathrm{Re}\{\vec{E}(r)e^{j\omega t}\}$, where ω is the angular frequency.

Under these assumptions, the Maxwell's equations can be expressed in the frequency domain as follows:

$$\begin{aligned}
&\nabla \times \vec{E}(r) = -j\omega\mu\vec{H}(r) \\
&\nabla \times \vec{H}(r) = j\omega n^2(r)\vec{E}(r) \\
&\nabla \cdot [n^2(r)\vec{E}(r)] = 0 \\
&\nabla \cdot \vec{H}(r) = 0
\end{aligned} \tag{2.1}$$

where $\vec{E}(r)$ and $\vec{H}(r)$ are electric and magnetic fields and r is a position vector to define a particular location in space (x, y, z) at which the field is measured. It is note that the vector sign "$\rightarrow$" of the position vector $\vec{r}$ is dropped without ambiguity. By taking the curl of the first (second) equation above and substituting into the second (first) equation, we can eliminate one of electric (magnetic) fields to obtain the well-known full-vector wave equations:

$$\begin{aligned}
&\nabla \times [\nabla \times \vec{E}(r)] - (\frac{\omega}{c})^2 n^2(r)\vec{E}(r) = 0 \\
&\nabla \times [\frac{1}{n^2(r)}\nabla \times \vec{H}(r)] - (\frac{\omega}{c})^2 \vec{H}(r) = 0
\end{aligned} \tag{2.2}$$

where c is the speed of light in free space.

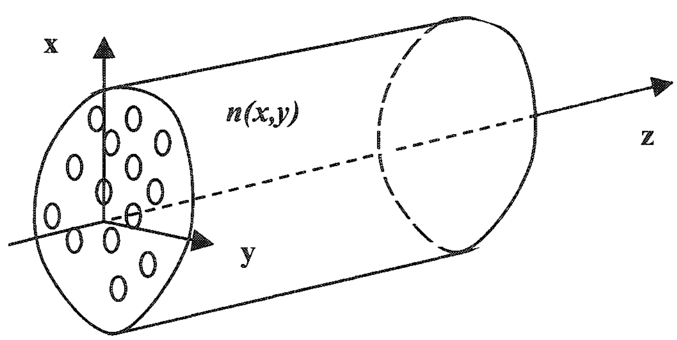

Figure 2.1 The generalized photonic crystal waveguide with off-plane propagation

Further, we assume that the PCW structure (i.e., the PCW with off-plane propagation) to be simulated consists of a cylindrical dielectric waveguide whose refractive index is invariant along the propagation direction z as shown in Figure 2.1. In general, the cross-section of the optical waveguide (i.e., the PCW) consists of the 1D or 2D PCs with some defects.

Due to the uniform nature of the waveguide along z, the solutions of the above wave equations (or so-called the modal solutions) with the appropriate boundary conditions take the following forms for the electric and magnetic (EM) fields:

$$\bar{E}(r) = (\bar{E}_t + \hat{z}E_z)e^{-jk_z z}$$
$$\bar{H}(r) = (\bar{H}_t + \hat{z}H_z)e^{-jk_z z} \tag{2.3}$$

where k_z is the propagation constant of the PCW modes along z and $\bar{E}_t / \bar{H}_t$ and E_z / H_z are modal field patterns related to transverse and longitudinal EM fields, respectively. By utilizing the operator ∇ (i.e., $\nabla_t + \hat{z}\partial/\partial z$), after some algebraic manipulations, the wave equation (2.2) can be written as the vector wave equations for the transverse fields and longitudinal fields, respectively:

$$\{\nabla_t^2 + k^2n^2 + \nabla_t(\nabla_t \ln n^2 \cdot)\}\bar{E}_t = k_z^2\bar{E}_t$$
$$\{\nabla_t^2 + k^2n^2 + (\nabla_t \ln n^2)\times(\nabla_t \times)\}\bar{H}_t = k_z^2\bar{H}_t \tag{2.4}$$

$$\{\nabla_t^2 + k^2n^2\}E_z - jk_z(\nabla_t \ln n^2 \cdot \bar{E}_t) = k_z^2 E_z$$
$$\{\nabla_t^2 + k^2n^2 - (\nabla_t \ln n^2)\cdot(\nabla_t)\}H_z - jk_z(\nabla_t \ln n^2 \cdot \bar{H}_t) = k_z^2 H_z \tag{2.5}$$

where ∇_t (i.e., $\hat{y}\partial/\partial y + \hat{x}\partial/\partial x$) is the transverse gradient operator and k (i.e., ω/c) is the propagating constant in free space. It is worth to note, after solving one of two above vector wave equations for $\bar{E}_t$ (or $\bar{H}_t$), the another transverse field for $\bar{H}_t$ (or $\bar{E}_t$) can be obtained according to the duality of Maxwell's equation. Also, from the divergence equations of the Maxwell's equation, the corresponding z-components (E_z and H_z) can be calculated, and vice versa. Here we focus only on the transverse fields. By extending the transverse electric and magnetic fields into the x and y directions with some derivations, the full-vectorial wave equations in terms of the transverse electric and magnetic fields of the waveguides are expressed in simple matrix forms [20]:

$$\begin{pmatrix} P_{xx} & P_{xy} \\ P_{yx} & P_{yy} \end{pmatrix}\begin{pmatrix} E_x \\ E_y \end{pmatrix} = k_z^2 \begin{pmatrix} E_x \\ E_y \end{pmatrix} \tag{2.6}$$

$$\begin{pmatrix} Q_{xx} & Q_{xy} \\ Q_{yx} & Q_{yy} \end{pmatrix}\begin{pmatrix} H_x \\ H_y \end{pmatrix} = k_z^2 \begin{pmatrix} H_x \\ H_y \end{pmatrix} \tag{2.7}$$

where $\bar{E}_t = \hat{x}E_x + \hat{y}E_y$, $\bar{H}_t = \hat{x}H_x + \hat{y}H_y$, and P and Q are the operators, which are defined as follows:

$$\begin{aligned}
P_{xx}E_x &= n^2k^2E_x + \frac{\partial}{\partial x}\left[\frac{1}{n^2}\frac{\partial}{\partial x}\left(n^2E_x\right)\right] + \frac{\partial^2 E_x}{\partial y^2} \\
P_{yy}E_y &= n^2k^2E_y + \frac{\partial}{\partial y}\left[\frac{1}{n^2}\frac{\partial}{\partial y}\left(n^2E_y\right)\right] + \frac{\partial^2 E_y}{\partial x^2} \\
P_{xy}E_y &= \frac{\partial}{\partial x}\left[\frac{1}{n^2}\frac{\partial}{\partial y}\left(n^2E_y\right)\right] - \frac{\partial^2 E_y}{\partial y \partial x} \\
P_{yx}E_x &= \frac{\partial}{\partial y}\left[\frac{1}{n^2}\frac{\partial}{\partial x}\left(n^2E_x\right)\right] - \frac{\partial^2 E_x}{\partial x \partial y}
\end{aligned} \tag{2.8}$$

$$\begin{aligned}
Q_{xx}H_x &= n^2k^2H_x + \frac{\partial^2 H_x}{\partial x^2} + n^2\frac{\partial}{\partial y}\left[\frac{1}{n^2}\frac{\partial H_x}{\partial y}\right] \\
Q_{yy}H_y &= n^2k^2H_y + \frac{\partial^2 H_y}{\partial y^2} + n^2\frac{\partial}{\partial x}\left[\frac{1}{n^2}\frac{\partial H_y}{\partial x}\right] \\
Q_{xy}H_y &= \frac{\partial^2 H_y}{\partial y \partial x} - n^2\frac{\partial}{\partial y}\left[\frac{1}{n^2}\frac{\partial H_y}{\partial x}\right] \\
Q_{yx}H_x &= \frac{\partial^2 H_x}{\partial x \partial y} - n^2\frac{\partial}{\partial x}\left[\frac{1}{n^2}\frac{\partial H_x}{\partial y}\right]
\end{aligned} \tag{2.9}$$

where all functions under the partial differential operators are continuous over the entire cross-section of the waveguide. It is worth to note that the full-vector wave equations are exact without any approximation and considers both the polarization dependence (i.e., $P_{xx} \neq P_{yy}$ and $Q_{xx} \neq Q_{yy}$) and the polarization coupling (i.e., $P_{xy} \neq 0$, $P_{yx} \neq 0$, $Q_{xy} \neq 0$, and $Q_{yx} \neq 0$), which are caused by the waveguide geometry. The full-vector modes have hybrid mode field patterns and are orthogonal with respect to the guided power along the propagation direction z (see Appendix B).

If the polarization coupling is weak and becomes negligible as in many practical optical waveguides, the full-vector equations are reduced to two decoupled semi-vector wave equations for the electrical and magnetic fields:

$$P_{xx}E_x = k_z^2 E_x$$

$$P_{yy}E_y = k_z^2 E_y \tag{2.10}$$

$$Q_{xx}H_x = k_z^2 H_x$$

$$Q_{yy}H_y = k_z^2 H_y \tag{2.11}$$

where P_{xy} = P_{yx} = Q_{xy} = Q_{yx} = 0 was assumed. From the above equations, the characteristics of the semi-vector modes (so-called the semi-vectorial approximation) are linearly polarized (i.e., the TE and TM modes), in which one of two components of the fields is zero.

Furthermore, if the waveguide is weakly guiding, even the polarization dependence can be ignored. Under this circumstance, the two semi-vector equations ($k_z^{TE} \neq k_z^{TM}$) are reduced to a single well-known scalar Helmholtz wave equation ($k_z^{TE} = k_z^{TM} = k_z$):

$$P\Phi = k_z^2 \Phi \tag{2.12}$$

where P is the scalar operator (i.e., $P_{xx} = P_{yy} = Q_{xx} = Q_{yy} = n^2k^2 + \partial^2/\partial x^2 + \partial^2/\partial y^2$) and Φ is the scalar field (i.e., E_x, E_y, E_z, H_x, H_y, or H_z). From the above equations, the characteristics of the scalar modes are linearly polarized (i.e., the degenerated TE and TM modes with the same k_z).

For 1D PCWs, where the refractive index $n(x)$ is the function of x and the y-dependence in above equations will disappear (i.e., $\partial/\partial y = 0$), the full-vector equations are simplified to two decoupled wave equations for the electrical and magnetic fields:

$$P_{xx}E_x = n^2k^2E_x + \frac{d}{dx}\left[\frac{1}{n^2}\frac{d}{dx}\left(n^2E_x\right)\right]$$

$$P_{yy}E_y = n^2k^2E_y + \frac{d^2E_y}{dx^2} \tag{2.13}$$

$$Q_{xx}H_x = n^2k^2H_x + \frac{d^2H_x}{dx^2}$$

$$Q_{yy}H_y = n^2k^2H_y + n^2\frac{d}{dx}\left[\frac{1}{n^2}\frac{dH_y}{dx}\right] \tag{2.14}$$

where $P_{xy} = P_{yx} = Q_{xy} = Q_{yx} = 0$ was used. These decoupled wave equations for the TE wave and the TM wave can be solved through the wave field E_y/H_x and E_x/H_y, respectively. It is noted that E_y/H_x and E_x/H_y are governed by the same wave equation.

Based on the above theoretical formulas, we can obtain the dispersion curves by solving the governing equations for the transverse electric or magnetic fields under the full-vector or semi-vector/scalar assumptions for the 1D and 2D PCWs.

2.3 Finite Difference Method

Due to the simplicity and easy implementation, the FDM method is one of the most commonly used numerical methods for the boundary-value eigen-value problem. It is based on a semi-local approximation of the partial derivative through low-order Taylor series expansions. For example, the central difference approximation of the second derivative for the function F with the variable f can be derived easily:

$$\frac{\partial^2 F}{\partial f^2} = \frac{2}{h_1 + h_2}\left(\frac{F^{i+1}}{h_1} - F^i\left(\frac{1}{h_1} + \frac{1}{h_2}\right) + \frac{F^{i-1}}{h_2}\right) + O(\Delta_i^2)$$

$$\frac{\partial}{\partial f}\left(\frac{1}{n^2}\frac{\partial(n^2 F)}{\partial f}\right) = \frac{2}{h_1 + h_2}\left(F^{i+1}\frac{n_{i+1}^2}{h_2 n_{i+1/2}^2} - F_x^i\left(\frac{n_i^2}{h_2 n_{i+1/2}^2} + \frac{n_i^2}{h_1 n_{i-1/2}^2}\right) + F^{i-1}\frac{n_{i-1}^2}{h_1 n_{i-1/2}^2}\right) + O(\Delta x_i^{\ 2})$$

where the non-uniform mesh sizes Δ_{i-1}, Δ_i, and Δ_{i+1} are used and n_i is the refractive index at the mesh i as shown in Figure 2.2. The mesh distances are that $h_1 = (\Delta_{i-1}+\Delta_i)/2$ and $h_2 = (\Delta_{i+1}+\Delta_i)/2$. The refractive indices at the mesh nodes are that $n_{i-1/2}^2 = (n_{i-1}^2\Delta_{i-1} + n_i^2\Delta_i)/2h_1$ and $n_{i+1/2}^2 = (n_{i+1}^2\Delta_{i+1} + n_i^2\Delta_i)/2h_2$.

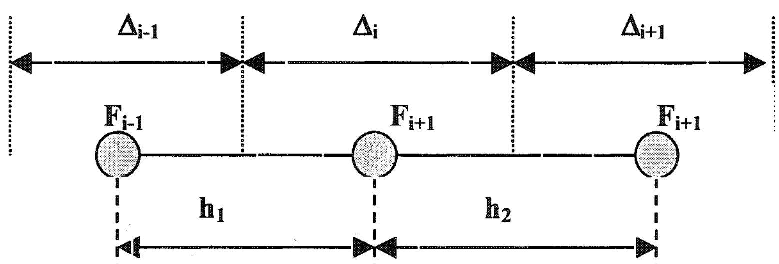

Figure 2.2 The 1D finite difference (FD) mesh

As mentioned early, all functions under the partial derivatives in the full-vector eigen-value equations of (2.5) and (2.6) are continuous and they are directly discretized by using the central difference approximations without any extra treatment at the dielectric interface of the waveguide. For example, the finite difference expressions of wave equations of (2.5) and (2.7) (for electric fields) can be expressed as follows [20]:

$$P_{xx}E_x = \frac{T_x^{i+1,j}E_x^{i+1,j} - T_x^{i,j}E_x^{i,j} + T_x^{i-1,j}E_x^{i-1,j}}{\Delta x^2} + n_{i,j}^2 k^2 E_x^{i,j} + \frac{E_x^{i,j+1} - 2E_x^{i,j} + E_x^{i,j-1}}{\Delta y^2}$$

$$P_{yy}E_y = \frac{T_y^{i,j+1}E_y^{i,j+1} - T_y^{i,j}E_y^{i,j} + T_y^{i,j-1}E_y^{i,j-1}}{\Delta y^2} + n_{i,j}^2 k^2 E_y^{i,j} + \frac{E_y^{i+1,j} - 2E_y^{i,j} + E_y^{i-1,j}}{\Delta x^2}$$

$$P_{xy}E_y = \frac{1}{4\Delta x\Delta y}\begin{bmatrix} \left(\dfrac{n_{i+1,j+1}^2}{n_{i+1,j}^2}-1\right)E_y^{i+1,j+1} - \left(\dfrac{n_{i+1,j-1}^2}{n_{i+1,j}^2}-1\right)E_y^{i+1,j-1} - \\ \left(\dfrac{n_{i-1,j+1}^2}{n_{i-1,j}^2}-1\right)E_y^{i-1,j+1} + \left(\dfrac{n_{i-1,j-1}^2}{n_{i-1,j}^2}-1\right)E_y^{i-1,j-1} \end{bmatrix}$$

$$P_{yx}E_x = \frac{1}{4\Delta x\Delta y}\begin{bmatrix} \left(\dfrac{n_{i+1,j+1}^2}{n_{i,j+1}^2}-1\right)E_x^{i+1,j+1} - \left(\dfrac{n_{i+1,j-1}^2}{n_{i,j+1}^2}-1\right)E_x^{i+1,j-1} - \\ \left(\dfrac{n_{i-1,j+1}^2}{n_{i,j-1}^2}-1\right)E_x^{i-1,j+1} + \left(\dfrac{n_{i-1,j-1}^2}{n_{i,j-1}^2}-1\right)E_x^{i-1,j-1} \end{bmatrix} \tag{2.15}$$

where

$$T_x^{i\pm1,j} = \frac{2n_{i\pm1,j}^2}{n_{i\pm1,j}^2+n_{i,j}^2}, T_y^{i,j\pm1} = \frac{2n_{i,j\pm1}^2}{n_{i,j\pm1}^2+n_{i,j}^2}$$

$$T_x^{i\pm1,j} = \frac{2n_{i,j}^2}{n_{i+1,j}^2+n_{i,j}^2} + \frac{2n_{i,j}^2}{n_{i-1,j}^2+n_{i,j}^2}, T_y^{i,j\pm1} = \frac{2n_{i,j}^2}{n_{i,j+1}^2+n_{i,j}^2} + \frac{2n_{i,j}^2}{n_{i,j-1}^2+n_{i,j}^2}$$

where the uniform meshes Δx and Δy are used for the sake of simplicity.

In order to facilitate numerical solution within a finite computation domain, proper numerical boundary conditions must be used. In this work, we utilizes the popular perfectly matched layer (PML) boundary conditions [38] at the edge of the computation window to reduce the computation effort without sacrifice for accuracy and the graded index averaging technique [25] to improve the numerical accuracy. By substituting the above finite difference expressions into the wave equation of (2.5), a system of the linear equations is obtained:

$$M\begin{bmatrix} E_x \\ E_y \end{bmatrix} = (kN_{eff})^2 \begin{bmatrix} E_x \\ E_y \end{bmatrix} \tag{2.16}$$

where k is the propagating constant in free space, N_{eff} is the complex modal effective index, and M is a band matrix with the bandwidth ($4N_x$+6) and dimension $2N_x$xN_y, in which N_x and N_y are the numbers of meshes in x and y directions. For the semi-vectorial and scalar cases, due to the decoupled wave equations, the band matrix M is simplified a matrix with the bandwidth $(2N_x+1)$ and dimension N_xxN_y. The effective indices and mode profiles can be obtained by using some eigen-value solvers such as the shifted inverse power method, the Lanczos method, and the Arnoldi method. Due to store all non-zero elements of the matrix, the FDM requires a larger computer memory. By taking the advantage of the geometric symmetry, only a half or a quarter of the PCW is need to be simulated. In comparison with the FEM method, the FDM method is free of spurious eigenvalues. It is worth to note that, by utilizing the variation theorem (see 3.3.3), the band structure of the PCs can be calculated by utilizing the periodic boundary conditions around the unit cell of the PCs.

2.4 Plane Wave Expansion Method

The modal expansion methods, such as the plane-wave expansion (PWE) method, employ a set of orthogonal functions (e.g., harmonic or Gauss-Hermite functions) to represent the unknown solution of the equations. Generally speaking, the dispersion curves and mode field patterns of the defect modes of the PCWs can be calculated by the so-called a supercell method as shown in Figure 2.3, which employs the periodic boundary condition. Theoretically, the coupling between the PCWs (or supercells) can be neglected when the width D (e.g., D = 5Λ in Figure 2.3) of the supercell is sufficiently large. However, the computation time will increase accordingly. Practically, the width of the supercell is taken from 5Λ to 32Λ. We present this theory very briefly to calculate the modal properties of the PCWs.

For the sake of simplicity, the wave equation (2.2) of the magnetic field $\bar{H}(r)$, which contain only two transverse fields $\hat{e}_n$ (n = 1 and 2), is considered and rewritten as

$$\nabla\times[\frac{1}{n^2(\rho)}\nabla\times\bar{H}(r)]=\frac{\omega^2}{c^2}\bar{H}(r) \tag{2.17}$$

where $n(\rho)$ is the refractive index of the media and $\bar{r}=x\hat{x}+y\hat{y}+z\hat{z}=\bar{\rho}+z\hat{z}$ is the position vector.

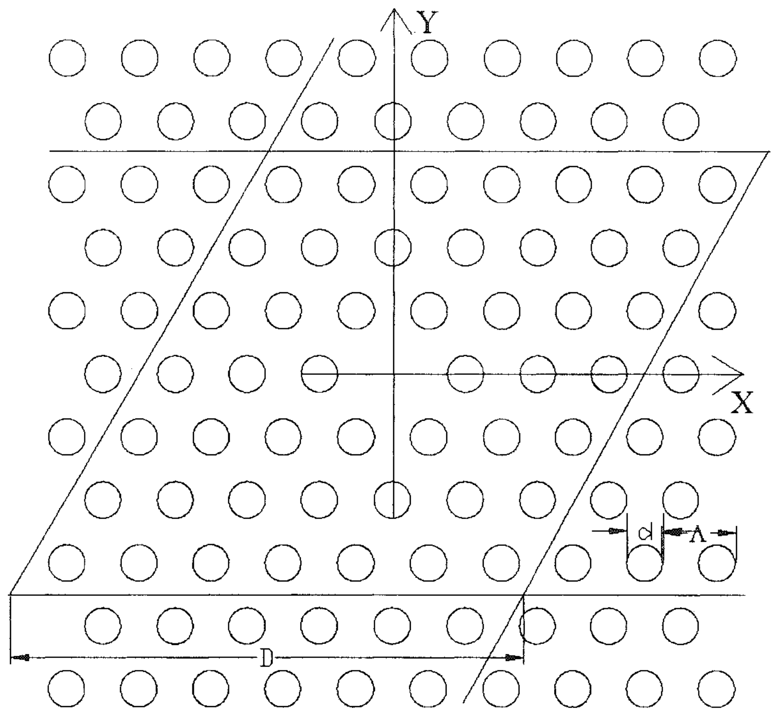

Figure 2.3 The cross-section of a 2D PCW with off-plane propagation

For the infinite supercell structure with periodic dielectric function ($n(\rho)=n(\rho+R)$), the well-known Bloch-Floquet theorem ($u(r)=u(r+R)$) can be applied, in which the fields of Bloch modes in periodic structures consist of plane waves:

$$\vec{H}(r)=\hat{e}_n u(r) e^{j\vec{k}\cdot\vec{r}}=e^{jk_z z}\sum_{G,n} u_{n,G}\hat{e}_n e^{j(\vec{k}_{//}+\vec{G})\cdot\vec{\rho}} \tag{2.18}$$

where $\vec{k}$ $(=\vec{k}_{//}+k_z\hat{z})$ is the wave vector of the plane waves, $\vec{G}$ is the reciprocal lattice vector in the *x-y* plane , $u_{n,G}$ (n =1 and 2) is the Bloch function of the magnetic fields along $\hat{e}_n$, and $\hat{e}_n$(n = 1 and 2) stands for two unit vectors, which are perpendicular to the propagation direction $\vec{k}+\vec{G}$. The relation between the reciprocal lattice vector $\vec{G}$ ($\vec{G}=m_1\vec{b}_1+m_2\vec{b}_2$) and the lattice vector $\vec{R}$ ($\vec{R}=l_1\vec{a}_1+l_2\vec{a}_2$) can be easily obtained through the orthogonality between their corresponding base vector components $\vec{a}_i$ and $\vec{b}_j$ (i, j = 1 and 2):

$$\vec{a}_i \cdot \vec{b}_j = 2\pi\delta_{ij} \tag{2.19}$$

where δ_{ij} is the Kronecker-δ function. On the other hand, due to the periodicity of the supercell, the index function can be expanded into the following Fourier series:

$$\frac{1}{n^2(\rho)} = n^{-2}(\rho) = \sum_G n_G^{-2} e^{j\vec{G}\cdot\vec{\rho}} \tag{2.20}$$

where $n_G^{-2} = (\int_S n^{-2}(\rho) e^{-j\vec{G}\cdot\vec{\rho}} dS)/S$ is the coefficient of the index function in the unit cell S. It is worth to note that, through a procedure for calculation of the Fourier transform n_G^2 of $n^2(r)$ and inversion numerically to obtain n_G^{-2}, rapid numerical convergence is achieved [12]. By substituting (2.18) and (2.20) into (2.17), after some algebraic manipulations, the equation (2.17) is reduced to a standard eigenvalue equation:

$$\sum_{G'} |\vec{k}+\vec{G}||\vec{k}+\vec{G}'| n_{G-G'}^{-2} \begin{bmatrix} \hat{e}_2 \cdot \hat{e}'_2 & -\hat{e}_2 \cdot \hat{e}'_1 \\ -\hat{e}_1 \cdot \hat{e}'_2 & \hat{e}_1 \cdot \hat{e}'_1 \end{bmatrix} \begin{pmatrix} u_{1,G'} \\ u_{2,G'} \end{pmatrix} = \frac{\omega^2}{c^2} \begin{pmatrix} u_{1,G} \\ u_{2,G} \end{pmatrix} \tag{2.21}$$

where the two orthogonal systems $(\vec{k}+\vec{G}, \hat{e}_1, \hat{e}_2)$ and $(\vec{k}+\vec{G}', \hat{e}'_1, \hat{e}'_2)$ are used. It is worth to note that the first column of the matrix is related to the fields along $\hat{e}'_1$ and the second column of the matrix is related to the fields along $\hat{e}'_2$. In general, the calculated mode is a hybrid mode because two polarizations of the modal fields are coupled with each other. For the N grid points of the G vector, the above equation is a set of $2N$ equations with $2N$ unknowns and can be written in matrix form:

$$\begin{bmatrix} P_{11} & P_{12} \\ P_{21} & P_{22} \end{bmatrix} \begin{bmatrix} U_1 \\ U_2 \end{bmatrix} = (\frac{\omega}{c})^2 \begin{bmatrix} U_1 \\ U_2 \end{bmatrix} \tag{2.22}$$

where ω is the angular frequency (eigenvalue) for the corresponding polarization, P_{11}, P_{12}, P_{21}, and P_{22} are the N by N coefficient matrices, and U_1, U_2 are the 1 by N matrices of the Bloch function (eigenvector). Here the elements of N by N coefficient matrices are defined as follows:

$$\begin{bmatrix} P_{11} & P_{12} \\ P_{21} & P_{22} \end{bmatrix}_{ij} = |\vec{k}+\vec{G}_i||\vec{k}+\vec{G}_j| n_{G_i-G_j}^{-2} \begin{bmatrix} \hat{e}_{2i}\cdot\hat{e}_{2j} & -\hat{e}_{2i}\cdot\hat{e}_{1j} \\ -\hat{e}_{1i}\cdot\hat{e}_{2j} & \hat{e}_{1i}\cdot\hat{e}_{1j} \end{bmatrix} \tag{2.23}$$

where $i, j = 1, 2, 3, \ldots, N$. Thus, the calculation of the guided modes for the PCWs has been reduced to the solution of a standard eigen-value problem.

Furthermore, for the 1D PCWs, $\vec{k}$ is in the x-z plane, $\vec{G}$ is along x axis, and $\vec{k}+\vec{G}$ are in the x-z plane with $\vec{k}+\vec{G} = |\vec{k}+\vec{G}|(\sin\alpha, 0, -\cos\alpha)$, where α is an arbitrary angle taken in the x-z plane. According to the orthogonal property of (2.18), two unit vectors can be set to $\hat{e}_1 = (\cos\alpha, 0, \sin\alpha)$ and $\hat{e}_2 = \hat{y}$. The elements of N-by-N coefficient matrices can be simplified as follows:

$$\begin{bmatrix} P_{11} & P_{12} \\ P_{21} & P_{22} \end{bmatrix}_{ij} = |\vec{k}+\vec{G}_i||\vec{k}+\vec{G}_j| n_{G_i-G_j}^{-2} \begin{bmatrix} 1 & 0 \\ 0 & \cos(\alpha_i - \alpha_j) \end{bmatrix} \tag{2.24}$$

Therefore, the eigenvalue equation can also be reduced to two decoupled equations:

$$\begin{bmatrix} P_{11} & 0 \\ 0 & P_{22} \end{bmatrix} \begin{bmatrix} U_1 \\ U_2 \end{bmatrix} = \left(\frac{\omega}{c}\right)^2 \begin{bmatrix} U_1 \\ U_2 \end{bmatrix} \tag{2.25}$$

where the former is for the TE wave with $U_2 = 0$ and the latter is for the TM wave with $U_1 = 0$. It is worth to note that, by replacing the supercell of the PCW with the unit cell of the PC, the band structure of the PC can be easily calculated.

2.5 Envelope Approximation Method

Due to similarities between the electric band-gap and the PBG, many theories of the electric band-gap (e.g., effective mass method, $k \cdot p$ theory, and multiple-scales analysis, etc.) can be borrowed for the analysis of the PCWs. The idea behind these methods is based on the perturbation theory, and the process of these methods involves two basic steps: first evaluate the band structure of the PC to obtain the effective "mass", and then replace the PC with this effective "mass" to construct a conventional waveguide [50]-[52]. This, in turn, leads to solve the conventional wave equations to obtain dispersion relations of the PCWs under the slowly varying envelope approximation. For the sake of simplicity, we focus on the analysis of the heterostructure PCWs as shown in Figure 2.4, which are considered as small perturbations of the bulk PCs and their physical dimensions (e.g., $2W$ or $2R$) are substantially larger than those of the PCs (e.g., the pitch Λ). By following Ref [50] and starting from the scalar wave equation (2.12), we present this theory very briefly.

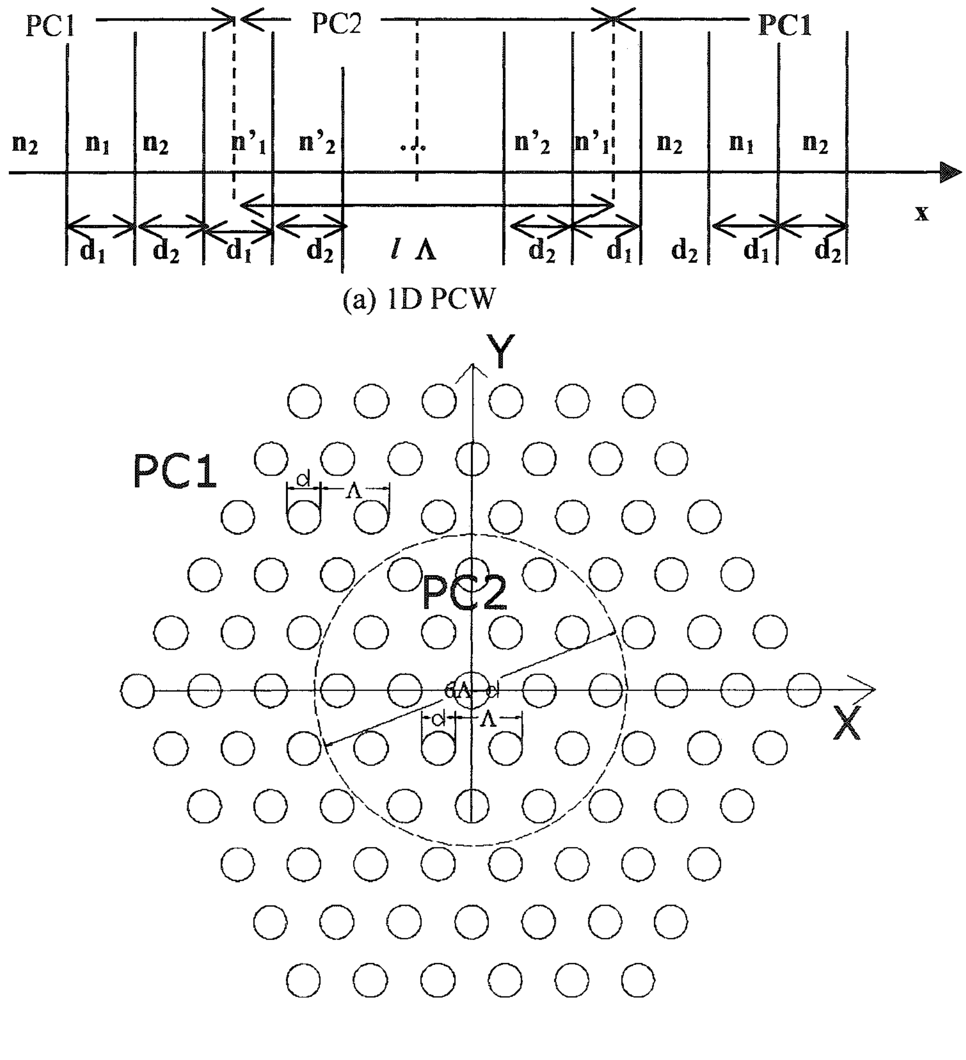

(a) 1D PCW

(b) 2D PCW

Figure 2.4 The cross-section of the 1D (a) and 2D (b) heterostructure PCWs

Here the heterostructure PCW is considered as small perturbations of the bulk PCs with the index of $n_d^2(\rho) = n^2(\rho)(1+\Delta(\rho))$ as shown in Figure 2.4 (here "PC1" represent the bulk PC and "PC2" represent the perturbated PC, and $\rho = x$ for the 1D PCW). The wave equation for the electric field $\vec{E}_d(\rho)$ with frequencies ω_d is expressed as follows

$$\nabla_t^2 \vec{E}_d(\rho) - k_z^2 \vec{E}_d(\rho) = \frac{\omega_d^{\ 2}}{c^2} n^2(\rho)(1+\Delta(\rho))\vec{E}_d(\rho) \tag{2.26}$$

where $n(\rho)$ is the refractive index of the bulk PC and $\Delta(\rho)$ is a relative small perturbation of the PCW. Due to the orthogonality of electric field modes, the electric field $\vec{E}_d(\rho)$ can be expanding into the basis of the bulk PC modes:

$$\vec{E}_d(\rho) = \sum_n \int_k W_n(k)\vec{E}_{nk}(\rho)dk \tag{2.27}$$

where $\vec{E}_{nk}(\rho)$ is the field pattern of bulk PC modes that meet the wave equation (2.12) without considering perturbations with its angular frequency ω_n and $W_n(k)$ is an unknown function defining the expansion of the modes in k space. Then the wave equation (2.26) can be expressed as

$$\sum_n \int_k W_n(k)\omega_n^{\ 2}(k)n^2(\rho)\vec{E}_{nk}(\rho)dk = \sum_n \int_k W_n(k)\omega_d^{\ 2} n_d^2(\rho)\vec{E}_{nk}(\rho)dk \tag{2.28}$$

By taking the inner product between the above equation and $\vec{E}^*_{n'k'}(\rho)$ and utilizing the orthogonality of the modes (see Appendix C), we have [50]

$$W_{n'}(k')\omega^2{}_{n'}(k') = \int_{cell} F_{n'}(\rho)\omega_d^{\ 2}(1+\Delta(\rho))e^{-jk'\rho}d\rho \tag{2.29}$$

where the wave equation of the PC modes and the definition of the envelope function of the mode $F_n(r) = \int_k W_n(k)e^{jk\cdot\rho}dk$ were used. The equation (2.29) contains the inverse Fourier transform of the product $F_{n'}(k)\Delta(\rho)$. By taking the Fourier transform of the projection of (2.29) along $E_{n'k'}$ and dropping the primes, the equation describing the behavior of the envelope of the mode of the PCWs is obtained [50]:

$$\int_k W_n(k)\omega^2{}_n(k)e^{jk\rho}dk = \omega^2{}_n(-j\nabla)F_n(\rho) = F_n(\rho)\omega_d{}^2(1+\Delta(\rho)) \tag{2.30}$$

where $\omega^2{}_n(-j\nabla)$ is the operator obtained from $\omega^2{}_n(k)$ by replacing the wave vector components k_x and k_y by their derivatives $-j\partial/\partial x$ and $-j\partial/\partial y$. The equation (2.30) is generally called as the envelope equation. If we assume that it is independent for every band and $\vec{E}_{dn}(\rho) = \int_k W_n(k)\vec{E}_{nk}(\rho)dk$ donates as the waveguide mode having the frequency ω_{dn} associated with the band n, the operator $\omega^2{}_n(-j\nabla)$ can be expanded in the vicinity of the wave vector k_0 of light in the PC as [50]

$$\omega^2{}_n(-j\nabla) = \omega_n{}^2(k_0) + \sum_{\xi=x,y}\frac{\partial\omega_n{}^2}{\partial k_\xi}|_{k_0}\left(\frac{\partial}{j\partial\xi} - k_{0\xi}\right) + \sum_{\xi=x,y}\frac{\partial^2\omega_n{}^2}{2\partial k_\xi^2}|_{k_0}\left(\frac{\partial}{j\partial\xi} - k_{0\xi}\right)^2 + \ldots \tag{2.31}$$

which suggests a solution of the envelope equation of the form $F_{nk_0}(\rho) = f_{nk_0}(\rho)e^{jk_0\rho}$. Therefore, the modes may be written due to the fact of $F_{nk_0}(\rho) = \int_k W_n(k)e^{jk\rho}dk$ and $W_n(k) = \tilde{f}_{nk_0}(k-k_0)$, and we have

$$\vec{E}_{dnk_0}(\rho) = e^{jk_0\rho}\int_k \tilde{f}_{nk_0}(k-k_0)u_{nk}(r)e^{j(k-k_0)\rho}dk \tag{2.32}$$

where $\tilde{f}_{nk_0}(k)$ denotes the inverse Fourier transform of $f_{nk_0}(\rho)$. Because the function $f_{nk_0}(\rho)$ varies over the same length scale as $\Delta(\rho)$, its Fourier components $\tilde{f}_{nk_0}(k-k_0)$ take large values for $k \approx k_0$ only. Assuming that $u_{nk}(\rho) = u_{nk0}(\rho)$ over this range, we remove $u_{nk0}(\rho)$ from the integral to obtain

$$\vec{E}_{dnk_0}(\rho) = u_{nk_0}(\rho)F_{nk_0}(\rho) = E_{nk_0}(\rho)f_{nk_0}(\rho) \tag{2.33}$$

The physical meaning behind the envelope functions F_{nk0} is the fact that the fields of the PCWs are determined by the bulk PC modes with modulation of the envelope functions. By getting the envelope equation (2.30) of the mode of the PCWs, the envelope equation can be solved by employing the conventional waveguide theory. For example, for the 1D and 2D perturbation function, we have

$$\Delta(\rho) = \Delta(x) = \begin{cases} \Delta_0 \text{ if } |x| < W \text{ or } R \\ 0 \quad \text{if } |x| > W \text{ or } R \end{cases} \tag{2.34}$$

Therefore, the corresponding PCWs are simplified into a 1D slab or coaxial waveguide as shown in Figure 2.5.

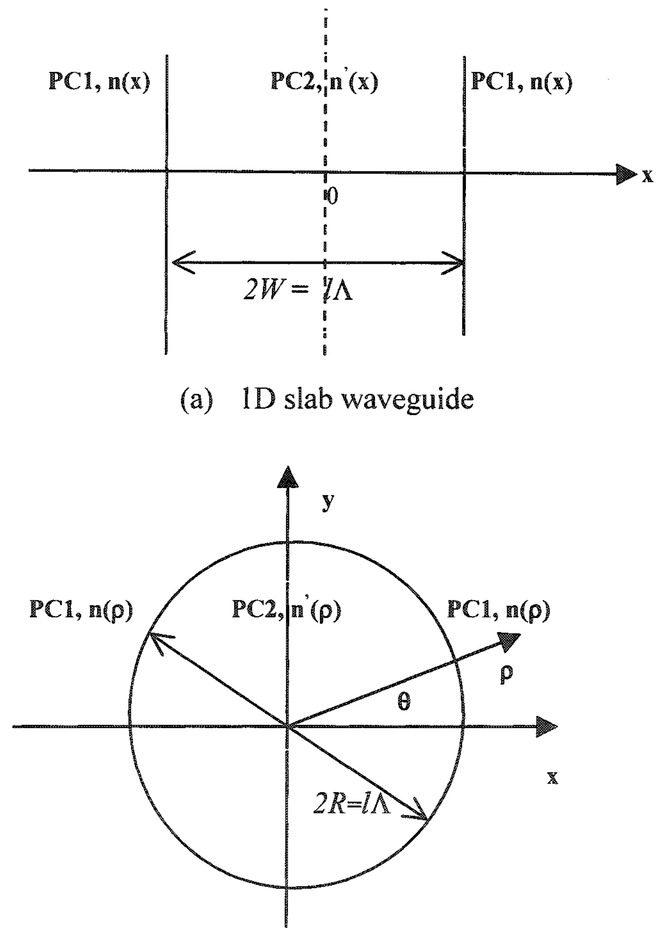

(a) 1D slab waveguide

(b) 2D coaxial waveguide

Figure 2.5 The equivalent cross-section of the 1D (a) and 2D (b) heterostructure PCWs

By expanding the frequency up to the second order in the Taylor expansion (2.31), the envelope equation (2.30) becomes

$$\frac{1}{2m_x}\frac{d^2 f_{nk_0}(\rho)}{dx^2}+\frac{1}{2m_y}\frac{d^2 f_{nk_0}(\rho)}{dy^2}=[\omega^2{}_n(k_0)-\omega_d{}^2(1+\Delta(\rho))]f_{nk_0}(\rho) \qquad (2.35)$$

where the wave vector k_0 corresponds to an extremum of the band structure in the transverse ($k_\perp$ or k_x) direction and m_x and m_y are the effective "mass" describing the curvature of the band and defined by

$$\frac{1}{m_x}=\frac{\partial^2\omega_n{}^2}{\partial k_x^2}|_{k_0} \quad \text{and} \quad \frac{1}{m_y}=\frac{\partial^2\omega_n{}^2}{\partial k_y^2}|_{k_0} \qquad (2.36)$$

The solution of (2.35) is easily solved by the optical fiber theory for 2D PCW or the slab waveguide theory for 1D PCW and its corresponding modal properties (e.g., the single-mode condition) are easily obtained. As can been seen clearly, if m_x is negative, guided modes can exist even though the average refractive index in the core is lower than that of the cladding (i.e., $\Delta_0 < 0$). In conclusion, the PC waveguiding is possible for the PCW where the curvature of the band in the transverse direction has the same sign as the dielectric contrast between the core and the cladding.

2.6 Effective Index Method

The idea of the effective index method (EIM) is to convert a complicated optical waveguide problem into a simplified optical waveguide probelm (e.g., a 2D waveguide into a equivalent 1D waveguide) through some approximations. Generally, the EIM method can be employed for two cases: the rectangular/radial optical waveguide with slow index variations in one direction and the optical periodic array waveguide (i.e., the PCW). The former is well known and is used widely in integrated optics (e.g., channel and ridge waveguides) [21]. The idea of the latter case is to first evaluate the band structure of the PC to obtain the effective index and then replace the PC with this effective index to construct a simplified step-index waveguide [49]. Usually, the effective index is calculated in terms of the lowest mode that could propagate in the PC (i.e., PC1 as shown in Figure 2.4), which is so-called the fundamental space-filling mode (SFM). In other words, the corresponding effective index n_{eff} is obtained by the first band of the band structure (or the band-gap map) of the PC:

$$n_{eff} = \frac{k_{z,FSM}}{k} \tag{2.37}$$

where $k_{z,FSM}$ is the propagating constant along z of the fundamental space-filling mode and k (i.e., ω/c) is the propagating constant in free space.

As long as getting the effective index of the PC, like the EAM mentioned in the previous section as shown in Figure 2.5, the modal properties of the PCWs are easily obtained by employing the conventional optical waveguide theory (e.g., the optical fiber theory for 2D PCW or the slab waveguide theory for 1D PCW). Due to different guiding mechanisms between the PBG-PCWs and conventional optical waveguides, unlike the EAM method, the EIM approach fails for the PCWs due to the PBG effect. Further, because the complex refractive index profiles within modes are neglected for the EIM method, it is very difficult to define the equivalent boundary between the core and cladding for the 2D PCWs (e.g., the equivalent radius of the PCFs that changes from $\Lambda/2$ to Λ [34] [49], where Λ is the pitch). Therefore, the EIM method can only approximate the optical properties of the PCWs (e.g., the single-mode operation and the estimation of the bending loss [53]) and cannot accurately predict more sensitive modal properties such as dispersion or birefringence.

2.7 Summary

In this chapter, in order to completely understand the basic principle and investigate the modal characteristics of the PCWs, four typical modeling methods (i.e., the finite difference method, the plane wave method, the envelope approximation method, and the effective index method), which are used in the rest of the thesis as a basis for the modeling and design of the PCWs with desired modal properties, are described. Compared with formulations of modeling techniques used by other workers, the proposed modeling methods have the following advantages:

- The plane wave method (PWE, or so called the supercell method with the plane wave expansion), which is summarized into simple matrix form by utilizing the symmetrical nature of general PCWs, is simple and powerful. And it was used as the reference results and also to calculate the band structure of the PCs.
- The envelope approximation method, which is originally used for the PCWs with in-plane propagation, and the effective index method, which is originally used without any explanation, are simple and intuitive. Based on the band structure of the PCs, the physical insight of the PCWs is easily gained and some modal properties such as the single-mode operation are obtained in a very simple way.
- The finite difference method, which is extended to utilize the perfect matching layer boundary conditions and the initial value extracted from the band structure of the PCs, is more accurate and versatile. It is a basis for the design of the PCWs with some desired modal properties.

Chapter 3

One-Dimensional Photonic Crystal Waveguides

In this chapter, we investigate the modal characteristics of the one-dimensional (1D) photonic crystal waveguides (PCWs) in great detail. By employing the transfer matrix method, we can put the design parameters related to the general multiplayer structure into a compact analytical expression, which serves as the basis for analysis of the band-gap structure of the general 1D photonic crystals (PCs) and the modal characteristics of the general 1D PCWs. The band structure of 1D PCs and modal properties of 1D PCWs, such as the effective index, the modal field profile, the dispersion, the confinement loss, and the confinement factor, are all calculated and simulated. With the help of the band-gap map of the 1D PCs, four guiding regimes for the 1D PCWs are recognized, in accordance with the index of the guiding core. It is shown that the modal characteristics for each regime behave differently from the point of view of guiding mechanism. Finally, some complex 1D PCWs (e.g., the heterostructure PCWs) are investigated and the relations between the 1D PCWs and 2D PCFs are discussed.

3.1 Introduction

As a starting point, we investigate the modal characteristics of the 1D PCWs. There are several reasons for studying such relatively simple structures. Firstly, the 1D PCWs are readily realized in both planar and cylindrical configurations to practical optical waveguide structures. Secondly, the simple 1D structure can be used to gain considerable understanding and insight into more complex 2D or even 3D structures. Thirdly, analytical methods can be used for the modeling and simulation of the 1D PCW structures and therefore such a study can be carried out in a much more efficient fashion than those of 2D and 3D structures for which intensive computational methods have to be utilized. Finally, a careful and somewhat exhausting examination of the literature in the field seems to suggest that a complete analysis and detailed description of the 1D PCWs are still lacking.

Generally, a 1D PC structure consists of a stack of multiplayer dielectric structures with different periods, and a 1D PC waveguide is formed by placing defects in between the multi-layer stacks with the wave propagation along the propagation direction (i.e., $k_z \neq 0$). In order to understand the operation principle of the 1D PCWs, it is instructive to investigate the band structure of the 1D PCs, which gives intuitive and physical insight (e.g., the regions of different guiding mechanisms, the effective index of the cladding, and the curvature of the band structure). In practice, the number of periodic units is limited, therefore the effect of the number of periodic units on the modal characteristics should be carefully studied.

For the 1D dielectric structure as shown in Figure 3.1, the wave equations are decoupled to yield two sets of independent modal solutions, namely, the TE and the TM waves, that are expressed in terms of the transverse electric field component E_y and the transverse magnetic field component H_y, respectively. However, because all the related parameters (e.g., in lasers) are defined according to the electric fields, it is convenient and simple to use the electric fields E for the both polarizations. In this chapter, we use the E–related parameters (i.e., the reflection coefficient r and transmission coefficient t) [15] unless otherwise mentioned.

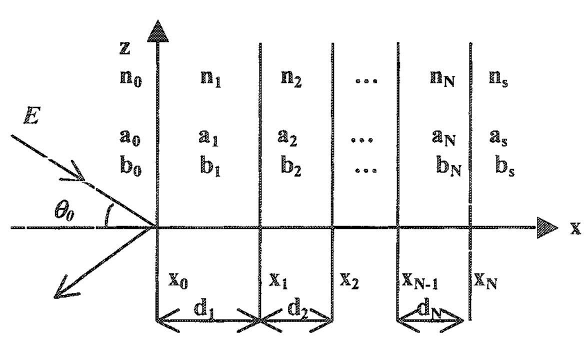

Figure 3.1 The 1D N-layered isotropic dielectric structure with two cladding layers.

3.2 The Multilayer Structure

In order to introduce the transfer matrix method (TMM), we start from the transfer matrix related to a general N-layered dielectric structure with two cladding layers as shown in Figure 3.1. In Figure 3.1, the refractive indices n_i (i = 1, 2, ..., N), n_0, and n_s are related to the N-layered dielectric structure, cover, and substrate, respectively. In the N-layered dielectric structure, the ith layer (i = 1, 2, ..., N) is located between x_{i-1} and x_i and its corresponding thickness d_i is that (x_i - x_{i-1}).

For the sake of simplicity, we assume that the electromagnetic (EM) wave is assumed to propagate in the xz plane. The electric field $E_i(x,z,t)$ in the ith layer, which satisfies Maxwell's equations, has the following form:

$$E_i(x,z,t) = E_i(x)e^{+j(\omega t - k_z z)} \tag{3.1}$$

where k_z is the z component of the wave vector and ω is the angular frequency. In general, the electric field $E_i(x)$ in each layer consists of two kinds of traveling waves (forward and backward) and can be written as

$$E_i(x) = a_i e^{-jk_{ix}(x-x_{i-1})} + b_i e^{+jk_{ix}(x-x_{i-1})} \tag{3.2}$$

where k_{ix} (i = 0, 1, 2, ..., N, and S) is the x component of the wave vector in the ith layer, and a_i and b_i are forward and backward propagation coefficients in each layer as shown in Figure 3.1. From the wave equations, two components of the wave vector hold the following relation:

$$k_{ix} = \sqrt{(kn_i)^2 - k_z^2} = kn_i \cos\theta_i \quad \text{with } k_z = kn_i \sin\theta_i \tag{3.3}$$

where k is the propagating constant in free space and θ_i is the incident or transmitted angle in the ith layer (only the incident angle θ_0 is shown in Figure 3.1). By utilizing the continuous conditions of each tangential and longitudinal fields (the latter can be derived from the derivatives of the transverse fields with respect to x) at each interface x_i (i = 1, 2, ..., N), the relations between propagation coefficients a_i and b_i (i = 0, 1, 2, ..., N, S), as shown in Figure 3.1, are obtained through transmission matrices D_i, D_{i+1} and the propagation matrix P_i [15],

$$\begin{pmatrix} a_i \\ b_i \end{pmatrix} = P_i D_i^{-1} D_{i+1} \begin{pmatrix} a_{i+1} \\ b_{i+1} \end{pmatrix} \tag{3.4}$$

where we assume that $a_{N+1} = a_S$, $b_{N+1} = b_S$, and P_0 is an unity matrix. The transmission matrix D_i and the propagation matrix P_i are defined by

$$D_i = \left(\frac{k_{ix}}{kn_i} \right)^{\delta} \begin{pmatrix} 1 & 1 \\ q_i & -q_i \end{pmatrix} \tag{3.5}$$

$$P_i = \begin{pmatrix} e^{+jk_{ix}d_i} & 0 \\ 0 & e^{-jk_{ix}d_i} \end{pmatrix} \tag{3.6}$$

where the integer δ is 0 for the TE wave and 1 for the TM wave. The normalized transverse constants q_i are given by

$$q_i = \begin{cases} \dfrac{k_{ix}}{k} & \text{for the TE wave} \\ \dfrac{kn_i^2}{k_{ix}} & \text{for the TM wave} \end{cases} \tag{3.7}$$

where q_i for both polarizations is equal to n_i at the normal incidence (i.e., $k_z = 0$) and the determinant of the matrix D_i for both polarizations is equal to $-2k_{ix}/k$. It is worth to note that, in order to be consistent with the definitions of the parameters for both polarizations, the k factor in the matrix D_i is added (a somewhat different convention from those in other texts and published papers [54]). However, this choice will not affect the final results obtained.

By cascading the above transmission matrices and propagation matrix, the transfer matrix M between the propagation coefficients of two cladding layers is obtained:

$$\begin{pmatrix} a_0 \\ b_0 \end{pmatrix} = D_0^{-1} D_1 P_1 D_1^{-1} D_2 P_2 D_2 \ldots D_N P_N D_N^{-1} D_s \begin{pmatrix} a_s \\ b_s \end{pmatrix} = M \begin{pmatrix} a_s \\ b_s \end{pmatrix} \tag{3.8}$$

where the transfer matrix M is further defined by the unimodular matrix Q_i (i.e., $\det(Q_i) = |Q_i| = 1$, where det(...) or |...| stands for the determinant of the matrix):

$$M = \begin{pmatrix} M_{11} & M_{12} \\ M_{21} & M_{22} \end{pmatrix} = D_0^{-1} m D_S = D_0^{-1} (\prod_{i=1}^{N} Q_i) D_S \tag{3.9}$$

where the unimodular matrix $m = \prod_{i=1}^{N} Q_i$ for the N-layered structure and $Q_i = D_i P_i D_i^{-1}$ are the transfer matrix for the ith layer [15]:

$$Q_i = \begin{pmatrix} \cos(k_{ix}d_i) & j\sin(k_{ix}d_i)/q_i \\ jq_i\sin(k_{ix}d_i) & \cos(k_{ix}d_i) \end{pmatrix} \tag{3.10}$$

where the normalized transverse constant q_i was given by (3.7). It is worth to note that, due to the different fields used, the normalized transverse constant q_i for the TM wave is different from that used in some texts and published papers [54], [55]. By using the symmetry property of the transfer matrix Q_i, it is shown that $M_{21} = M_{12}^*$, $M_{22} = M_{11}^*$, and $\det(M) = k_{sx}/k_{0x}$. Through the transfer matrix, the reflection and transmission coefficients r and t are calculated if we assume the light is incident from the cover (n_c) and $b_S = 0$,

$$r = \left(\frac{b_0}{a_0}\right)_{b_s=0} = \frac{M_{21}}{M_{11}} = \frac{(m_{11}+m_{12}q_s)-(m_{21}+m_{22}q_s)/q_0}{(m_{11}+m_{12}q_s)+(m_{21}+m_{22}q_s)/q_0} \tag{3.11}$$

$$t = \left(\frac{a_s}{a_0}\right)_{b_s=0} = \frac{1}{M_{11}} = \frac{2(n_s k_{0x}/n_0 k_{sx})^{\delta}}{(m_{11}+m_{12}q_s)+(m_{21}+m_{22}q_s)/q_0} \tag{3.12}$$

where the integer δ is 0 for the TE wave and 1 for the TM wave. And their corresponding reflectance and transmittance of plane waves through a multiplayer dielectric structure can be obtained [15]:

$$R = |r|^2 \quad \text{and} \quad T = \frac{k_{sx}}{k_{0x}}|t|^2 \tag{3.13}$$

where we note that $R + T = 1$. On the other hand, if we consider the light is incident from the substrate (n_s), the reflection and transmission coefficients r' and t' can be calculated as follows:

$$r' = \left(\frac{A_s}{B_s}\right)_{A_0=0} = -\frac{M_{12}}{M_{11}} = -\frac{(m_{11}-m_{12}q_s)+(m_{21}-m_{22}q_s)/q_0}{(m_{11}+m_{12}q_s)+(m_{21}+m_{22}q_s)/q_0} \tag{3.14}$$

$$t' = \left(\frac{B_0}{B_s}\right)_{A_0=0} = \frac{|M|}{M_{11}} = \frac{2(k_{sx}/k_{0x})(n_s k_{0x}/n_0 k_{sx})^{\delta}}{(m_{11}+m_{12}q_s)+(m_{21}+m_{22}q_s)/q_0} \tag{3.15}$$

where we note that $t' = |M|t$ and the corresponding reflectance and transmittance R' and T' are given as follows:

$$R' = |r'|^2 \quad \text{and} \quad T' = \frac{k_{0x}}{k_{sx}} |t'|^2 \tag{3.16}$$

where we again note that $T = T'$. Through the above-mentioned formulae, the reflectance, transmittance, and some related parameters can all be obtained.

For the guided modes of the 1D multilayer waveguide, their dispersion curve can be solved with the help of the transfer matrix. Because their filed amplitudes vanish at infinity, the coefficients a_0 and b_s are set to zero in (3.8),

$$\begin{pmatrix} 0 \\ b_0 \end{pmatrix} = \begin{pmatrix} M_{11} & M_{12} \\ M_{21} & M_{22} \end{pmatrix} \begin{pmatrix} a_s \\ 0 \end{pmatrix} \tag{3.17}$$

So the following dispersion relation is easily obtained from the transfer matrix of the 1D multiplayer structure:

$$M_{11} = 0 \quad \text{or} \quad (m_{11} + m_{12} q_s) q_0 + m_{21} + m_{22} q_s = 0 \tag{3.18}$$

where (3.9) was used. If we use the positive transverse decay constants $\gamma_i = -jk_{ix} = \sqrt{k_z^2 - (kn_i)^2}$ in cover and substrate (i.e., $i = 0$ and S), and the equation (3.18) becomes the familiar dispersion relation for the 1D multilayer waveguide. For example, the dispersion relation for the TE wave is shown as follows:

$$(k^2 m_{21} - m_{12}\gamma_0\gamma_s) + jk(m_{11}\gamma_0 + m_{22}\gamma_s) = 0 \tag{3.19}$$

In general, how to find the complex solution of the dispersion curve of the 1D multilayer waveguide is a highly challenging task and still attracts research attention. Here we introduce a simple and rigorous slab leaky model (or so-called the transverse resonance method, TRM [56]) to solve the guided or leaky modes of the 1D multiplayer slab waveguide involving a core layer with the index n_c and the thickness d as shown in Figure 3.2 (here we assume that the ith layer is the core layer of the waveguide, or $n_c = n_i$ and $d = d_i$). By considering the boundary conditions (continuity of the tangential electric and magnetic fields) at the core-cladding interfaces, the dispersion curve of the modes can be obtained as follows [2]:

$$r_1 r_2 e^{2j(n\pi - k_{cx}d)} = 1 \tag{3.20}$$

where n is the order of the guided modes, k_{cx} is the transverse (x) component of the wave vector in the core, and r_1 and r_2 are the reflection coefficients from either sides inside the core, which can be easily calculated by the transfer matrices (e.g., 3.11 and 3.14). The zeros of (3.20) are found by employing a general complex root-searching scheme such as the Muller scheme with a suitable initial value (e.g., got from the band structure for the PCs).

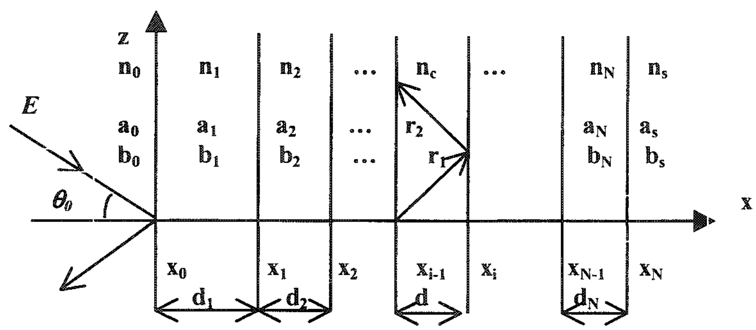

Figure 3.2 The 1D N-layered waveguide structure by the transverse resonance method.

3.3 Band Structure of 1D Photonic Crystals

After reviewing the transfer matrix method (TMM) of the 1D multiplayer, we are ready to investigate the 1D photonic crystal (PC) structure. We consider a general 1D PC structure with finite thickness surrounding by the cover (n_c) and the substrate (n_s), in which each periodic period consists of P-layered dielectric materials, as shown in Figure 3.3. This practical PC structure is made of N periods with pitch Λ ($n = 1, 2, \ldots, N$) and each period consists of P layers with refractive index n_p and thickness d_p ($p = 1, 2, \ldots, P$). Ideally, when increasing the number N into infinite, this dielectric structure becomes semi-infinite or infinite. In this section, we discuss the 1D infinite PC structure or simply the 1D PC. For the practical case of the band-gap structure, the 1D finite PCs with defects (i.e., PCWs) will be discussed in the next section (see 3.4).

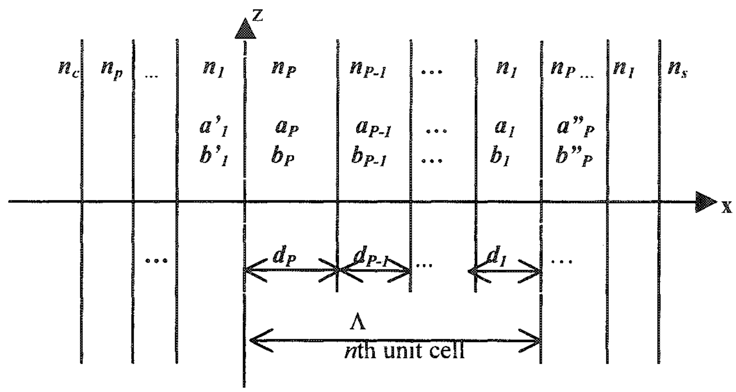

Figure 3.3 A schematic drawing of a 1D periodic layered media and the propagation coefficients associated with the *n*th unit cell and its neighboring layers.

By using the TMM method, the relation between forward and backward propagation coefficients of the unit cell (e.g., the *n*th period in as shown in Figure 3.3) can be express as follows:

$$\begin{pmatrix} a'_1 \\ b'_1 \end{pmatrix} = \begin{pmatrix} M_{11} & M_{12} \\ M_{21} & M_{22} \end{pmatrix} \begin{pmatrix} a_1 \\ b_1 \end{pmatrix} = M \begin{pmatrix} a_1 \\ b_1 \end{pmatrix} \tag{3.21}$$

where M is the matrix for the unit cell,

$$M = D_1^{-1} \left(\prod_{i=P}^{2} Q_i \right) D_1 P_1 \tag{3.22}$$

where we note that $M_{21} = M_{12}^*$ and $M_{22} = M_{11}^*$. For example, the components of the unit cell's transfer matrix of the simplest PC (i.e., $P = 2$), which consists of two alternating layers of low refraction index n_1 and high refraction index n_2 and the corresponding thickness d_1 and d_2, are given,

$$\begin{aligned} M_{11} &= e^{jk_{1x}d_1}\left[\cos(k_{2x}d_2) + \frac{j}{2}\left(\frac{\xi_1 k_{2x}}{\xi_2 k_{1x}} + \frac{\xi_2 k_{1x}}{\xi_1 k_{2x}}\right)\sin(k_{2x}d_2)\right] \\ M_{12} &= e^{-jk_{1x}d_1}(-1)^m \frac{j}{2}\left(\frac{\xi_1 k_{2x}}{\xi_2 k_{1x}} - \frac{\xi_2 k_{1x}}{\xi_1 k_{2x}}\right)\sin(k_{2x}d_2) \end{aligned} \tag{3.23}$$

where $\xi = 1$ for the TE wave and $\xi = n_i^2$ ($i = 1$ and 2) for the TM wave.

According to the Bloch-Floquet theorem, the periodicity $n(x) = n(x + \Lambda)$ of the structure leads to the Bloch wave solutions $E_K(x,z)$ of the Maxwell's equations:

$$E_K(x,z) = E_K(x)\exp[-j(k_z\, z + Kx)] \tag{3.24}$$

where $E_K(x)$ is the Bloch wave function [$E_K(x) = E_K(x+\Lambda)$] and K is the Bloch wave number. With the help of the TMM method and (3.24), the eigen-value equation between the Bloch wave number and frequency can be obtained [15]:

$$\begin{pmatrix} M_{11} & M_{12} \\ M_{21} & M_{22} \end{pmatrix}\begin{pmatrix} a_1 \\ b_1 \end{pmatrix} = e^{+jK\Lambda}\begin{pmatrix} a_1 \\ b_1 \end{pmatrix} \tag{3.25}$$

After some simple algebraic manipulations, the dispersion relation between the Bloch wave number K and frequency ω can be obtained [15]:

$$K(k_z,\omega) = \cos^{-1}\left(\frac{M_{11}+M_{22}}{2}\right)/\Lambda \tag{3.26}$$

where k_z is the tangential component of the wave vector and ω is the angular frequency. Also the corresponding eigenvector can be calculated [15]:

$$\begin{pmatrix} a_1 \\ b_1 \end{pmatrix} = \begin{pmatrix} M_{12} \\ e^{jK\Lambda} - M_{11} \end{pmatrix} \tag{3.27}$$

It is worth to note that, for the lossless PCs, a real Bloch wave number means the propagation state and an imaginary Bloch wave number means the evanescent state, which forms a band-gap for the PCs. The analytical forms for a typical period layered structure can be obtained from the transfer matrix of the unit cell of the structure (i.e., 3.22) and its band structure can be solved analytically. For instance, the dispersion relation for the simplest PC (i.e., $P = 2$) can be obtained as follows:

$$\cos[K(\beta,\omega)\Lambda] = \cos(k_{1x}d_1 + k_{2x}d_2) - \frac{(q_2-q_1)^2}{2q_1q_2}\sin(k_{1x}d_1)\sin(k_{2x}d_2) \tag{3.28}$$

where the normalized transverse constants q_i (i = 1 and 2) was defined in (3.7). It is worth to note that, if $(n_2\text{-}n_1)/n_1 << 1$, the approximate n-th order Bragg condition, which we will employ frequently to interpret some features of the PCs (e.g., the closure of the band-gap), is obtained when we set

$$k_{1x}d_1 + k_{2x}d_2 = n\pi \tag{3.29}$$

where n is the order of the band structure.

3.3.1 On-Axis Propagation

In general, one considers that light propagates or resonates entirely in the x-direction (or on-axis propagation, e.g., Bragg grating and DFB lasers). Because on-axis propagation (i.e., $k_z = 0$) is a special case of off-axis propagation, here we calculate the band structure (or so-called band-gap map) with on-axis propagation of some typical two-material PCs to show some interesting properties of 1D PCs. Figure 3.4 shows the photonic band structure with on-axis propagation of 1D PCs with silica-air layers of width 0.5Λ. As can be seen, there are some band-gaps along the frequency axis where the Bloch wave number K is imaginary. Usually, these gaps are called the photonic band-gaps (PBGs). The physical insight of the PBGs can be understood by considering the electric field modes for the different order (or band) states at the middle ($K = 0$) and edge ($K = \pi/\Lambda$) of the Brillouin zone, in which the low-frequency mode concentrates its energy in the high index region and the high-frequency mode concentrates its energy in the low index region, respectively [19]. Further, it is found that the bandwidth of the band-gaps is different from each other and depends on the index ratio and the size-to-pitch ratio. Usually, when the index ratio increases, the band-gaps widen considerably [7]. Figure 3.5(a) and Figure 3.5(b) show the photonic band-gap as a function of the index ratio n_2/n_1 and the size-to-pitch ratio d_2/Λ, respectively. It can be seen from figures that the first gap has following properties for the 1D PCs with on-axis propagation ($k_z = 0$) [7]:

1. The band-gap always opens up when $n_2/n_1 \neq 1$.
2. The larger the index ratio n_2/n_1, the wider the relative gap $\Delta\omega/\omega_0$.
3. The largest relative gap $\Delta\omega/\omega_0$ is reached at the quarter-wave stack ($n_2/n_1 = d_1/d_2$).

However, unlike summarized in Ref [7], the above conclusions for the first band-gap do not hold for the high-order band-gaps. It is observed in Figure 3.5 that the band-gaps for the high-order bands oscillate when the index ratio n_2/n_1 or the size-to-pitch ratio d_2/Λ changes, and the number of band-gap nulls or peaks increases with the band order. This can be understood theoretically by the Bragg condition $k_{2x}d_2 + k_{1x}d_1 = n\pi$ (i.e., 3.29), where n is the order of the band-gap and the band-gap closes m times when meeting the condition of $k_{2x}d_2 = m\pi (0 < m < n)$.

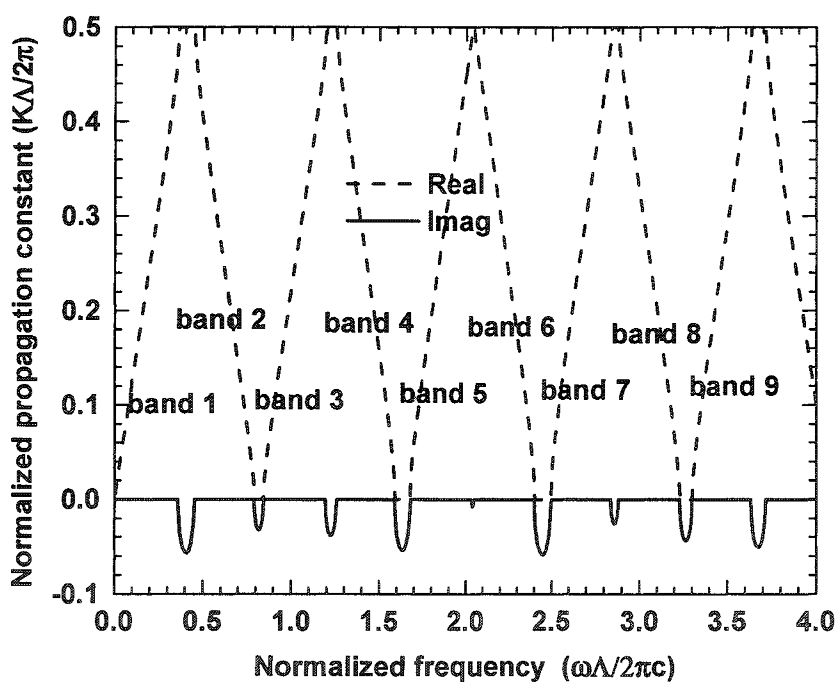

Figure 3.4 The photonic band structure (ω-K) with on-axis propagation ($k_z = 0$) with silica-air layers of $n_1 = 1.0$, $n_2 = 1.45$ and $d_1 = d_2 = 0.5\Lambda$.

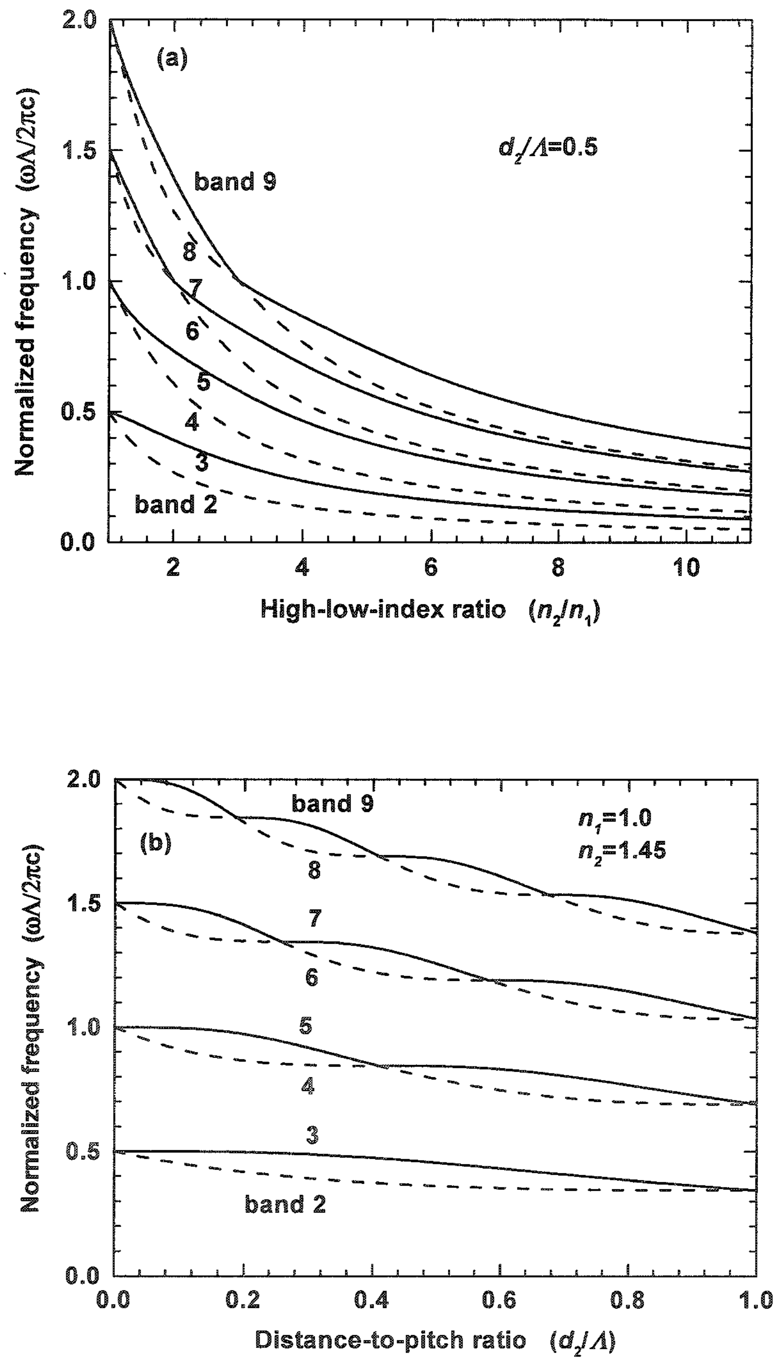

Figure 3.5 The photonic band-gap with on-axis propagation as a function of the index ratio n_2/n_1 of width 0.5Λ (a) and the size-to-pitch ratio d_2/Λ with silica-air layers (b).

3.3.2 Off-Axis Propagation

In order to understand the operation principle of the PCWs, the band structure with off-axis propagation should be considered. Since there is no index variation along the z direction, there are no complete band-gaps with off-axis propagation. However, when we consider the PCs as a semi-finite structure and the wave propagation along the z direction inside the defects, the complete band-gap with off-axis propagation is not important. So, the partial band-gap with off-axis propagation is enough. Figure 3.6 shows the photonic band structure with off-axis propagation of 1D PCs with silica-silicon layers (n_1 = 1.4 and n_2 = 3.4) of width 0.5Λ. As expected, several well-known features of the PBGs with off-axis propagation of 1D PCs are observed as follows [7]:

1. The band-gaps shift toward the higher frequency when k_z increases.
2. The band-gaps for TE and TM behave differently. The bandwidth of all TE gaps increases when k_z increases. However, when k_z increases, all TM gaps shrink to zero at the Brewster line ($\omega = c\ k_z/n_1/\theta_B$ with $\theta_B = \tan^{-1}(n_2/n_1)$), and then open up.
3. The first band for both polarizations has different dispersion slopes when k_z decreases to zero and the slope of the TM gap is larger than that of the TE gap.
4. The bands shrink to zero when k_z increases.

These properties can be understood as follows. In order to meet the Bragg condition (i.e., 3.29) for the transverse constants k_{ix} (i = 1 and 2) and $k_{ix} = \sqrt{(kn_i)^2 - k_z^2}$, the band-gap must shift toward the higher frequency when k_z increases. As we know, the TM wave propagates without any reflection from n_2 ($or\ n_1$) to n_1 ($or\ n_2$) at the Brewster angle θ_B. This, in turn, leads to all propagation states and all band-gaps should close at the Brewster angle θ_B. Due to the more energy concentrated in the high (or low) index region for the TE wave than that of the TM wave at long wavelengths, in general, the band-gaps of the TE wave are larger than those of the TM wave.

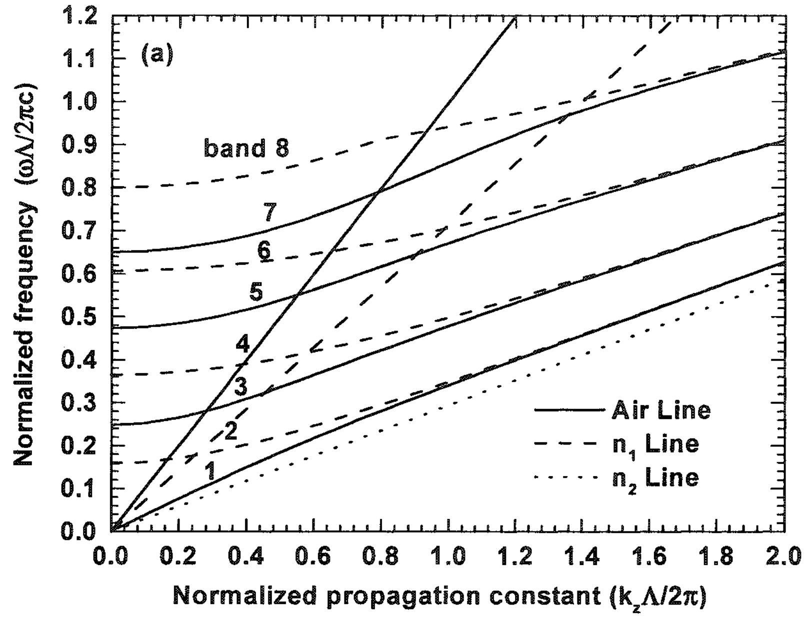

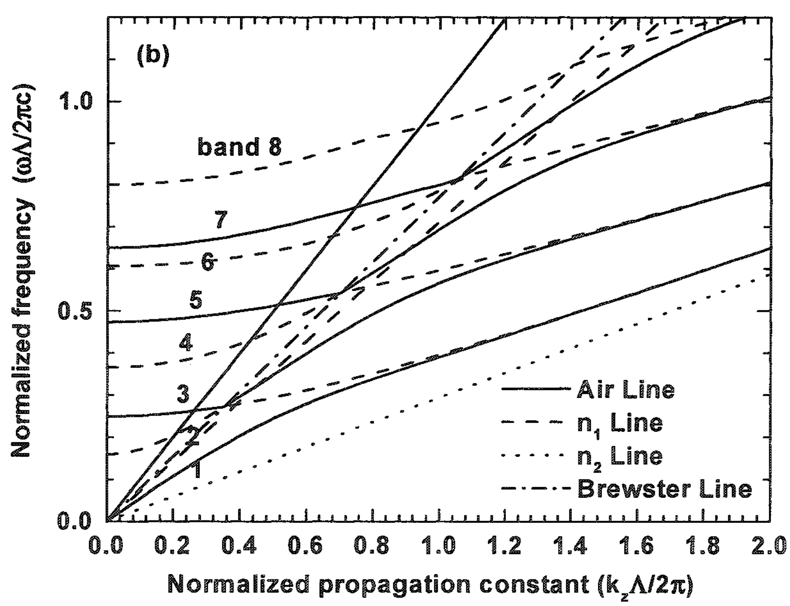

Figure 3.6 The photonic band structure of the TE(a) and TM(b) waves with off-axis propagation for 1D PCs with layers of width 0.5Λ and layers between n_2= 3.4 and n_1=1.4.

When the wavelength further increases, for the first band of 1D PCs, light actually propagates an effective homogeneous dielectric media for both polarizations with an average index ($n_{12} = n_1 d_1/\Lambda + n_2 d_2/\Lambda$) [7]. If we redraw Figure 3.6(a) into our familiar *V-b* diagram for the single symmetrical slab waveguide [here $V = kd_2(n_2^2 - n_1^2)^{1/2}$ and $b = ((k_z/k)^2 - n_1^2)/(n_2^2 - n_1^2)$] as shown in Figure 3.7, the short-wavelength asymptotic behavior of 1D PCs can be understood easily as follows. As can be seen from Figure 3.7, when the normalized frequency *V* increases (or the wavelength decreases), all band-gaps open up to the limitations and are the same with the corresponding *V-b* curves of the slab guided modes, which mean that the coupling between the period dielectric structures is neglectable and the PC structure acts like the slab waveguide. As can be seen from the band-gap structure of the PCs, this "threshold" wavelength point depends on the index ratio n_2/n_1 and the size-to-pitch ratio d_2/Λ of 1D PCs. In other words, the larger the index ratio n_2/n_1 and the size-to-pitch ratio d_2/Λ, the longer the "threshold" wavelength point.

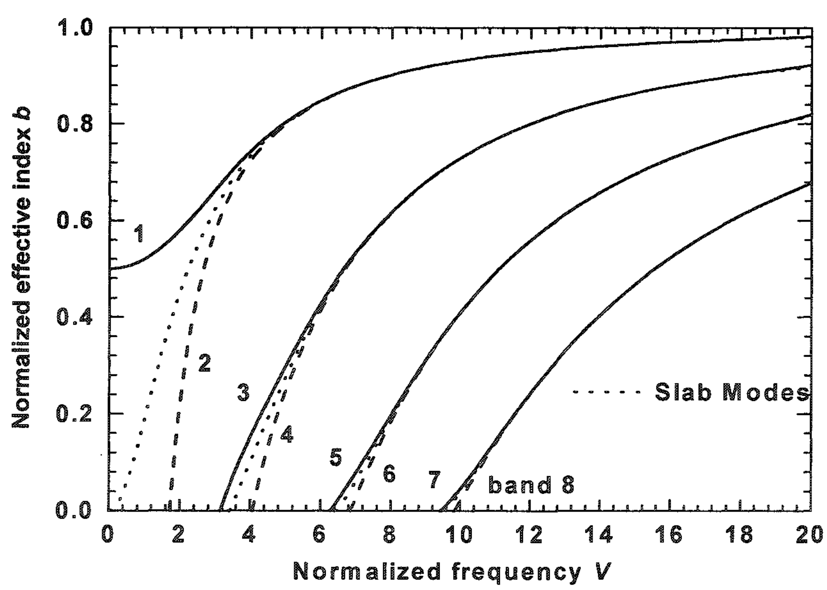

Figure 3.7 The photonic band structure (*V-b*) of the TE waves with off-axis propagation for 1D PCs with layers of width 0.5Λ and layers alternate between $n_2 = 3.4$ and $n_1 = 1.4$.

As we know from the slab waveguide theory, the normalized effective index b for both polarizations tends to unity at short wavelengths. It leads to that all band-gaps of 1D PCs meet the n_2 line when wavelength decreases. It is worth to note that, because the difference between the TE and TM wave is well known for the slab waveguide, the vector nature of the guided and unguided modes of 1D PCs and their related structures (e.g., PCWs) must be considered.

3.3.3 Space-Filling Modes

In the previous section, the band structure of 1D PCs is analyzed by using the Bloch-Floquet theorem. It is shown that there are always the band-gaps for 1D PCs in which the EM waves cannot propagate in the direction along the periodic multilayer (i.e., x). In other words, the Bloch wave number K is imaginary in the band-gaps and real off the band-gaps. In this section, we consider the band structure of 1D PCs by using the variation theorem [7]. According to the variation theorem, there are always two ways to allocate the EM energy, which is located at the edge of the Brillouin zone (i.e., $K\Lambda/2\pi =$ 0 or 1/2). The first set of modes (SFM1) with low frequency (or high effective index), in which the first mode is called the fundamental space-filling mode, concentrates their energy in high index regions with perfect magnetic wall boundary condition (PMC) at the center of high index regions. On the other hand, the second set of modes (SFM2) with higher frequency (or low effective index) concentrates their energy in low index regions with perfect electric wall boundary condition (PEC) at the center of low index regions. Here we use the simplest (two-layer) PC structure as shown in Figure 3.8 to demonstrate this concept.

Generally speaking, by the symmetry of the unit cell of the PC, only half of the unit cell should be considered. In order to utilize the transfer matrix of the unit cell, here we consider a unit cell as shown in Figure 3.8, which is a previous unit cell (as shown in Figure 3.3) with $d_1/2$-shifted toward $-x$ direction. The corresponding transfer matrix M' can be easily calculated from the matrix M (i.e., 3.23) for the unit cell of the PC:

$$M' = \begin{pmatrix} M'_{11} & M'_{12} \\ M'_{21} & M'_{22} \end{pmatrix} = P_{1,d1/2} M P_{1,d1/2}^{-1} \tag{3.30}$$

where

$$\begin{aligned} M'_{11} &= M_{11} = e^{jk_{1x}d_1}[\cos(k_{2x}d_2) + \frac{j}{2}(\frac{\xi_1 k_{2x}}{\xi_2 k_{1x}} + \frac{\xi_2 k_{1x}}{\xi_1 k_{2x}})\sin(k_{2x}d_2)] \\ M'_{12} &= M_{12}e^{jk_{1x}d_1} = (-1)^{\sigma}\frac{j}{2}(\frac{\xi_1 k_{2x}}{\xi_2 k_{1x}} - \frac{\xi_2 k_{1x}}{\xi_1 k_{2x}})\sin(k_{2x}d_2) \end{aligned} \tag{3.31}$$

where $\xi = 1$ and $\sigma = 0$ for the TE wave, and $\xi = n^2_i$ (i = 1 and 2) and $\sigma = 1$ for the TM wave. We note that $M'_{21} = M'_{12}{}^*$ and $M'_{22} = M'_{11}{}^*$. According to the definition of the SFM modes, two sets of modes are determined by the variation theorem with two boundary conditions: PMC ($a'_{n-1} = b'_{n-1}$, $a'_n = b'_n$) and PEC ($a'_{n-1} = -b'_{n-1}$, $a'_n = -b'_n$) with respect to the transfer matrix M'. After some simple algebraic manipulations, the modal index can be calculated:

$$(M_{11} - M_{22}) = \mp 2M_{12}e^{jk_{1x}d_1} \tag{3.32}$$

or

$$\begin{aligned} &2\sin(k_{1x}d_1)\cos(k_{2x}d_2) + (\frac{\xi_1 k_{2x}}{\xi_2 k_{1x}} + \frac{\xi_2 k_{1x}}{\xi_1 k_{2x}})\cos(k_{1x}d_1)\sin(k_{2x}d_2) \\ &= \mp(-1)^{\sigma}(\frac{\xi_1 k_{2x}}{\xi_2 k_{1x}} - \frac{\xi_2 k_{1x}}{\xi_1 k_{2x}})\sin(k_{2x}d_2) \end{aligned} \tag{3.33}$$

where "-/+" stands for the modes that concentrate their energy in the high/low index regions. Figure 3.9 shows that the calculated band structure of TE and TM SFM modes with off-axis propagation for 1D air-silica PCs with layers of the silica width 0.8Λ, in which the solid lines stand for the SFM1 modes and the dash lines for the SFM2 modes. As expected, the SFM modes coincide with the curves of band edges. Therefore, as shown in the previous simulation results (e.g., Figure 3.5, Figure 3.6 and Figure 3.7), the even number of the bands, which are represented by solid lines, is related to the SFM1 modes of 1D PCs and the odd number of the bands, which are represented by dash lines, is related to the SFM2 modes of 1D PCs.

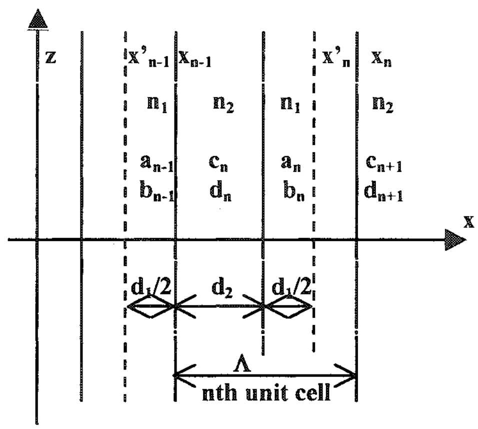

Figure 3.8 A schematic drawing of a 1D periodic two-layer isotropic media and the plane-wave amplitudes associated with the *n*th unit cell and its neighboring layers.

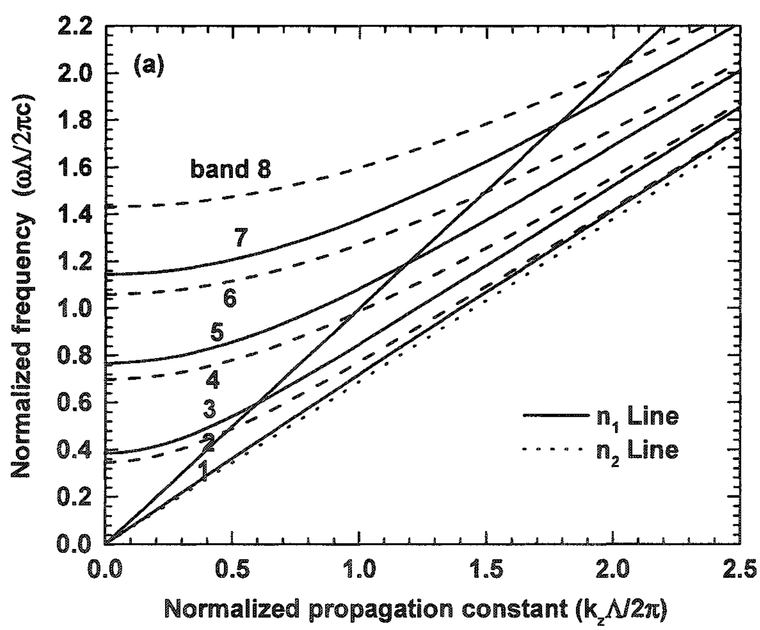

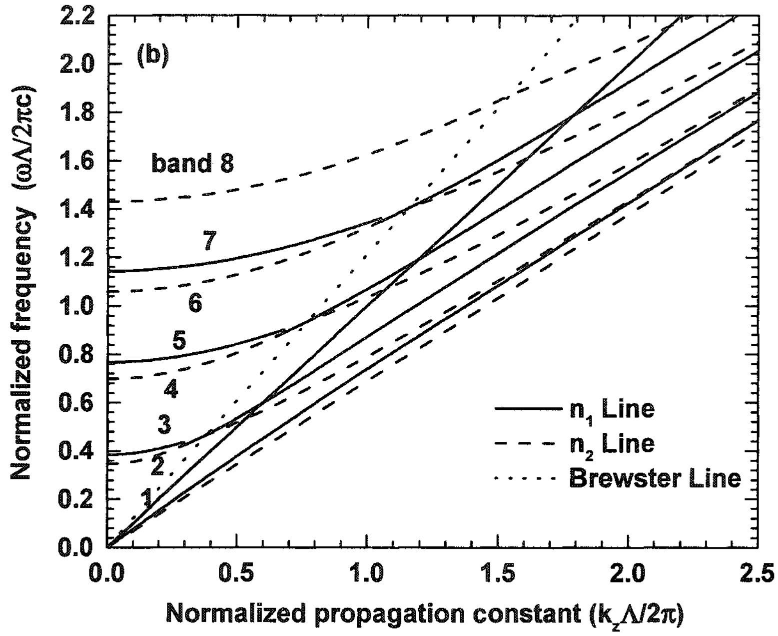

Figure 3.9 The spacing filling modes (k_z-ω) of the TE (a) and TM (b) waves with off-axis propagation for 1D air-silica PCs with layers of the silica width 0.8Λ and layers alternate between $n_2 = 1.45$ and $n_1 = 1.0$.

3.4 Photonic Crystal Waveguides

After understanding the main features of 1D PCs, now we can examine the 1D photonic crystal waveguides (PCWs) in which the transactional symmetry of 1D PCs is broken by a core or defects. As a result, it creates an allowed state (a guided mode) in the band-gap, thereby permitting a so-called localized mode around the core of 1D PCWs. General speaking, type of guiding mechanisms (i.e., PBG or TIR) depends on the properties of the core (i.e., the index and width of the core). By using the transverse resonance method (TRM), the modal properties of 1D PCWs can be calculated. Once the effective index N_{eff} and mode profile $E(x)$ are obtained, other modal properties (see Appendix A) can be readily obtained. In order to make the 1D PCWs close to the practical case, the high index (n_2 in Figure 3.10) of the cladding is assumed, and hence 1D PCWs considered here are essentially leaky in nature. Figure 3.10 shows the schematic view of a general 1D PCW consisting of a core layer n_c with the thickness d surrounding by N pairs of the PCs. In general, each pair of the structure may contain an arbitrary number of layers. For the sake of simplicity, we assume that each pair only has two alternative low and high index layers of index n_1 and thickness d_1, and index n_2 and thickness d_2, respectively. Also we assume that the range of n_c is from n_L (e.g., 1.0) to n_H (e.g., 2.2 or ∞). The pitch Λ of each pair is equal to d_1+d_2. It is worth to note that, as shown in Figure 3.10(b), the core layer is neighboring with the low index layer (i.e., n_1) for the TIR-PCWs.

3.4.1 Band-gap Map and Four Guiding Regions

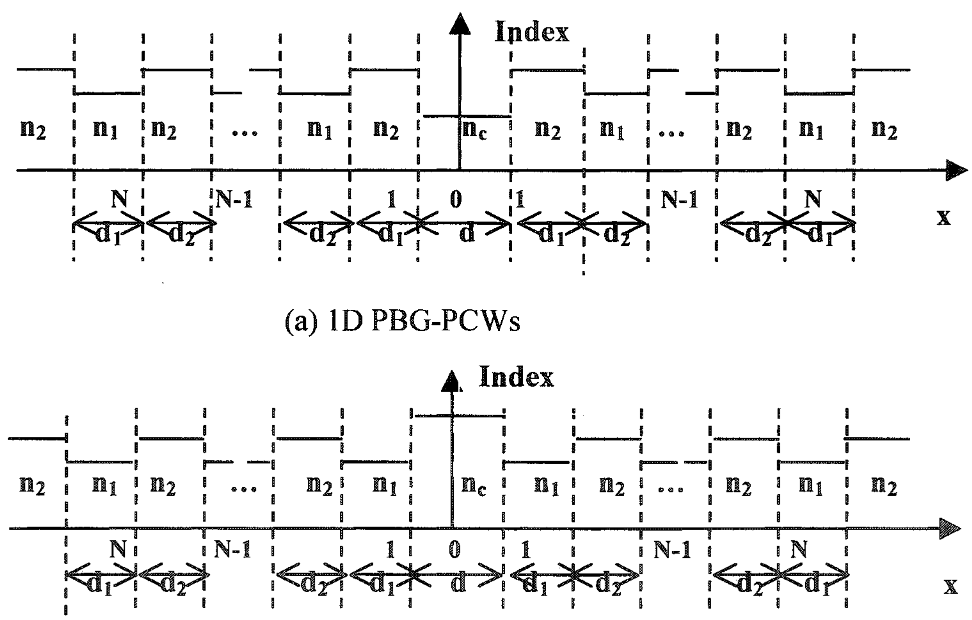

(a) 1D PBG-PCWs

(b) 1D TIR-PCWs

Figure 3.10 The schematic view of a general 1D PCW consisting of a core layer n_c with the thickness d surrounding by N pairs of two alternative layers n_1 and n_2 with the high index thickness d_2 and the pitch Λ: (a) 1D PBG-PCWs and (b) 1D TIR-PCWs.

As mentioned before, the band structure (or band-gap map) of the PCs is very important to help us to judge the simulation results of 1D PCWs [7]. In order to compare the simulation results with the published results [19], typical design parameters for the 1D PCWs are given as follows: d_2 = 0.6092Λ = 3.437 μm, Λ = 5.642 μm, d = 3.391Λ = 19.131 μm, N = 2, 4, 8, 16, and 32, n_1 = 1.4, and n_2 = 1.8, which are obtained by comparing the 1D PCW with a practical 2D PBG fiber studied and measured by Bise *et al.*[57]. By comparing the difference of band-gap maps between the TE and TM modes, calculated from (3.28), for 1D PCs with different n_1/n_2 and d_2/Λ values (i.e., Figure 3.4-Figure 3.7, Figure 3.9), we find that the band-gap maps for both the TE and TM modes have almost similar shapes except that all band-gaps are closed at the Brewster radiation line ($\omega = ck_z / n_1 / \sin(\tan^{-1}(n_2 / n_1)) = ck_z / 1.105$) for TM modes. Hence, here we only consider the TE modes unless otherwise mentioned.

Figure 3.11 shows the band-gap maps of TE modes of the 1D PCs with the n_1 = 1.4, n_2 = 1.8, and d_2 = 0.6092Λ. In Figure 3.11, four different radiation lines are also shown: the solid line for the air line (i.e., n_L = 1.0), the dashed line for the low index line (i.e., n_1 = 1.4), the dotted line for the high index line (i.e., n_2 = 1.8), and the dash-dotted line for the higher index line (i.e., n_H = 2.2). By comparing the difference of the band-gap maps for different n_1/n_2 and d_2/Λ values, four typical guiding regions are clearly identified, and defined as follows. Region I is the radiation area between 0 and n_1, and region II is the radiation area between $n_1$and n_{12}, in which n_{12} is defined as its corresponding radiation line that is tangential with the first band of 1D PCs, or $n_{12} = n_1d_1/\Lambda+n_2d_2/\Lambda$. The difference between them is that the band-gaps in region I close and then open up frequently and the band-gaps in region II never close and arrange along the radiation line regularly. The former, due to small value of k_z, has a chance to meet the condition of the gap closure ($k_{2x}d_2 = m\pi$, where m is the number of the gaps closure) under the Bragg condition $k_{2x}d_2 + k_{1x}d_1 = n\pi$ ($0 < m < n$, where n is the order of the gap). The higher the order of the band-gaps, the larger the closure times of the band-gaps. Especially, for the TM wave, all band-gaps are closed at the Brewster radiation line. On the other hand, the later, due to the large value of k_z and small value of k_x, has no chance to meet the condition of the gap closure and all gaps are open. Region III is the radiation area between n_{12} and n_2, and region IV is the radiation area between n_2 and ∞. The difference between them is that the radiation line in region III crosses all bands and the radiation line in region IV crosses none of bands because the all bands have the asymptotic (short-wavelength) behavior when they close to the n_2 radiation line.

When a core layer with index n_c and thickness d is inserted into a finite 1D PC, the 1D PCW is formed as shown in Figure 3.10. With the assistance of the band-gap map of 1D PCs, when the index of the core is changed (it is equivalent to the thickness change of the core), four different guiding regimes are clearly recognized, which correspond to the four regions as shown in Figure 3.11. As shown later, regimes I and II belong to the long-wavelength and the short-wavelength regimes, respectively, and light for both regimes is guided due to the PBG effect. In regime III, light is guided due to the PBG effect in the short-wavelength and the TIR effect in the long-wavelength. In regime IV, light is guided due to the TIR effect. Due to the nature of different guiding regimes, the modal characteristics in each regime behave differently, as clearly shown in the next section.

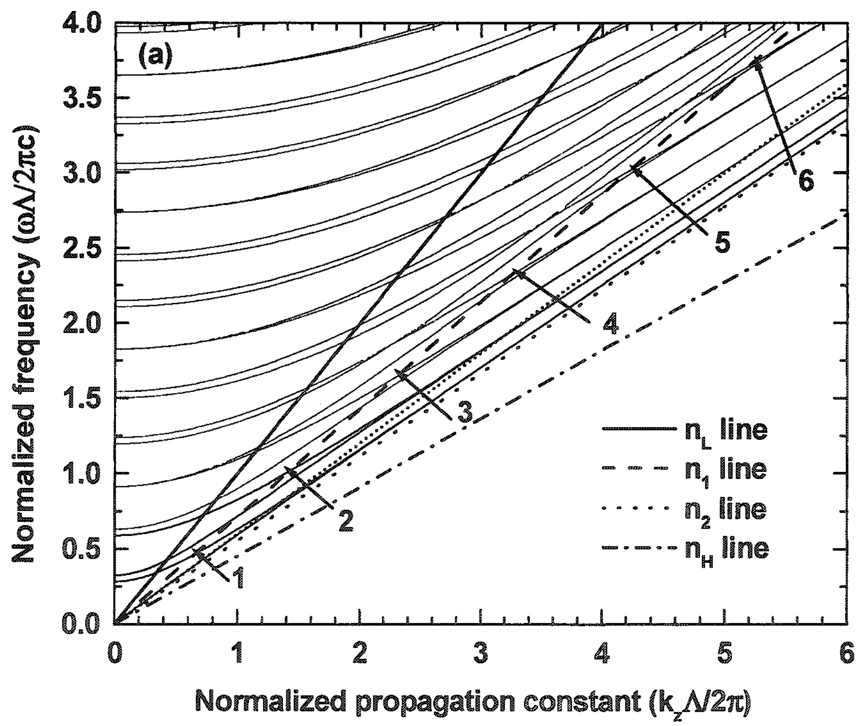

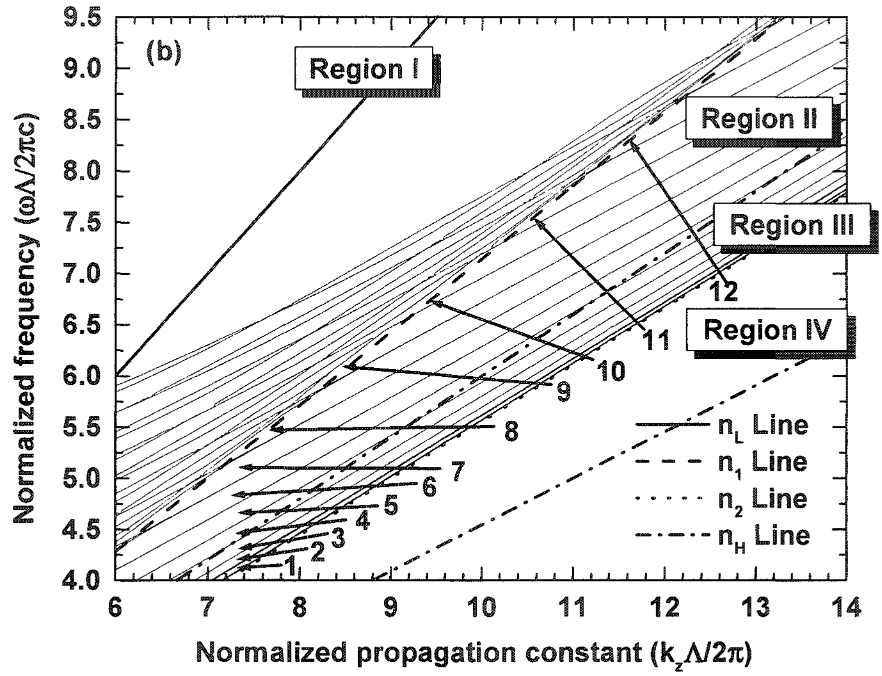

Figure 3.11 The band-gap map of TE waves of 1D PCs with the $n_1 = 1.4$, $n_2 = 1.8$, and $d_2 = 0.6092\Lambda$, in which four different radiation lines are shown: solid line for n_L (i.e., 1.0), dashed line for n_1, dotted line for n_2, and dash-dotted line for n_H (i.e., 2.2). Also four guiding regions are indicated, which belong to $(1, n_1)$, $[n_1, n_{12}]$, (n_{12}, n_2), and $[n_2, \infty]$.

3.4.2 TIR and PBG Guiding

For 1D PCWs defined in the previous section with $N = 32$, the effective indices and mode profiles (see Appendix A) can be calculated by the transverse resonance method (TRM) for different core indices $n_c = 1.0$, 1.4, 1.7, and 2.2, which belong to four guiding regimes mentioned in the previous section. For the sake of simplicity, here only guided modes of 1D PCWs in the second band-gap (i.e., the PBG band-gap between band 4 and band 5) and the semi-infinite band-gap are considered.

Figure 3.12 and Figure 3.13 show the effective indices n_{eff} and the corresponding mode profiles $E(x)$ for 1D PCWs with the core width of $d = 19.131$ μm. In Figure 3.13, the operating wavelengths and corresponding confinement factors in the core are presented in Table 3.1. From Figure 3.12 and Figure 3.13, for the PBG guided modes in the same band-gap, it is observed that the operating wavelengths move from long wavelength to short wavelength and the number of guided modes increases when the index n_c of the waveguide core increases. Consequently, the modal index closes to the radiation line of the core (so the dispersion of the mode decreases) and the mode energy is confined mostly within the low index core and the first high index layer on either side (so the confinement factor of the mode increases). This phenomenon resembles the case when the operating wavelength of the mode increases for the fixed radiation line (e.g., $n_c = n_1$) [7]. On the other hand, for the TIR guided modes in the semi-infinite band-gap, the similar effect is observed except the dispersion of modes. It is demonstrated that the dispersion of the mode increases when the index of the waveguide core increases. This is understood as the width of the semi-infinite band-gap (between the radiation lines of the core and the band 1) increases when the index of the waveguide core increases. Also, it is interesting to note that, for the same number of the layer pairs, the confinement loss of 1D PCWs decreases when the index of the waveguide core increases. Also, at short wavelengths, the fundamental mode of the PCWs with a core index of $n_c < n_2$ experiences cut-off. We will show this result in detail later (see 3.4.3).

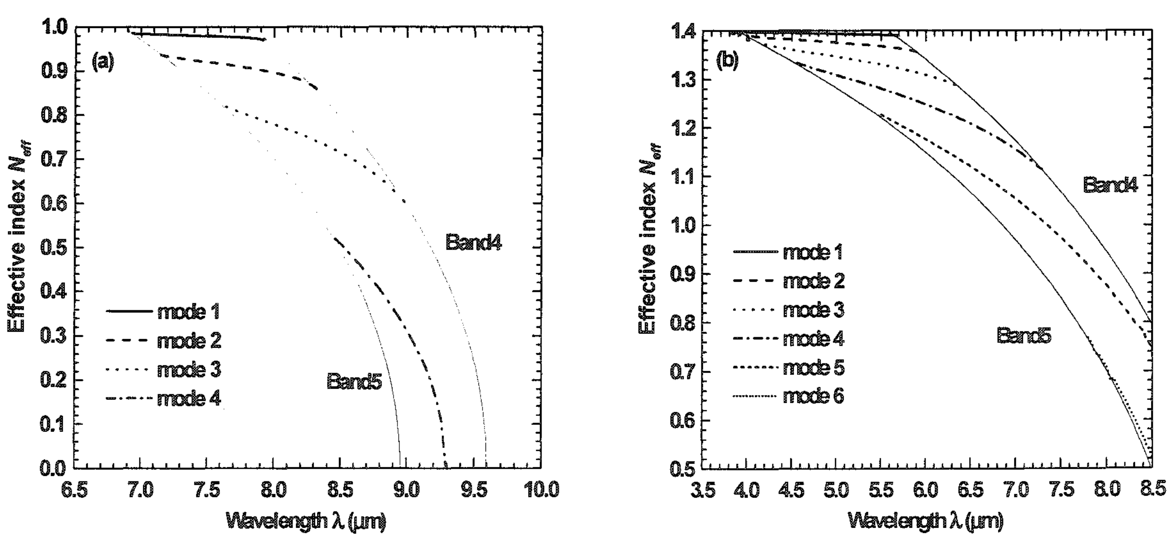

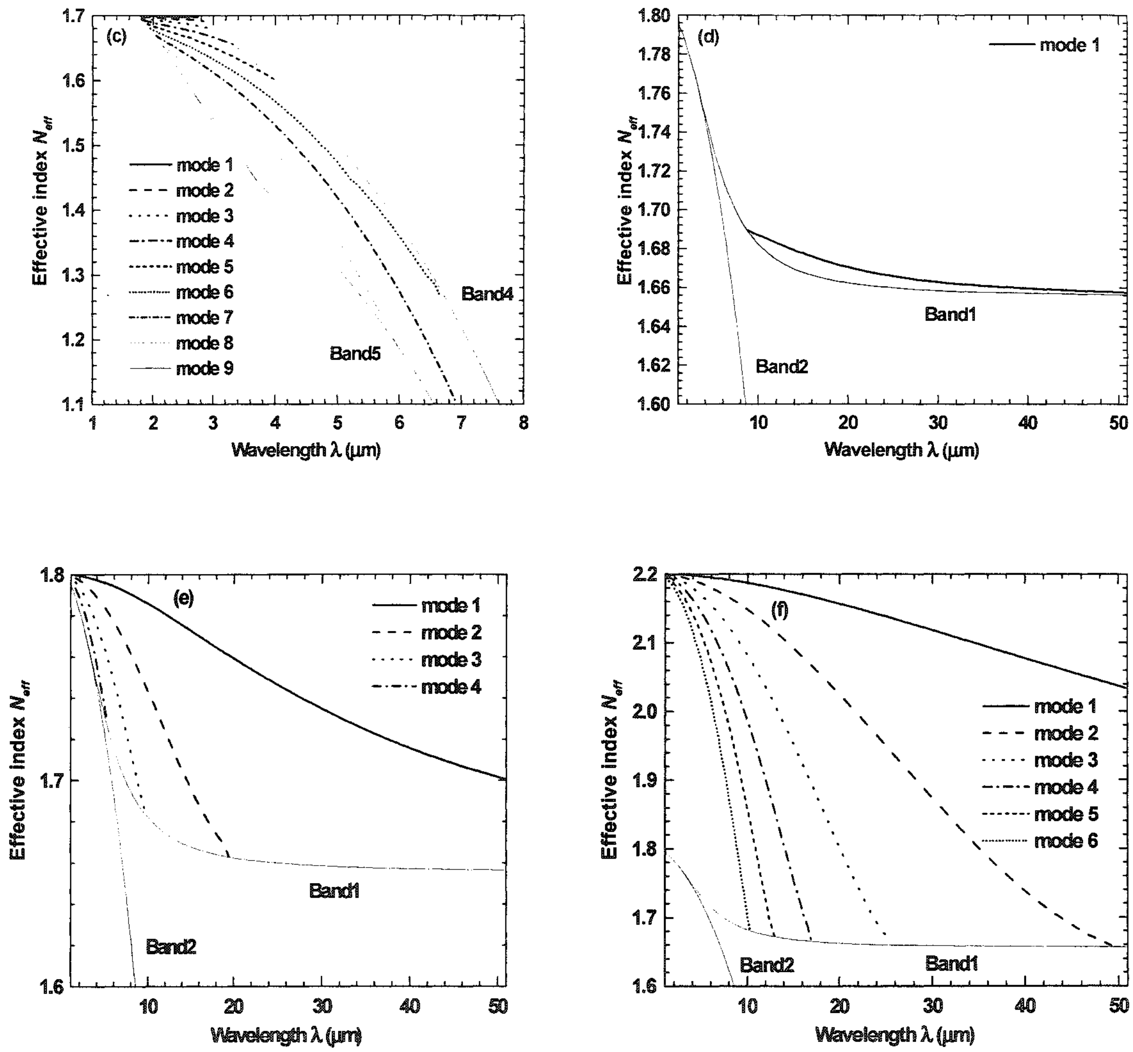

Figure 3.12 The TE effective indices n_{eff} as a function of wavelength of the guided modes for the core index n_c = 1.0 (a), 1.4 (b), 1.7 (c,d), 1.8 (e), and 2.2 (f) of 1D PCWs in the second band-gap (a, b, and c) and semi-infinite band-gap (d, e, and f). The fixed design parameters for 1D PCWs are as follows: d_2 = 0.6092 Λ = 3.437 μm, Λ = 5.642 μm, d = 3.391 Λ = 19.131 μm, N = 32, n_1 = 1.4, and n_2 = 1.8.

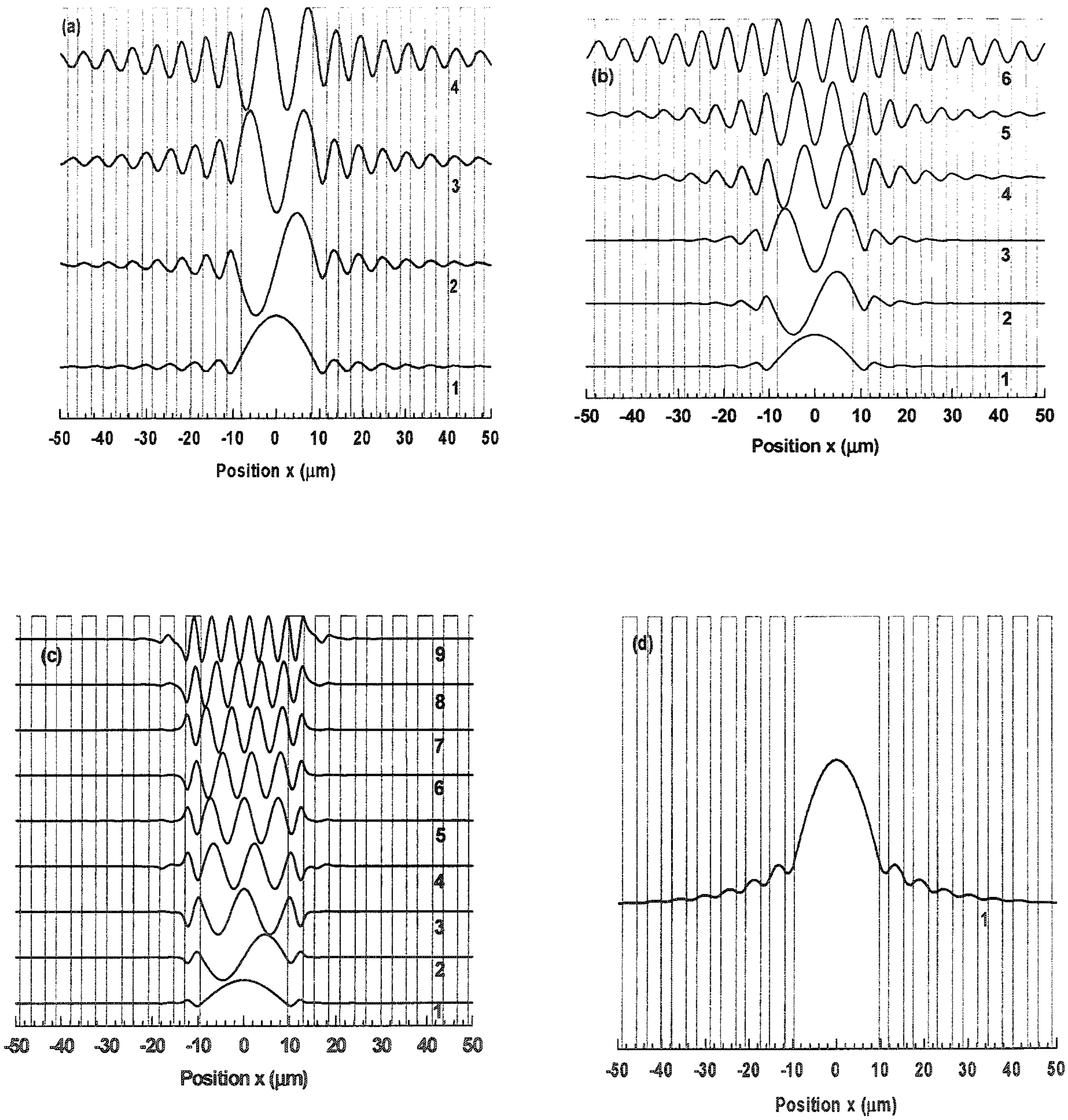
(a)
4
3
2
1
-50 -40 -30 -20 -10 0 10 20 30 40 50
Position x (μm)
(b)
6
5
4
3
2
1
-50 -40 -30 -20 -10 0 10 20 30 40 50
Position x (μm)
(c)
9
8
7
6
5
4
3
2
1
-50 -40 -30 -20 -10 0 10 20 30 40 50
Position x (μm)
(d)
1
-50 -40 -30 -20 -10 0 10 20 30 40 50
Position x (μm)

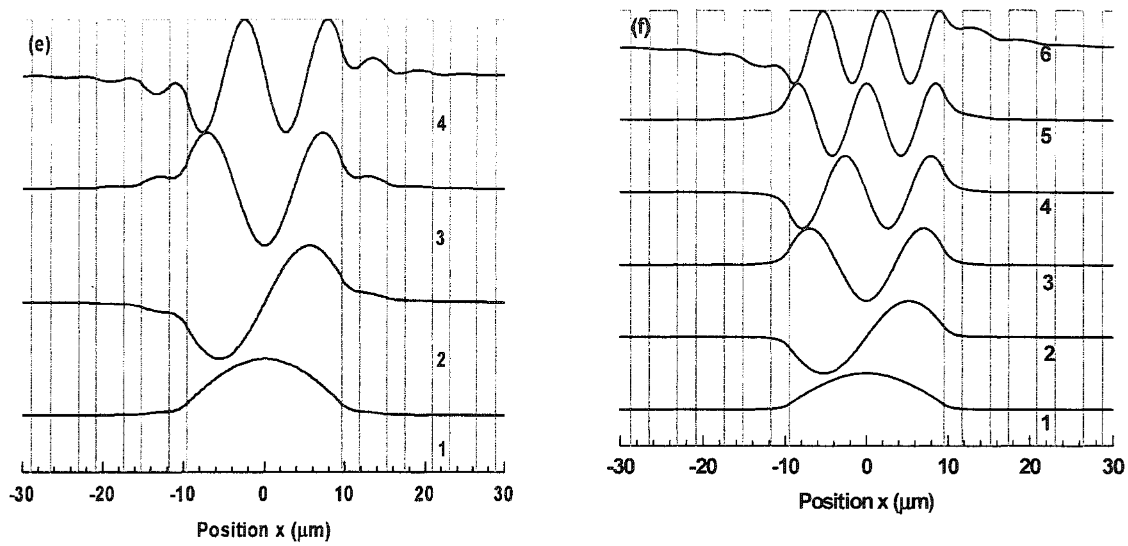

Figure 3.13 The electric field E_y of the guided modes for the core index n_c = 1.0 (a), 1.4 (b), 1.7 (c, d), 1.8 (e), and 2.2 (f) of 1D PCWs in the second band-gap (a, b, and c) and semi-infinite band-gap (d, e, and f). The fixed design parameters for 1D PCWs are the same as in Figure 3.12.

Table 3.1 Wavelengths and confinement factors of the modal profiles shown in Figure 3.12.

Field Profiles	# of modes	Guiding mechanism	Wavelengths, μm	Confinement factors
Fig13a	4	PBG	7.40,7.40,8.30,8.90	0.981,0.918,0.798,0.660
Fig13b	6	PBG	5.07,5.07,5.07, 6.5,7.3,9.0	0.991,0.970,0.935, 0.774,0.678,0.408
Fig13c	9	PBG	2.5,2.5,3.0,3.0,3.0, 3.0,3.0,3.0,3.5,3.5	0.991,0.973,0.937,0.844,0.856, 0.856,0.841.0.791,0.6882
Fig13d	1	TIR	10.0	0.916
Fig13e	4	TIR	10.0,10.0,10.0,10.0	0.993,0.961,0.946.0.935
Fig13f	6	TIR	10.0,10.0,10.0,10.0, 10.0, 4.5	0.998,0.993,0.982,0.965, 0.932,0.726

3.4.3 Effects of the Number of Layer Pairs on Modal Properties

Using the proposed analytical model, it is very convenient to predict the number of layer pairs needed to avoid possible modal leakage, which is one of important design considerations, for any desired wavelengths. Here the previous mentioned 1D PCWs are used to investigate the effects on modal properties for different number of layer pairs (N).

When the number of layer pairs (N) decreases from a large number (e.g., 64) to unity, it is observed that the effect of the number of layer pairs on the effective index, the modal profiles, and dispersion is negligible at the short wavelength region and more pronounced at the long wavelength region. As expected, it can be understood by the nature of the band structure with off-axis propagation [7]. At the short wavelength region (i.e., the high-order band-gap and larger k_z region), light is trapped in the high index region due to the TIR effect as an isolated optical waveguide. So the modal properties of 1D PCWs are mainly determined by an optical waveguide consisting of the low/high index core and the first high/low index layers on either side. When the operating wavelength increases, the modal fields spread more into the cladding, and the accumulated contribution to modal properties is much more pronounced. Overall, the effect of the number of layer pairs on the confinement loss is more significant. It is worth to note, in some sense, that the ARROW waveguide is a special kind of 1D PCWs with N = 1. Figure 3.14 shows the confinement loss L_c of the fundamental mode for the core index n_c = 1.0, 1.4, 1.6, and 1.7. In general, the effect of the number of layer pairs on the confinement loss in the PBG-PCWs is more pronounced than that in the PCF-PCWs because of different guiding regimes.

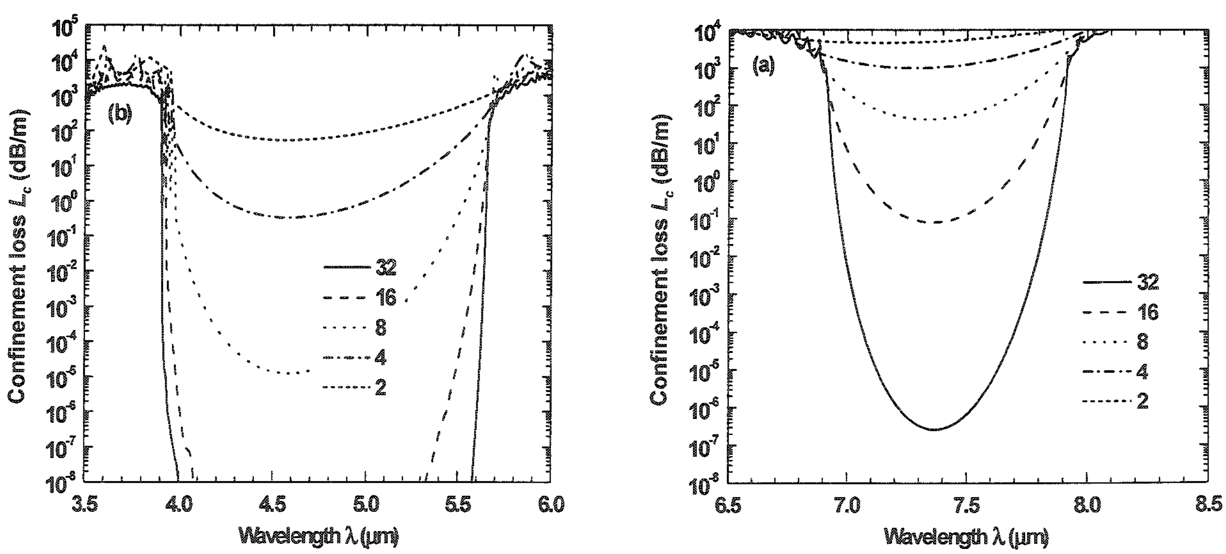

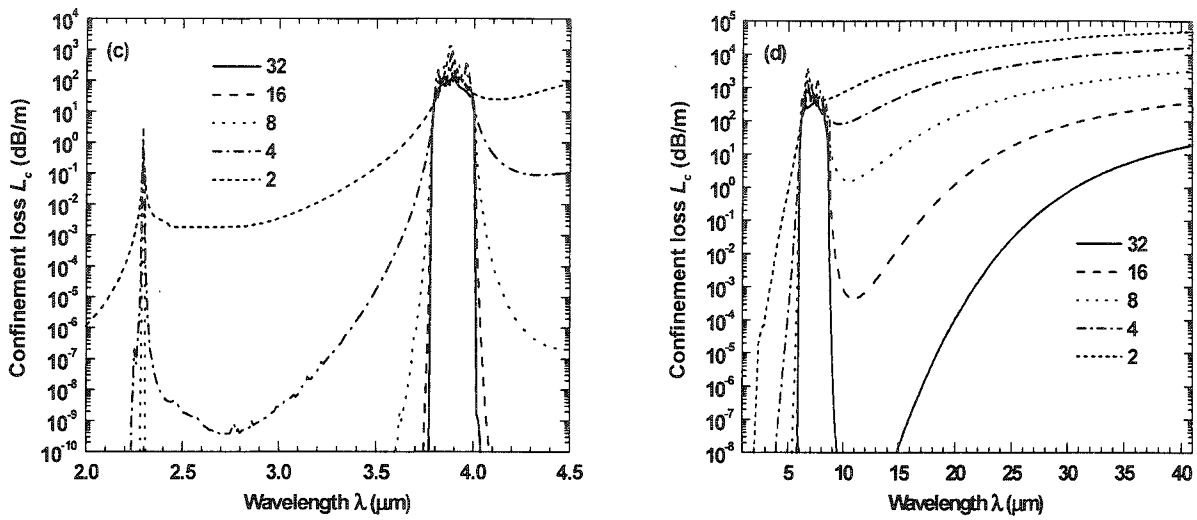

Figure 3.14 The confinement loss L_c of the fundamental guided modes for the core index $n_c = 1.0$ (a), 1.4 (b), 1.6 (c), and 1.7 (d) of 1D PCWs in the second band-gap (a, b, and c) and semi-infinite band-gap (d). The fixed design parameters for 1D PCWs are the same as in Figure 3.12 except the number of layer pairs.

3.4.4 Scaling Transformation with the Core Thickness

As we know, one of most important features of the PCs is the scaling transformation with the pitch Λ (see Appendix C). In some sense, in order to assist the design process of waveguides, the scaling transformation of modal properties with the ratio d_2/Λ can also be approximately obtained [58], [59]. With the similar thought, in order to design the waveguides with specific modal properties such as the single-mode operation and group velocity dispersion, the scaling transformation of the basic modal properties with the thickness d of the core should be understood. Like the scaling transformation of the basic modal properties with the ratio d_2/Λ, the relation of the basic modal properties with the thickness d of the core is no longer linear with the scaling parameter P (i.e., d/d_0). For this reason, we have to calculate modal properties numerically and extract a nonlinear relationship. For example, for the waveguide dispersion D_g, Figure 3.15 shows the simulation results of the fundamental guided modes for the core index $n_c = 1.0$, 1.4, 1.8, and 2.2 of 1D PCWs in the second band-gap and semi-infinite band-gap, respectively. As expected, when the thickness d of the core decreases, the effective index decreases and the modal profile spreads more into the cladding so that the dependence of the effective index on the wavelength is more pronounced. This, in turn, increases the dispersion of the PCWs. As seen from figure, however, the dispersion curves for the different guiding mechanisms (e.g., PBG with (a) and (b) and TIR with (c) and (d)) behave differently. This can be understood as follows. For the PBG-PCWs, according to (3.20), in order to meet the Bragg phase condition of the mode, $k_{cx}d$ should keep constant and k_{cx} is inversely proportional with the thickness d of the core. So, with the help of (3.3), the effective index n_{eff} decreases and the modal profile spreads more into the cladding according to the variation theorem. After some algebraic manipulations, we can obtain that $D_g \propto 1/d^2$, which is also consistent with the dispersion relation of the metallic plate (see 3.5.2). For the TIR-PCWs, the scaling transformation of the waveguide dispersion of the PCWs with respect to the core thickness d can be obtained from the slab waveguide theory with the help of the EIM method, and we have that $D_g \propto 1/d$.

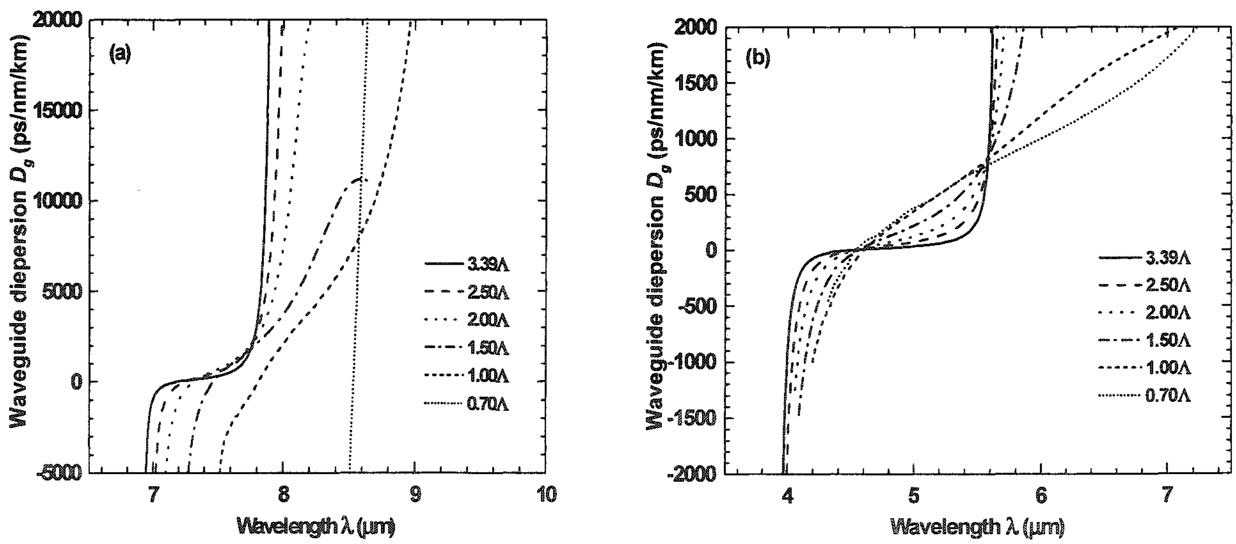

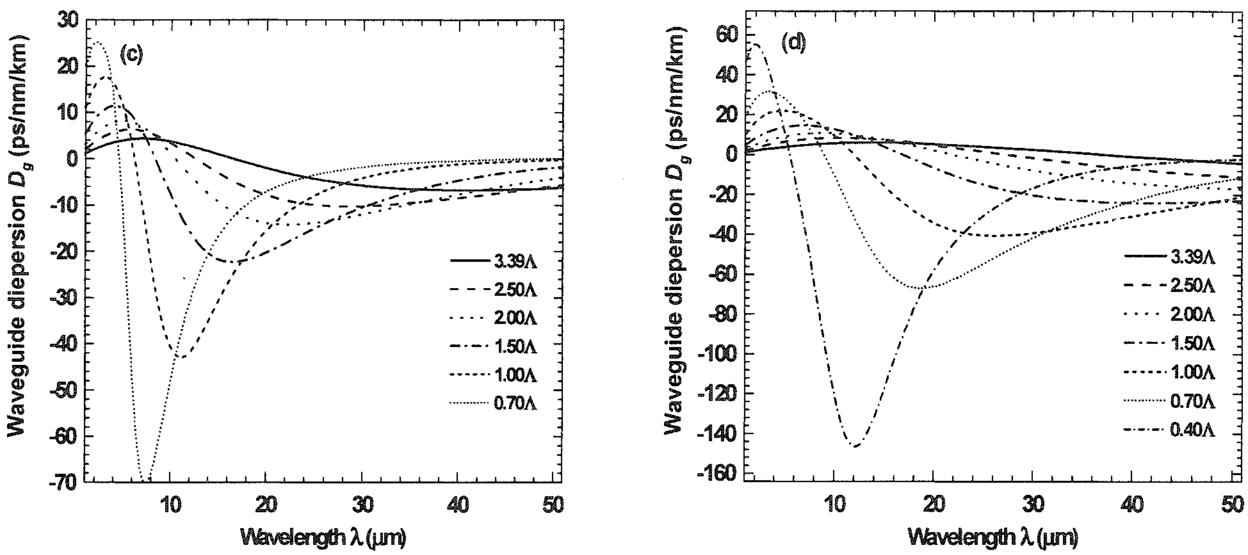

Figure 3.15 The waveguide dispersion Dg of the fundamental guided modes for the core index n_c = 1.0 (a), 1.4 (b), 1.8(c), and 2.2 (d) of 1D PCWs in the second band-gap (a and b) and semi-infinite band-gap (c and d). The fixed design parameters for 1D PCWs are the same as in Figure 3.12 except the thickness of the core layer.

3.4.5 Envelope Approximation Analysis

Now we start to investigate the modal characteristics and physical meaning of 1D PCWs by way of examples through the EAM and EIM methods. The PCW under study is a 1D heretostructure PCW as shown in Figure 3.16. The thickness d_2 of the high index layer n_2 is 0.4Λ and the core width of the waveguide is that $2W = l\Lambda$ (l = 1, 2, 3, 4, ...).

Firstly, we need to understand the optical properties of the PC structure used as the cladding material, which consists of two alternative layers with index n_2 = 3.1623 and n_1 = 1.0 (air). As we know, in order to confine the light in the PCWs, the positive large curvature is appreciated for the TIR-based PCWs and the negative large curvature for the PBG-based PCWs. Figure 3.17 shows the band curvature with relation of the propagation constant for the 1D PCs with two alternative layers with index n_2 = 3.1623 and n_1 = 1.0 (air) at d_2/Λ = 0.5. As can be seen, bands with the odd number have the positive curvature (or effective "mass") and bands with the even number have the negative curvature, and low-order bands have larger curvature than high-order bands. As expected, the curvature with larger propagation constants, which is located in short wavelengths, is larger than that with less propagation constants, which is located in long wavelengths. Figure 3.18 shows the band curvature of band 1 and 2 with relation of propagation constant for the 1D PCs with two alternative layers with index $n_2 = 3.1623$ and $n_1 = 1.0$ (air). As can be seen, larger band-gaps have larger curvature. Also from the simulation results, it is shown that, for the first and second bands, the largest curvature is around the quarter wavelength thickness $d_2/\Lambda = 0.24$.

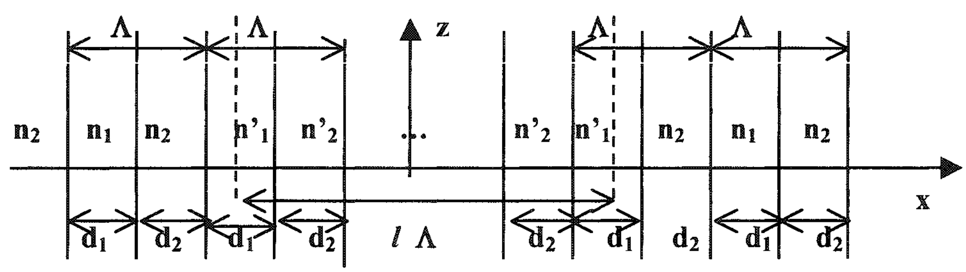

Figure 3.16 The schematic view of a 1D heretostructure PCW consisting of two alternative layers n_1 and n_2 with the high index thickness d_2 and the pitch Λ with core layer of N pairs of two same lattice layers n'_1 and n'_2.

Secondly, we consider the case in which the average index in the core is higher than in the cladding with two alternative layers with index $n_2 = 3.1623$ and $n_1 = 1.0$ (air) at $d_2/\Lambda = 0.24$. We choose a contrast $\Delta_0 = 0.1$, which means that the core has with two alternative layers with index $n'_2 = 3.3166$ and $n'_1 = 1.0488$ at $d_2/\Lambda = 0.24$. As we know from the band structure, guided modes exist where the curvature is positive. This occurs at $k_x = 0$ for the odd number of bands or at $k_x = \pi/\Lambda$ for the even number of bands in the band structure with on-axis propagation. On the other hand, this occurs for the odd number of bands in the band structure with off-axis propagation. For the sake of simplicity, we just focus on the first band.

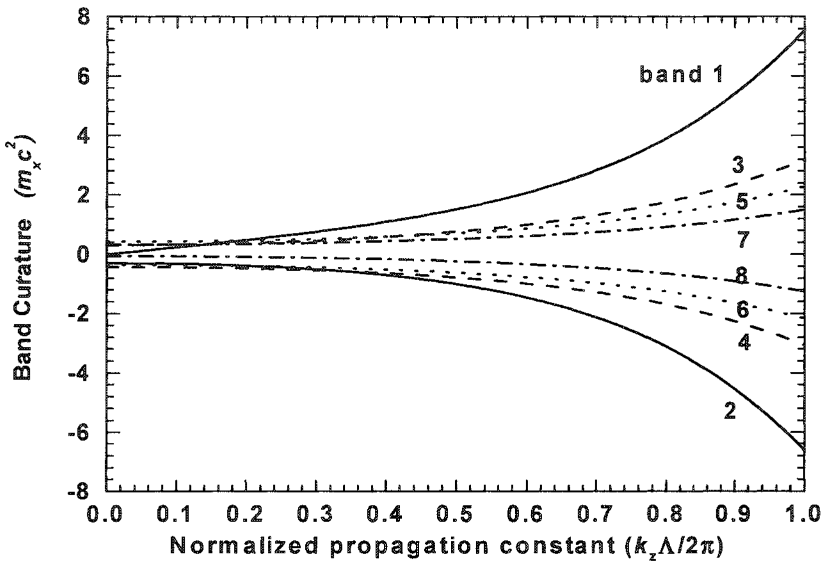

Figure 3.17 Band curvature with relation of propagation constant for the 1D PCs with two alternative layers with index $n_2 = 3.1623$ and $n_1 = 1.0$ (air) at $d_2/\Lambda = 0.5$.

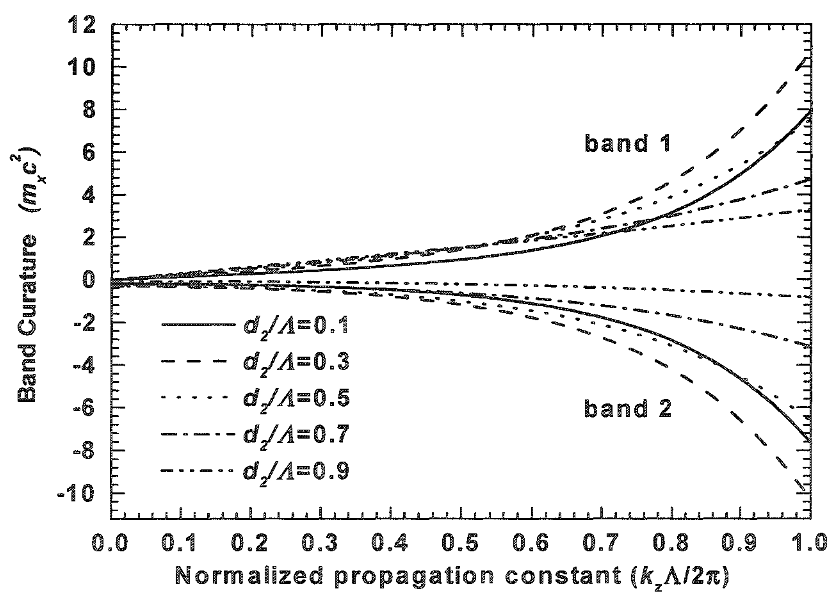

Figure 3.18 Band curvature of band 1 and 2 with relation of propagation constant for the 1D PCs with two alternative layers with index $n_2 = 3.1623$ and $n_1 = 1.0$ (air).

Figure 3.19 shows the dispersion relation for k_z sweeping from zero to the $2\pi/\Lambda$ point by two methods for the PCW with $2W = 5\Lambda$. The field patterns of the modes at $k_z = \pi/\Lambda$ is shown in Figure 3.20. The simulated results are good agreement with those computed numerically by the PWE method at an arbitrary position along the z axis (not shown in figure). As can be seen from figure, the simulated result by the EIM method is in good agreement with that by the EAM method at long wavelengths and the effective index of modes by the EIM method is larger than that by the EAM method at the short wavelengths, which are also explained by the field patterns as shown in Figure 3.20.

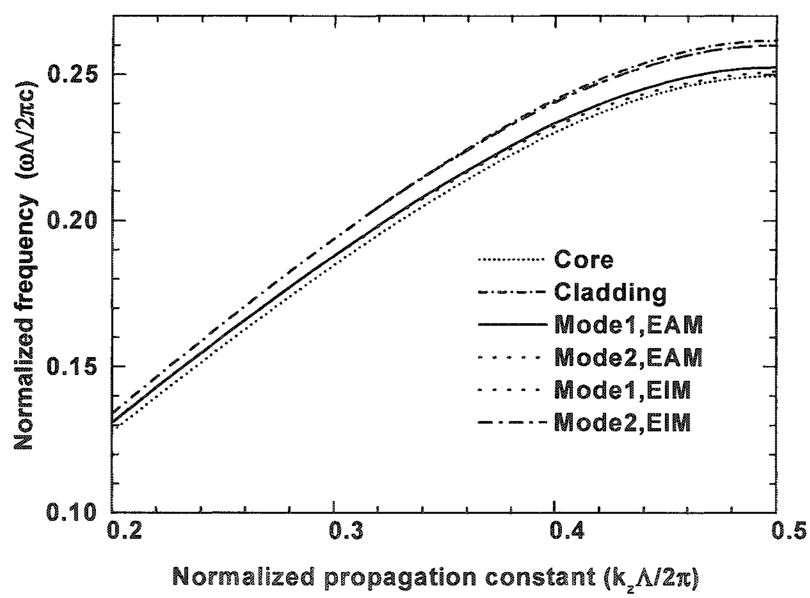

Figure 3.19 Dispersion relation of the waveguide and band structure of the core and cladding materials of the first band at $k_x = 0$.

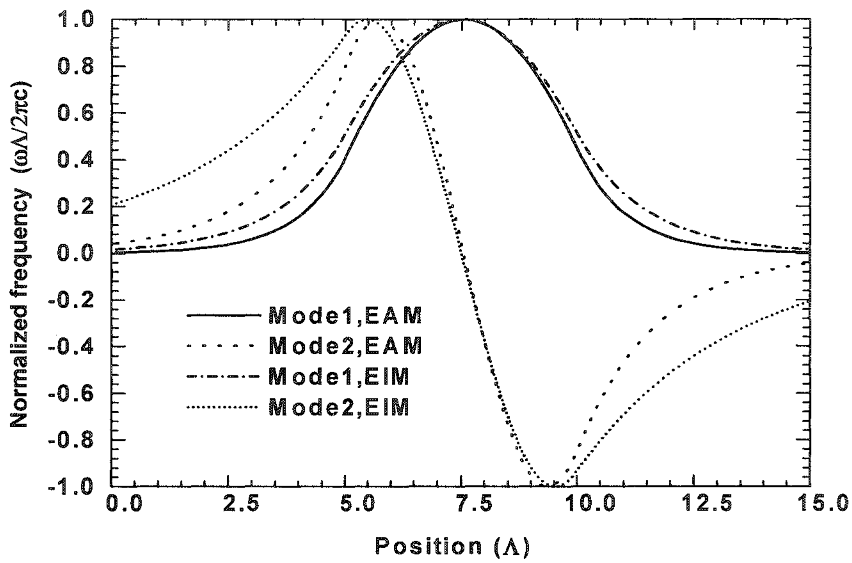

Figure 3.20 Even modes of the first band calculated by EAM and EIM for $k_z = \pi/\Lambda$ for the average refractive index higher in the core than in the cladding ($k_x = 0$).

Finally, we consider the case in which the average index in the core is lower than that in the cladding. As mentioned earlier, the PBG wave guiding is possible even when the average index in the core is lower than that in the cladding. We interchange the roles of the core and the cladding in the example above: the cladding material is now made of rods of $n_1 = 3.3166$ in a background of $n_2 = 1.0488$, while the core is made of rods having $n'_1 = 3.1623$ lying in air ($n'_2 = 1.0$). In this case, the contrast is $\Delta_0 = -0.091$. Guided modes are allowed where the curvature of the bands is negative, which occurs at $k_x = \pi/\Lambda$ in the case of the first two bands. As seen in the previous analysis, this transverse component of the wave vector introduces a modulation to the envelope function in the transverse direction, so that the actual slowly varying envelope of the mode is the function f_{nk0}. This modulation explains why the envelope function and the actual field have opposite parities. The dispersion relation and shapes of the modes are displayed in Figure 3.21 and Figure 3.22, respectively.

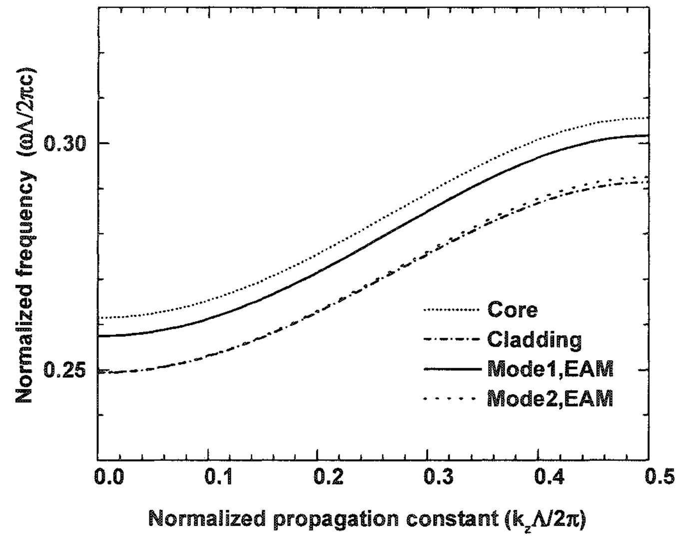

Figure 3.21 Dispersion relation of the waveguide and band structure of the core and cladding materials of the first band at $k_\perp$ (k_x) = π/Λ.

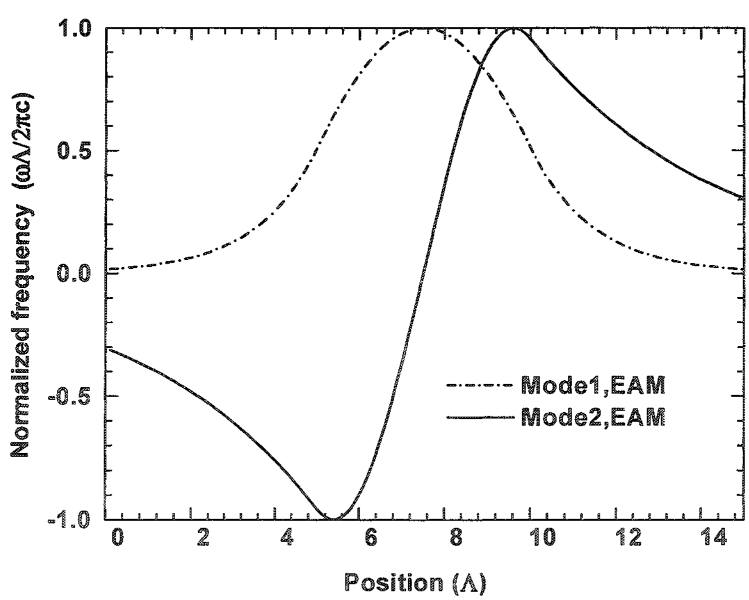

Figure 3.22 Even modes of the first band calculated by EAM for $k_z = \pi/\Lambda$ for the average refractive index higher in the core than in the cladding at $k_x = \pi/\Lambda$.

3.5 Discussions

After understanding some basic concepts such as space-filling modes, vector nature, and modal properties, here we discuss some issues such as the effect of the ratio d_2/Λ on modal properties, the single-mode condition, and relation with PCFs (i.e., 2D PCWs).

3.5.1 Effect of the Layer Size-to-Pitch Ratio

By using the definition of the normalized propagation constant b and the normalized frequency V in 3.3.2, the normalized propagation constants of first eight bands of TE modes of 1D PCs with the function of V for 1D PCWs with the ratio $d_2/\Lambda = 0.8$ (dash-dot lines), 0.6209 (dot lines), 0.3 (dash lies), and 0.0 (solid lines) are shown in Figure 3.23. All other design parameters for 1D PCWs are fixed and the same as those in Figure 3.12. As can be seen from the figure, the effect of different ratio d_2/Λ on modal properties of 1D PCWs is similar with the one of wavelengths. For the small d_2/Λ ratio PCW (e.g., $\leq$ 0.3), light is well confined within the core by the first and second cladding layers and small number of the layer pairs is enough to confine light due to a very wide band-gap. On the other hand, for the large d_2/Λ ratio PCW (e.g., ≥ 0.9), light is weakly confined and field penetrates into a large area of air holes and large number of the layer pairs is needed to confine light due to a very narrow band-gap.

3.5.2 Comparison with 1D Metallic Parallel-Plate Waveguide

In general, the modal fields and the transverse constants of the metal parallel plates with the index n_c are easily obtained as follows

$$E(x) = \begin{cases} a\sin(k_x(x+d/2)) & \text{for the TE wave} \\ a\cos(k_x(x+d/2)) & \text{for the TM wave} \end{cases} \tag{3.34}$$

$$k_x = \begin{cases} (n+1)\pi/d & \text{for the TE wave} \\ m\pi/d & \text{for the TM wave} \end{cases} \tag{3.35}$$

where d is the thickness of the waveguide, and integers n, m = 0, 1, 2, 3, ...(TEM wave for m = 0). The effective indices of the metal parallel plates are obtained by using

$k_x^2 = k(n_c^2 - n_{eff}^2)$ and their corresponding dispersions can be calculated. For example, the waveguide dispersion of the fundamental mode (i.e., n = 0 and m = 1) can been analytically calculated in the unit of ps/nm/km

$$D_g = \frac{\lambda}{c} \frac{(n_c / 2d)^2}{\sqrt[3]{(n_c^2 - (\lambda / 2d)^2}} \tag{3.36}$$

where c is the speed of light and λ is the operating wavelength.

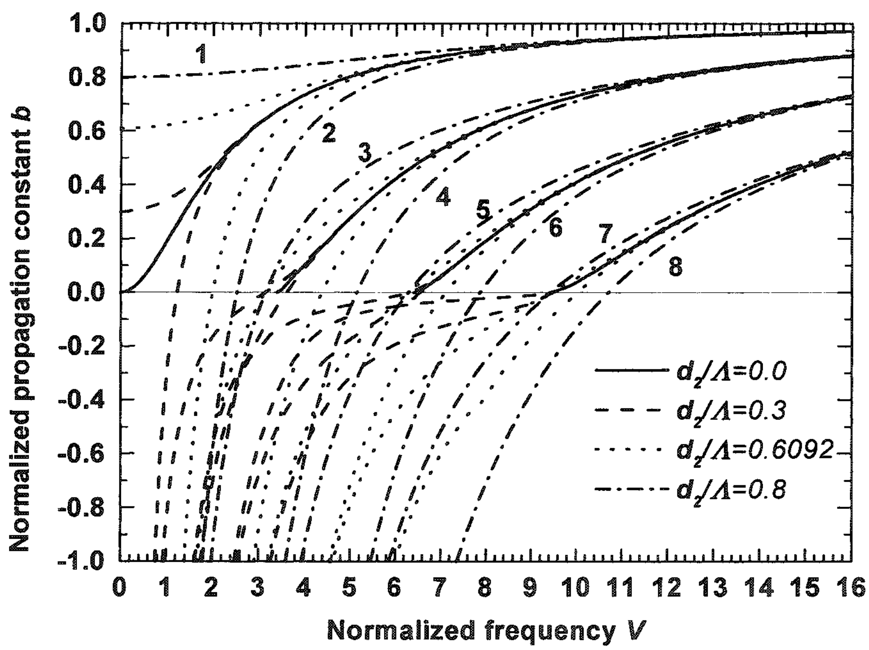

Figure 3.23 The normalized frequency b of first eight bands of TE waves of 1D PCs with the function of normalized propagation constant V for 1D PCWs with the ratio $d2/\Lambda$ = 0.8 (dash-dot lines), 0.6209 (dot lines), 0.3(dash lies), and 0.0 (solid lines). All other fixed design parameters for 1D PCWs are the same as in Figure 3.12.

Figure 3.24 shows the TE effective indices n_{eff} of the fundamental guided mode as a function of wavelength for the different core thickness d of the equal-thickness metal waveguides. For comparison, the TE effective indices n_{eff} (Figure 3.12b) of the fundamental guided mode of 1D PCWs in the second band-gap are also plotted. As can be seen, when the thickness d is large enough (e.g., > 2Λ), the effective index difference between the 1D PBG-PCWs and metallic wavguides is very small except near the band-gap edge. When the thickness d decreases, the effective index difference becomes large. However, when we compare the dispersion, the dispersion difference between them is still large even the thickness d increases to 10Λ. In general, the differences between the 1D PBG-PCWs and metallic wavguides are summarized as follows:

1. Metallic wavguides only have mode cut-off of $k_z = 0$, and PBG-PCWs also have the band edge cut-off.
2. Metallic wavguides only have the positive (anomalous) dispersion, and PBG-PCWs also have the negative (normal) dispersion with the positive dispersion slope.
3. In general, PBG-PCWs have larger dispersion than metallic wavguides.
4. PBG-PCWs have similar dispersions with metallic wavguides only when the index ratio n_2/n_1 and the core thickness d are large enough.

3.5.3 Mode Cut-Off and Single-Mode Operation

Like conventional step index slab waveguides, the TIR-PCWs guide light due to the TIR effect. For the guided modes, their effective indices n_{eff} meet the following relation

$$n_c > n_{eff} > n_{FSM1} \tag{3.37}$$

Where n_c is the refractive index of the core of waveguides and n_{FSM1} is the cladding effective index of the PCWs (i.e., the fundamental space-filling mode of the PCs). The normalized effective frequency V_{eff}, less than π for the single-mode operation as the slab waveguide, is defined

$$V_{eff} = \frac{2\pi}{\lambda} d \sqrt{n_c^2 - n_{\mathrm{FSM1}}^2} \tag{3.38}$$

Where d is the core thickness and λ is the operating wavelength.

For the PBG-PCWs, it is found that modal properties for both 1D PBG-PCWs and metallic waveguides are similar so that the single-mode condition of metallic waveguides can be utilized for 1D PBG-PCWs. From (3.38), the single-mode operation can be calculated as $\lambda_c < n_c d$. More precise cut-off condition and single-mode operation can be obtained by employing the more accurate methods as mentioned in previous chapter. The possible cut-off conditions of the guided modes of 1D PCWs are shown in Table 3.2.

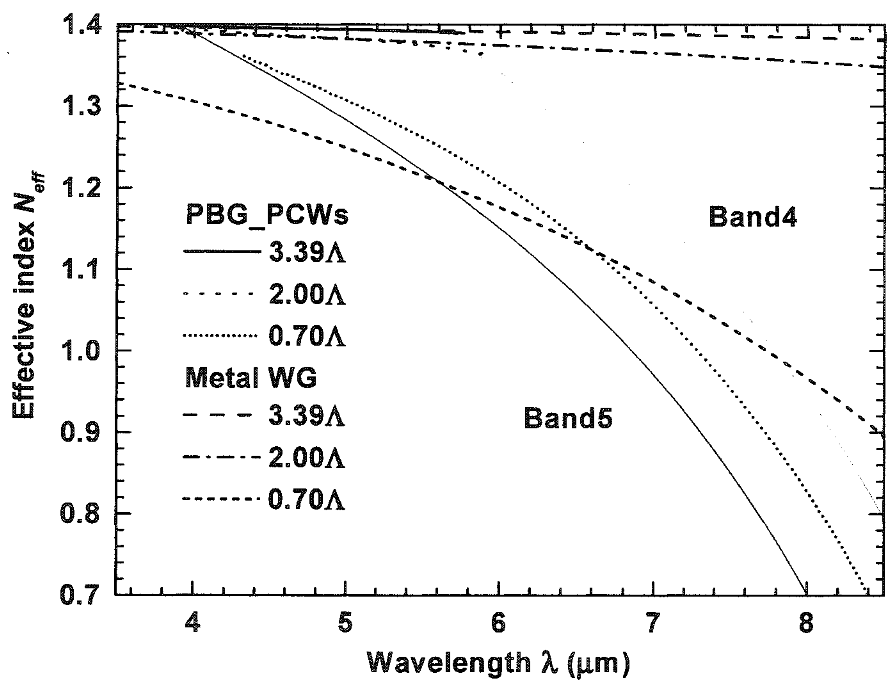

Figure 3.24 The TE effective indices n_{eff} of the fundamental guided mode as a function of wavelength for the different core thickness d of 1D PCWs in the second band-gap and the equal-thickness metal waveguides. The fixed design parameters for 1D PCWs are as follows: $d_2 = 0.6092\Lambda = 3.437$ μm, $\Lambda = 5.642$ μm, $N = 32$, $n_c = 1.4$, $n_1 = 1.4$, and $n_2 = 1.8$.

Table 3.2 Possible cut-off of the guided modes of 1D PCWs

Guiding Regime	Guiding mechanism	Cut-off (short wavelength edge)	Cut-off (long wavelength edge)	Cut-off ($k_z = 0$)
1	PBG	Yes	Yes	Yes
2	PBG	Yes	Yes	No
3	PBG	Yes	Yes	No
3	TIR	Yes	No	No
4	TIR	No	No	No

3.5.4 Relation with PCFs

As we know, due to variety of propagation directions, the band-gap of 2D PCs is much narrower than that of 1D PCs. However, there are still many common features between the PCFs (i.e., 2D PCWs) and 1D PCWs as long as the 2D PCs have a reasonable band structure. For example, instead of forming the PCFs by changing the core index, we can also form the PCFs by changing the size d_0 of the defect hole. The relation between 1D PCWs and the PCFs is shown in Table 3.3, where d and d_0 are diameters of the air-hole and defect-hole of the PCFs, and D (note we use D to replace d to avoid the symbol confusion) and d_2 are the thickness of the core and high index layer of 1D PCWs, respectively.

Table 3.3 Relation between 1D PCWs and 2D PCFs.

Guiding region	1D PCWs, $D > d_2$	2D PCFs
Regime 1	$n_c = 1$	N/A
Regime 2	$n_c \in [1, n_{12}]$	$d_0 > d$
Regime 3	$n_c \in (n_{12}, n_2)$	$d_0 \in (0, d)$
Regime 4	$n_c = n_2$	$d_0 = 0$

3.6 Summary

In this chapter, by employing some analysis methods (i.e., the transfer matrix method, the transverse resonant method, the effective index method, and envelope approximation method), the modal characteristics (e.g., the effective index, the dispersion, the confinement loss, and the model field profiles) of the guided modes of 1D PCWs are comprehensively investigated.

Firstly, in order to gain some insight of 1D PCs, a generalized transfer matrix method is used to calculate the band structure. The band structure of 1D PCs with on-axis and off-axis propagation is investigated in some detail. Through the complete analysis of the band structure, some salient features (e.g., the closure of the band-gap) of 1D PCs are recognized and understood through the Bragg condition. By employing the variation theorem, the band structure of 1D PCs is easily understood with the concept of the space-filling modes. It is this theorem that provides another way to calculate the band structure through some numerical algorithms without any approximations.

Secondly, in order to calculate the modal properties of 1D PCWs, a rigorous modeling method (i.e., the transverse resonant method) with combination of the transfer matrix method is proposed. With the help of the band structure of 1D PCs, four guiding regimes in 1D PCWs are identified for the different indices of the core of 1D PCWs. The modal characteristics for each regime behave differently from the guiding mechanism point of view. Some effects (e.g., the number of layer pairs) on modal properties are investigated and scaling transformations of modal properties related to the design parameters of the waveguide structures are derived. Through some approximation methods (e. g., the EIM and EAM methods), the physical insight (e.g., the effective cladding/core index) of 1D PCWs can be easily understood.

Finally, some basic issues, such as effects of the layer size-to-pitch ratio and core thickness, cut-off condition and single-mode operation, comparison with 1D metallic waveguide, and relation with the PCFs, are discussed.

Chapter 4
Photonic Crystal Fibers

In this chapter, with the help of the band structure of the 2D PCs, the modal characteristics of the photonic crystal fibers (PCFs, or 2D PCWs) with low and high index defects (i.e., the PBG-PCFs and TIR-PCFs) are thoroughly analyzed and evaluated. The simulation results are validated by comparison with published simulated and measured results. The vector nature of the PCFs is examined through a systematic comparison among the full-vector, semi-vector, and scalar models. The dependences of the important design parameters such as the size of interstitial holes and the number of air-hole rings on modal characteristics of the PCFs are investigated. The scaling transformations of the modal properties with respect to the key design and operation parameters of the PCFs are obtained.

4.1 Introduction

There has been intensive research recently into photonic crystal fibers (PCFs) [63]-[65], also known as the holley fibers (HFs) or the microstructured fibers (MOFs), in which a waveguide structure is formed by a two-dimensional periodic structure made from an array of air holes with some defects. One of the important features of the PCWs is the ability to localize the modal field around the defects. Based on the knowledge we have acquired from the analysis of 1D PCWs, we will focus on the analysis of modal properties of some typical 2D PCWs (i.e., the PCFs with 2D triangular lattice structrure).

According to light guided mechanisms, the PCFs are divided into two general categories, namely, the photonic band-gap (PBG) and total internal reflection (TIR) PCFs. The PBG-PCFs are made by a low-index core (e.g., the air defect) within the 2D PC and the guidance of light is due to the stop-band (or band-gap) of the PBG effect, as the effective index of the cladding is always higher than that of the core. The TIR-PCFs are made by a high-index core (e.g., the pure silica defect) and light is guided in the core due to the lower effective refractive index in the surrounding cladding. A number of methods based on scalar and vector formulations have been developed to analyze the modal characteristics of the PCFs. Despite the seemingly plethora of methods for modal analysis, the level of accuracy and scope of validity for the scalar and the vector formulations with respect to the calculation of the mode properties (e.g., dispersion) of the PCFs have not been studied in a systematic fashion. In this chapter, firstly, based on the band structure of 2D PCs, the modal characteristics of both PBG-PCFs and TIR-PCFs are systematically analyzed and evaluated. Secondly, the vector nature of the PCFs is evaluated through the vector, semi-vector and scalar models. Thirdly, some basic effects on modal characteristics of the PCFs (e.g., size of interstitial holes and number of air-hole rings), which are very helpful for design and optimization of the practical PCFs, are investigated. Finally, the scaling transformations of the modal properties are discussed.

4.2 2D Photonic Crystals and Photonic Band-Gap

As we know from the previous chapters, the 2D photonic crystals (PCs) are homogeneous in the z direction. There are several typical lattice structures of 2D PCs such as the square and the hexagonal lattice structures (e.g., triangular [7], honeycomb [66], and Kagome [67]). For the sake of simplicity, we only consider the triangular lattice structure as shown in Figure 4.1(a).

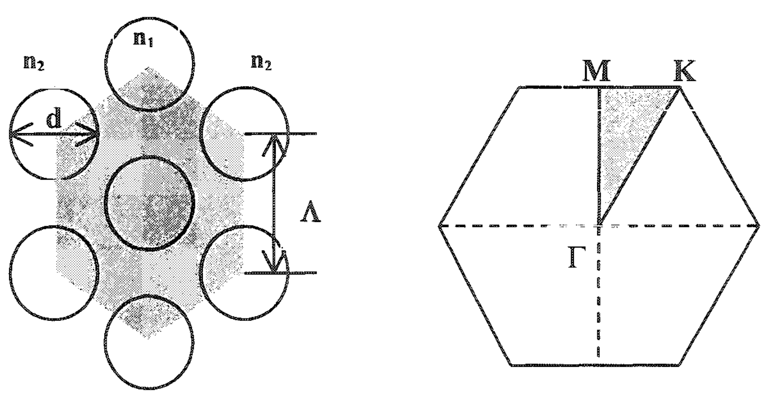

Figure 4.1 The unit cell and its irreducible Brillouin zone (shaded area) of a 2D PC with triangular lattice of air columns (n_1) with the size d drilled in a dielectric substrate (n_2).

We first discuss the band structure of the 2D PC with in-plane propagation. As discussed before, the mirror symmetry allows us to classify the modes by separating them into two polarizations: the TE wave and the TM wave. For the triangular lattice, the unit cell and its irreducible Brillouin zone (shaded area) are shown in Figure 4.1, with typical physical dimensions (i.e., d = 0.96Λ) and indices (i.e., n_1 = 1.0 and n_2 = 3.6056). Figure 4.2 shows their corresponding band structures for both polarizations. As can be seen from the figure, the band structures for the TE and TM waves are different. Further, unlike the square lattice in which there is no band-gap for the TE wave, the triangular array has a complete band-gap for both polarizations. However, when the index ratio n_2/n_1 decreases (e.g., the silica-air PCFs), unlike its counterpart in the 1D PCs, this complete band-gap disappears.

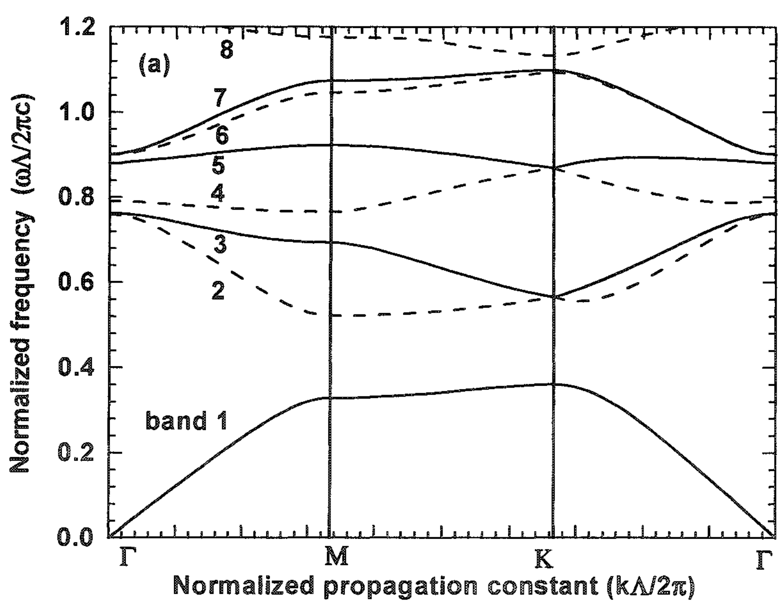

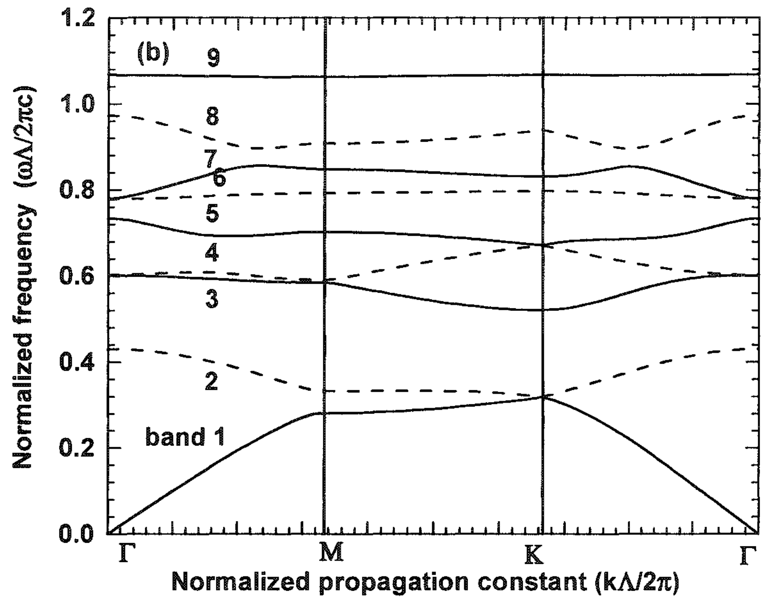

Figure 4.2 The photonic band structure of a 2D PC with a triangular array of air columns (n_1 = 1.0) with the size d = 0.96Λ drilled in a dielectric substrate (n_2 = 3.6056) for both polarizations: TE (a) and TM (b).

As we know, albeit no band-gap for the low index-ratio PCs with in-plane propagation, the band-gap with off-plane propagation opens up for a large enough k_z. This, in turn, leads to a fact that the small index-contrast PCFs can guide light due to the PBG effect. Once there is a band-gap in the PCs, it is possible to propagate in the PCFs by utilizing the PBG effect. Figure 4.3 and Figure 4.4 show the band structure of a 2D PC with a silica-air triangular array of air columns with the size d = 0.7044Λ [60] and 0.9Λ [61] drilled in a silica substrate, respectively. It is note that our simulation results agree well with some published results such as the finite element method (FEM) [60], [61]. On the other hand, for the triangular array with dielectric columns (i.e., $n_1 > n_2$), the similar results are also obtained. Figure 4.5 shows the photonic band structure of a 2D PC with a silica-polymer triangular array of polymer columns with the size d = 0.6Λ and 0.9Λ drilled in a silica substrate, respectively.

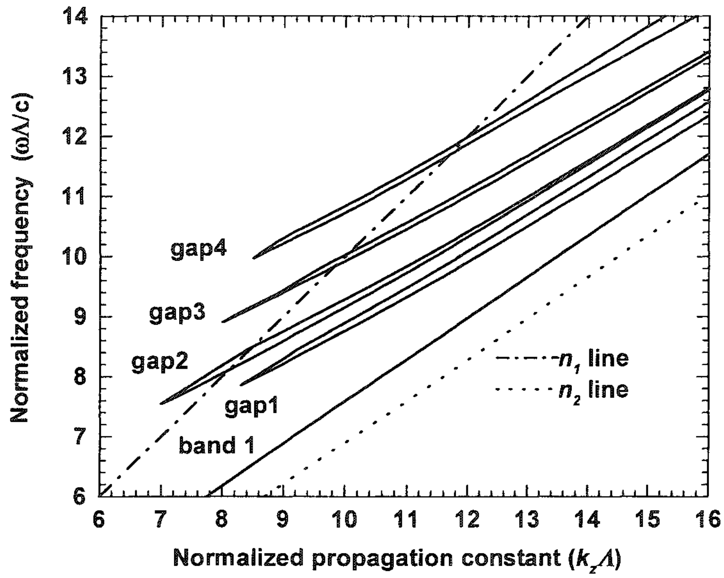

Figure 4.3 The photonic band structure of a 2D PC with a silica-air triangular array of air holes with the size d = 0.7044Λ drilled in a silica substrate (n_2 = 1.45).

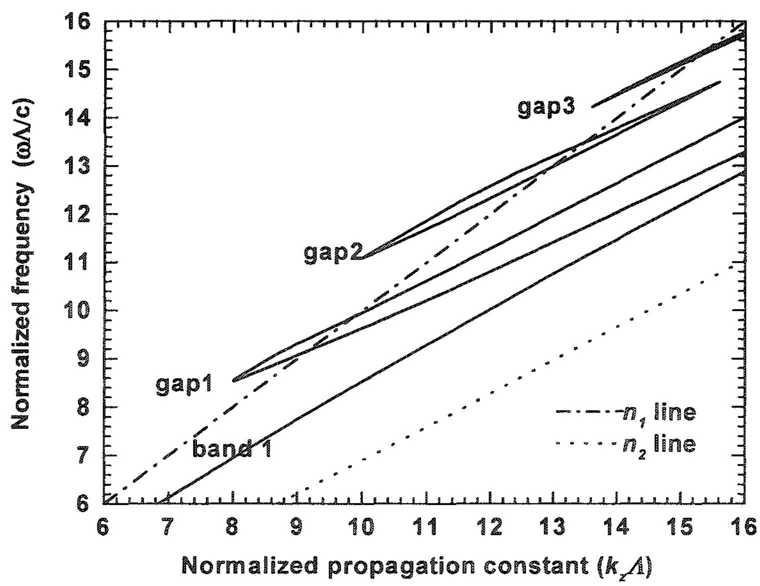

Figure 4.4 The photonic band structure of a 2D PC with a silica-air triangular array of air holes with the size d = 0.9Λ drilled in a silica substrate (n_2 = 1.45).

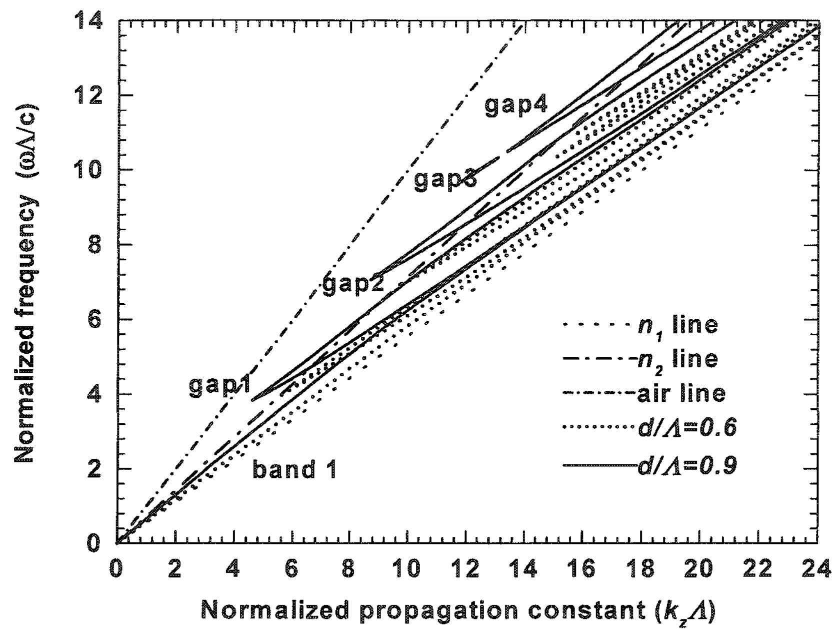

Figure 4.5 The photonic band structure of a 2D PC with a silica-polymer triangular array of polymer columns (n_1 = 1.8) with d = 0.6Λ and 0.9Λ drilled in a silica substrate (n_2 = 1.4).

Through further simulations, it is found that there are the similarity and difference between the off-plane propagation of 1D PCs and that of 2D PCs. The difference is at the area above the low index line where the band-gaps close when k_z decreases for 2D PCs and the gap never close completely (albeit closes at some discrete frequency points) for 1D PCs. The similarity is at the area below the low index line where the band-gaps open up for both 1D and 2D PCs when k_z decreases. This leads to the short-wavelength asymptotic behavior of the modes and only a few areas around defects affect the optical properties of the PCFs. It is also observed that, when the size-to-pitch ratio d/Λ increases for air columns or decreases for dielectric columns, the first band-gap goes up to cross the air line (or the low index line), which is an essential condition for the wave propagation of the PCFs in air (or the low index core), and the bandwidth of the band-gap along the air line (or the low index line) also increases. Although there is no complete band-gap for

2D PCs with off-plane propagation, fortunately, it is not important for the PCFs. Accordingly, in order to confine light in the core, it is very important to have a band-gap above the index line of core. It is worth to note that the region between the band 1 (or semi-infinite gap) and the index line of the core allows the TIR guiding and all others belong to the PBG guiding. Therefore, it is very helpful to investigate the band structure with the functions of the PC dimensions and wavelengths. Here we discuss the band structure of the 2D triangular PCs in some detail. Figure 4.6 shows the band structure of a 2D PC with function of the normalized propagation constant for different d/Λ values with a triangular array of polymer columns ($n_1 = 1.8$) drilled in a silica substrate ($n_2 = 1.4$).

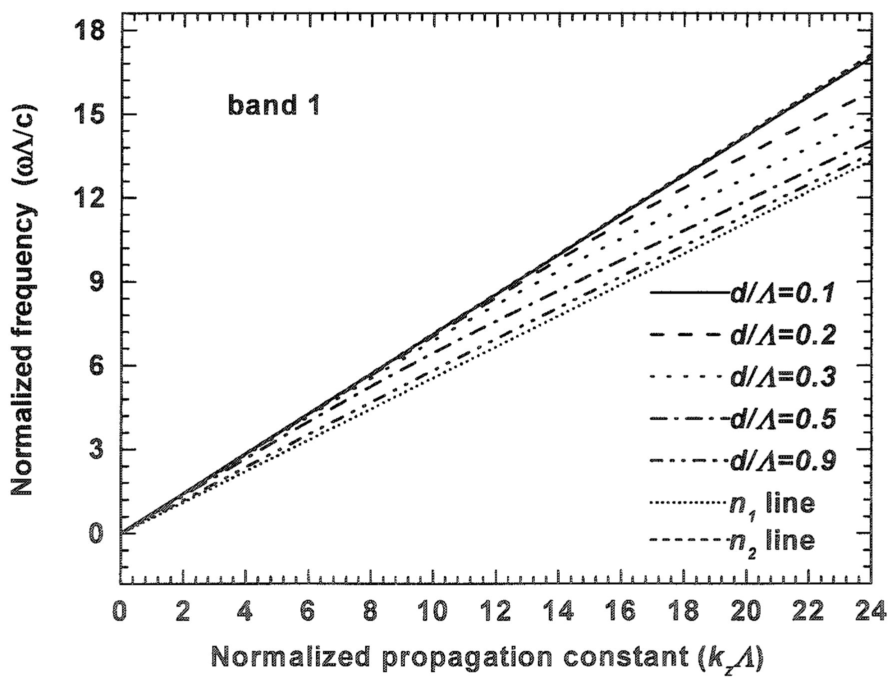

Figure 4.6 The photonic band structure of a 2D PC with function of the normalized propagation constant for different d/Λ values with a triangular array of polymer columns ($n_1 = 1.8$) drilled in a silica substrate ($n_2 = 1.4$).

Because the complete band-gap, which is generally measured by the gap-midgap ratio, is not important for the PCFs, here we define a new measure parameter along the low index line to measure the relative bandwidth to confine light in the PCFs. This new gap-midgap ratio can be defined by

$$\frac{\Delta\omega}{\omega_0} = \frac{2(\omega_H - \omega_L)}{\omega_H + \omega_L} \tag{4.1}$$

where ω_H and ω_L are the cross points between the gap and the low index line. Figure 4.7 shows this new gap-midgap ratio with function of d/Λ of a 2D PC with a triangular array of polymer columns ($n_1 = 1.8$) drilled in a silica substrate ($n_2 = 1.4$).

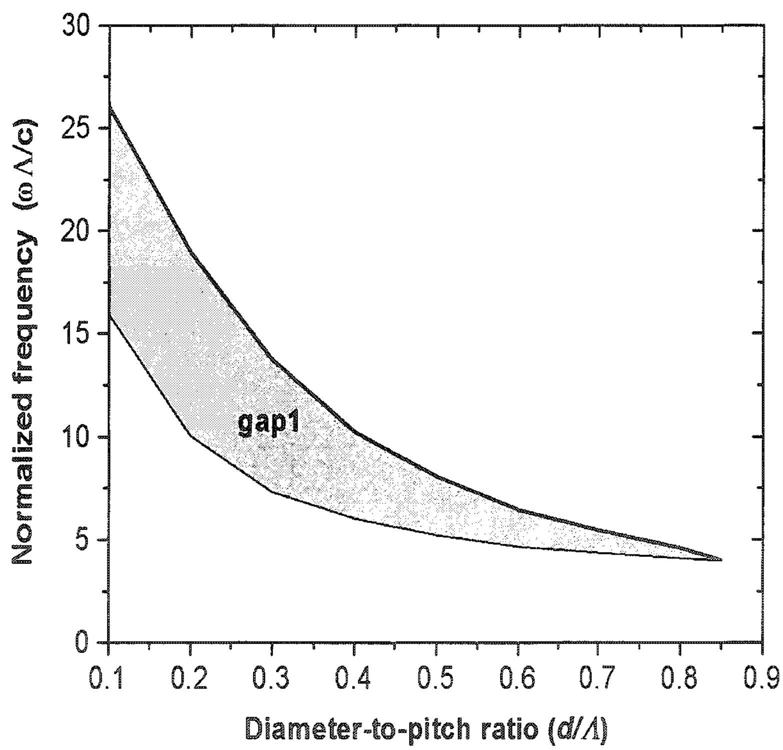

Figure 4.7 The new gap-midgap ratio with function of d/Λ of a 2D PC with a triangular array of polymer columns ($n_1 = 1.8$) drilled in a silica substrate ($n_2 = 1.4$).

4.3 PCFs with Low Index Defect

As mentioned before, the PBG-PCFs (or simply PBGFs) are made by a low-index core (e.g., air) and thus light is guided in the core region due to the PBG effect. Due to the guide of light through air, the PBGFs have the potential applications for the low-loss, linear, high-power delivery, and controllable dispersion transmission. Like the counterpart in 1D form (i.e., 1D PBG-PCWs), the guided modes exist in the corresponding band-gaps and are cut-off when the frequency of the mode is larger or less than the cut-off frequency (i.e., off the band-gap). In addition, practical PBGFs have only limited number of air-hole rings, and hence all modes are essentially leaky modes. As the PBGFs guide light at the long wavelength, their transmission loss mainly depends on the confinement loss of the fiber and the confinement loss, which is very sensitive to the number of air-hole rings.

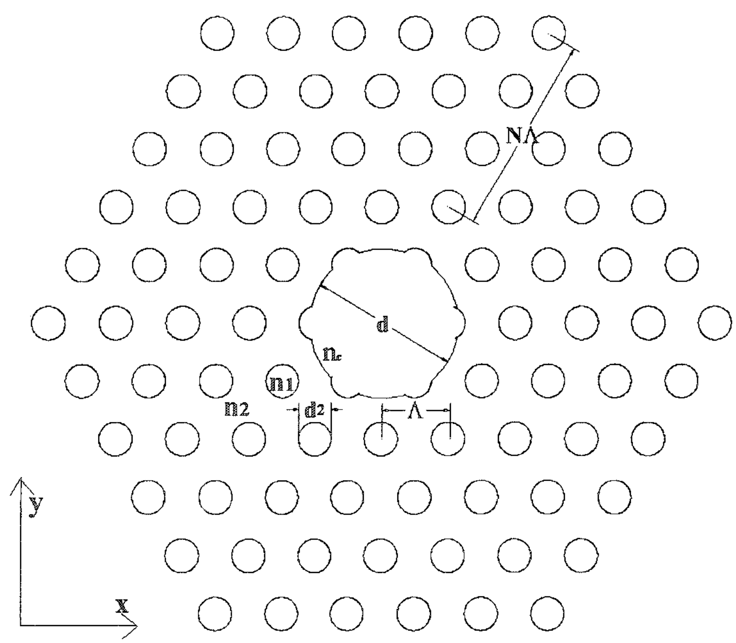

Figure 4.8 The cross section of a BPGF consisting of a regular triangular air-hole array consisting of the air (n_1 = 1.0) and silica (n_2 = 1.45) with four physical parameters: the number N of air-hole rings, air core diameter d, air-hole size d_2, and the pitch Λ.

Due to the mode cut-off of the fundamental modes in the BPGFs, in which the air core consists of one unit cell [62], we assume that the core of the BPGFs covers the area around seven unit cells as shown in Figure 4.8 with four physical parameters: the number N (e.g., 4) of air-hole rings, air core diameter d (e.g., $2\Lambda + d_2$), air-hole size d_2, and the pitch Λ. For the sake of simplicity, here we assume that the PBGF consists of an air core is surrounded by a uniform PC cladding with circular air holes. By employing the PML boundary conditions, numerical solution methods can be readily applied.

4.3.1 Validation: Comparison with FEM Simulation

Because of the high index-contrast of the PBGFs with respect to the single-mode fiber, it is necessary to validate our model with the published results (e.g., the effective index and the confinement loss). For this purpose, we use the commonly used large air-hole silica PBGFs with $\Lambda = 2.0$ μm and $d_2/\Lambda = 0.9$ [61]. Figure 4.9 presents the dispersion curve of the guided mode of the PBGFs in the first gap as a function of normalized propagation constant $k_z\Lambda$. As can be seen from Figure 4.9, the discrepancies between simulation results by the three methods are indistinguishable. Because the plane wave expansion (PWE) method cannot handle the PBGF with the limited number of air-hole rings, we calculated the confinement loss of the PBGFs through the finite difference method (FDM). Figure 4.10 shows the confinement loss of the PBGFs as a function of the number N of air-hole rings. As can be seen from Figure 4.10, the simulation results by the FDM method are in excellent agreement with those by the vector finite element method (FEM) [61]. It is also shown that the confinement loss in air-guiding PBGFs is very sensitive to the number of air-hole rings. Unlike the TIR-PCFs, larger number of air-hole rings is needed to preserve the similar confinement loss (e.g., $N = 20$ for the confinement loss of 0.01 dB/km). Through the scaling transformation of the confinement loss with respect to the pitch Λ (see Appendix C), the effect of the pitch on the confinement loss is easily obtained. For the similar wavelength of 1.55 μm, with the help of the band structure of 2D PCs (e.g., Figure 4.3 and Figure 4.5), the guiding regimes for the PBG-PCFs and TIR-PCFs are easily recognized: the PBG-PCFs operate at the long wavelength region and the TIR-PCFs operate at the short wavelength region. Because of different guiding regimes, the PBG-PCFs and TIR-PCFs behave differently. Due to the short wavelength region, it is possible for the TIR-PCFs to drastically reduce the confinement loss at a fixed wavelength by increasing the pitch. On the other hand, due to the long wavelength region, the increase of the pitch of the PBG-PCFs with preserving the ratio does not significantly reduce the confinement loss at a fixed wavelength.

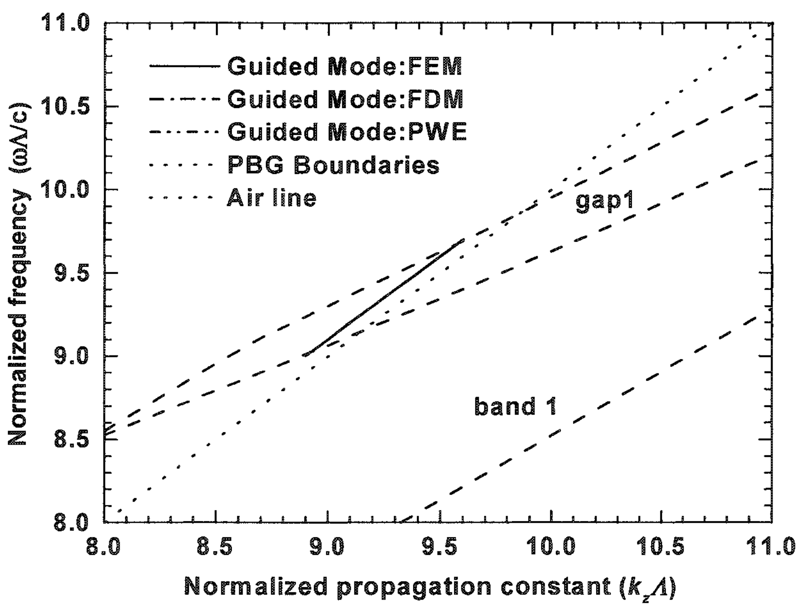

Figure 4.9 The modal dispersion ($\omega\Lambda/c$) of the guided mode of PBGFs with Λ = 2.0 μm and d_2/Λ = 0.9 in the first gap as a function of normalized propagation constant $k_z\Lambda$.

4.3.2 Mode Cut-off and Single-Mode Operation

As we know from the 1D PBG-PCWs, the fundamental modes of the PBGFs could be cut-off for the small size of the low index core. The number of the modes depends on the band structure of the PC cladding (e.g., the curvature of the band) and the parameters of the core (e.g., the core size and core index). In other words, with the help of the band structure of the PCs, the number of the guided modes in each band-gap can be easily calculated by some numerical methods. Like their counterpart in 1D form (i.e., 1D PBG-

PCFs), there are three kinds of cut-off, which were summarized in table 3.2. The single-mode condition can be easily evaluated through some analytic methods mentioned in the previous chapter. Here we give an analytical formula for the calculation of number of the guided modes with analogy to the conventional fiber [62]:

$$N = \frac{(k_{z,H}^2 - k_{z,L}^2)d^2}{16} \tag{4.2}$$

where $k_{z,H}$ and $k_{z,L}$ are the upper and lower edges of the PC at the fixed wavelength.

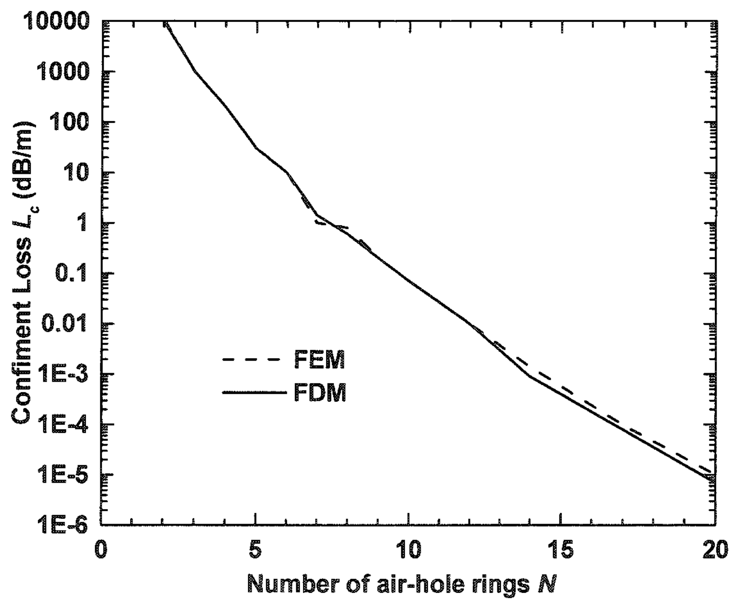

Figure 4.10 The confinement loss of PBGFs in the first gap with $\Lambda/\lambda = 1.5$, $\Lambda = 2.0$ μm and $d_2/\Lambda = 0.9$ as a function of the number N of air-hole rings.

4.3.3 Modal Characteristics

After verifying the simulation methods and understanding the single mode operation, we are ready to investigate the modal properties (see Appendix A) of the PBGFs. For instance, Figure 4.11 presents a typical dispersion curve of the guided mode of PBGFs in the first gap as a function of normalized propagation constant $k_z\Lambda$. Through further analysis, it is found that there are the similarity and difference between 1D PBG-PCWs and 2D PBGFs, which were summarized in 3.5.4.

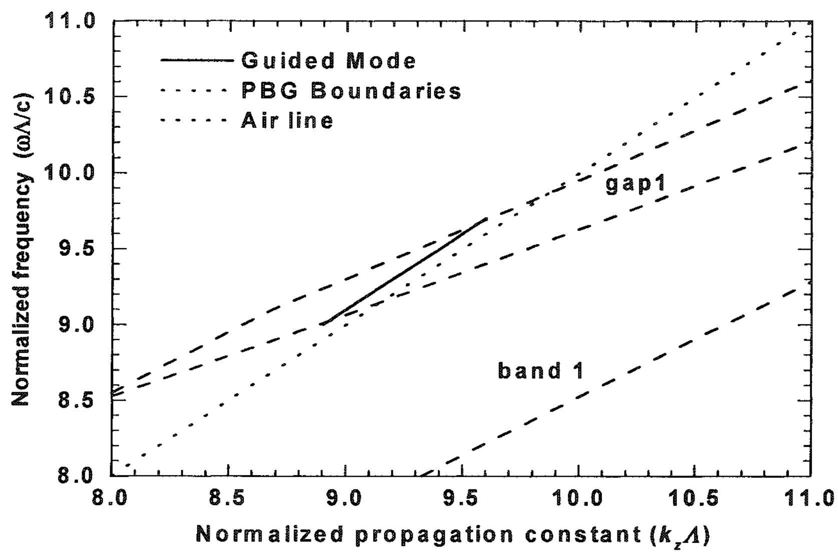

Figure 4.11 The modal dispersion ($\omega\Lambda/c$) of the guided mode of PBGFs with $\Lambda = 2.3$ μm and $d_2/\Lambda = 0.9$ in the first gap as a function of normalized propagation constant $k_z\Lambda$.

4.4 PCFs with the High Index Defect

As mentioned before, the TIR-PCFs (or simply PCFs) are made by a high-index core (e.g., pure silica) and thus light is guided in the core region due to the TIR effect. They are, however, different from the conventional single-mode fiber in several aspects. First of all, the index difference between the core and the effective cladding in the PCFs is a strong function of wavelength, and hence the modes supported by the fibers are essentially more dispersive. Secondly, practical PCFs have only limited number of air-hole rings, and hence all modes are essentially leaky in nature. Finally, the large index contrast between silica and air gives rise to strong vector properties of the modal characteristics, so the vector feature of the PCFs must be considered.

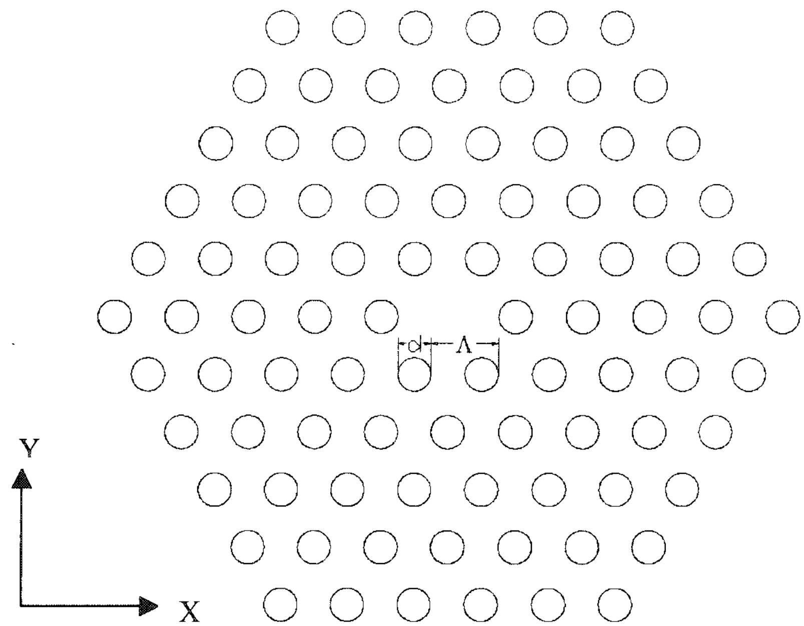

Figure 4.12 The cross section of a PCF consisting of a regular triangular air-hole array with five rings of air holes with two physical parameters: air-hole size d and pitch Λ.

Based on the above-mentioned reasons, we investigate the modal properties by the rigorous numerical methods (e.g., the FDM method). Figure 4.12 shows a typical PCF with five rings of air holes, in which only two physical parameters (i.e., the air-hole size d and the pitch Λ) are critical. For the sake of simplicity, we assume that the number of air-hole rings is larger enough (we will investigate this effect in 4.5.2) and the PCF consists of a pure silica core (i.e., defect) surrounded by a uniform PC cladding with circular air holes. By employing the PML boundary conditions, numerical solution methods such as the FDM method can be readily applied.

4.4.1 Validation with Simulated and Measured Results

The FDM method has been widely used and validated for many cases of optical waveguides with small index contrast [20]. Due to the high index contrast of the PCFs, it is necessary to validate the FDM model by way of examples. For this purpose, we investigate the commonly used air-filled silica PCFs with the fixed pitch (Λ = 2.3 μm) for different air-hole sizes. Due to the high sensitivity on the accuracy of the modal calculation in the context of the PCF, a significant discrepancy of the dispersion and confinement loss between the different published results can be seen for the PCFs with the fixed pitch Λ = 2.3 μm [18] [43], [44], [63], [64]. Because it is very important to make sure that the accurate simulation method is used to calculate the crucial group velocity dispersion and confinement loss of the PCFs, we validate the FDM method through those two modal properties with some published simulation and measurement results. Figure 4.13 presents the total dispersion of the PCFs as a function of wavelength for different hole sizes (i.e., d = 0.345, 0.621, 1.0, and 1.84 μm). It is apparent from Figure 4.13 that the simulation results by the full-vector FDM mode solver for d = 0.621 and 1.0 μm are in excellent agreement with those by the vector finite element method (FEM) at the all range of wavelength (only available from 0.6 to 1.3 μm for d = 0.621 μm) [63]. The dispersion value for d = 0.621 μm has been experimentally determined at a wavelength of 0.813 μm [70]. The simulated dispersion and its slope of –77.34 ps/nm/km and 0.468 ps/nm^2/km as shown in Figure 4.13 are in excellent agreement with the measured dispersion and its slope of –77.7 ps/nm/km and 0.464 ps/nm^2/km [70]. From Figure 4.13, it is also observed that the dispersion induced by the air holes increases as the air-hole size increases and the zero dispersion wavelength can be shifted to visible wavelength ranges by increasing as the hole size. Two design scenarios with practical significance are identified: the flat dispersion for a range from d = 0.621 to 1.0 μm, and the anomalous dispersion at shorter wavelengths (e.g., less than 1.0 μm) for large hole-size (e.g., d > 1.0 μm). We further assert that the zero-dispersion wavelength can be shifted into the visible wavelengths by simply reducing the core diameter $D = 2\Lambda - d$ (i.e., decreasing the pitch size Λ or increasing the air-hole size d). As we show later, if we only consider the geometrical dispersion D_g, in which the refractive index of the silica is set as a constant (e.g., 1.45), the scaling transformations of dispersion can be utilized and the design efforts of the PCFs can be simplified.

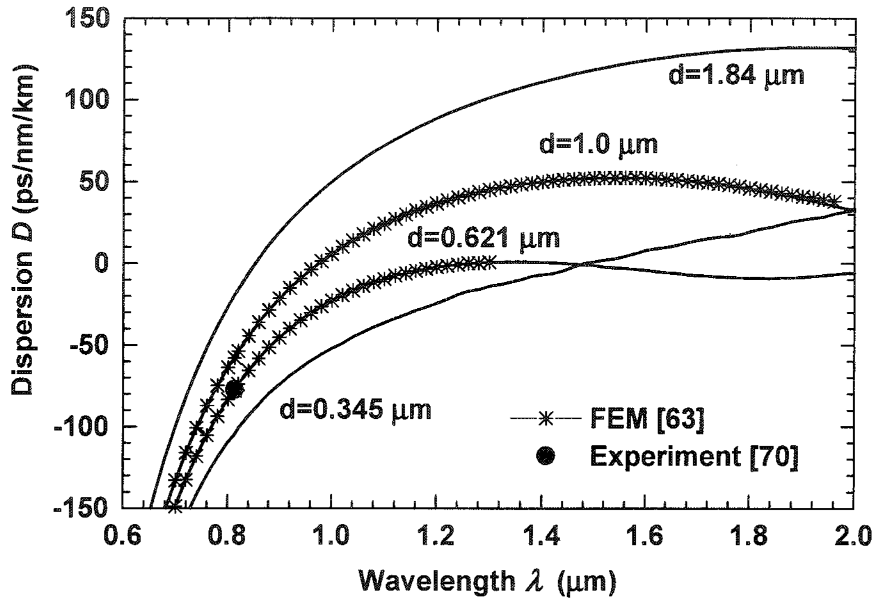

Figure 4.13 Dispersion D as a function of wavelength for PCFs with the fixed pitch (Λ = 2.3 μm) for different hole sizes d = 0.345, 0.621, 1.0, and 1.84 μm.

In addition to the dispersion, which is high sensitivity on the accuracy of the modal calculation (e.g., the second derivative of the real part of the effective index, see Appendix A), the confinement loss is another sensitive performance parameter (e.g., be proportional with the imaginary part of the effective index, see Appendix A). Therefore, it is necessary to verify the FDM method for the confinement loss. In the first example (a PCF with Λ = 4.0 μm, d = 2.26 μm, and N = 1), the effective index N_{eff} is (1.440101-j1.67x10^{-5}), which is in good agreement with N_{eff} (1.440136 - j1.708x10^{-5}) by the multipole expansion method (MEM) [74]. In the second example, the commonly used air-filled silica PCFs with the fixed pitch (Λ = 2.3 μm) and air-hole size (d = 1.15 μm) are used. Figure 4.14 presents the confinement loss of the PCFs as a function of wavelength for different number of air rings N (1, 2, 3, 4, and 5), respectively. It can be seen that the simulation results by the FDM method are in excellent agreement with those by the FEM (only available from 1.4 to 1.7 μm) [73] and the MEM (only available from 1.0 to 1.7 μm for $N = 3$ and 1.55 μm for $N = 1, 2$, and 4) [75] at the all range of wavelength. It is worth to note that the simulation results by the MEM method are calculated with considering the material dispersion of silica [69] and it means that, unlike on the dispersion, the effect of the material dispersion of silica on the confinement loss of the PCFs is negligible.

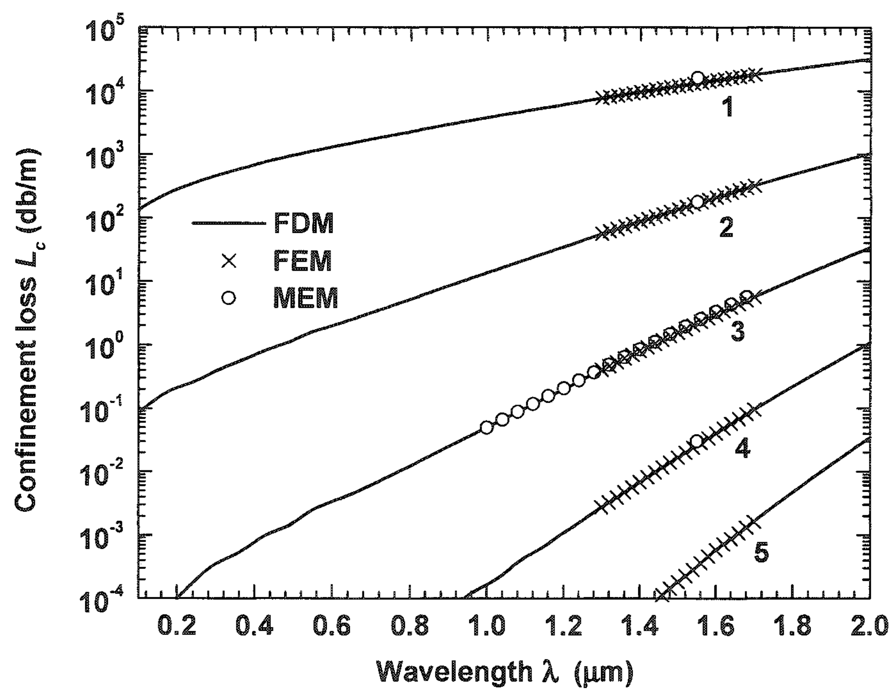

Figure 4.14 Confinement loss L_c as a function of wavelength for PCFs with $\Lambda = 2.3$ μm and $d = 1.15$ μm for different number of air-hole rings.

4.4.2 Comparisons among Full-Vector, Semi-Vector, and Scalar Models

By utilizing the FDM mode solvers based on the full-vector, semi-vector and scalar formulations, we investigate the modal characteristics of the PCFs with emphasis on the vector properties. So far, although there appeared to be paid attention to this feature of the PCFs, much less appreciation for the effect of vector properties of the modal fields in the PCFs with different design parameters of the PCFs is considered. It is very important, at least from the design point of view, to assess the accuracy and the scope of validity for the scalar and the semi-vector approximations. In order to gain some physical insight into the vector feature of the PCFs, we investigate this effect through the modal properties of the commonly used air-filled silica PCFs with the fixed pitch (Λ = 2.3 μm) in some detail [72]. This effect on the modal properties to all other cases (e.g., with the fixed air-hole size-to-pitch ratio) can be easily obtained through their scaling transformations (see Appendix C).

Figure 4.15 shows the effective index as a function of wavelength of the PCFs with different air-hole sizes of d = 0.46 (d/Λ = 0.2), 1.38 (0.6), and 2.3 μm (1.0), respectively. It is observed that the difference between the scalar and the vector models is small at short wavelength, but becomes significant for long wavelengths. Further, this difference increases as the air-hole size d increases. This is understood as the modal fields spread more into the cladding and the accumulated contribution to the vector property is more pronounced for the small air-hole PCF. Also, it is interesting to note that the difference between the semi-vector and the full-vector analyses is small, which indicates that the semi-vector model is sufficient for accurate prediction of the modal characteristics of the PCFs.

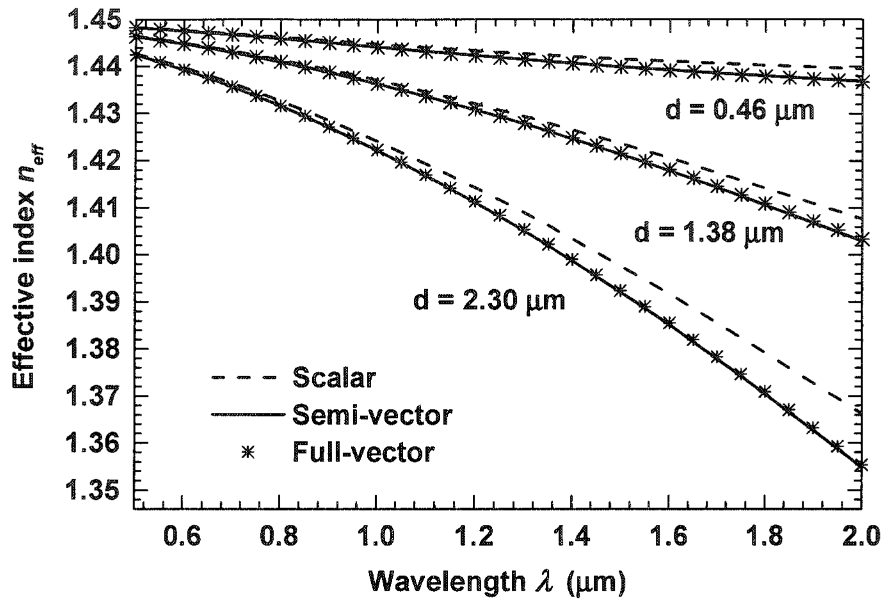

Figure 4.15 Effective index n_{eff} as a function of wavelength for PCFs with the fixed pitch (Λ = 2.3 μm) for different air-hole sizes d = 0.46, 1.38, and 2.3 μm.

In order to assess the accuracy and the scope of validity for the different models, the waveguide dispersion D_g of the PCFs is calculated and compared for different air-hole sizes d as shown in Figure 4.16. For the case of d = 0.46 μm, the simulated results calculated by the scalar modal expansion method [44] is also shown in Figure 4.16. It can be seen from Figure 4.16 that the simulation results for the scalar modes obtained by the scalar FDM method and the scalar modal expansion method are indistinguishable over a wavelength range of 0.5-1.5 μm. On the other hand, the differences between the scalar and the vector models are significant and cannot be ignored. Similar to the situation with the modal effective index, the semi-vector solution is capable of producing reasonably accurate results for the modal dispersion.

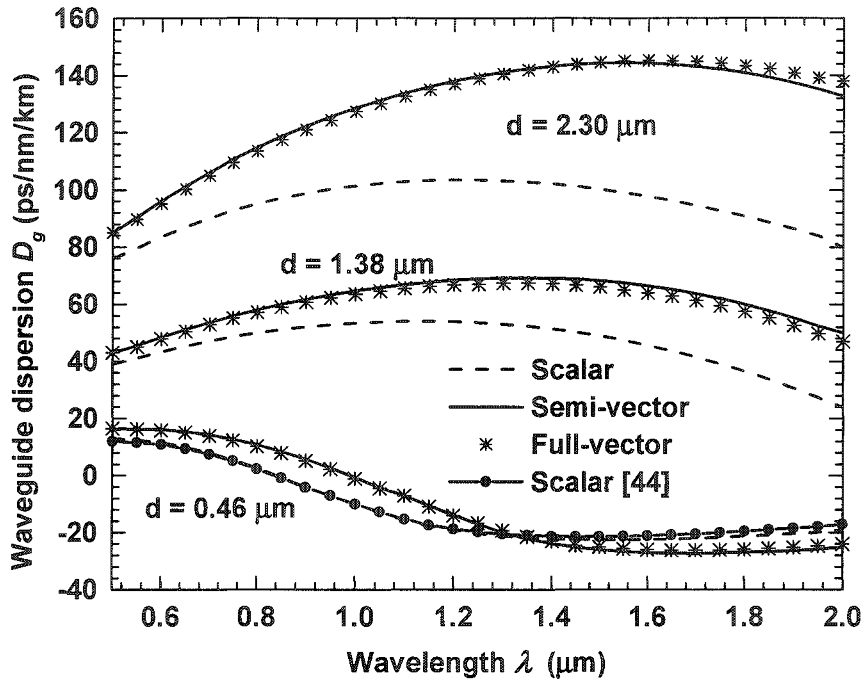

Figure 4.16 Waveguide dispersion D_g as a function of wavelength for PCFs with the fixed pitch (Λ = 2.3 μm) for different air-hole sizes d = 0.46, 1.38, and 2.3 μm.

In order to understand the vector nature of the PCFs, the Y-polarized modal electric field distribution along the Y-axis of a PCF with the air-hole size d = 0.46 μm for different wavelengths of 0.5, 1.0, 1.5, and 2.0 μm are shown in Figure 4.17. It can be seen that there is less energy in the air hole and the contribution of the vector terms is small at short wavelengths, which confirms the observations in Figure 4.15. The vector nature of the modal field profile is clearly demonstrated at long wavelengths, which leads to the lower effective index of the waveguide mode. Therefore, for the small air-hole PCFs, the accumulated vector contribution at long wavelengths cannot be neglected as modal fields spread more into the cladding.

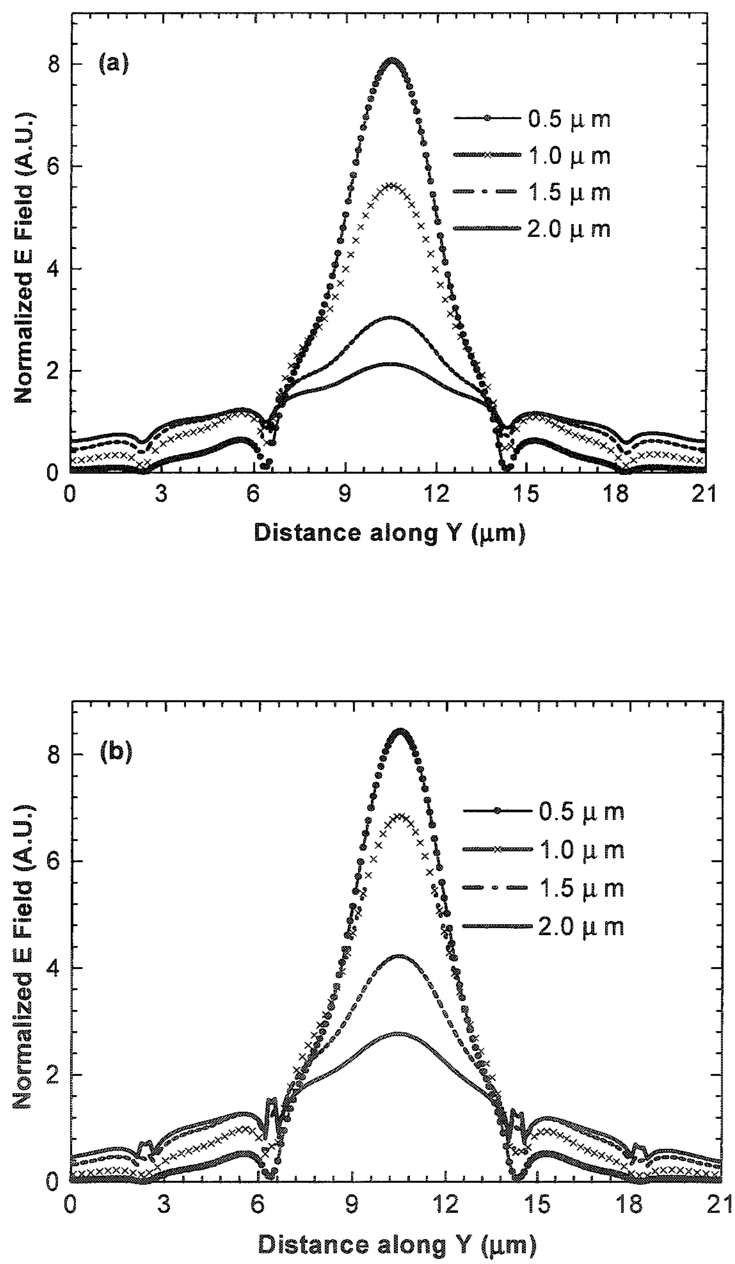

Figure 4.17 Y-polarized Electric field of a PCF with Λ = 2.3 μm and d = 0.46 μm at different wavelength values along the Y-axis with the air-hole position (2.30, 2.76 μm), (6.29, 6.75 μm), (14.25, 14.71 μm), and (18.24, 18.70 μm). (a) The scalar model, and (b) The vector model.

After investigating the effect of the vector nature on the modal properties of the PCFs, we further investigate this effect for the practical PCFs with the limited number of air-hole rings. Because the effect of the number of air-hole rings of the PCFs on the modal properties will be investigated thoroughly later (see 4.5.2), here we evaluate this effect for a small air-hole PCF (e.g., $d = 0.5$ μm and $\Lambda = 3.2$ μm), where the vector nature of modal properties is more pronounced.

Figure 4.18 and Figure 4.19 show the effect of different number of air-hole rings on modal electrical field profiles at short and long wavelengths, respectively. It can be seen from Figure 4.18 and Figure 4.19 that the effect of different number of air-hole rings on the modal profile is negligible at the short wavelength and shows some differences at the long wavelength. As expected, it can be seen from Figure 4.18 that modal field profiles for different number of air-hole rings between the scalar and vector models are similar at short wavelengths as modal fields tend to concentrate more in the core region with very small contribution of vector terms. However, at the long wavelength as shown in Figure 4.19, the modal field profiles for different number of air-hole rings change dramatically between the scalar and vector models as the modal fields spread around air holes and the accumulated contribution of the vector terms is non-negligible.

Figure 4.20 and Figure 4.21 show the modal effective index and the waveguide dispersion for different number of air-hole rings based on the scalar and vector models, respectively. It is observed that the overall modal index of the PCFs decreases as the number of rings decreases, which indicates that the model field penetrates more into the low-index air region. Again, the difference between the scalar and the vector models for the mode indices is negligible at short wavelengths, but much more pronounced at long wavelengths.

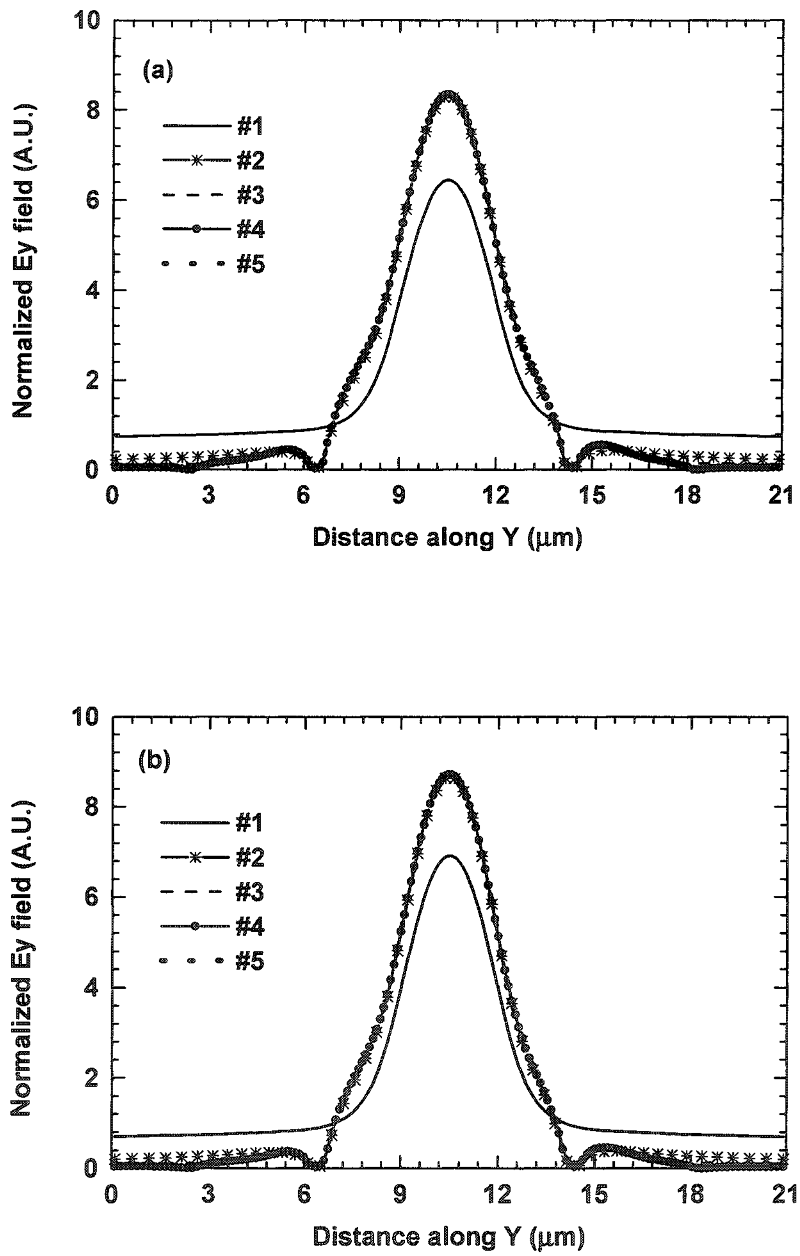

Figure 4.18 Y-polarized electric field distribution of a PCF with Λ = 2.3 μm and d = 0.5 μm along the Y-axis for different number of air-hole rings at the short wavelength λ = 0.5 μm with the possible air-hole position (2.28, 2.78 μm), (6.27, 6.77 μm), (14.23, 14.73 μm), and (18.22, 18.72 μm). (a) The scalar model, and (b) The vector model.

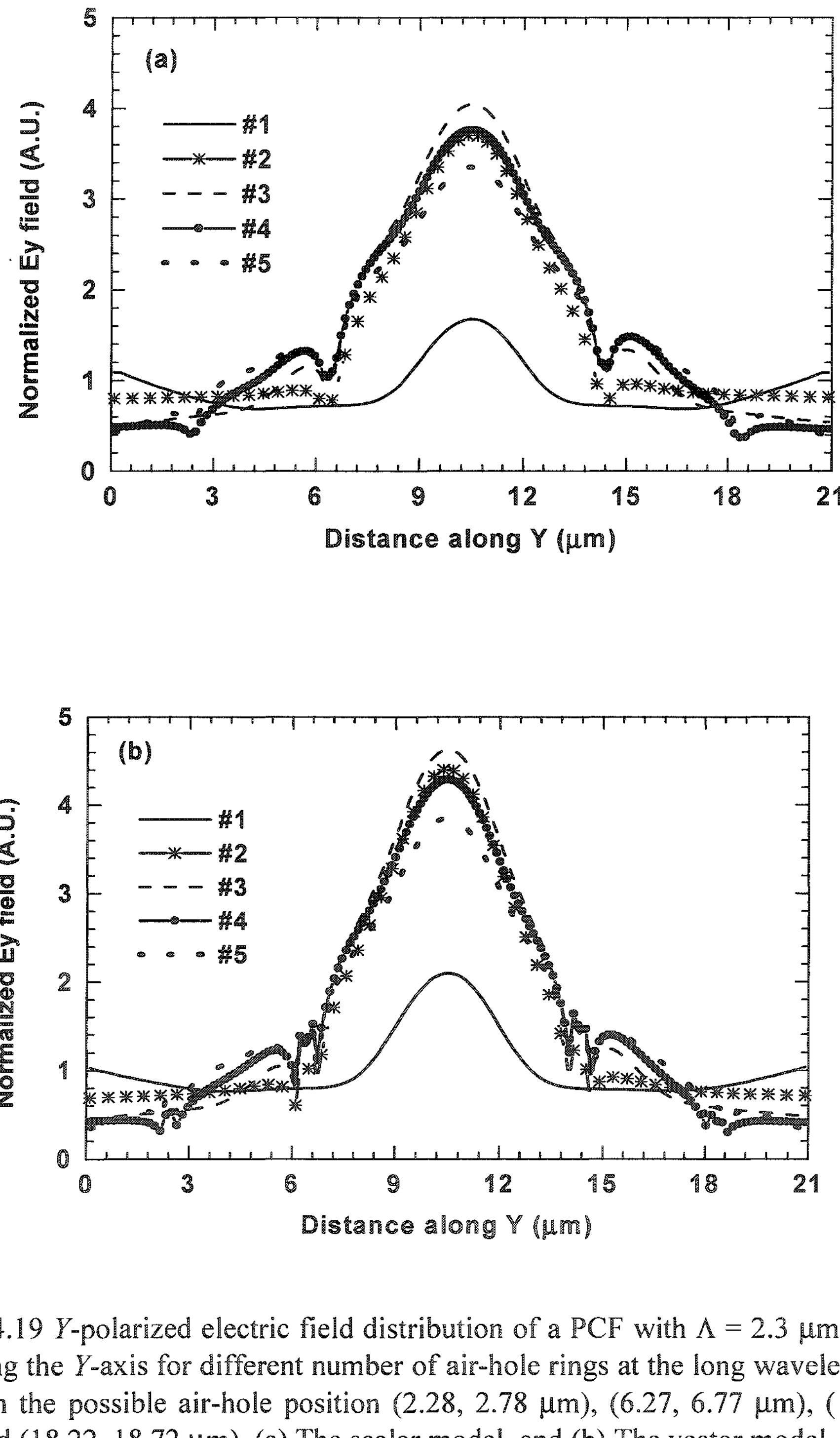

Figure 4.19 Y-polarized electric field distribution of a PCF with $\Lambda = 2.3$ μm and $d = 0.5$ μm along the Y-axis for different number of air-hole rings at the long wavelength $\lambda = 2.0$ μm with the possible air-hole position (2.28, 2.78 μm), (6.27, 6.77 μm), (14.23, 14.73 μm), and (18.22, 18.72 μm). (a) The scalar model, and (b) The vector model.

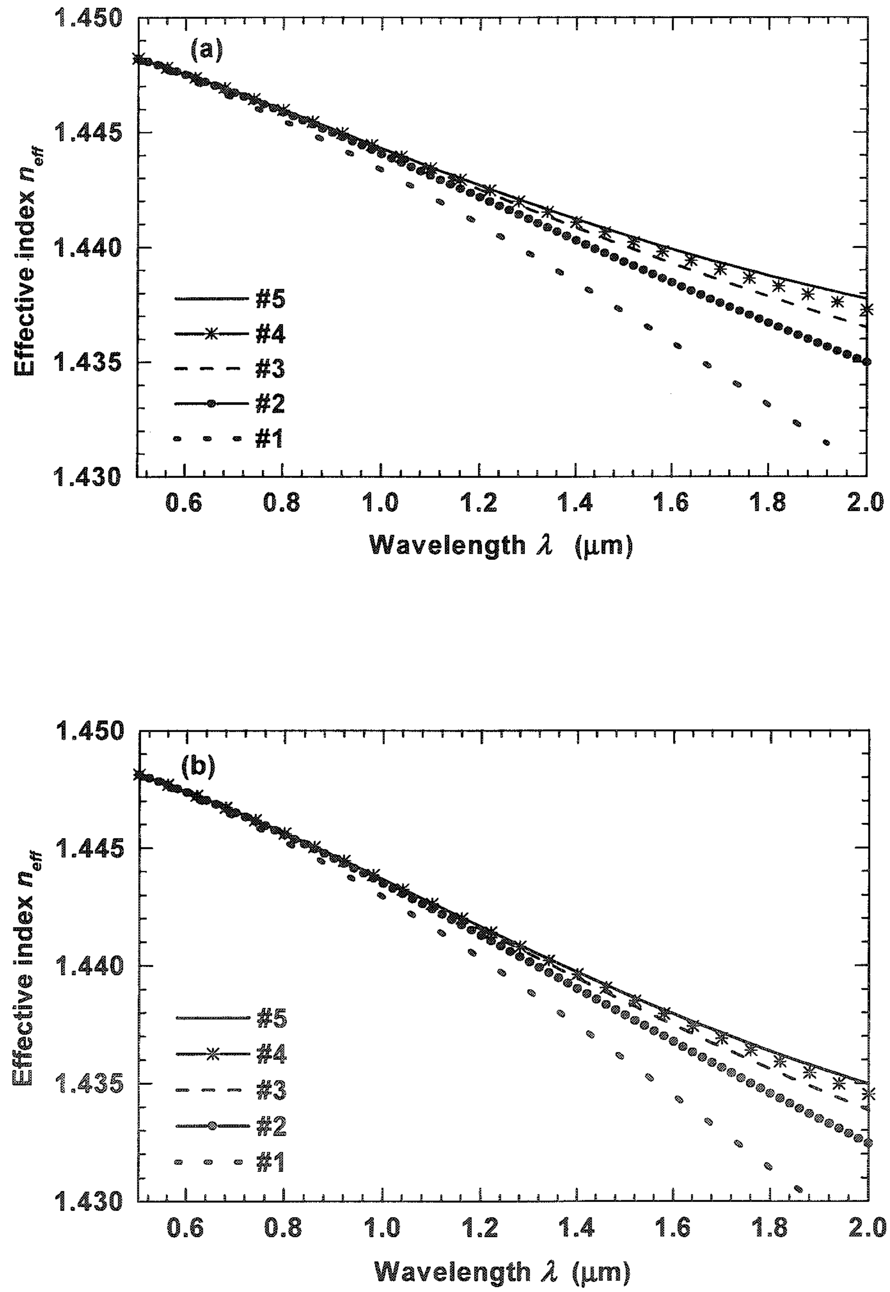

Figure 4.20 Effective indices of PCFs with $\Lambda = 2.3$ μm and $d = 0.5$ μm for different number of air-hole rings. (a) The scalar model, and (b) The vector model.

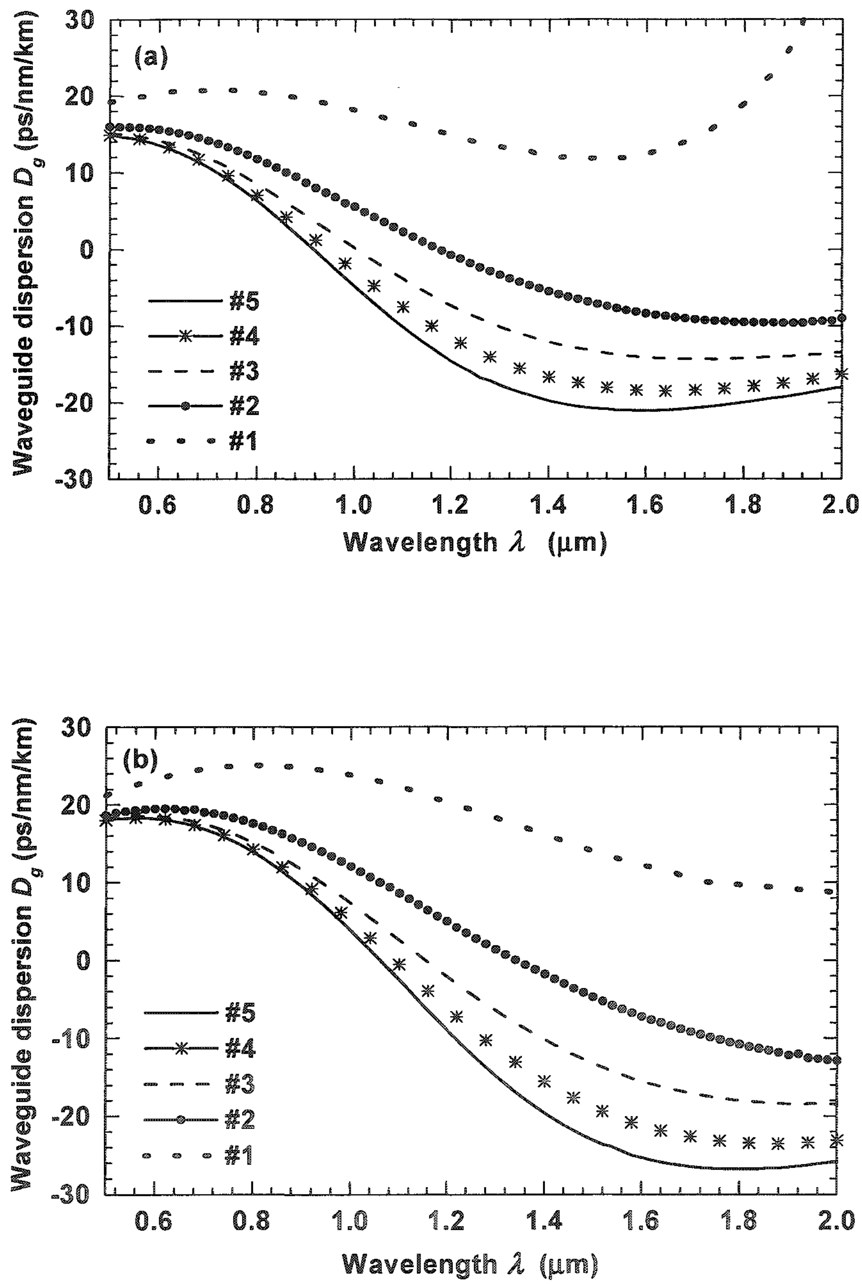

Figure 4.21 Waveguide dispersion of PCFs with Λ = 2.3 μm and d = 0.5 μm for different number of air-hole rings. (a) The scalar model, and (b) The vector model.

In this section, it is demonstrated that the vector nature of the guided modes of the PCFs must be considered in analyzing the modal properties. Despite the weakly guiding modal characteristics due to the small index contrast between the core and the "effective" cladding, the vector property of the PCFs plays an important role in the accurate prediction of the mode properties, owing to the large index contrast between silica and air. Through the comparison, the level of accuracy and the scope of validity for the scalar and the semi-vector approximations are assessed. We show that the semi-vector formulations, which are commonly used for planar optical waveguides, are highly accurate, whereas the scalar approximations are often not adequate in prediction of the modal characteristics of the PCFs. Further, the effect of the vector nature on modal characteristics for practical small air-hole PCFs with limited number of air-hole rings is investigated.

4.4.3 Mode Cut-Off and Single-Mode Operation

Like conventional step index fibers, the PCFs guide light due to the TIR effect. For the guided modes, by following the similar definition employed in 1D PCWs, their effective indices n_{eff} should meet the following relation

$$n_c > n_{eff} > n_{FSM1} \tag{4.3}$$

where n_c is the refractive index of the core of PCFs and n_{FSM1} is the cladding effective index of the PCFs (i.e., the fundamental space-filling mode of the PCs). On the other hand, the normalized effective frequency V_{eff}, less than 2.405 for the single-mode operation as the step index fibers, is defined

$$V_{eff} = \frac{2\pi}{\lambda} \mathrm{a_{eff}} \sqrt{n_c^2 - n_{\mathrm{FSM1}}^2} \tag{4.4}$$

where a_{eff} is the equivalent core radius (usually 0.58Λ, where Λ is the pitch of the PCF) and λ is the operating wavelength. Through the FDM vectorial analysis, the endlessly single-mode operation is found for the small air-hole size PCF (e.g., $d < 1.0$ μm) with the fixed patch Λ = 2.3 μm. Further, (4.4) has been confirmed by the effective index method for the PCFs with different air-hole sizes and pitches [49].

It is natural to analyze the single-mode condition of the PCFs by applying an analogy to the standard step index fibers because the analytical formula of the fibers can be used for the PCFs. However, it is un-sufficient or al least un-efficient to judge the singe mode operation of the PCFs through the EIM method due to its limitations such as the calculation of the cladding effective index, or even the strikingly different properties. Here we propose a method to judge the singe-mode operation of the PCFs without the calculation of the cladding effective index n_{FSMI}.

As we know, the cladding effective index n_{FSMI} of the PCFs is wavelength-dependent and so is the effective index of fundamental modes of the PCFs. Unlike step-index fibers, we find that the wavelength dependence of both effective cladding and effective indices of the PCFs has a similar behavior, which means the equivalent core radius a_{eff} is a function of wavelength. Now we define two new parameters: the normalized transverse phase constant (or NA-like) S and the dimensionless parameter (product of the transverse phase constant and pitch) U:

$$S = \sqrt{n_{co}^2 - n_{eff}^2} \tag{4.5}$$

$$U = \frac{2\pi}{\lambda}\Lambda\sqrt{n_{co}^2 - n_{eff}^2} \tag{4.6}$$

where n_{eff} is the effective modal index of the PCFs. Figure 4.22 shows the wavelength and air-hole size dependence of normalized modal constant S of the PCFs with fixed pitch $\Lambda = 2.3$ μm for different air-hole sizes and different wavelengths, respectively. The linear dependence of S with d and λ is observed for lager air-hole size PCFs (e.g., $d > 0.8$ μm), which confirms that wavelength dependence of both n_{eff} and n_{FSMI} has a similar behavior because the normalized effective frequency V_{eff} is wavelength-independent for short wavelengths. It is this linear behavior that makes the parameter U be wavelength-independent for short wavelengths like V_{eff}. Figure 4.23 shows the wavelength dependence of the parameter U with fixed pitch $\Lambda = 2.3$ μm for different air-hole sizes. It can be seen from Figure 4.23 that the PCFs operate in the single-mode state if $U < 2.6$. Therefore, we can easily judge the single-mode condition of the PCFs from the effective index of fundamental modes of the fiber.

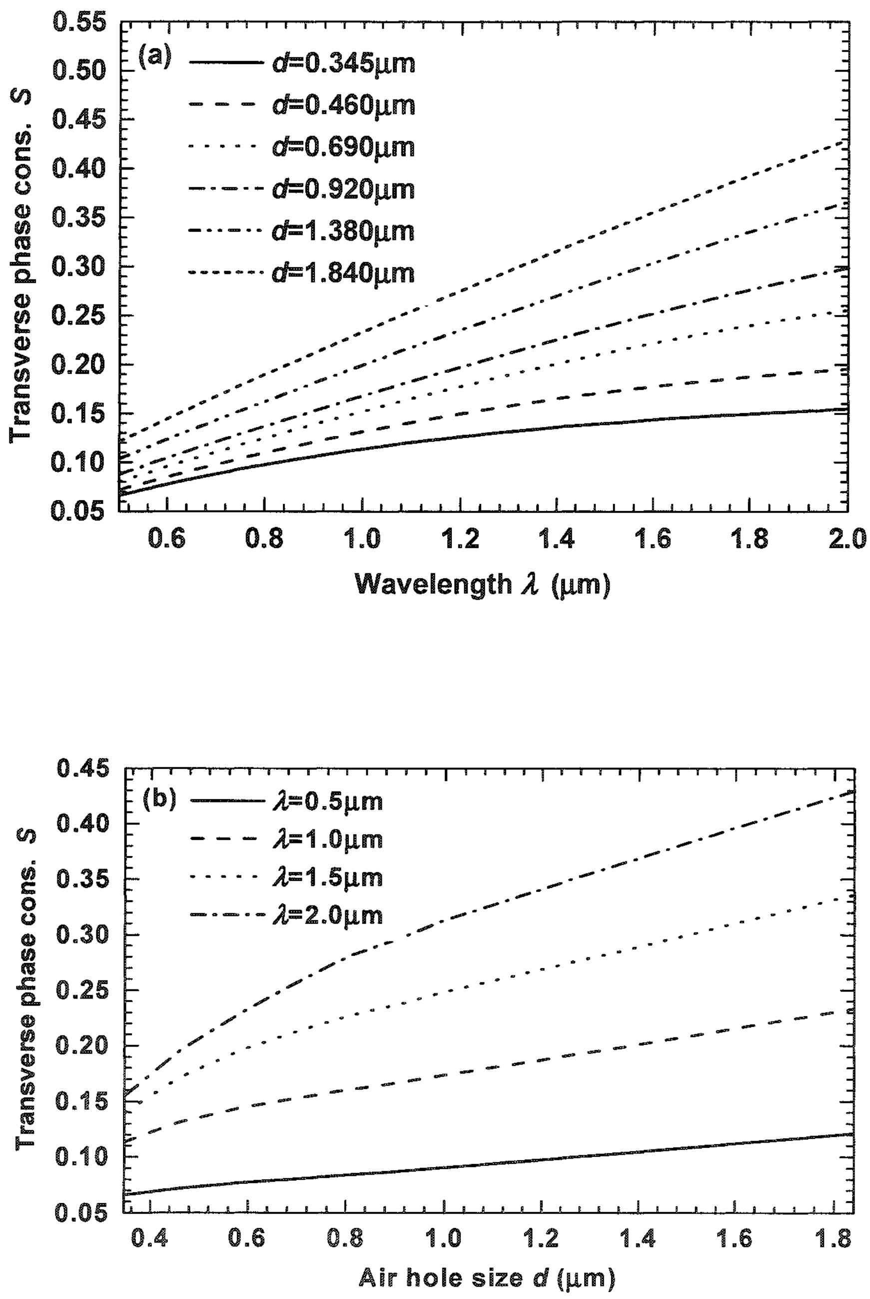

Figure 4.22 Transverse phase constant S of fundamental modes of PCFs with fixed pitch Λ = 2.3 μm. (a) As a function of wavelength λ, and (b) As a function of the air-hole size d.

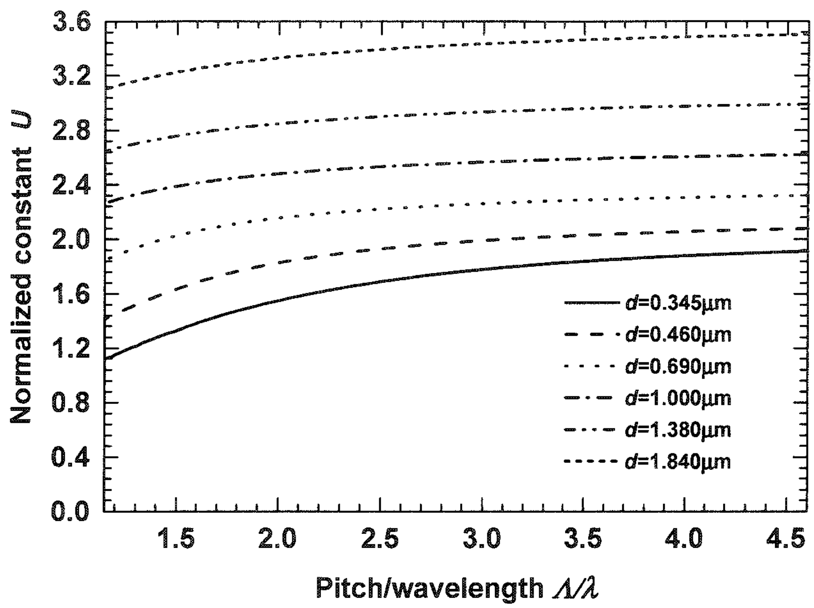

Figure 4.23 Normalized constant as a function of Λ/λ for the PCFs with fixed pitch $\Lambda = 2.3$ μm.

4.4.4 Group Velocity Dispersion

The group velocity dispersion (GVD) (or simply the dispersion) D of the PCFs is one of the important modal properties and can be directly calculated from the modal effective index n_{eff} of the fundamental mode over a range of wavelength (see Appendix A). In order to obtain the accurate dispersion, the values of the effective index are calculated with a small wavelength step (e.g., 0.02 μm), which is a real challenge for some numerical methods because there are more than hundred of wavelength points for each curve. Fortunately, by using the first order approximation, the total dispersion D is calculated as the sum of the geometrical dispersion (or waveguide dispersion) D_g and the material dispersion D_m (see 5.2). Here we only focus on the waveguide dispersion D_g.

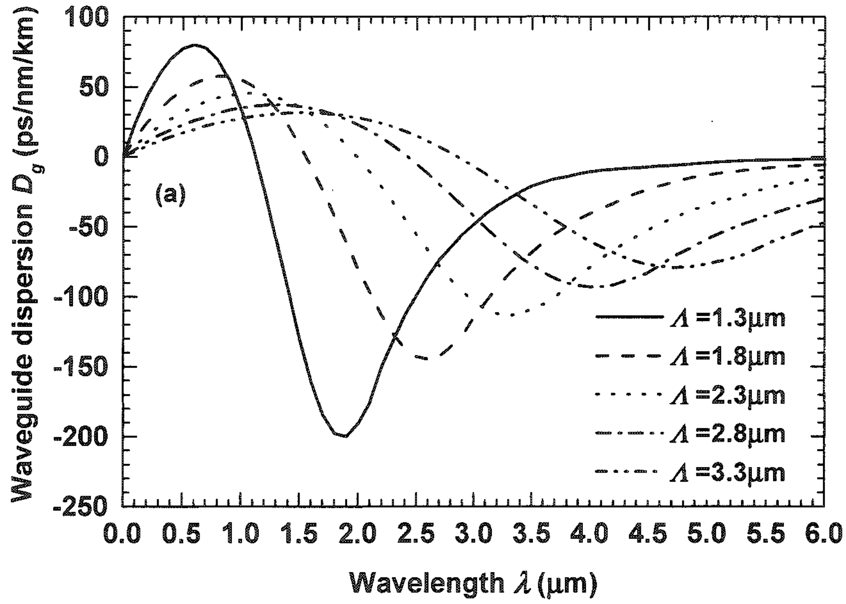

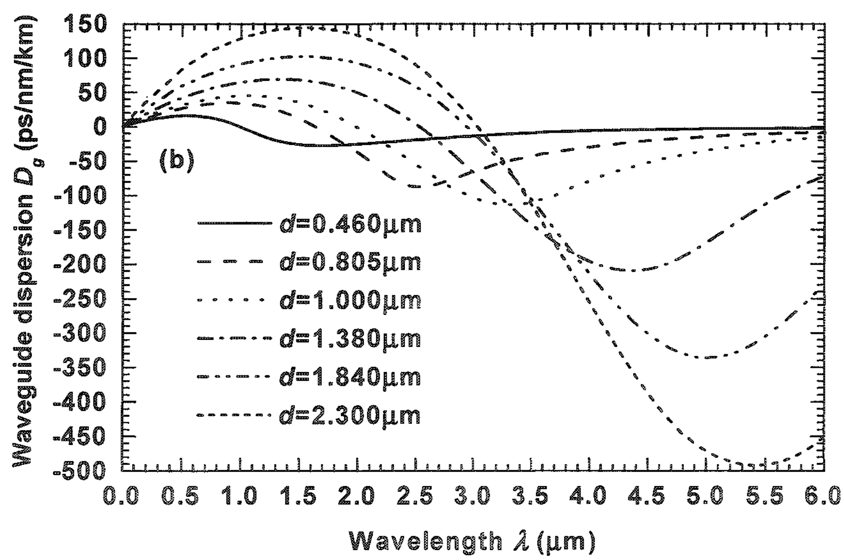

Figure 4.24 Waveguide dispersion D_g as a function of wavelength for PCFs with (a) different Λ values with fixed $d/\Lambda = 0.435$, (b) different d/Λ values with fixed Λ = 2.3 μm.

In order to gain some physical insight of the PCFs, we investigate the dispersion D_g of commonly used silica PCFs with the whole range of the design parameters d and Λ. Figure 4.24 shows the calculated waveguide dispersion D_g as a function of wavelength for the PCFs with (a) different Λ values with fixed $d/\Lambda = 0.435$, and (b) different d/Λ values with fixed $\Lambda = 2.3$ μm. In Figure 4.24(a), the scaling transformation of the waveguide dispersion D_g with respect to the pitch Λ is clearly demonstrated (see Appendix C). This, in turn, verifies the accuracy of the numerical methods. In Figure 4.24(b), the scaling behavior of the dispersion D_g of large air-hole PCFs is different from that of small air-hole PCFs and the magnitude of D_g changes dramatically when d/Λ increases, in which D_g makes dominant contribution to the total dispersion of the PCFs. Although the scaling effect for the fixed d/Λ of the small air-hole PCFs (e.g., $d/\Lambda < 0.4$) was investigated in [58], here we extend the scaling effect to the large air-hole PCF (e.g., $d/\Lambda \geq 0.4$), in which the vector effect is more pronounced as demonstrated previously (see 4.4.2).

4.4.5 Mode Effective Area and Beam Divergence

After obtaining the modal profile, we are ready to calculate the mode effective area A_{eff}, mode spot size w, and beam divergence θ of the fundamental modes (see Appendix A). Except obtaining directly from the far-field through the Fourier transfer of the modal profile, the beam divergence θ can also be calculated from the mode spot size w, which can be obtained by the Gaussian approximation $A_{eff} = \pi w^2$ of the modal profile:

$$\theta = \tan^{-1}\left(\frac{\lambda}{\pi w}\right) \tag{4.7}$$

Here we consider the commonly used PCF first studied in [49] with an air-hole size $d = 0.345$ μm and a pitch $\Lambda = 2.3$ μm. Figure 4.25 shows the mode effective area A_{eff}/Λ^2, which is in good agreement with the plane wave expansion (PWE) method [71]. It can be seen from Figure 4.25 that, unlike almost constant in the conventional fiber, the mode effective area of the PCFs can been drastically changed by simply altering the design parameters d or Λ of the PCFs, which can be easily done during fabrication by drawing the PCF fiber using different conditions (such as pulling speed and temperature). In general, the large mode effective area can be obtained by the choice of small d/Λ and Λ/λ values through the weak TIR-guiding, in which a significant fraction of the fundamental mode's energy can be located in the cladding region (see 4.5.2). Therefore, we can easily design a PCF with a large mode effective area to support the high power without inducing the nonlinear process. On the other hand, we can design the small mode effective area to enhance the nonlinear effect in the PCFs. Further, we can also calculate the mode spot size w, and beam divergence θ by the above-mentioned equations. The calculated beam divergence θ for a PCF with d = 3.82 μm and Λ = 7.2 μm is shown in Figure 4.26, which is in good agreement with the experimental and simulation result [71].

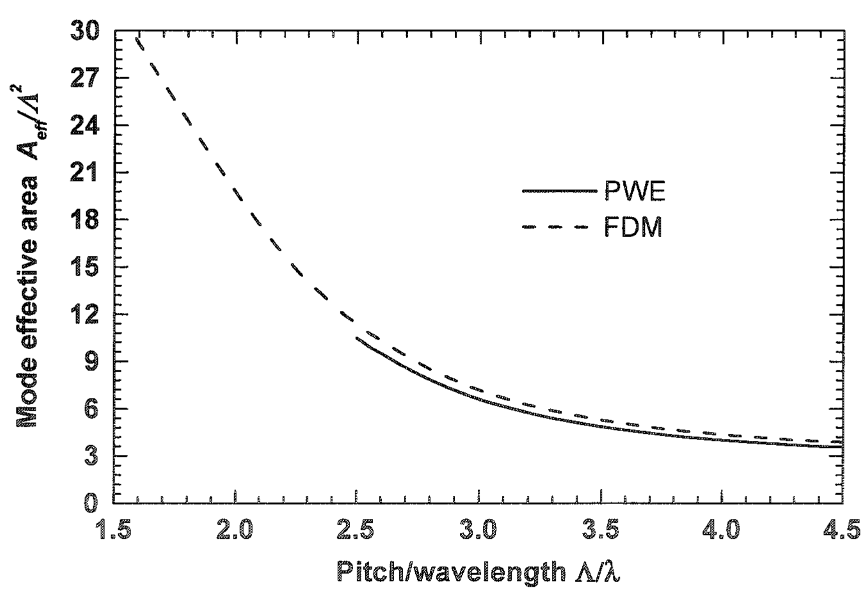

Figure 4.25 Mode effective area A_{eff}/Λ^2 with function of pith/wavelength Λ/λ for a PCF with d = 0.345 μm and Λ = 2.3 μm without considering material dispersion.

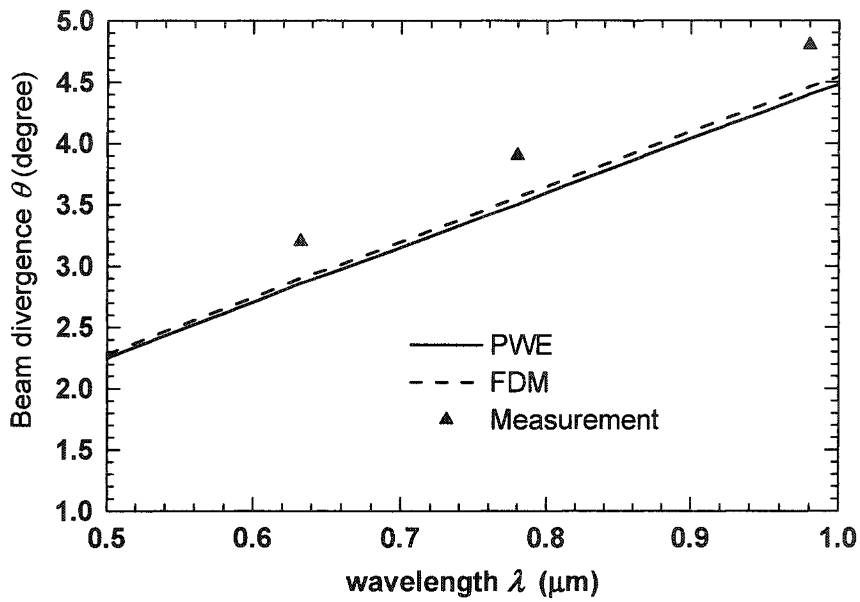

Figure 4.26 Beam divergence with function of pith/wavelength Λ/λ for a PCF with Λ = 7.2 μm and d = 3.82 μm.

4.4.6 Modal Polarization and Modal Birefringence

As we know, the polarization insensibility is a very important requirement for most of optical waveguides. Due to a six-fold (or $\pi/3$) rotational symmetry and lack of a concrete physical explanation of the degeneration of the fundamental modes of the PCFs, the numerical investigation of the existence of modal birefringence in the PCFs is needed.

Here we investigate the modal birefringence of the PCFs by using the FDM method. For the sake of simplicity, we use the PCF with one ring of six holes shown in Figure 4.12, where the air-hole size d = 5.0 μm, the pitch Λ = 6.75 μm, and refractive index of silica n_c = 1.45 [46] without considering the material dispersion. Figure 4.27 shows the convergence behavior of modal birefringence of fundamental modes for different mesh sizes at the wavelength of 1.55 μm. In order to demonstrate the difference between the semi-vectorial and full-vectorial FDM method, the effective indices and modal birefringence by the semi-vectorial FD method is also shown in Figure 4.27. The effective index of the fundamental mode is converged to 1.444765401 (only –0.00013% error with 1.444767275 by the multipole method [46]). Here an error of –0.001% is found for the semi-vectorial FDM method. It can be found from Figure 4.27 that the less mesh size, the less the modal birefringence. Like other methods (e.g., Multipole method [46] and FEM method [63]), the degeneracy is in the order of 10^{-8}. Therefore, the degeneracy of fundamental modes is verified through the FDM method. Although the modal birefringence of fundamental modes has been very often observed experimentally, we believe that this modal birefringence is caused by the rotational asymmetry of the PCFs for some manufactured reasons.

On the other hand, we can understand the degeneracy of fundamental modes through the modal profile calculations. From the modal profile calculation, it is found that the linear polarization ratio (LPR, ratio between two electric major and minor components) is very high (> 30 dB). Therefore, each fundamental mode is a linearly polarized field. With considering the $\pi/3$ rotational symmetry of the PCF structure and the orthogonality of two fundamental modes, all six rotated fields are also linearly polarized and their effective indices are the same, which requires that two fundamental modes have the same effective indices although their modal profiles may not be the same. In conclusion, the PCFs with the $\pi/3$ rotational symmetry are not birefringent.

4.4.7 Confinement Loss and Bending Loss

As mentioned before, the PCFs guide light by the TIR effect due to the lower cladding effective index. Practically, light can leak out into the silica cladding, especially for the weak-guided PCF fiber, because only certain number of rings of the PCFs is used. Although the confinement of light is improved by increasing the number of rings of air holes, it is necessary to know the suitable number of rings of air holes of the PCFs with given parameters (e.g., d, Λ and λ). On the other hand, the related bending loss increases when the mode effective area of the PCFs increases. Therefore, in order to design the

PCFs, their loss mechanism related to the confinement and bending should be understood.

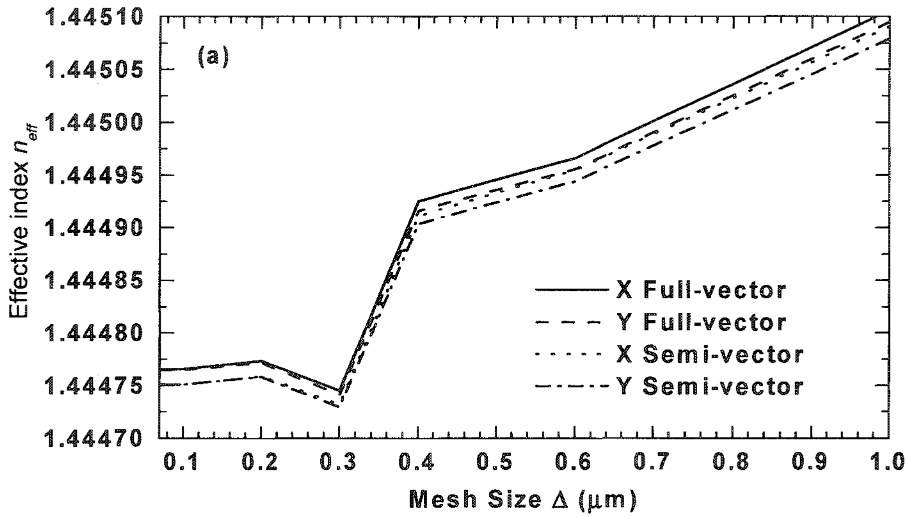

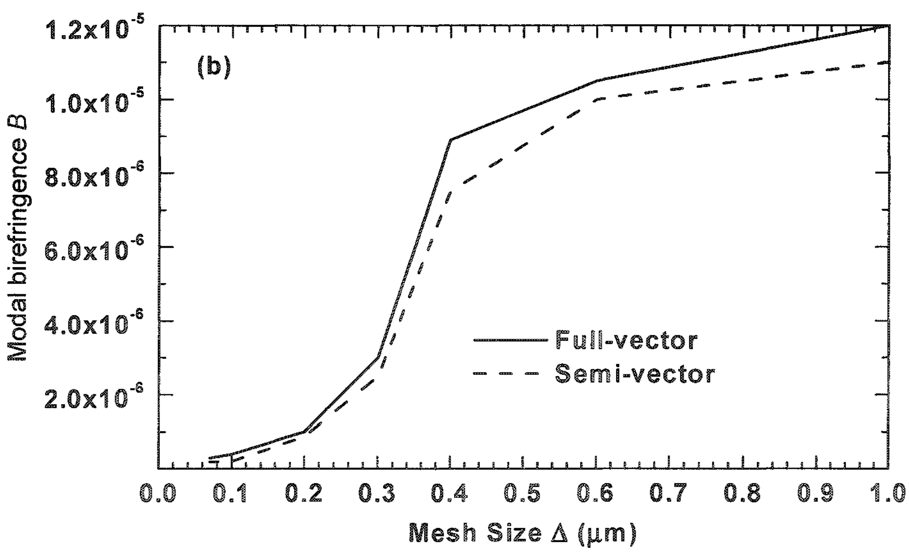

Figure 4.27 Convergence of effective indices and modal birefringence of fundamental modes of a PCF with Λ = 6.75 μm and d = 5.0 μm at the wavelength of 1.55 μm. (a) Effective Index n_{eff}, and (b) Modal birefringence B.

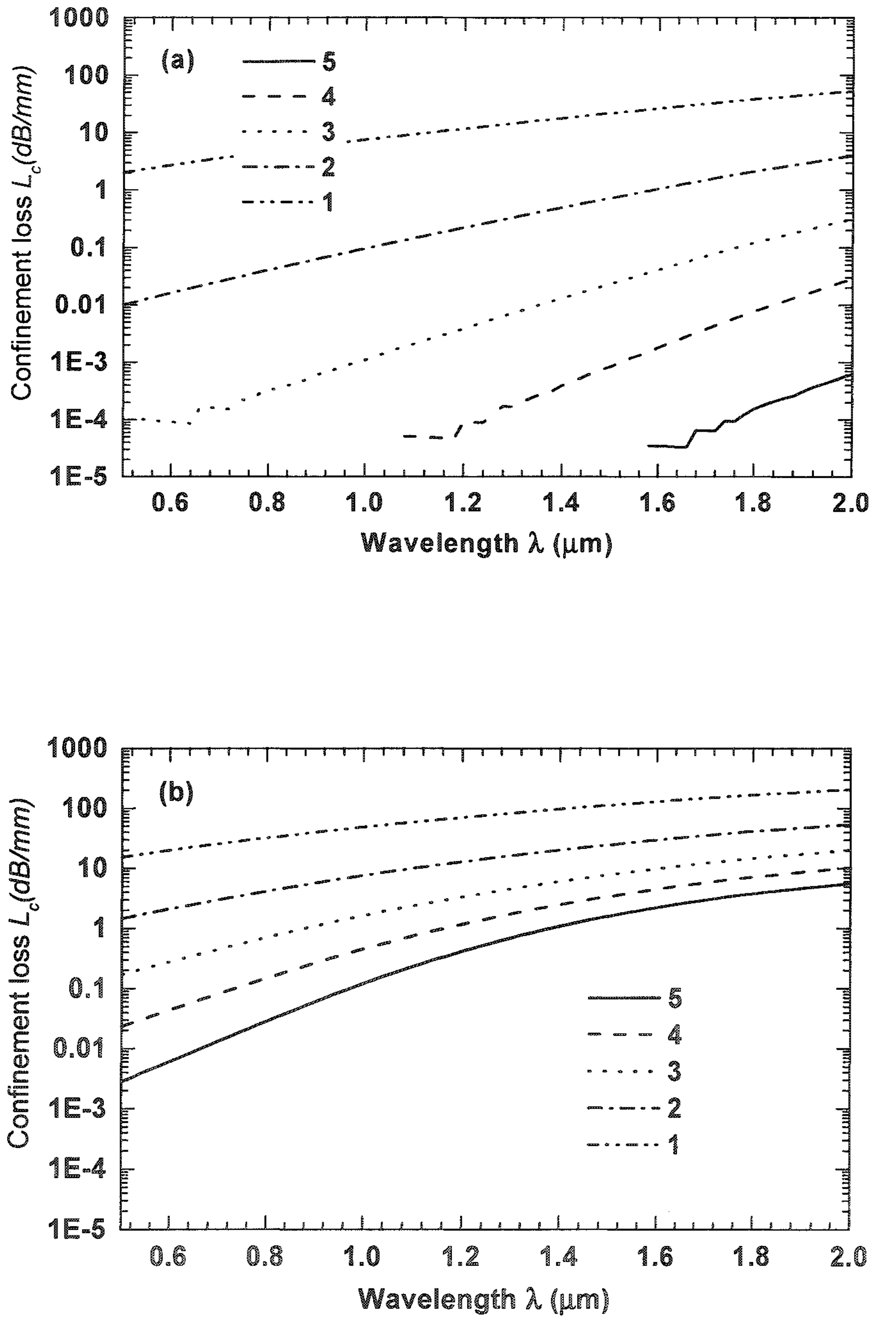

Figure 4.28 Confinement loss L_c with function of wavelength λ for the PCFs with $\Lambda = 2.3$ μm for different number N (1-5) of rings of air holes. (a) $d = 1.0$ μm, and (b) $d = 0.5$ μm.

Figure 4.28 shows the confinement loss L_c with function of wavelength λ for commonly used PCFs with Λ = 2.3 μm for different number N (e.g., 1-5) of rings of air holes. As expected, the PCFs have the less confinement loss for large air-hole d/Λ at short wavelengths. In some sense, light is well confined within the core by the first ring of six air holes (e.g., d/Λ = 0.8 and Λ/λ = 4). In other words, the outer rings of air holes of the PCFs do not appear to affect the fiber modal properties because similar effective indices are obtained when the number of rings of air holes changes. On the other hand, light is leaky within more than eight rings of air holes for small d/Λ at long wavelengths (e.g., d/Λ = 0.1 and Λ/λ = 1). We will discuss this effect in great detail later (see 4.5.2).

From previous calculations of (4.4.5), it is found that large mode effective areas of the PCFs can be achieved by deceasing the air-hole size-to-pitch ratio d/Λ or the normalized frequency Λ/λ. Due to the weak guiding, those fibers suffer a larger bending loss than that with small mode effective areas. Like the conventional fibers, the PCFs have a bend-loss edge at long wavelengths due to extremely weak guiding mode with very small of normalized frequency Λ/λ. Furthermore, unlike conventional fibers, the PCFs also have a bend-loss edge at short wavelengths due to the less index contrast of fibers. Here we verify the bend-loss edge at short wavelengths for a PCF with air-hole size d = 0.345 μm and the pitch Λ = 2.3 μm. It is first time, as our knowledge, to verify the bend-loss edge through the numerical method [68]. Figure 4.29 presents the real component of electric field profiles of a PCF for the bending radius R = 25 and 4 mm, respectively. As expected, it is clearly shown that the electric field penetrates away from the fibers at a short bending radius. Figure 4.30 shows the short-wavelength bend-loss edge for different bending radii, which is in good agreement with the measured result [49].

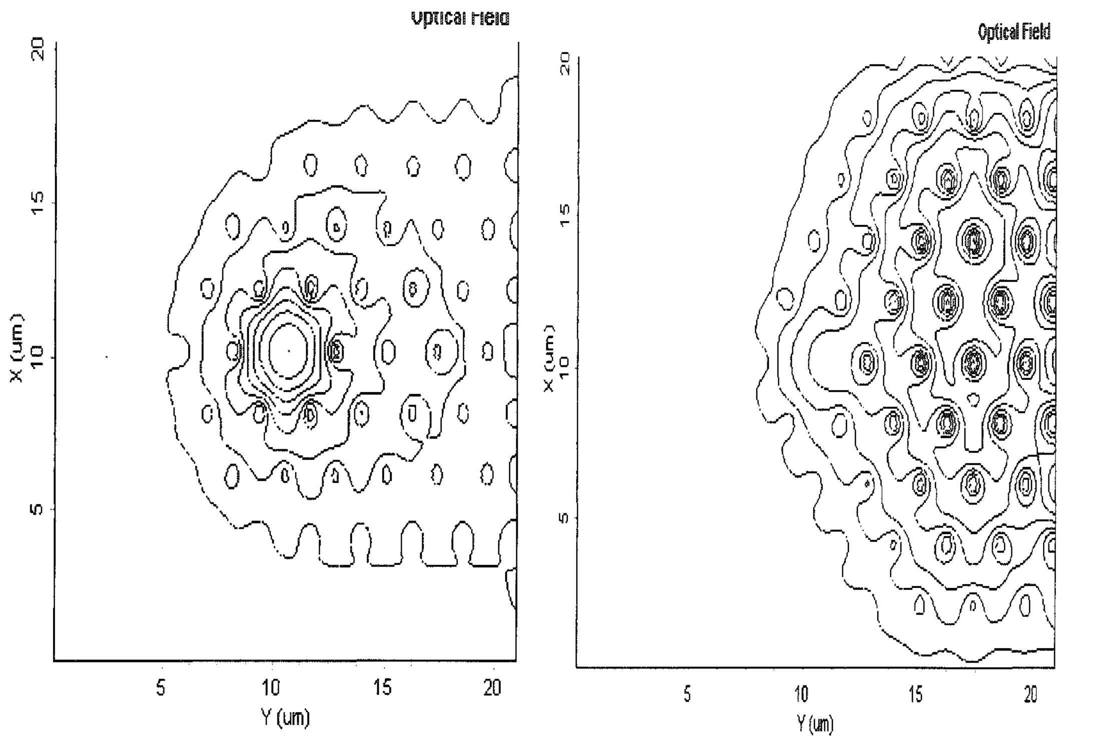

Figure 4.29 Electric field profile for bending radii at Λ = 2.3μm and d = 0.345 μm at λ = 0.8 μm. (a) R = 25 mm, and (b) R = 4 mm. The contour levels are separated by 2 dB.

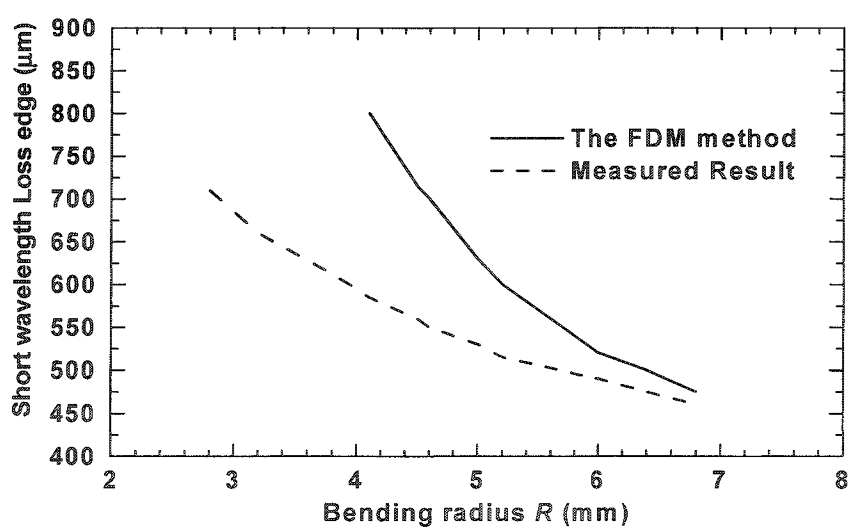

Figure 4.30 The bending loss at short-wavelength bend edge with function of the bending radius for a PCF with Λ = 2.3 μm and d = 0.345 μm.

4.5 Numerical Study of Some Effects on Modal Characteristics

4.5.1 Effect of Interstitial Holes

The PCFs presented in previous sections is an ideal PCF geometry without considering interstitial holes. Actually interstitial holes exist in large air fraction PCFs due to the multiple capillary drawing processes [45]. Here we explore the influence of additionally interstitial holes on the modal properties of the PCF. For the sake of simplicity, we assume that the interstitial holes are circular with the hole size d_i as shown in Figure 4.31.

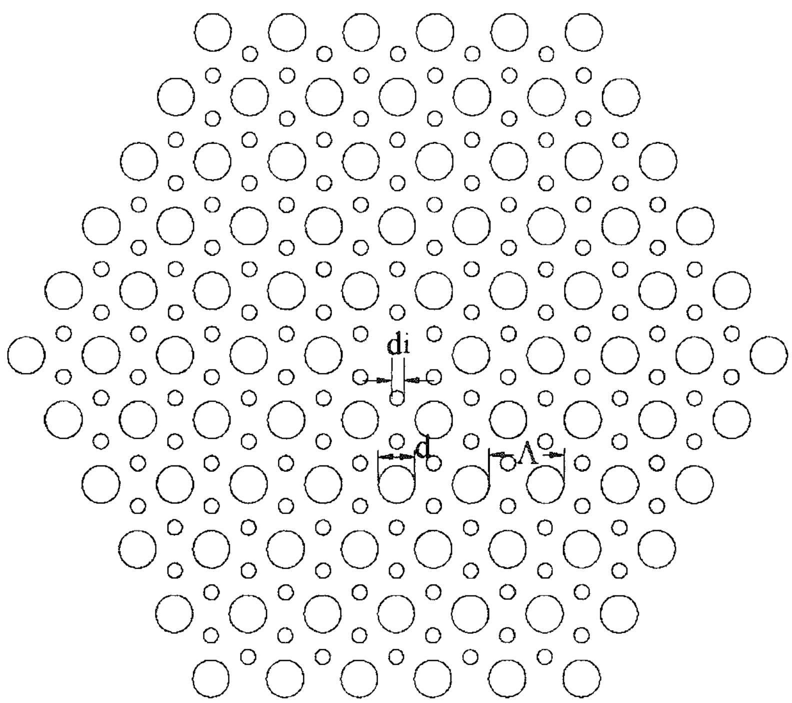

Figure 4.31 The cross section of PCFs with interstitial holes.

As we know, the interstitial holes affect the modal properties by equivalently increasing the air-hole size-to-pitch ratio d/Λ of the PCFs. When their size d_i is much less than the air-hole size d, the interstitial holes do not significantly influence the modal properties of the PCFs [45]. When the interstitial hole size d_i increases, the modal field decays inside them, and the modal effective index of the PCFs decreases.

Here we take a large air-fraction PCF with the air-hole size d = 1.92 μm and the pitch Λ = 3.2 μm as an example [45]. Figure 4.32 presents the effect of interstitial holes on modal properties (i.e., the effective index and dispersion) for the interstitial hole size d_i = 0, 0.068, 0.272, and 0.544 μm, respectively. From the simulation results, the modal properties change dramatically when d_i/Λ is large, especially for the crucial dispersion. The dispersion still keeps decreasing at long wavelengths and starts to increase at short wavelengths. It is also found that, when d_i/Λ increases, the modal effective area of the PCFs decreases and the coupling loss with standard fibers increases, which are in good agreement with other numerical results [45]. However, for the vital calculation of dispersion, there is a large discrepancy between two methods. The calculated dispersions by the wave expansion method for d_i = 0 and 0.272 μm are 30 and 8 ps/nm/km, respectively [45]. From Figure 4.32(b), the calculated dispersions by the FDM method are 66 and 57 ps/nm/km, respectively. The difference between those two methods is that the semi-analytical expansion method takes hardly care the vector feature of modes. It is worth to note that there are similar computation efforts for investigation of the effect of interstitial holes by the FDM method. However, it is crucial for the expansion method because it needs large enough number of expansion terms to ensure an accurate result.

4.5.2 Effects of Number of Air-Hole Rings and Design Parameters

By using the FDM method, it is possible to predict the number of rings of holes needed to avoid the mode leakage at any desired wavelengths, which is one of important considerations for design and optimization of practical PCFs. In this respect, we investigate the effects of number of air-hole rings on the basic modal properties such as the modal profile, effective index, dispersion, and confinement loss [59].

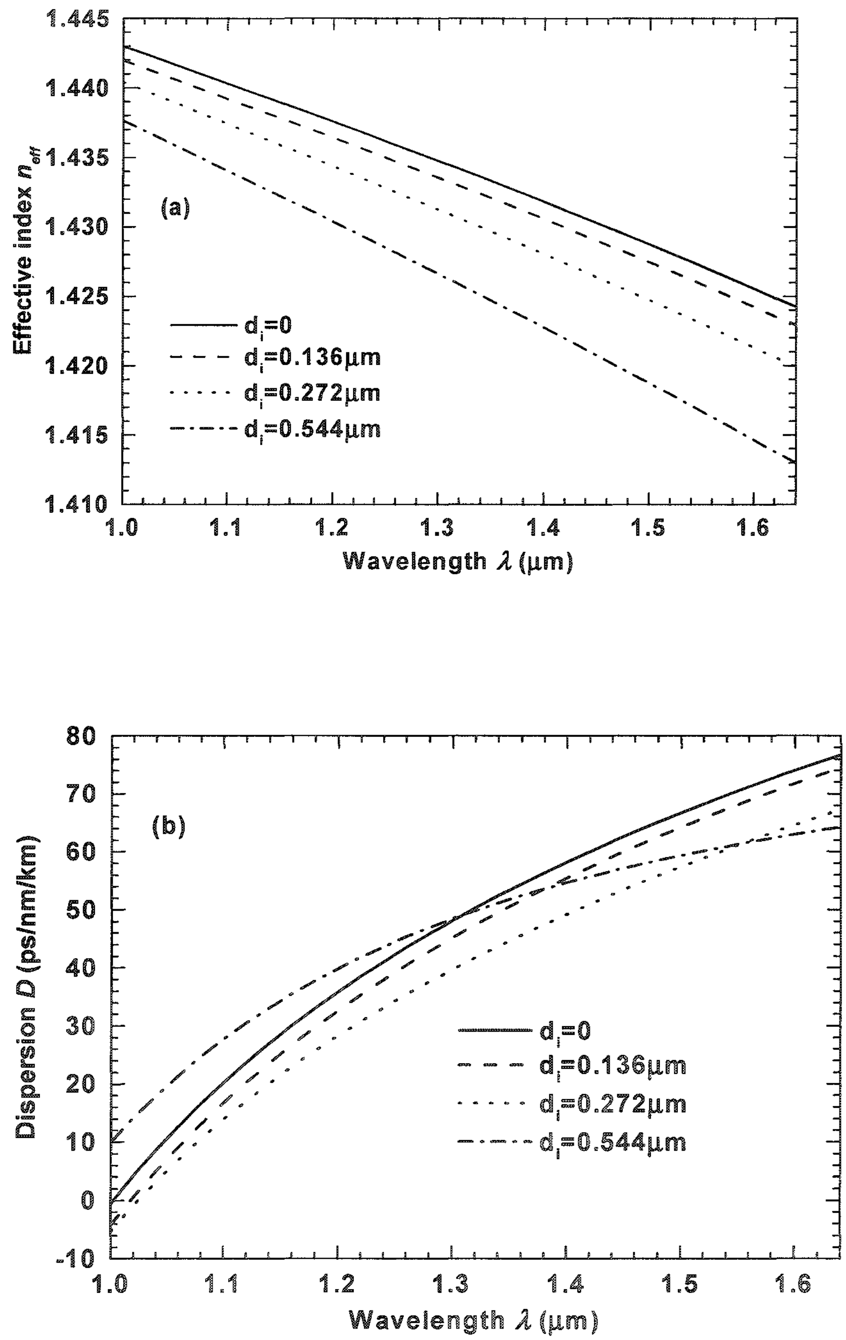

Figure 4.32 Effect of interstitial hole size d_i on modal properties of the PCF at Λ = 3.2 μm and d = 1.92 μm. (a) Effective index n_{eff}, and (b) Dispersion D.

Modal electric field distributions of the PCFs with the air-hole size $d = 1.55$ μm for different wavelengths (0.5 and 4.0 μm) and number of air-hole rings (1 and 5) are shown in Figure 4.33. As expected, the mode confinement increases by increasing the number of air-hole rings. The mode is almost fully confined inside the innermost ring of air holes ($N = 1$) at short wavelengths, which corresponds to large pitches of the PCFs at the wavelength of 1.55 μm. In order to show the effects of number of rings for different air-hole PCFs, Figure 4.34 shows the effective index of the PCFs as a function of wavelength for different air-hole sizes $d = 0.46$ ($d/\Lambda = 0.2$), 1.15 (0.5), and 1.84 μm (0.8), respectively. It is clearly observed that the difference among different number of air-hole rings is small at short wavelengths, but becomes significant at long wavelengths. Further, this difference decreases as the air-hole size d increases. It is also shown that the overall modal index of the PCFs decreases as the number of rings decreases, which indicates that the model field penetrates more into the low-index air region.

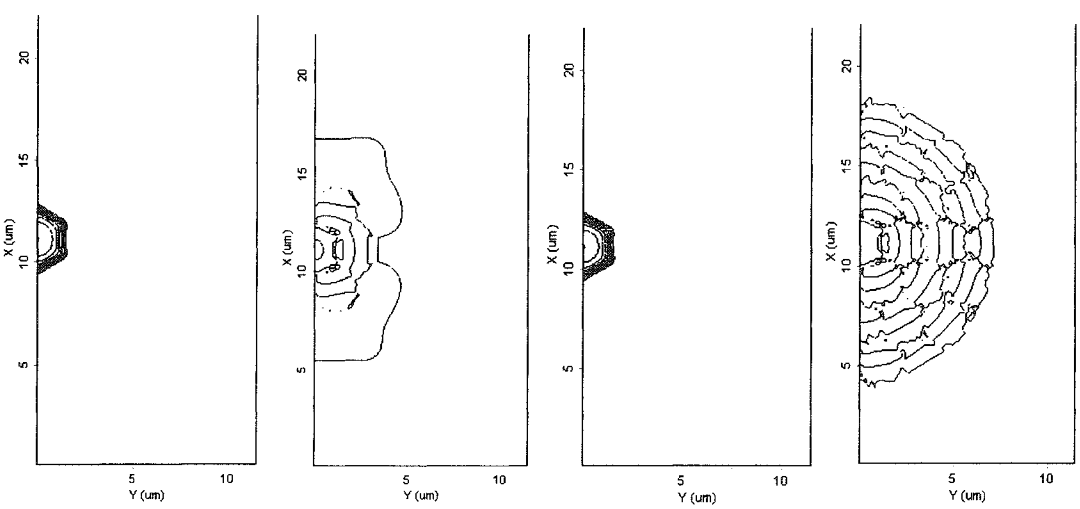

(a) (b) (c) (d)

Figure 4.33 Y-polarized Electric field of a PCF with $\Lambda = 2.3$ μm and $d = 1.15$ μm at different wavelengths and number of air-hole rings. (a) $\lambda = 0.5$ μm and $N = 5$, (b) $\lambda = 4.0$ μm and $N = 1$, (c) $\lambda = 0.5$ μm and $N = 5$, (d) $\lambda = 4.0$ μm and $N = 5$. Field contours are separated by 3 dB.

To further assess the effects of the different number of air-hole rings on other modal properties of the PCFs, the waveguide dispersion, the mode effective area, and the confinement factor in silica are calculated and compared for different air-hole sizes as shown in Figure 4.35, Figure 4.36, and Figure 4.37, respectively. Similar to the situation with the model effective index as shown in Figure 4.34, the difference among different number of air-hole rings is negligible at short wavelengths, but much more pronounced at long wavelengths. Also this difference decreases as the air-hole size d increases. As expected, waveguide dispersion and confinement factor decrease as the number of air-hole rings increases because the overall modal index of PCFs increases and mode field penetrates less into the low-index air region as the number of air-hole rings increases. For the mode effective area, there are two folds: first it decreases and then increases as the number of air-hole rings increases.

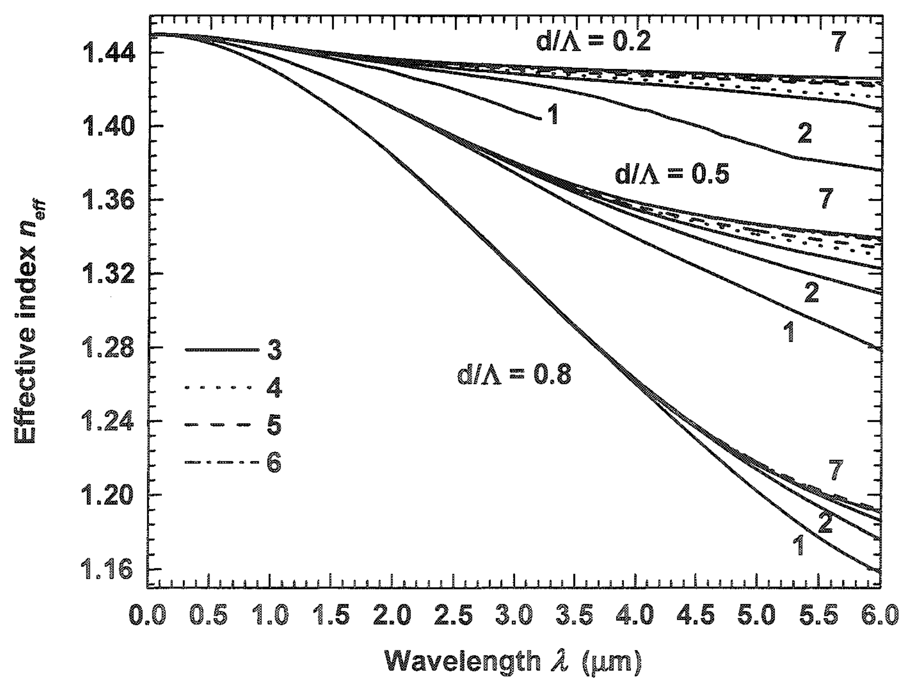

Figure 4.34 Effective indices as a function of wavelength for the PCFs with different number of air-hole rings at $\Lambda = 2.3$ μm and $d/\Lambda = 0.2$, 0.5, and 0.8, respectively.

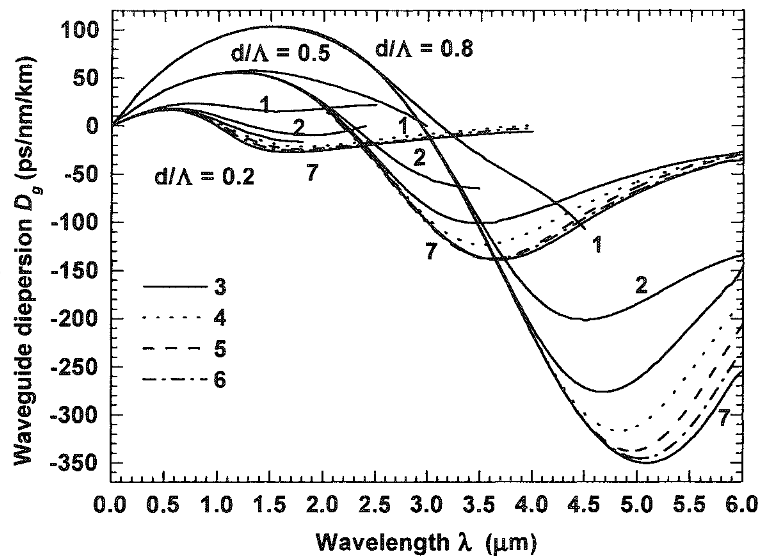

Figure 4.35 Waveguide dispersion as a function of wavelength for the PCFs with different number of air-hole rings at Λ = 2.3 μm and d/Λ = 0.2, 0.5, and 0.8, respectively.

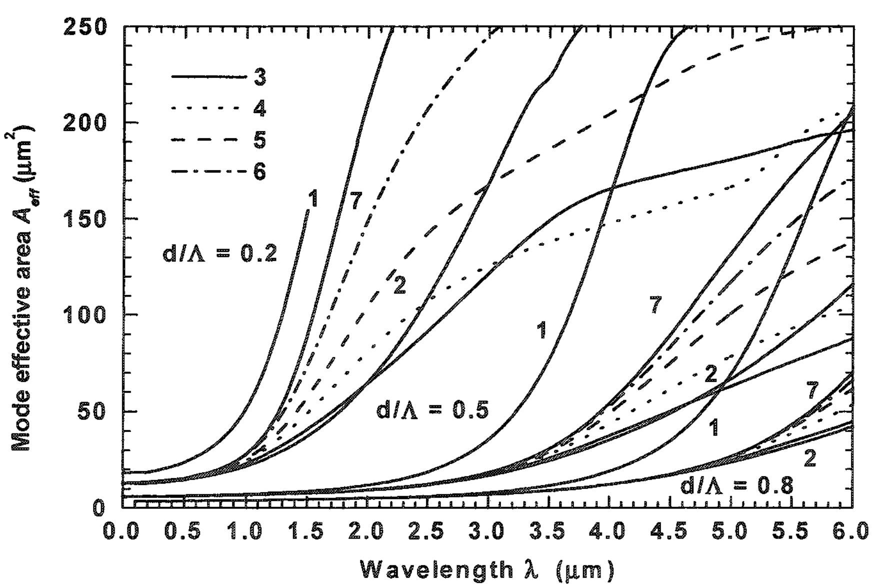

Figure 4.36 Mode effective area as a function of wavelength for the PCFs with different number of air-hole rings at Λ = 2.3 μm and d/Λ = 0.2, 0.5, and 0.8, respectively.

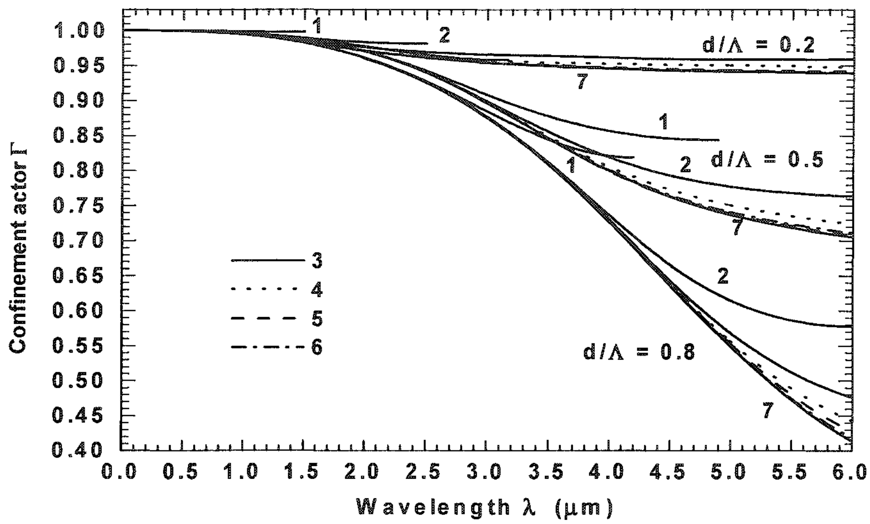

Figure 4.37 Confinement factor as a function of wavelength for the PCFs with different number of air-hole rings at Λ =2.3 μm and d/Λ = 0.2, 0.5, and 0.8, respectively.

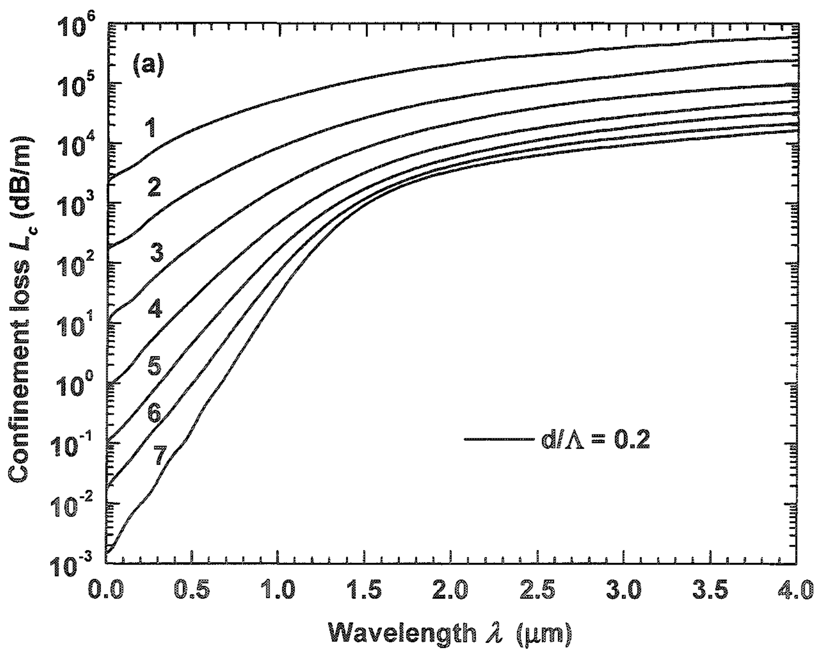

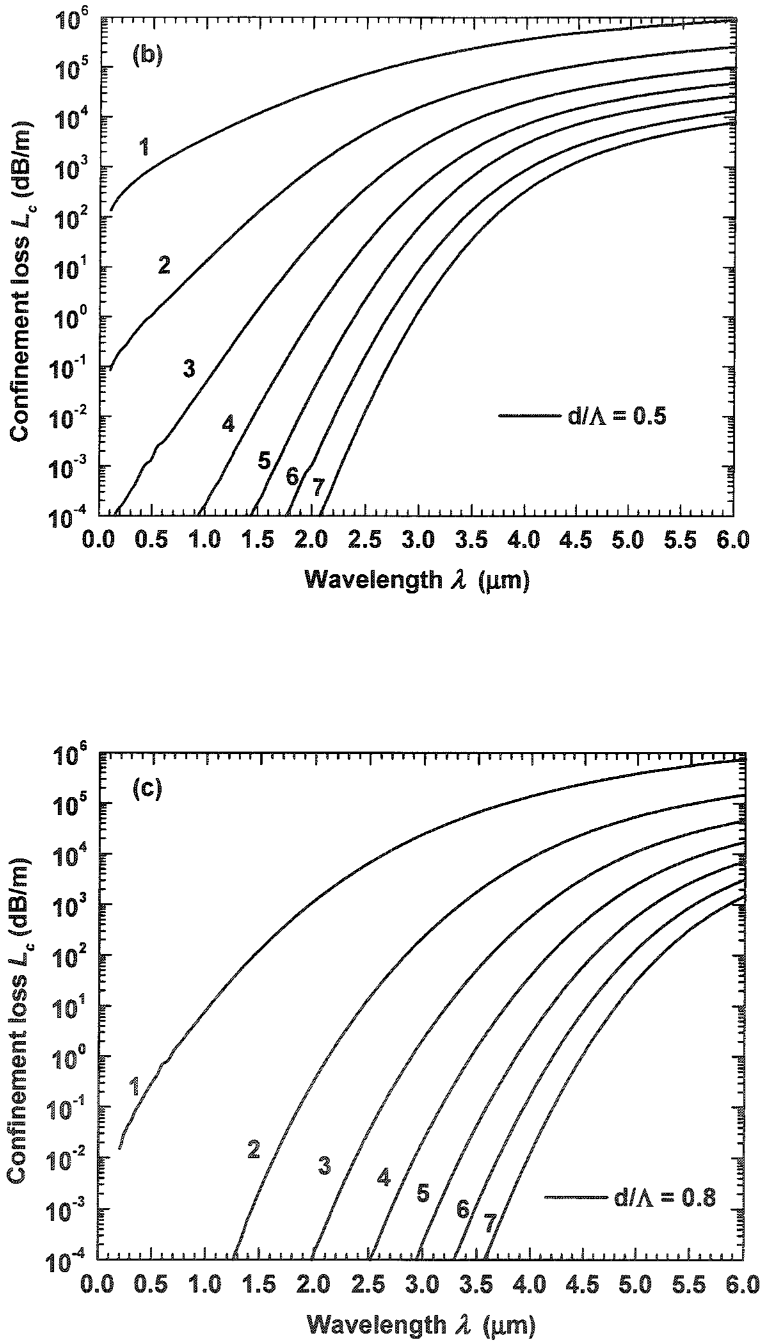

Figure 4.38 Confinement loss as a function of wavelength for the PCFs with different number of air-hole rings at $\Lambda = 2.3$ μm. (a) $d/\Lambda = 0.2$, (b) $d/\Lambda = 0.5$, and (c) $d/\Lambda = 0.8$.

Finally, the effect of the different number of air-hole rings on the confinement loss is calculated for different air-hole sizes d as shown in Figure 4.38. Similar to the situation with the other modal properties, the confinement loss is small and negligible at short wavelengths, but increases exponentially when wavelength increases. Also the confinement loss decreases as the air-hole size d increases. As expected, the confinement loss decrease as the number of rings increases because the overall modal index of the PCFs increases and mode field penetrates less into the low-index air region as the number of rings increases.

In general, the effect of different number of air-hole rings on modal properties of the PCFs depends on the operation wavelength and the design parameters of the PCFs. At the short wavelengths, the effect is small and negligible mainly due to the isolated effect of the PCs, and at the long wavelengths, the effect is more pronounced mainly due to the band-gap effect of the PCs. On the other hand, for large d/Λ PCFs (e.g., $d/\Lambda \geq 0.7$), this effect is equivalent to the short wavelength operation and small as the light is well confined within the core by the first and second air-hole rings. For small d/Λ PCFs (e.g., $d/\Lambda \leq 0.1$), this effect is equivalent to the long wavelength operation and significant as light is weakly confined and the modal field penetrates into many rings of air holes, in which the outer rings of air holes of PCF affect dramatically the modal properties.

4.5.3 Scaling Transformation

As we know, there is no fundamental length scale for the EM wave due to the nature of the Maxwell's equations. Therefore, we can easily derive the scaling transformation of the modal properties such as the effective index and the modal field pattern with respect to the change of design parameters of the PCFs (e.g., the pitch Λ and index $n(r)$) for the fixed air-hole size-to-pitch ratio (see Appendix C). In order to evaluate the PCF with any pitches and air-hole sizes, it is useful to explore scaling approximations of modal characteristics of the PCFs with the fixed pitch Λ. By following the similar way, scaling approximations of modal properties of the PCFs with the fixed pitch Λ can be approximately calculated [26], [58]:

$$D_g(\lambda, N)\,|_{fixed\,\Lambda} \approx A(N) D_g(\frac{\lambda}{B(N)}) \tag{4.8}$$

$$A_{eff}(\lambda, N)\,|_{fixed\,\Lambda} \approx \frac{1}{C(N)} A_{eff}(\frac{\lambda}{D(N)}) \tag{4.9}$$

$$L_c(\lambda, N)\,|_{fixed\,\Lambda} \approx \frac{1}{E(N)} L_c(\frac{\lambda}{F(N)}) \tag{4.10}$$

$$\Gamma(\lambda, N)\,|_{fixed\,d/\Lambda} \approx \Gamma(\frac{\lambda}{G(N)}) \tag{4.11}$$

where N is the air-hole size ratio (i.e., d/d_0 with d_0 = 1.15 μm). Unlike the scaling transformation for the fixed air-hole size-to-pitch ratio, the dependence of modal properties on the scaling parameter N for the fixed pitch Λ is no longer linear (e.g., for the waveguide dispersion D_g as evidenced in Figure 4.39). For this reason, we have to calculate modal properties numerically and extracted nonlinear relationships for corresponding coefficients based on the results of the numerical calculations.

For instance, the waveguide dispersion D_g as a function of wavelength λ for different PCFs with fixed Λ = 2.3 μm is shown in Figure 4.39. For small air-hole PCFs (e.g., $d/\Lambda < 0.5$), the approximate linear scaling [$A(N) \approx N$ and $B(N) \approx N$)] for D_g can be obtained, based on the fact that the negative slope of D_g curves remains approximately the same, as shown in Figure 4.39(b), when the air-hole size is changed. From Figure 4.39(a), the nonlinear scaling functions for the coefficients $A(N)$ and $B(N)$ in scaling transformations of D_g, with Λ_0 = 2.3 μm and d_0 = 1.0 μm, can be fitted into polynomial and cosine forms [58]:

$$A(N) \approx a + bN + cN^2 + dN^3 + eN^4 \tag{4.12}$$

$$B(N) \approx N^2[f + g\cos(hN+i)]/A(N) \tag{4.13}$$

where the fitting coefficients $a \approx 0.1510$, $b \approx -0.1391$, $c \approx 1.6458$, $d \approx -0.8221$, $e \approx 0.1648$, $f \approx 0.94$, $g \approx 0.082$, $h \approx 3.39$, and $i \approx -4.5$. By utilizing the coefficients $A(N)$ and

$B(N)$ in the scaling transformations of D_g, the modified coefficients $A(N)$ and $B(N)$ for different d_0 values of the PCFs with the fixed Λ_0 can be analytically obtained.

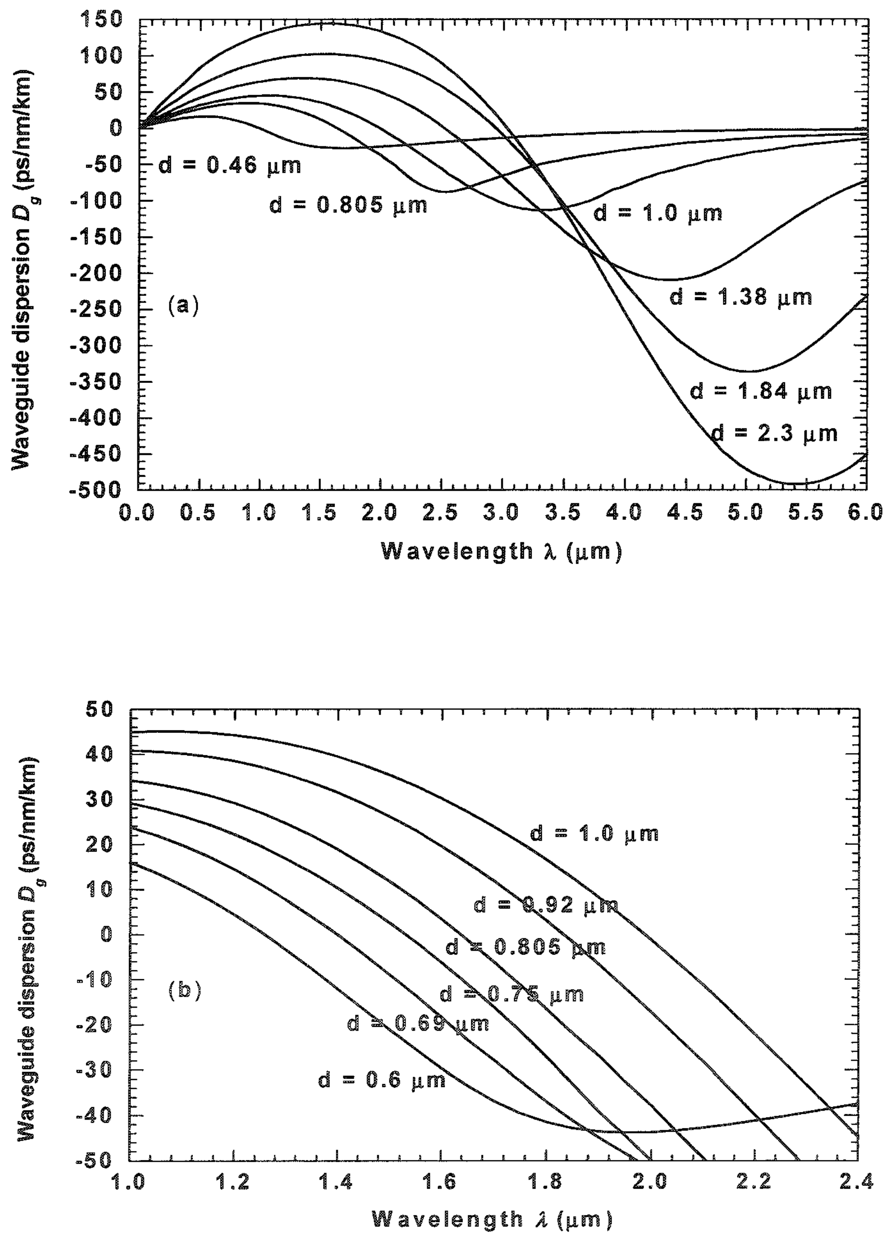

Figure 4.39 Geometrical dispersion D_g as a function of wavelength λ for different PCFs with fixed $\Lambda = 2.3$ μm. (a) General case, and (b) Small air-hole case.

In addition to the dispersion properties, it is also desirable to consider other modal properties (e.g., the mode effective area A_{eff}, the single-mode condition, etc.) in the PCF-based applications. For example, large mode effective areas A_{eff} can support extremely high power without exciting unwanted nonlinear effects, and small mode effective areas can be used to explore highly nonlinear effects in fibers. For the fixed d/Λ, we can obtain the families of the mode effective areas A_{eff} analytically as functions of the pitch ratio M (see Appendix C). For the fixed Λ of the small air-hole PCFs (e.g., $d/\Lambda < 0.5$), it is shown that, from the numerical results, the scaling coefficients $C(N)$ and $D(N)$ are approximately linear (e.g., $\approx N$) with respect to N. However, for the fixed Λ of large air-hole PCFs (e.g., $d/\Lambda > 0.5$), the scaling coefficients $C(N)$ and $D(N)$ are well approximated by the following functions [26]:

$$C(N) \approx N \tag{4.14}$$

$$D(N) \approx 1.0 + 0.61(N-1.0) + 0.85(N-1.0)^2 \tag{4.15}$$

where $\Lambda_0 = 2.3$ μm and $d_0 = 1.0$ μm.

Overall, for the scaling approximations of modal properties of the PCFs with the fixed pitch ratio Λ, the scaling coefficients A, B, C, D, E, F, and G can be linearly approximately (e.g., $\approx N$) when air-hole size-to-pitch ratio of the PCFs is small (e.g., $d/\Lambda < 0.5$) [26]. However, for large air-hole PCFs, the scaling coefficient A, B, C, D, E, F, and G are approximately obtained through the nonlinear function of N. By utilizing scaling transformations, modal properties of the PCFs with any values of the design parameters (e.g., d, Λ, and λ) are easily calculated. For example, with certain confinement loss requirement, the minimum number of air-hole rings as a function of pitch is approximately obtained. As we show later, those approximate scaling transformations of modal properties as a function of N can assist us in the design and optimization of the practical PCFs. It is worth noting that the sensitivity analysis of the modal properties with respect to d and Λ can be also easily obtained through their respective scaling transformations.

4.6 Summary

In this chapter, modal characteristics of the photonic crystal fibers (PCFs) guided by the PBG and TIR effects are investigated by way of simulations using some analytical and numerical methods in great detail. Through the comprehensive analysis, some unique features related to the PCFs are obtained and the scaling transformations of modal properties related to the design parameters of the PCF structure are derived.

Firstly, like the 1D PCWs, the band-gap structure of the 2D PCs is calculated and their main properties of the 2D PCs are discussed. With the similar idea of the gap-midgap ratio used for measuring the complete band-gap, a new measure parameter along the low index line is proposed for measuring the partial band-gap of the PCs, which is very useful for the analysis of the modal properties of the PCFs.

Secondly, the modal characteristics, such as the effective index, the model field profile, the dispersion, the confinement loss and bend loss, the confinement factor, and the mode effective area and beam divergence, the model polarization and modal birefringence, etc., of the PCFs are investigated thoroughly. The numerical model is validated through the critical modal parameters of the PCFs by way of examples. With the help of the band-gap map of the 2D PCs, different guiding regimes for the PCFs are recognized and physical insight of the guided modes of the PBG-PCFs and TIR-PCFs can be understood easily. Further, the level of accuracy and the scope of validity for the scalar and the semi-vector approximations are assessed. It is demonstrated that the vector nature of the guided modes on the PCFs must be considered in analyzing the modal characteristics such as the effective indices and the dispersions. Furthermore, one new parameter is proposed to judge the single-mode operation of the PCFs, and the bending loss of the PCFs is calculated by the numerical method for the first time.

Finally, for the practical PCF, some effects (e.g., number of air-hole rings and size of interstitial holes) on the modal characteristics are investigated. The scaling transformations of modal properties related to the design parameters of the PCFs are also derived.

Chapter 5

Design of Dispersion Component Elements

Due to the unique and controllable dispersion properties of the PCFs, it is very natural to employ the PCFs as the dispersion component elements. In this chapter, we propose a general design model for the PCFs with the dispersion-related applications and give some typical examples.

5.1 Introduction

Optical fibers as a superb transmission media for telecommunications still suffer from the chromatic dispersion. Except the polarization modal dispersion (PMD), which occurs because the two orthogonal polarization modes that comprise a wavelength travel at different speeds along a fiber, the chromatic dispersion refers to the pulse broadening due to the fact that different optical wavelengths travel at different speeds within a fiber. The effect of chromatic dispersion can be greatly reduced if special fibers (e.g., dispersion-shifted fibers and dispersion-flattened fibers) are employed, which have more favorable dispersion characteristics at the wavelength of optical communications. Further, in order to overcome the signal distortion caused by the chromatic dispersion in the conventional single-mode fibers, the dispersion compensating fibers (DCFs) are also needed to compensate the dispersion of the existing optical fibers. Therefore, there are huge applications for the dispersion component elements in optical communication systems.

Conventional single-mode fibers (CSFs) based on weakly guiding structures of doped silica can be tailored to exhibit a variety of desirable modal characteristics in terms of loss/gain, dispersion, and field confinement [76], [77]. Due to the small index variation over the transverse cross-section, however, modal characteristics of the CSFs cannot be changed drastically to fulfill requirements of certain demanding dispersion-related applications. Examples of such applications are the ultra-dispersion-shift (e.g., to the green wavelength range), the ultra-broadband dispersion flattening, the broadband dispersion compensation, etc. This limitation may be circumvented by the use of the PCFs [64], [65] whose modal characteristics are strong functions of wavelength and whose transverse cross-section consists of a central high-index defect (or missing a hole) in a regular triangular (or hexagonal) array of air holes as shown in Figure 5.1. There are only two main design parameters, namely, the air-hole size d and the pitch Λ. The PCFs can be tailored to produce unique and useful modal characteristics such as single-mode operation at a wide wavelength range [49], highly tunable dispersion [78]-[80], and highly controllable mode effective areas for linear and nonlinear applications [81]. The utilization of some of these modal characteristics is the basis for the design of novel fibers with desired dispersion properties to be discussed in this chapter.

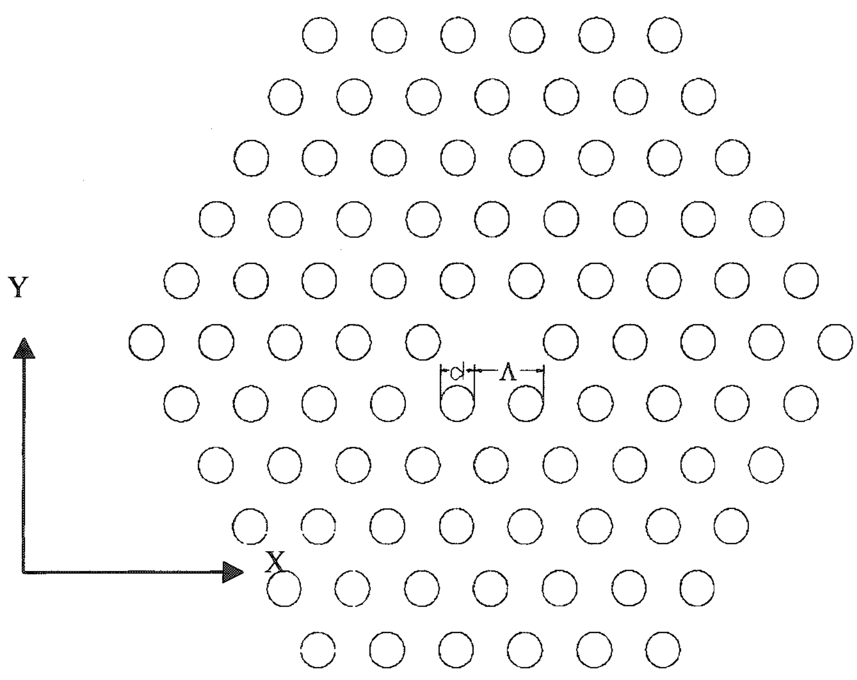

Figure 5.1 The cross section of a PCF with a regular triangular air-hole array defined by the air-hole size d and the pitch Λ.

Several dispersion applications for the PCFs are presented in [78]-[80], [82]. Ferrando *et al.* proposed to use the PCFs to obtain the flattened dispersion near wavelengths of 1.13 [78] and 0.8 μm [80]. Nearly zero ultra-flattened dispersion around the wavelength of 1.55 μm was achieved [79] by a trial-and-error manual procedure. The idea to use the PCFs for the dispersion compensation was suggested in Ref [82], in which a simplified model consisting of a pure silica core surrounded by air was used for the proof-of-concept demonstration. In order to design practical dispersion-compensating fibers (DCFs), an improved model was presented in Ref [58]. For the dispersion-shifted applications, however, few reports have so far addressed the design issue in a systematic fashion, except for some experimental results (e.g., [83]).

5.2 Design Considerations

In order to model the PCFs with general index profiles, the full-vector wave equations based on transverse electric fields can be solved by using some rigorous methods mentioned in previous chapters (e.g., the FDM method [20], [68]). Once the modal effective indices and field patterns are obtained, the other related modal properties (e.g., dispersion D) can be readily obtained (see Appendix A). In order to design the PCFs with the required dispersion and utilize the scaling transformation for the dispersion of the PCFs, the total dispersion D is calculated as the sum of the geometrical (or waveguide) dispersion D_g and the material dispersion D_m in the first order approximation [58], [69]:

$$D(\lambda) \approx D_g(\lambda) + \Gamma(\lambda) D_m(\lambda) \tag{5.1}$$

where Γ is the confinement factor in silica, which is close to unity for most practical PCFs as the modal power is confined almost all in silica with high refractive index [8], [69]. In general, the waveguide dispersion D_g can be calculated without considering the material dispersion (i.e., the refractive index of silica n_{silica} = 1.45) and the material dispersion D_m can be obtained directly from the three-term Sellmeier formula [69]. Because the waveguide dispersion D_g is strongly related to the design parameters of the PCFs, they can be optimized to achieve desired dispersion properties.

As far as the PCFs are concerned, the waveguide dispersion D_g can be calculated through the following scaling transformations (see Appendix C.3 and 4.5.3):

$$D_g(\lambda, M)\,|_{fixed\ \mathrm{d}/\Lambda} = \frac{1}{M} D_g(\frac{\lambda}{M}) \tag{5.2}$$

$$D_g(\lambda, N)\,|_{fixed\ \Lambda} \approx A(N) D_g(\frac{\lambda}{B(N)}) \tag{5.3}$$

where M is the pitch ratio (i.e., Λ/Λ_0 with Λ_0 = 2.3 μm) and N is the air-hole size ratio (i.e., d/d_0 with d_0 = 1.0 μm). For the fixed air-hole size-to-pitch ratio d/Λ, we can obtain the families of D_g analytically by changing the pitch ratio M, which can easily derived from the scaling transformation of the effective index $n_{eff}(\lambda, M)\,|_{fixed\ \mathrm{d}/\Lambda} = n_{eff}(\lambda / M)$ (see Appendix C.3). For the fixed pitch Λ, the dependence of D_g on the scaling parameter N is no longer linear. For this reason, we have to calculate D_g numerically and extract a nonlinear relationship for coefficients $A(N)$ and $B(N)$ in (5.3) based on the results of the numerical calculations with some approximations [58]. For small air-hole PCFs (e.g., d/Λ < 0.5), the approximate linear scaling [i.e., $A(N) \approx N$ and $B(N) \approx N$)] for D_g can be obtained, based on the fact that the negative slope of D_g curves remains approximately the same when the air-hole size is changed. By utilizing the coefficients $A(N)$ and $B(N)$ in (5.3), the modified coefficients $A(N)$ and $B(N)$ for different d_0 values of the PCFs with respect to the fixed Λ_0 can be analytically obtained. As we show later, this approximate scaling of D_g as a function of N can assist us in the design of the PCFs.

In addition to the dispersion properties, it is also desirable to consider other modal properties (e.g., the mode effective area A_{eff} [69], the single-mode condition, etc.) in the dispersion-related applications of the PCFs. For example, large mode effective areas can support extremely high power without exciting unwanted nonlinear effects, and small mode effective areas can be used to explore highly nonlinear effects in the PCFs. Further, albeit there is theoretically no cut-off for the fundamental modes, light in practice is not really guided by the PCFs when the normalized wavelength (i.e., λ/Λ) is large. By utilizing the scaling transformation of A_{eff}, the cut-off wavelengths of the fundamental and the second-order modes are easily calculated by setting $A_{eff,1}$ and $A_{eff,2}$, the mode effective areas of the fundamental and the second-order modes, to some certain values. Figure 5.2 shows such curves of $A_{eff,1}$ and $A_{eff,2}$ with a relation between λ/Λ and d/Λ. The operation wavelength range of the single-mode operation for the practical PCFs is also shown (dot-dash line) [49]. It is seen from the figure, three operation regions (single-mode, multi-mode, and cut-off) of the PCFs are easily recognized through the simple scaling transformation of the mode effective area of the PCFs. It is worth noting that the sensitivity analysis of the modal properties with respect to d and Λ can be easily obtained through the scaling transformations of the modal properties.

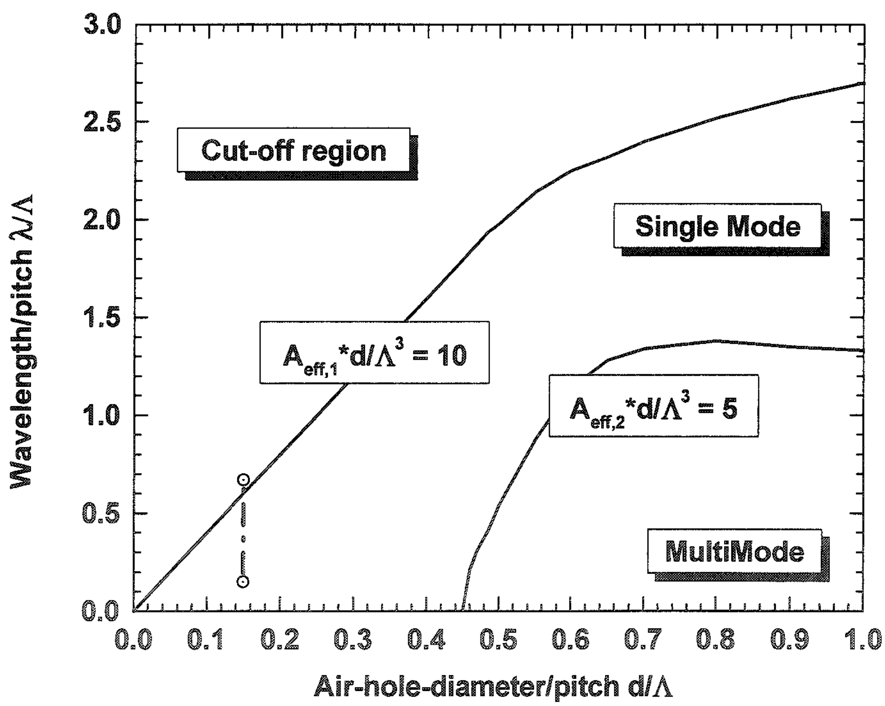

Figure 5.2 Three operation regions (single-mode, multi-mode, and cut-off) of the PCFs as a function of λ/Λ and d/Λ. The cut-off wavelengths of fundamental modes and second-order modes are calculated from their mode effective area, in which $A_{eff,1}$ and $A_{eff,2}$ are mode effective areas of fundamental modes and second-order modes, respectively.

5.3 General Design Procedure

In order to design the PCFs with desired dispersion properties, we should develop a general procedure so that the design optimization for practical dispersion-related applications of the PCFs can be performed in a systematic and efficient manner. The idea of this procedure is first proposed in Ref [58] for the design of practical DCFs. Here we extend this procedure to general dispersion-related applications such as the dispersion-shifted fibers (DSFs), the dispersion flattened fibers (DFFs), and the ultra-flattened dispersion (UDFs) [26]. As a matter of fact, the only difference among these different applications for dispersion component elements is the choice of the target functions and the constraints for the design optimization.

By following the design procedure proposed in Ref [26], [58], a general design procedure for dispersion-related applications of the PCFs is presented as follows:

Step 1: Target function with proper constraints: Given a set of desirable dispersion values at some specific wavelengths (e.g., $\lambda_0 = 0.8$ μm), define a target function in the form of $O_T = f(\lambda_0, D_F, \Delta D_F)$ with constraints (e.g., A_{eff} and the single-mode operation).

Step 2: Preliminary optimization based on scaling transformations: With varying of the air-hole size d and the pitch Λ, optimize the PCFs by minimizing the target function through scaling transformations of (5.2) and (5.3) (starting from $\Lambda_0 = 2.3$ μm) and first order dispersion approximation of (5.1) without considering Γ (i.e., ≈ 1.0).

Step 3: Model refinement for the dispersion D_g: With the optimized PCF ($d^{(2)}$ and $\Lambda^{(2)}$) obtained by **Step 2**, calculate D_g of the PCF with $n_{silica} = n_{silica}(\lambda_0)$ through the rigorous vector solvers at a few selected wavelengths and repeat **Step 2** (starting from $\Lambda_0 = \Lambda^{(2)}$ and $d_0 = d^{(2)}$) with consideration of Γ. This step can update the scaling transformations of D_g in (5.3) and may avoid simulation errors caused by (5.2) and (5.3) due to the setting of the solvers and the value of n_{silica}.

Step 4: Model refinement for the dispersion D: With the optimized PCF ($d^{(3)}$ and $\Lambda^{(3)}$) obtained by **Step 3**, calculate D of the PCF through the rigorous vector solvers at the required wavelength range and repeat **Step 2** (starting from $d_0 = d^{(3)}$ and $\Lambda_0 = \Lambda^{(3)}$) with considering Γ. This step can avoid simulation errors caused by first order dispersion approximation in (5.1).

Step 5: Verification of the final design: With the optimized PCF ($d^{(4)}$ and $\Lambda^{(4)}$) obtained by **Step 4**, calculate D of the PCF through the rigorous vector solvers with high accuracy setting at the required wavelength range to check if the optimized PCF design meets the required dispersion properties. If so, calculate other the modal parameters and end the design. If not, change the target function and repeat **Steps 2-5.**

In general, the final PCF structure can be obtained after two or three refinements by the rigorous vector solvers, provided that the target function is set properly. The entire design procedure is highly computation-efficient due to the use of the scaling transformations of the modal properties of the PCFs.

5.4 Design Applications

In order to further illustrate the design procedure, the basic requirements and the detailed target functions for several typical applications as dispersion component elements are given in this section. Figure 5.3 shows a typical dispersion curve of a PCF as a function of wavelength with the dispersion wavelengths λ_{D1}, λ_{D2}, and λ_{D3} for the required dispersion D_F (i.e., $D(\lambda_{Di}) = D_F, i = 1$, 2, and 3). Two wavelengths λ_{S1}, λ_{S2} for zero third-order dispersion and one wavelength λ_F for zero fourth-order dispersion are also marked. As demonstrated in the next section (e.g., $D_F = 0$ in Figure 5.6), the dispersion curve shown in Figure 5.3 is reasonable for the PCFs with $d/\Lambda > 0.2$. This is fortunately the case for most of the dispersion applications using the PCFs.

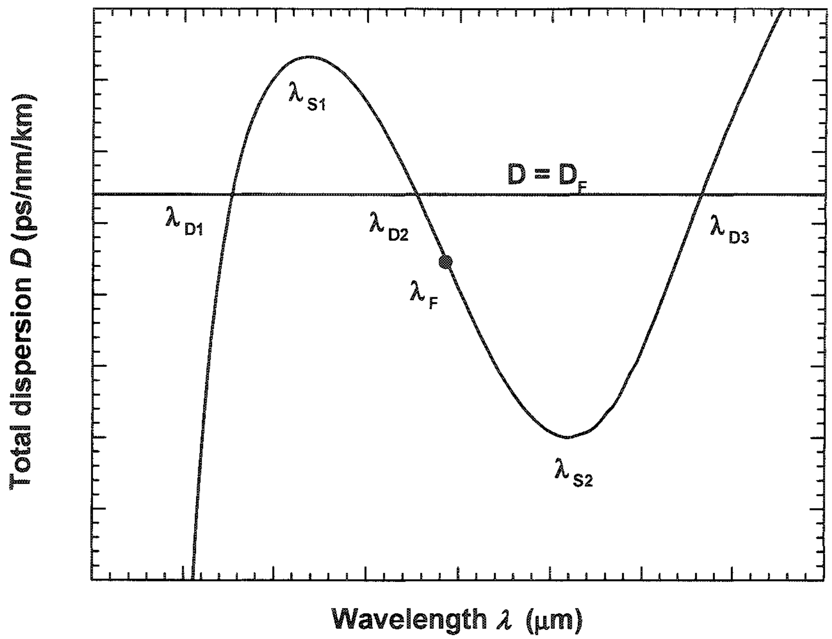

Figure 5.3 Total dispersion D of the PCFs as a function of wavelength with some possible dispersion wavelengths λ_{D1}, λ_{D2}, λ_{D3}, two wavelengths λ_{S1}, λ_{S2} of zero third-order dispersion, and one wavelength λ_F of zero fourth-order dispersion.

5.4.1 Dispersion-Shifted Fibers

The basic requirement of the dispersion-shifted fibers (DSFs) is that a desired total dispersion D_F at a wavelength point λ_0 is prescribed such that

$$D(\lambda_0) = D_F \tag{5.4}$$

where λ_0 is the operation wavelength for the desired total dispersion D_F (e.g., λ_0 is the zero dispersion wavelength if $D_F = 0$). Therefore, the target function O_T is to let one of the dispersion wavelengths (λ_{D1}, λ_{D2}, and λ_{D3}) equal to the required wavelength point λ_0,

$$O_T = |\lambda_0 - \lambda_{Di}|,\ i = 1, 2, \text{and } 3 \tag{5.5}$$

where |...| stands for the absolute value. In general, the first dispersion wavelength (λ_{D1}) should be selected because it has large parameter yields (less sensitive to the change of design parameters). Unlike the CSFs, the PCFs have a wide dispersion range, and there exist many possibilities to obtain the same desired dispersion. Therefore, some other constraints, such as the single-mode operation and the mode effective area, need to be imposed. For example, for the application of the supercontinuum generation, the small mode effective area is required to enhance the nonlinear effects of the PCFs.

5.4.2 Dispersion-Flattened Fibers

According to the definition of the dispersion flattened fibers (DFFs), at least one wavelength point of zero third-order dispersion are required in the operating range of wavelength. From the typical dispersion curve shown in Figure 5.3, there are two possible dispersion-flattened regions around λ_{S1} and λ_{S2}, respectively. We focus on the first dispersion-flattened region only, and the object function for the second dispersion-flattened region may be defined in a similar way. For the first dispersion-flattened region as shown in Figure 5.4, there are two wavelengths λ_{D1}, λ_{D2} of dispersion D_F and one wavelength λ_{S1} of zero third-order dispersion. The basic requirement for the dispersion flattening is that a wide range of wavelength with dispersion D_F and its variation $\pm\,\Delta D_F$ at the center wavelength point λ_0 are given as follows:

$$D(\lambda_{S1}) \leq D_F + \Delta D_F \quad \text{with } \lambda_{S1} = \lambda_0 \tag{5.6}$$

where λ_{S1} is the first wavelength of zero third-order dispersion. Therefore, after considering the symmetry of the dispersion curve, the target function O_T is to let λ_{S1} with the desired dispersion ($D_F + \Delta D_F$) equal to λ_0,

$$O_T = |\lambda_0 - \lambda_{S1}| + w \times |D(\lambda_{S1}) - (D_F + \Delta D_F)| \tag{5.7}$$

where w is a weight function to balance between the wavelength and the dispersion. The operating bandwidth $\Delta\lambda$ with the required dispersion $D_F \pm \Delta D_F$ is equal to (λ_2-λ_1) as shown in Figure 5.4. In general, the DFF with reasonable D_F and λ_0 can be obtained because the PCFs have very wide dispersion ranges with proper design parameters.

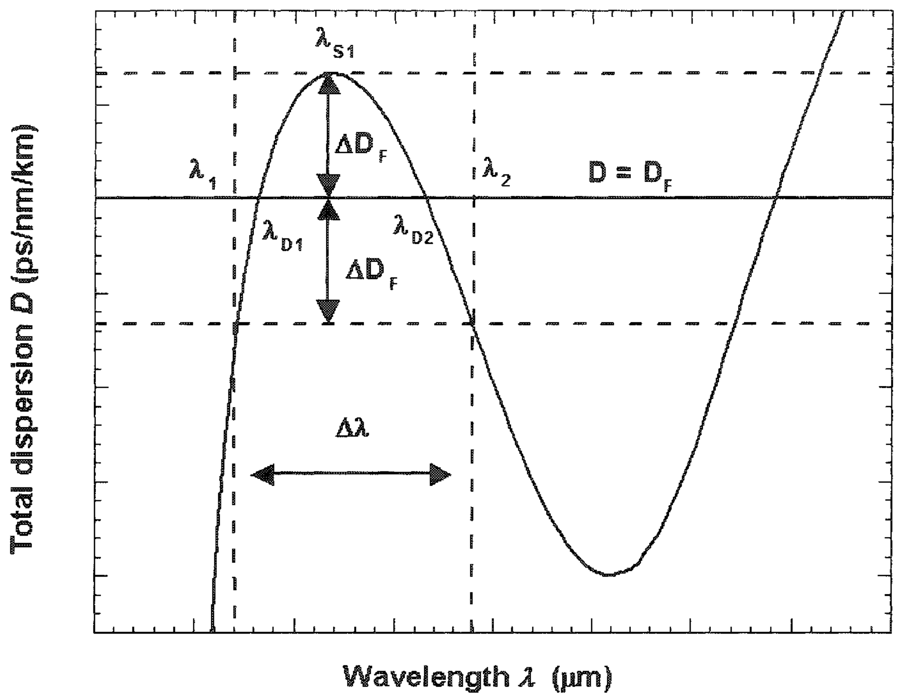

Figure 5.4 First dispersion-flattened region of the PCFs used for DFFs.

Furthermore, the PCFs with the ultra-flattened dispersion (UDFs), in which there is at least one wavelength point of zero fourth-order dispersion in the operating range of wavelength, can also be designed. From the typical dispersion curve in Figure 5.3, there is one possible ultra-flattened dispersion region around one wavelength λ_F of zero fourth-order dispersion as shown in Figure 5.5. In this ultra-flattened dispersion region, there are two wavelengths λ_{S1} and λ_{S2} of zero third-order dispersion. The basic requirement for ultra-flattened dispersion is that a wide range of wavelength with dispersion D_F and its variation $\pm\,\Delta D_F$ at the center wavelength point λ_0 are given as

$$D(\lambda_{S1}) \leq D_F + \Delta D_F, D(\lambda_{S2}) \geq D_F - \Delta D_F, \text{ with } \lambda_F = \lambda_0 \qquad (5.8)$$

where λ_F is the wavelength of zero fourth-order dispersion. Therefore, after considering the symmetry of the dispersion curve, the target function O_T is to let λ_F equal to λ_0 and λ_{S1} and λ_{S2} have the desired dispersion ($D_F + \Delta D_F$) and ($D_F - \Delta D_F$), respectively,

$$O_T = |\lambda_0 - \lambda_F| + w \times [|D(\lambda_{S1}) - (D_F + \Delta D_F)| + |D(\lambda_{S2}) - (D_F - \Delta D_F)|] \quad (5.9)$$

where w is a weight function to balance between the wavelength and the dispersion. The operating bandwidth $\Delta\lambda$ with the required dispersion $D_F \pm \Delta D_F$ is equal to $(\lambda_2-\lambda_1)$ as shown in Figure 5.5.

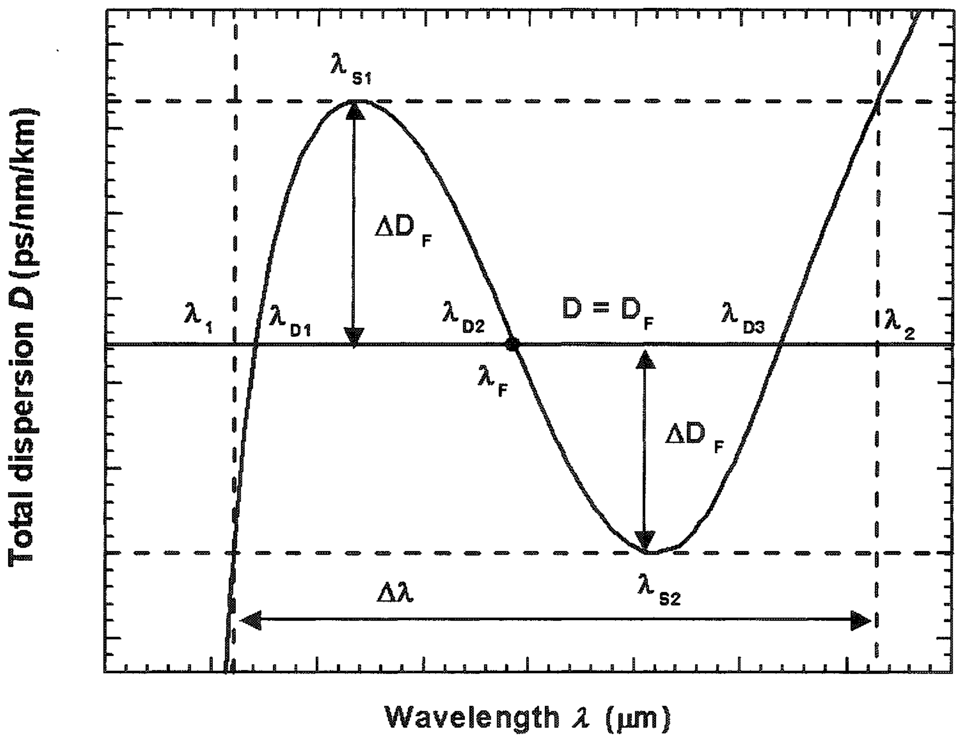

Figure 5.5 The ultra-flattened dispersion region of the PCFs used for UDFs

5.4.3 Dispersion Compensation Fibers

One of the widely used methods for the dispersion compensation is to use the dispersion compensation fibers (DCFs), which possess a negative dispersion to counteract the positive dispersion of the existing conventional single-mode fibers (CSFs). Numerous kinds of the DCFs have been designed. In general, optical communication links can be composed of a combination of the CSFs and the DCFs to achieve a small net chromatic dispersion for the entire link.

In order to compensate the dispersion of the CSFs with anomalous dispersion and positive dispersion slope, the desired DCFs should have large normal dispersion and negative dispersion slope. From the typical dispersion curve in Figure 5.3, there is one possible dispersion compensation region between λ_{S1} and λ_{S2} with a negative dispersion slope. The basic requirement for the DCFs is that large negative dispersion and dispersion slope to compensate the dispersion of the CSFs over a wide range of wavelength are achieved. Or equivalently, the same parameter K [58] as the CSFs to be compensated at the center wavelength point λ_0 should be obtained as given by

$$K(\lambda_0) = K_{CSF} \tag{5.10}$$

where K_{CSF} is defined as the dispersion divided by the dispersion slope of the CSFs. Therefore, the target function O_T is to let the parameter K of the DCFs equal to that of the CSFs at λ_0,

$$O_T = | K(\lambda_0) - K_{CSF} | \tag{5.11}$$

From the previous calculations [58], we know that there is an optimum region to realize the DCF. Therefore, we can consider some additional requirements such as maintaining possible large negative dispersion, ensuring single-mode operation, or keeping certain mode effective area, etc. It is worth noting that only a simple and intuitive form of target functions is described here. In practice, more complicated forms of the target functions are also possible and can be obtained based on the specific dispersion requirements. We will discuss the individual applications for design of dispersion component elements in great detail.

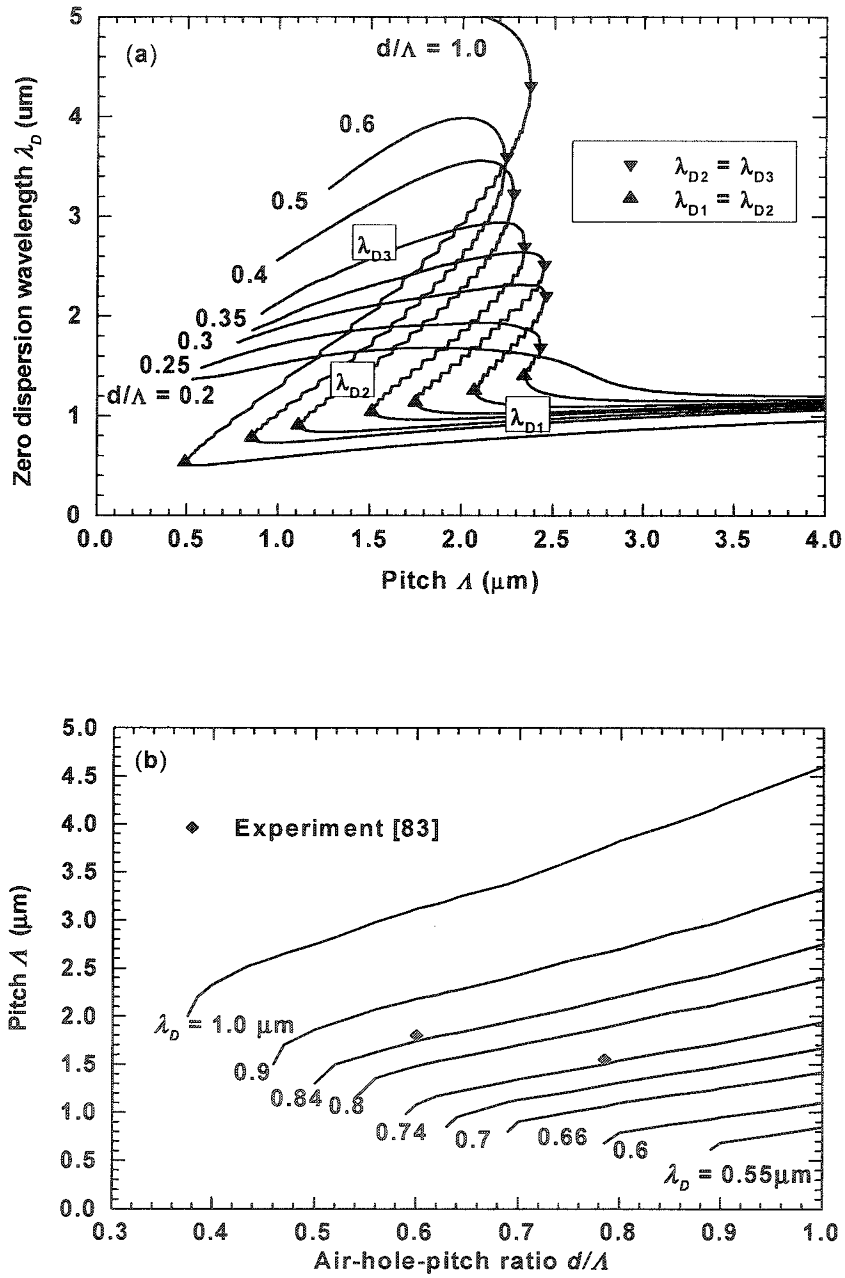

Figure 5.6 (a) Zero dispersion wavelength as a function of pitch for different d/Λ values of the PCFs, and (b) The pitch of the PCFs as a function of d/Λ for different first zero dispersion wavelength values. Diamond shapes represent the experimental results [83] of two DSFs for λ_{D1} = 0.74 and 0.84 μm, respectively.

After defining the target functions for each of the specific applications and obtaining the scaling transformations for the dispersion D_g, which are described in 5.2, we are now ready to design the PCFs with desired dispersion through a highly automated process. For the sake of simplicity, we assume the required dispersion value D_F is set to zero (i.e., $D_F = 0$). Through the scaling transformations of D_g, the relation between the wavelength λ_D of zero dispersion and the design parameters of the PCFs can be easily obtained and utilized as the starting point of the design optimization. Figure 5.6(a) shows the wavelength λ_D of zero dispersion with dependence of Λ and d/Λ of the PCFs. The three regions for each d/Λ curve represent λ_{D1}, λ_{D2}, and λ_{D3}, and the two turning points (down and up triangular shapes) for each d/Λ curve represent the wavelengths λ_{S1}, λ_{S2} of zero third-order dispersion, respectively. From Figure 5.6(a), it is clearly shown that the possible solutions for different dispersion applications such as the DSFs, the DFFs, and the UDFs. For example, for the UDFs, only one possible solution can be obtained when λ_{S1} and λ_{S2} are close to each other. The design procedure for those applications is described as follows.

5.5 Dispersion-Shifted Fibers

One of the current applications for the DSFs is to increase the light intensities for generating supercontinuum spectrum from 0.5 to 1.3 μm. In this application, the single-mode operation is not important. However, the minimum mode effective area is desirable. From Figure 5.6(a), some interesting characteristics for the DSFs can be observed, such as the possible minimum λ_D is around 0.5 μm, which is in good agreement with experimental results [83]. Also it is found that the coverage of λ_D over the full wavelength range from 0.5 to 5.0 μm is achievable and the possible λ_D can be realized by many combinations of design parameters of the PCFs. Further, the relation between the design parameters (Λ and d/Λ) for different first-order zero dispersion wavelength values, as shown in Figure 5.6(b), can be obtained through the scaling transformations of (5.2) and (5.3). The experimental results (diamond shapes) of the two

DSFs [12] for λ_{D1} = 0.74 and 0.84 μm are also shown in Figure 5.6(b). It is found that Λ depends linearly on d/Λ for certain value of λ_{D1} (the opposite effect for λ_{D2}) and the minimum A_{eff} can be obtained at the possible minimum of the pitch because Λ depends linearly on square of d/Λ of (C.20) and (4.9) for certain value of A_{eff}. In order to demonstrate the design of the DSFs using the proposed approach, the pitch Λ is respectively set to 1.0, 1.58, and 1.85 μm for the corresponding zero dispersion wavelengths λ_D = 0.66, 0.74, and 0.84 μm [12]. The optimum results for those three applications (DSF1, DSF2, and DSF3) can be easily obtained as shown in Table 5.1. It is observed that there is a discrepancy between the simulation and the experimental results, especially for the small-pitch PCFs, mainly due to errors (about ± 10 % on the absolute values) of electron micrograph analysis and deviations from circular holes [85], [86].

Table 5.1 Three typical applications of DSFs with required dispersion D_F = 0.

Type	Wavelength λ_0 (μm)	After step 1 Λ(μm), d/Λ	After step 2 Λ(μm), d/Λ	After step 3 Λ(μm), d/Λ	Mode status	MEA (μm^2)	Ref [12] Λ(μm), d/Λ
DSF1	0.66	1.00, 0.744	1.00, 0.747	1.00, 0.754	multi	0.92	1.00, 0.620
DSF2	0.74	1.58, 0.824	1.58, 0.837	1.58, 0.832	multi	1.84	1.58, 0.785
DSF3	0.84	1.85, 0.646	1.85,0.653	1.85, 0.652	multi	3.77	1.85, 0.595

5.6 Dispersion-Flattened Fibers

In this section, the designs of the DFFs with D_F = 0 and ΔD_F = 1 ps/nm/km are demonstrated. In order to compare the design with available PCF structures [78]-[80], the operating wavelength λ_0 is set to 0.8, 1.13, and 1.55 μm, respectively. The optimum results for these three applications (DFF1, DFF2, and UDF) can be easily obtained as shown in Table 5.2. In Table 5.2, the single-mode condition and the mode effective area for each dispersion application are also given. Figure 5.7 shows the total dispersion, in which the dot and dash lines represent the dispersion of the PCFs followed by Step 1, Step 2, and Step 3, respectively. It is clearly seen from Figure 5.7 that the errors caused in the scaling approximation of (5.3) and in the first order approximation of (5.1) are eliminated by the proposed general design process approach. From Table 5.2, it is found that the operating bandwidths of the newly designed fiber are almost the same as those in [78]-[80] with slight difference of the PCF structures due to the different models used for the silica material.

Table 5.2 Three applications of DFFs with required dispersion D_F = 0 and dispersion variation ΔD_F = 1ps/nm/km.

Type	Wavelength λ_0 (μm)	After step 1 Λ (μm), d/Λ	After step 2 Λ (μm), d/Λ	After step 3 Λ (μm), d/Λ	Mode status	MEA (μm^2)	Bandwidth $\Delta\lambda$ (nm)
DFF1	0.80	0.905, 0.585	0.904, 0.583	0.904,0.581	multi	1.41	58
DFF2	1.13	1.73, 0.357	1.731, 0.361	1.732, 0.3652	single	7.74	145
UDF	1.55	2.40, 0.250	2.40, 0.253	2.39, 0.256	single	31.6	550

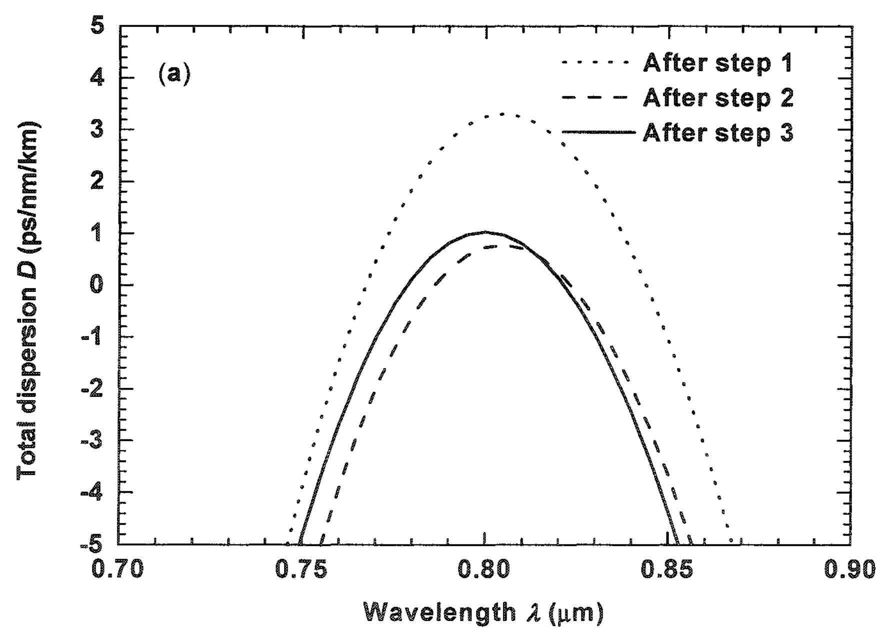

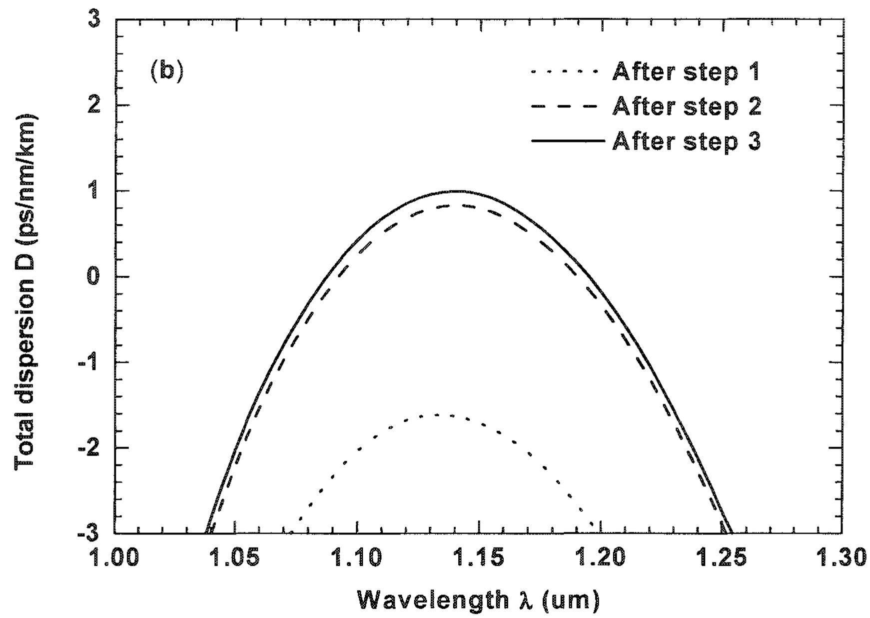

Figure 5.7 The total dispersion in which the dot, dash, and solid lines represent dispersions of the PCFs followed by Step 1, Step 2, and Step 3, respectively. (a) $\lambda_0 = 0.8$ μm, and (b) $\lambda_0 = 1.13$ μm.

5.7 Dispersion Compensation Fibers

The idea to use the PCFs for the dispersion compensation was first proposed in Ref [82], in which a simplified model consisting of a silica core in air was used for the proof of concept. In order to optimize the dispersion, it is necessary to systematically investigate dispersion properties of the PCFs with the combination of the PCF parameters by a rigorous vector solver [26]. It is, therefore, of practical interest to improve the existing design so as to explore the potential of the PCFs for broadband dispersion compensation.

Here we assume that a fiber link consists of a CSF of length L_1 with dispersion $D_1(\lambda)$ and a DCF of length L_2 with dispersion $D_2(\lambda)$, the effective compensated dispersion $D_e(\lambda)$ on the fiber link in series can be written as

$$D_e(\lambda) = \frac{D_1(\lambda)L_1 + D_2(\lambda)L_2}{L_1 + L_2} \tag{5.12}$$

which only considers the effect of dispersion. In order to compensate the accumulated dispersion of the CSF at $\lambda = \lambda_0$ by the DCF, the following condition has to be satisfied:

$$R = \frac{L_1}{L_2} = -\frac{D_2(\lambda_0)}{D_1(\lambda_0)} \tag{5.13}$$

where R is the fiber dispersion (or length) ratio and λ_0 is the center of the operating wavelength range. Furthermore, the accumulated dispersion of the CSF should be compensated over a wavelength range. For the sake of simplicity, we assume that both fibers have slowly varying dispersion slopes $S_1(\lambda)$ and $S_2(\lambda)$ [58]. In order to compensate the accumulated dispersion over a range of wavelength (e.g., $D_e(\lambda) = 0$ with $\lambda \neq \lambda_0$), we have

$$R = \frac{L_1}{L_2} = -\frac{S_2(\lambda_0)}{S_1(\lambda_0)} \tag{5.14}$$

where (5.13) was used. By combining (5.13) with (5.14), a new parameter K is introduced to judge the dispersion compensation satisfaction over a range of wavelength,

$$K = \frac{D_1(\lambda_0)}{S_1(\lambda_0)} = \frac{D_2(\lambda_0)}{S_2(\lambda_0)} \tag{5.15}$$

From (5.15), it is apparent that once the parameter K of the DCF, with the maximum of R or some other constraints, reaches the required one of the CSF, the design of the DCF is accomplished. Based on the above requirement, a design procedure for the broadband DCF is similar with the general design procedure described in the previous section.

The desired DCF should have a normal dispersion and negative dispersion slope. From the first order approximation (5.1) of $D(\lambda)$ and scaling transformations (5.2) and (5.3) of $D_g(\lambda)$ with Λ_0 = 2.3 μm, the PCF with required dispersion properties can be analytically obtained. Figure 5.8(a) shows the parameter K for the CSF and PCF as a function of pitch Λ with different d/Λ values. It is seen from Figure 5.8(a) that the possible pitch range of the PCF is from 0.7 to 1.4 μm, which corresponds the parameter K

from 1000 nm to 0. Here we assume that the CSF is made of silica with a step-index core of diameter 9.0 μm and numerical aperture 0.1 [82] and its K is a constant value over the DWDM wavelength range [58]. The intersection points (diamond shapes) between the PCF and the CSF, which have the same K, are the possible pitch of the PCF. It can be seen from Figure 5.8(a) that the pitch of the PCF decreases or converges into one value (around Λ = 0.9 μm) when d/Λ increases from 0.6 to 1.0. By considering the practical PCF with a rough silica bridge of 0.12 μm [82], we assume that the narrowest width of the bridge to be 0.1 μm (i.e., $\Lambda - d = 0.1$ μm) as shown in Figure 5.8(b). It can be seen from Figure 5.8(b) that the possible PCF with $\Lambda^{(2)} = 0.928$ μm and $d^{(2)}/\Lambda^{(2)} = 0.892$ is obtained with $D(\lambda)$ of –432 ps/nm/km at the wavelength of 1.55 μm. Further, through the calculation of $D(\lambda)$, the final PCF with $\Lambda^{(4)} = 0.932$ μm and $d^{(4)}/\Lambda^{(4)} = 0.893$ is confirmed with –474.4 ps/nm/km at the wavelength of 1.55 μm, which is summarized in Table 5.3. Figure 5.9 shows the effective dispersion of the fiber link at the wavelength of 1.55 μm and $D(\lambda)$ of the PCF (solid line) and CSF (dot line), in which the dot line represents the product of dispersion of the CSF and dispersion ratio R, respectively. It is seen from Figure 5.9 that the optimum PCF can compensate CSF within ± 0.05 ps/nm/km over 236-nm wavelength range. The corresponding dispersion at 1.55 μm is of about –474.4 ps/nm/km, which means it can compensate the dispersion of over 28 times of length of the CSF. From the judgment of the core parameter U (e.g., $U < 2.6$) [72], the PCF with $d/\Lambda \approx 0.9$ and $\Lambda < 1.1$ μm is of single-mode operation. It is worth mentioning that the designed PCF with small core has small mode effective area (1.6 μm^2) and large coupling loss with the standard fiber. Fortunately, the taper PCF structure can be used for mode converter with only 0.3 dB coupling loss with the CSF [84].

Table 5.3 The DCF application with required K coefficient of the CSF at the wavelength of 1.55 μm is 301.8 nm within an effective dispersion variation (± 0.05 ps/nm/km).

Type	Wavelength λ_0 (μm)	After step 1 Λ (μm), d/Λ	After step 2 Λ (μm), d/Λ	After step 3 Λ (μm), d/Λ	Mode status	MEA (μm^2)	Bandwidth $\Delta\lambda$ (nm)
DCF	1.55	0.928,0.892	0.930,0.891	0.932,0.893	single	1.60	236

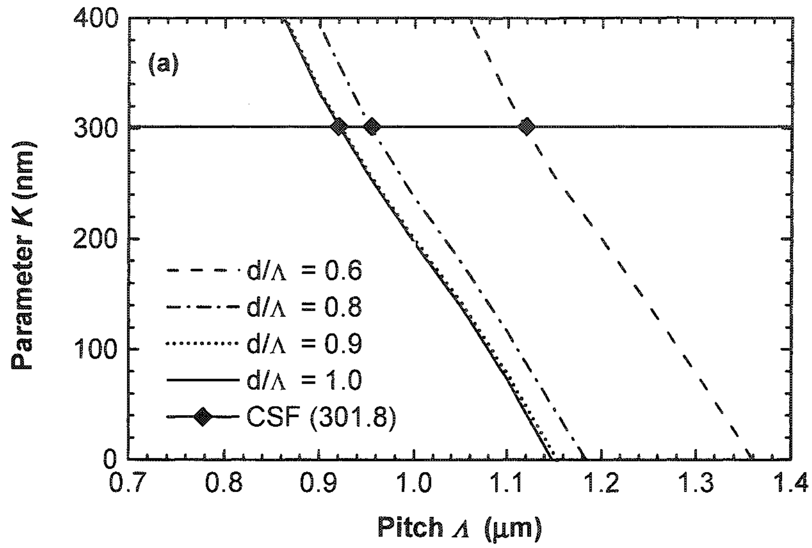

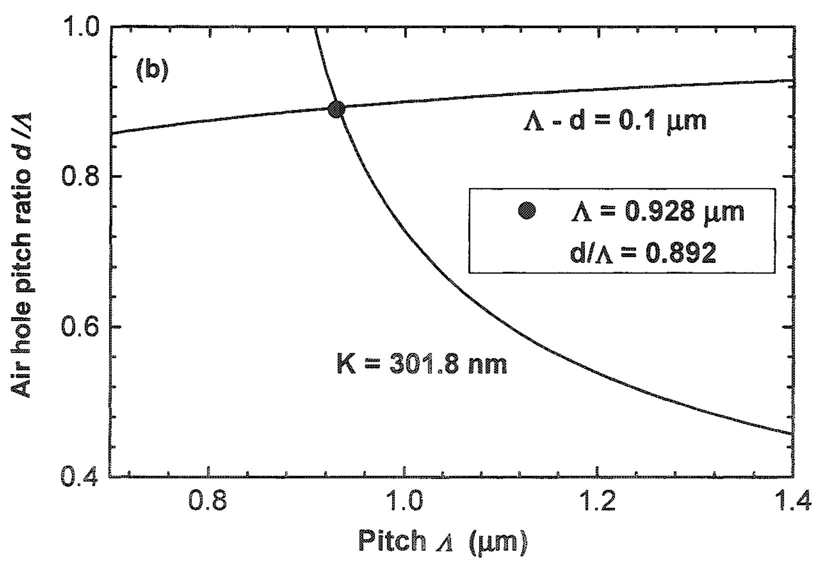

Figure 5.8 (a) The parameter K as a function of pitch for the PCFs with $d/\Lambda = 0.6$ (broken line), 0.8 (dashed line), 0.9 (dot line), 1.0 (solid line) and CSF (diamond line), in which K of CSF is 301.8 nm over all wavelength range, and (b) the possible PCF structure (circle point) with $\Lambda = 0.928$ μm and $d/\Lambda = 0.892$ that meets two design requirements: $K =$ 301.8 nm and $\Lambda - d = 0.1$ μm.

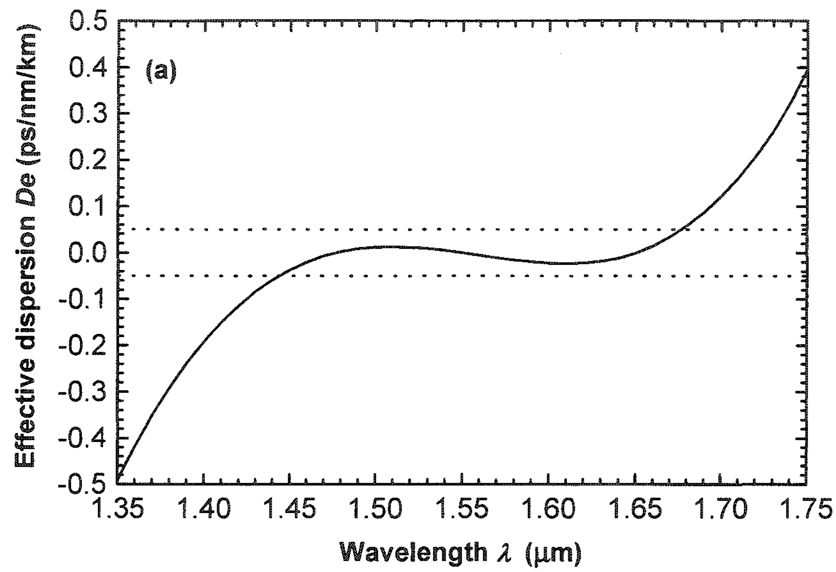

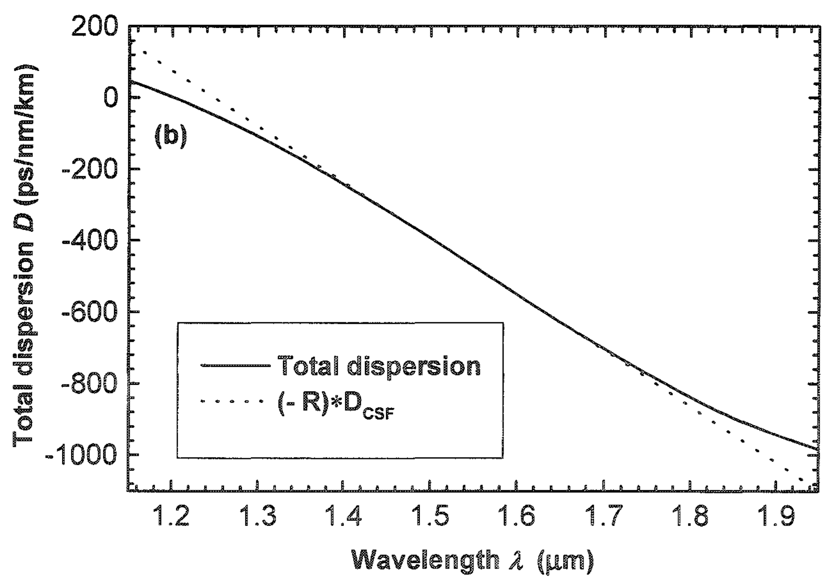

Figure 5.9 (a) The effective dispersion of the fiber link after compensated by the PCF, and (b) total dispersion of the PCF (solid line) and CSF (dot line), in which the dot line represents the product of dispersion of the CSF and dispersion ratio R.

5.8 New Dispersion Design for DCFs

In this section, a new PCF structure that allows first two rings of the air holes to have different radii is proposed and analyzed for the purpose of broadband dispersion compensation. The new structure of the PCF to some extent resembles the index profile of the W-shape conventional fiber (or simply W-fiber) in which an additional cladding layer with the depressed refractive index is placed near the core [2]. By properly optimizing the index, width and position of the cladding layer, the W-fiber can exhibit enhanced dispersion characteristics for various applications. In other words, by increasing the air-hole size of the first air-hole ring and decreasing the air-hole size of the second air-hole ring, a similar index distribution with the W-fiber PCF can be realized in the PCF. For the sake of simplicity and the limitation of fabrication, we assume that the radius of the first air-hole ring is unchanged and the same with the air-hole size d of the PCF.

The transverse cross-section of the modified PCF is shown in Figure 5. 10. Like the conventional PCF, the air holes are arranged in a hexagonal (or triangular) array with the air-hole size d and the pitch Λ. In order to optimize the index distribution in the cladding area, an extra design parameter, the air-hole size d_l of the second ring of air holes, is introduced. Due to the large dispersion requirement, the PCF used for the DCF have large air-hole size-to-pitch ratio (e.g., d/Λ = 0.9 [58]). Therefore, we restrict our discussion to the regime of $d \geq d_l$. In order to utilize the scaling transformation of modal properties of the PCF [58], a typical PCF with d = 0.81 μm and Λ = 0.9 μm is used as the starting point of design and optimization of the DCFs.

Because of the additional degree of freedom provided by this new structure, a large K coefficient (dispersion divided by the dispersion slope) can be realized without too much reduction in the mode effective area of the PCF. Furthermore, by employing the design model and methodology in the previous sections, a general design optimization procedure can be developed for the PCFs to realize various desirable dispersion applications, especially for broadband dispersion compensation.

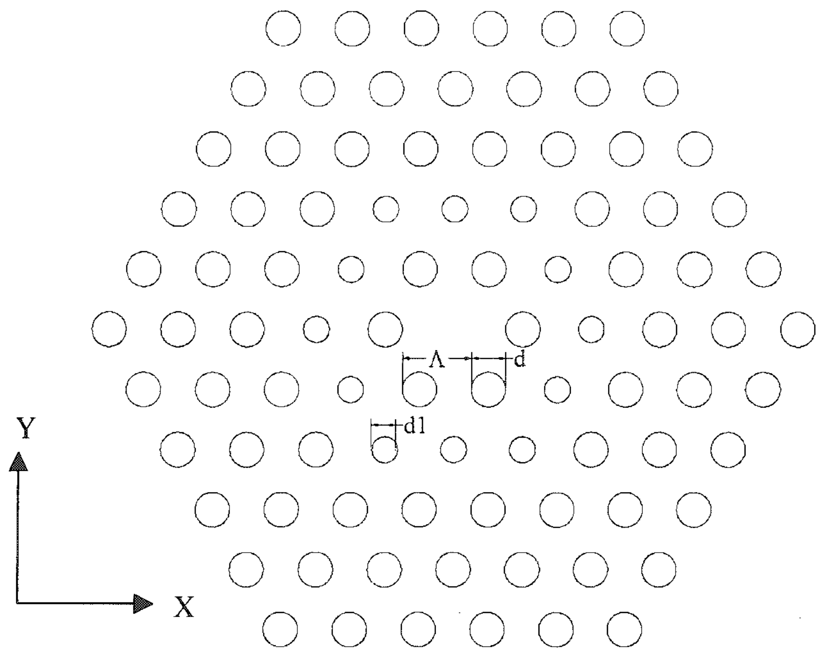

Figure 5. 10 The cross section of a PCF with a regular triangular air-hole array.

Figure 5.11 shows the effective index n_{eff} and the geometrical dispersion D_g as a function of wavelength for the fixed pitch Λ = 0.9 μm and air-hole size d = 0.81 μm. It is noted from Figure 5.11(a) that, when the size d_l of air holes of the second ring of PCF decreases, the "turning point" of the effective index n_{eff} moves toward the short wavelength and the slope of the effective index at the turning point becomes more dramatic. Accordingly, as shown in Figure 5.11(b) when the size d_l decreases, the point of the minimum geometrical dispersion D_g moves toward the short wavelength and the slope of the geometrical dispersion D_g increases.

We also calculated the geometrical dispersion D_g with the minimum dispersion at the wavelength of 2.0 μm through the scaling transformation mentioned in 5.2. The results are shown in Figure 5.12 in which the corresponding pitches are 1.09, 1.29, 1.50, and 1.87 μm for $d_l = d$, $0.75d$, $0.6d$, $0.5d$, and $0.4d$, respectively.

As we know, the conventional single-mode fibers (CSFs) have an anomalous dispersion and positive dispersion slope at the operating wavelength near 1.55 μm. From (5.4), the desired DCF should have a normal dispersion and negative dispersion slope with the same K of the CSF within a range from 30 to 400 nm around the same operation wavelength. It also can be seen from Figure 5.12 that the portion of curves with a negative slope are the corresponding periods because the dispersion slope of material such as silica is relative small in the PCF at the wavelength range of 1.55 μm. From scaling transformations of the dispersion, the possible pitch range of the PCF is from 0.7 to 1.6 μm. Two examples of the PCF structures compensated for dispersion of typical commercial deployed transmission fibers at the wavelength of 1.55 μm are demonstrated as follows.

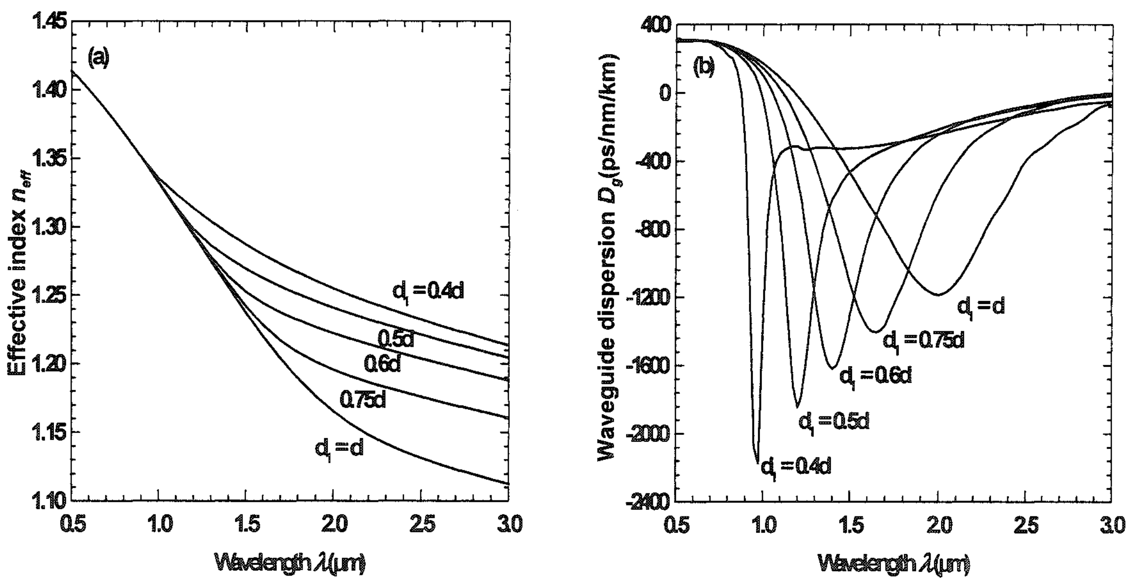

Figure 5.11 Modal parameters as a function of wavelength for the PCFs with fixed pitch Λ = 0.9 μm and air-hole size d = 0.81 μm. (a) The effective index n_{eff}, and (b) The geometrical dispersion $D_g(\lambda)$.

The dispersion properties of two typical commercial deployed transmission fibers at the wavelength of 1.55 μm are taken from Ref [87], which are shown in Table 5.4. Here we assume that the K coefficient of the CSF is a constant value over the DWDM wavelength range. Figure 5.13 shows the K coefficient as a function of pitch for different d/Λ values of the PCF and CSF. The intersection points between them, which have the same K coefficient, are the corresponding pitch of the PCF. The optimum PCF structure and corresponding dispersion are shown in Figure 5.14 and Table 5.5, respectively.

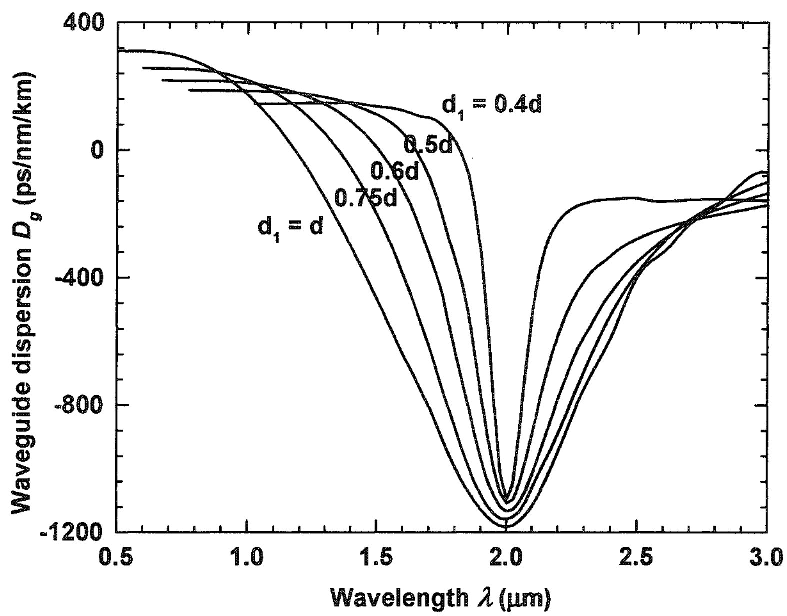

Figure 5.12 Geometrical dispersion $D_g(\lambda)$ as a function of wavelength for the PCFs with fixed minimum dispersion at the wavelength of 2.0 μm through the scaling transformation of $D_g(\lambda)$.

Table 5.4 Typical dispersion properties of some commercial deployed transmission fibers at the wavelength of 1.55 μm.

Type of CSF fiber	Dispersion (ps/nm/km)	Dispersion slope (ps/nm^2/km)	K coefficient (nm)
Standard SMF	17.0	0.058	298
True wave-RS	4.5	0.045	100

Compared with the conventional PCFs, as evident from Table 5.5, the newly design of the PCFs is shown to provide large normal dispersion (up to -811 ps/nm/km from -521 ps/nm/km) and large mode effective area (up to 2.2 μm^2 from 1.5 μm^2) at a typical C band wavelength range (up to 50 nm). With a dispersion of –811 ps/nm/km and a mode effective area of 2.2 μm^2 (or –703 ps/nm/km and 4.0 μm^2), a PCF could compensate the dispersion of over 50 times (or 150 times) its length of the CSF within ±0.05ps/nm/km.

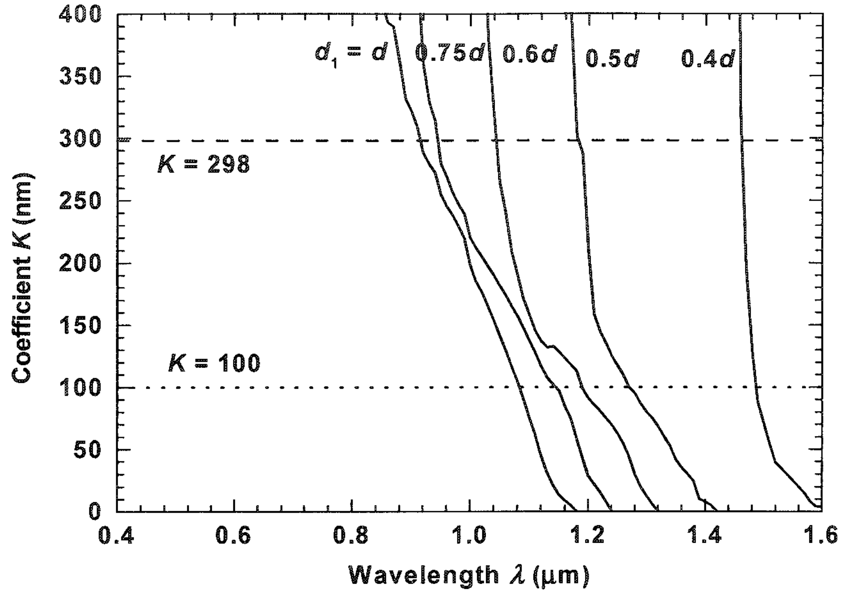

Figure 5.13 Coefficient K as a function of pitch for the PCFs with different d/Λ values.

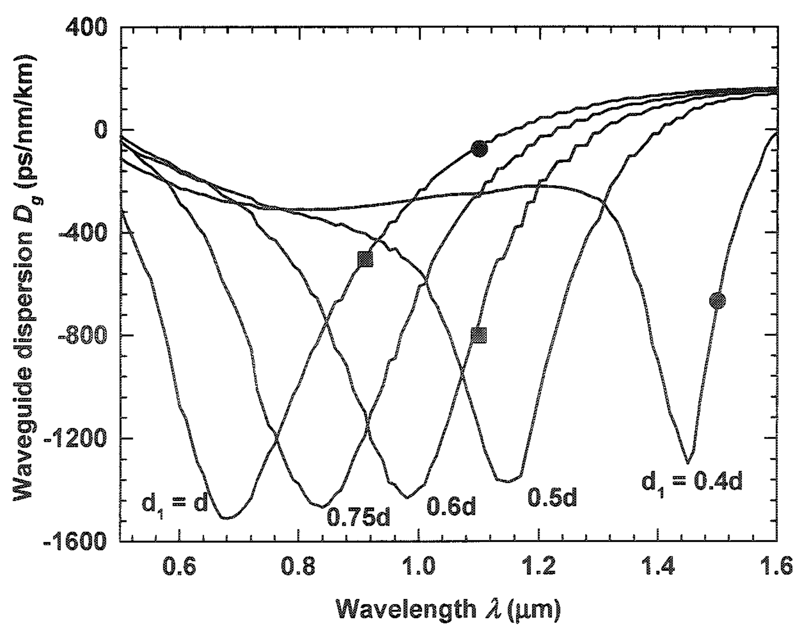

Figure 5.14 Total dispersion $D(\lambda)$ as a function of pitch for different PCFs with d/Λ = 0.9 at the wavelength of 1.55 μm.

Table 5.5 Typical PCF structure compensated for dispersion of some commercial deployed transmission fibers at the wavelength of 1.55 μm.

Type of CSF fiber	Original design ($d_I = d$)	New design
Standard SMF (Square shape in Figure 5.14)	$\Lambda = 0.922$ μm $d = 0.830$ μm $D = -521$ ps/nm/km $A_{eff} = 1.5$ μm^2	$\Lambda = 1.1$ μm $d = 0.99$ μm and $d_I = 0.6$ μm $D = -811$ ps/nm/km $A_{eff} = 2.2$ μm^2
True wave -RS (Circle shape in Figure 5.14)	$\Lambda = 1.1$ μm $d = 0.99$ μm $D =-80$ ps/nm/km $A_{eff} = 2.2$ μm^2	$\Lambda = 1.5$ μm $d = 1.35$ μm and $d_I = 0.54$ μm $D = -703$ ps/nm/km $A_{eff} = 4.0$ μm^2

5.9 Summary

Based on the rigorous vector mode solvers and the scaling transformations of the modal properties, a general design model of the PCFs for the dispersion-related applications is proposed. By using the proper combination of the numerical mode solvers and the scaling transformations, the design parameters of the PCFs can be optimized automatically to realize the desired dispersion properties. Several typical examples for dispersion-related applications are given in great detail. For certain dispersion-related applications, we show that other modal properties such as the mode effective area and the single-mode operation can also be accounted for as additional considerations in the overall design process. And some typical examples for dispersion-related applications are given.

By following the general design model and methodology for designing the broadband DCF based on the PCF structure, an optimized broadband dispersion design is obtained through proper scaling of two design parameters of the PCF and refinement by the rigorous numerical analysis. Two typical design examples for the DCF are demonstrated. With a dispersion of –811 ps/nm/km and a mode effective area of 2.2 μm^2 (or –703 ps/nm/km and 4.0 μm^2), a conventional PCF (or the PCF with the different air-hole size of the second air-hole ring) could compensate the dispersion of over 50 (or 150) times its length of the CSF within ±0.05ps/nm/km over a 150-nm wavelength range.

Chapter 6

Conclusions and Suggestions for Further Research

6.1 Conclusions

In this thesis, the modal characteristics of photonic crystal waveguides (PCWs) in both one and two-dimensional configurations were investigated theoretically in a systematic and comprehensive fashion by both approximate and rigorous methods. Depending on the design parameters of the PCWs, there exist two different guiding mechanisms, i.e., the total internal reflection (TIR) and the photonic band-gap (PBG). Firstly, through the comprehensive analysis of modal properties and transmission characteristics of 1D PCWs, the deep physical insight was gained and salient features were revealed. In addition, we also presented and compared the scope of validity and degree of accuracy for several approximate solution methods (e.g., the effective index method and the envelope approximation method). Secondly, we studied in depth the modal characteristics of 2D PCWs (i.e., PCFs) by using the versatile finite difference method and the physically more revealing plane-wave expansion method. In this context, we for the first time to our best knowledge carried out a comprehensive assessment of the scalar and the semi-vector approximations by way of examples. It is shown clearly that the semi-vector approximation is sufficient for accurate prediction of the modal properties of the typical PCFs, whereas the scalar approximation may lead to significant errors. Finally, we discussed the design optimization of the PCWs with respect to applications in broad-band fiber-optic communications. A general scaling transformation of the modal properties related to the design parameters of the PCFs are derived. Based on the high accuracy analysis models and scaling transformations of modal properties, a powerful procedure of design and optimization of the PCFs for desired modal properties is proposed and applied to several practical examples. High-performance PCFs with such an optimization procedure are designed and demonstrated.

In the following, a summary of the major contributions made in this thesis is given:

1. Comprehensive Investigation of Modal characteristics of 1D PCWs

One of the major contributions of this thesis is the comprehensive investigation for the modal characteristics of the 1D photonic crystal waveguides (PCWs). Despite their structural simplicity, the 1D PCWs provide a revealing example for analyzing and understanding the underlying guiding mechanisms and the modal characteristics of the PCWs in general. By using the standard transfer matrix method, we performed a systematic analysis of typical 1D PCWs. With the help of the band-gap map of the corresponding photonic crystal structure, we have, for the first time, identified four different guiding regions in which different transmission characteristics of the waveguides are analyzed and discussed. The modal properties of the PCWs, such as the effective index, the modal field, the group velocity dispersion, the mode effective area, the beam divergence, the model polarization and modal birefringence, the confinement loss, and the single-mode operation, are all examined in detail. Also, we employed two approximate methods, namely, the envelope approximation method and the effective index method. Their scope of validity and level of accuracy are assessed by comparison with the exact solutions. Further, scaling transformations of the modal properties related to the design parameters of the waveguide structure are derived. Finally, the similarity and difference between the 1D PCWs and 2D PCWs are discussed.

2. Scope of Validity and Level of Accuracy for the Semi-Vector and Scalar Formulations

It is well established that the scalar formulations is accurate enough for analysis of the modal properties of the weakly-guided optical waveguides such as the conventional single-mode fibers. For the PCWs, it was generally believed that the scalar approximation could be used for small air-hole PCWs. A more in-depth examination of this issue by the systematic simulation for typical PCFs is carried out by using the rigorous finite difference method, which helps to fill certain holes in knowledge of the vector properties of the PCFs. Through the comparisons among the full-vector, the semi-vector, and the scalar formulations, it is demonstrated clearly that the vector nature of the guided modes on the PCFs needs to be considered in analyzing the modal characteristics such as the effective indices, the dispersions, and the model field profiles. In this respect, the semi-vector formulation can be used to obtain solutions of high accuracy with the same level of computation effort as the scalar solutions. This conclusion is of considerable practical significance, considering the simplification of the semi-vector formulation and the reduction of the computation resources required in comparison with the full-vector formulation and computation.

3. Study of Dependence of the Modal Characteristics of Practical PCWs on New Design Parameters

Another important contribution of this thesis is to study and clarify the dependence of the modal characteristics (e.g., the modal field, effective index, dispersion, confinement loss, bending loss, mode effective area, and confinement factor) of the 1D and 2D PCWs on certain key design parameters such as the number of air holes and size of interstitial holes. Such effects are practically important, yet have not yet been examined and reported in literature prior to this work. Furthermore, some scaling transformations of modal properties related to the design parameters of the PCWs, which are very helpful in design of practical optical waveguides, are given.

4. A General Procedure for Design Optimization of the PCFs

Efficient and reliable procedure that can be used to perform design optimization for the PCFs is highly desirable for the application of such waveguides as a transmission medium. Such a procedure for design of the PCFs with desirable dispersion properties is developed and presented in this thesis. The design model is based on the combination of a rigorous vector mode solver and a scaling transformation for the dispersion properties of the PCFs. In comparison with the conventional design method, the new design procedure is more efficient and can be readily automated for the purpose of design optimization. Several applications of the design procedure, e.g., the design optimization for the dispersion shifted fibers, the dispersion flattened fibers, and the dispersion compensation fibers, are demonstrated and discussed.

5. Designs of High-Performance Dispersion Compensation Fibers

As a good example for the application of the powerful design optimization methodology described in the previous section, a PCF is designed and shown to exhibit large normal dispersion up to -474.5 ps/nm/km, nearly five times of conventional dispersion compensating fibers, and compensate conventional single-mode fibers within ± 0.05 ps/nm/km over a 236-nm wavelength range. Further, through the change the size of the second air-hole rings, a novel design of the PCFs for the dispersion compensation is obtained. In comparison with the performance by the conventional PCFs, the newly designed PCF is capable of providing large normal dispersion (up to -811 ps/nm/km from -521 ps/nm/km) and large mode effective area (up to 2.2 μm^2 from 1.5 μm^2) at a typical C band wavelength range (up to 50 nm), which represent the best overall performance ever reported in literature.

6.2 Suggestions for Further Research

Based on the modal properties of the PCWs, which are investigated thoroughly in this thesis, future work and research should focus on the development of the new devices and related solvers. In the following, suggestions for further research are given.

As we know, the research and development of the PC-based devices and components, such as couplers and multiplexers, just begin. Many novel devices with some unique features need to be discovered and assessed. Except the optical communication, different application areas, such as optical signal processing, bio-optics, and optical sensors, also call for the novel devices. Based on the unique features of the PCWs, it is very natural extension of the current work. Further research can also be devoted to the design and optimization of the PC-based devices with in-plane propagation.

On the other hand, further research is needed to develop the new analytical and semi-analytical solvers by utilizing the unique features of the PCs. By analogy with the electronic band-gap material and the microwave/RF transmission theory, more mature analytical and semi-analytical methods are desirable for design and optimization of the PC-based devices and circuits.

Appendix A

Performance Parameters of Optical Waveguides

The overall parameters of optical waveguides can be categorized into the design parameters (e.g., physical dimensions, refractive indices, and environmental effects), performance parameters (i.e., modal properties or transmission characteristics), and mechanical parameters. Among them, modal properties are of utmost importance for optical communication systems. By solving the eigen-value equations of the waveguide modes through some approaches mentioned in Chapter 2, we can obtain two fundamental modal properties: complex effective indices N_{eff} (e.g., $n_{eff}+jn_i$) and modal field profiles (e.g., E_x and E_y) of the corresponding modes. From them, other modal properties of optical waveguides, which are frequently used in this thesis, can be derived.

A.1 Performance Parameters Related to Mode Effective Index

A.1.1 Confinement Loss

The confinement loss L_c, an attenuation caused by the waveguide geometry (i.e., without considering the material absorption and waveguide imperfection), is given by

$$L_c(\lambda) = -20\log_{10} e^{-kn_i} = 5.45751\times 10^7 \times \frac{n_i}{\lambda}, \text{ dB/m} \tag{A.1}$$

where k is the propagating constant in free space, λ is the operating wavelength in μm, and n_i is the imaginary part of N_{eff}. It is worth to note that, if the waveguide is bended with a radius R, the loss calculated by (A.1) includes the bending loss.

A.1.2 Group Index and Group Velocity

The group index n_g is defined by

$$n_g(\lambda) = c\frac{dk_z}{d\omega} = n_{eff} - \lambda\frac{dn_{eff}}{d\lambda} = n_{eff} + \omega\frac{dn_{eff}}{d\omega} \tag{A.2}$$

where n_{eff} is the real part of the complex effective index N_{eff}, k_z is the propagation constant, and ω is the angular frequency. The group velocity v_g is defined by

$$v_g(\lambda) = \left(\frac{dk_z}{d\omega}\right)^{-1} = \frac{c}{n_g(\lambda)} = \frac{1}{\tau_g} \tag{A.3}$$

where c is the velocity of the light in a vacuum and τ_g is the group delay.

A.1.3 Group-Velocity Dispersion and Dispersion Slope

The group-velocity dispersion D is defined as the change in pulse width per unit distance of propagation and given by

$$D(\lambda) = \frac{d}{d\lambda}\left(\frac{1}{v_g(\lambda)}\right) = -\frac{\lambda}{c}\frac{d^2 n_{eff}(\lambda)}{d\lambda^2}, \ \text{ps/km/nm} \tag{A.4}$$

where λ is the operating wavelength. The dispersion slope S is defined by

$$S(\lambda) = \frac{dD(\lambda)}{d\lambda} \tag{A.5}$$

A.1.4 Modal Birefringence and Beat Length

Modal birefringence B is defined as the difference in the effective index between the two orthogonal polarizations, and given by

$$B(\lambda) = | n_{eff,x}(\lambda) - n_{eff,y}(\lambda) | \tag{A.6}$$

where $n_{eff,x}$ and $n_{eff,y}$ are the effective indices of two orthogonal polarizations, respectively. The beat length L_B is defined as a period with the power exchange between two polarizations, and defined by

$$L_B(\lambda) = \frac{2\pi}{| k_{z,x}(\lambda) - k_{z,y}(\lambda) |} = \frac{\lambda}{B(\lambda)} \tag{A.7}$$

where λ is the operating wavelength.

A.1.5 Propagation Constant and Phase

The propagation phase ϕ is calculated by

$$\phi(\lambda) = \frac{2\pi}{\lambda} n_{eff}(\lambda) L = k_z(\lambda) L = \frac{\omega}{v_p} L \tag{A.8}$$

where λ is the operating wavelength, L is the length of the optical waveguide, k_z is the propagation constant ($k_z = kn_{eff} = 2\pi\, n_{eff} / \lambda$), and v_p is the phase velocity ($v_p = \omega / k_z$).

A.1.6 Mode Cut-Off Conditions and Single-Mode Operation

The basic criteria to judge a mode cut-off is that the modal effective index n_{eff} is less than the index of the cladding, and given by

$$n_{eff} < n_{cl} \tag{A.9}$$

where n_{cl} is the refractive index of the cladding of the optical waveguide. The single-mode operation of the optical waveguide is that only fundamental modes exist and all high-order modes are cut-off.

A.2 Performance Parameters Related to Modal Field Pattern

A.2.1 Confinement Factor

The confinement factor in silica Γ is defined by

$$\Gamma = \frac{\iint_{silica} (|E_x(x,y)|^2 + |E_y(x,y)|^2) dxdy}{\iint_{all} (|E_x(x,y)|^2 + |E_y(x,y)|^2) dxdy} \tag{A.10}$$

where E_x and E_y are the modal electric field profiles along x and y, respectively.

A.2.2 Far-Field Divergence Angle

Except obtaining directly from the far-field through the Fourier transfer of the modal field profile, the beam divergence angle θ can be calculated from the mode spot size w_0, which can be obtained through the Gaussian approximation $A_{eff} = \pi w_0^2$ of the modal field profile by

$$\theta = tan^{-1}\left(\frac{\lambda}{\pi w_0}\right) \tag{A.11}$$

where λ is the operating wavelength.

A.2.3 Mode Effective Area

The mode effective area A_{eff} is defined by

$$A_{eff}(\lambda) = \frac{[\int\int(|E_x(x,y)|^2 + |E_y(x,y)|^2)dxdy]^2}{\int\int(|E_x(x,y)|^2 + |E_y(x,y)|^2)^2 dxdy} \tag{A.12}$$

where E_x and E_y are the modal electric field profiles along x and y, respectively.

A.2.4 Mode Spot Size and Mode Field Diameter

The mode spot size w_0, also called the mode effective radius, is defined by fitting the field pattern into the Gaussian field pattern,

$$E_g(x,y) = E_0 \exp\left(-\frac{x^2+y^2}{w^2}\right) \tag{A.13}$$

where w takes the value w_0 to maximize the coupling coefficient

$$\max_{w \to w_0} \iint E_g(x,y)E(x,y)dxdy \tag{A.14}$$

where $E(x,y)$ is the modal field pattern. The mode field diameter (MFD) d is defined by

$$d = 2w_0 \tag{A.15}$$

where w_0 is the mode spot size.

Appendix B
Optical Properties of Optical Waveguide Modes

B.1 Mode Classification

For the 1D optical waveguides, the polarization of modes is defined in terms of components of the EM fields. For the 2D optical waveguides, the modes are hybrid modes and the polarization of modes is defined in terms of the dominant component of electric fields with respect to the y direction (or dielectric interface of the waveguide) as shown in Figure 2.1. The detailed polarizations and components involved in each category of the optical waveguide are summarized in Table B.1.

Table B.1 Mode classification of optical waveguides

Polarization	1D, $n(x)$	2D semi-vector, $n(x,y)$	2D full-vector, $n(x,y)$
TE	E_y, H_x, H_z	E_y, H_x, H_z	Dominant E_y, H_x (Quasi-TE) H_y, E_x, E_z, H_z
TM	H_y, E_x, E_z	H_y, E_x, E_z	Dominant H_y, E_x (Quasi-TM) E_y, H_x, E_z, H_z

B.2 Modal Orthogonality

The mode orthonormal relation between normalized guided modes with respect to the propagation direction +z are given as follows:

$$\frac{1}{2}\mathrm{Re}\int(\vec{e}_i\times\vec{h}_j^*)\cdot\hat{z}dxdy=\frac{1}{4}\int(\vec{e}_i\times\vec{h}_j^*+\vec{e}_j^*\times\vec{h}_i)\cdot\hat{z}dxdy=\delta_{ij} \tag{B.1}$$

where δ_{ij} is the Kronecker-δ function, and $\vec{e}_i$ and $\vec{h}_i$ are the electric field and its associated magnetic field of the ith mode. The modal orthogonality is the basis of the waveguide theory involving waveguide excitations, discontinuities, and perturbations. For 1D slab waveguide, modal orthogonality of guided modes is given by

$$-\frac{1}{2}\int_{-\infty}^{\infty} e_{yi}h_{xj}dx = \frac{k_z}{2\omega\mu_0}\int_{-\infty}^{\infty} e_{yi}e_{yj}dx = \frac{\omega\mu_0}{2k_z}\int_{-\infty}^{\infty} h_{xi}h_{xj}dx = \delta_{ij} \qquad \text{(B.2)}$$

for the TE wave

$$\frac{1}{2}\int_{-\infty}^{\infty} e_{xi}h_{yj}dx = \frac{k_z}{2\omega\varepsilon_0}\int_{-\infty}^{\infty} \frac{1}{n^2(x)}h_{yi}h_{yj}dx = \frac{\omega\varepsilon_0}{2k_z}\int_{-\infty}^{\infty} n^2(x)e_{xi}e_{xj}dx = \delta_{ij} \qquad \text{(B.3)}$$

for the TM wave.

B.3 Overlap Integral

The overlap integral between an arbitrary given field and a guided mode is a very useful to calculate the guided power involving the waveguide excitation, discontinuity, and perturbation. An arbitrary electric field $\vec{E}$ and its associate magnetic field $\vec{H}$ can be decomposed as a sum of all modes including radiation modes,

$$\vec{E} = \sum_i (a_i + b_i)\vec{e}_i \qquad \vec{H} = \sum_i (a_i - b_i)\vec{h}_i \qquad \text{(B.4)}$$

where $\vec{e}_i$ and $\vec{h}_i$ are the electric field and its associated magnetic field of the ith mode, and a_i and b_i are the expansion coefficients of the forward wave (+z) and backward wave (-z) for the ith mode. By applying the modal orthogonality, we calculate the overlap integrals a_i and b_i as follows:

$$a_i = \frac{1}{4}\int\left(\vec{E}\times\vec{h}_i^* + \vec{e}_i^*\times\vec{H}\right)\cdot\hat{z}dxdy \qquad \text{(B.5)}$$

$$b_i = \frac{1}{4}\int\left(\vec{E}\times\vec{h}_i^* - \vec{e}_i^*\times\vec{H}\right)\cdot\hat{z}dxdy \qquad \text{(B.6)}$$

where the power guided in the ith mode should be that $P_i = (|a_i|^2 - |b_i|^2)$ provided the input mode power is the unity. Therefore, the modal orthogolity permits us to express the power carried by the total field in terms of the expansion coefficients.

Appendix C

Optical Properties of PC Bloch Modes

C.1 Mode Classification

Unlike these of optical waveguides, due to the periodic dielectric function ($n(\vec{r}) = n(\vec{r} + \vec{R})$), the modes of the PCs are Bloch modes ($u(\vec{r}) = u(\vec{r} + \vec{R})$), where $\vec{R}$ is the lattice vector in the x-y plane. The modal field of the Bloch mode in the PCs consists of plane waves:

$$\vec{E}_{nk}(r) = \hat{e}_n u_{nk}(r) e^{j\vec{k}\cdot\vec{r}} = \sum_{G,n} u_{nk,G} \hat{e}_n e^{j(\vec{k}+\vec{G})\cdot\vec{r}} \tag{C.1}$$

where $\vec{k}$ is the wave vector of the plane waves (or Bloch wave number), $\vec{G}$ is the reciprocal lattice vector, $u_{n,G}$ (n = 1 and 2) is the coefficient of the magnetic fields along $\hat{e}_n$, and $\hat{e}_n$ stands for two unit vectors, which are perpendicular to the propagation direction $\vec{k} + \vec{G}$. According to the reciprocal lattice vector $\vec{G}$ and wave vector of the plane waves $\vec{k}$, the detailed polarizations and components involved in each category of PC Bloch modes are summarized in Table C.1.

Table C.1 Mode classification of the PCs

Polarization	1D, $n(x)$	1D, off-plane	2D, $n(x,y)$	2D, off-plane	3D, $n(x,y,z)$
TE	E_y, H_x, H_z	E_y, H_x, H_z	E_x, E_y, H_z	N/A	N/A
TM	H_y, E_x, E_z	H_y, E_x, E_z	H_x, H_y, E_z	N/A	N/A
Hybrid	N/A	N/A	N/A	E_x, E_y, E_z, H_x, H_y, H_z	E_x, E_y, E_z, H_x, H_y, H_z

C.2 Modal Orthogonality

According to the definition of the Hermitian operator Θ [7]: $(\bar{F},\Theta\bar{G})=(\Theta\bar{F},\bar{G})$, where $(\bar{F},\bar{G})$ is the inner product of two vector fields $\bar{F}$ and $\bar{G}$, the operator related to wave equation $\Theta\bar{H}(r)=(\omega/c)^2\bar{H}(r)$ of the magnetic field $\bar{H}(r)$ is the Hermitian operator [7], and the orthogonality of the magnetic modal fields and normalized Bloch functions over a unit cell of volume V_0 are expressed by

$$\int_{cell}\bar{H}^*{}_{n'k'}(r)\cdot\bar{H}_{nk}(r)dr=\delta_{nn'}\delta(k-k') \tag{C.2}$$

$$\int_{cell}\bar{u}^*{}_{n'k}(r)\cdot\bar{u}_{nk}(r)dr/V_0=\delta_{nn'} \tag{C.3}$$

where δ_{ij} is the Kronecker-δ function and $\delta(k-k')$ is the Dirac δ function. Because the operator related to wave equation $\Xi\bar{E}(r)=(\omega/c)^2\bar{E}(r)$ of the electric field $\bar{E}(r)$ isn't the Hermitian due to the density function $n^2(r)$ [7], the orthogonality (C.2) of the magnetic modal fields cannot directly be used for the electric modal fields. However, we can derive it from (C.2) with the help of the Maxwell's equations and the periodic boundary conditions. After some simple derivations and dropping the constant term ($\omega_n\mu_0/\omega_{n'}\varepsilon_0$), we have

$$\int_{cell}\bar{E}^*{}_{n'k'}(r)\cdot n^2(r)\bar{E}_{nk}(r)dr=\delta_{nn'}\delta(k-k') \tag{C.4}$$

$$\int_{cell}\bar{u}^*{}_{n'k}(r)\cdot n^2(r)\bar{u}_{nk}(r)dr/V_0=\delta_{nn'} \tag{C.5}$$

where the Divergence (or Gauss) theorem was used. So the electric modal fields are orthogonal with respect to the density function $n^2(r)$. In general, the wave equation $\Theta\bar{E}(r)=(\omega/c)^2n^2(r)\bar{E}(r)$ with the Hermitian operator Θ is a generalized Hermitian eigenvalue problem (GHEP) [88]. And the electric modal fields related to this wave equation are orthogonal each other with respect to the density function $n^2(r)$.

For the TE wave with off-plane propagation in the 1D PCs, the wave equation related to E_y and H_x of (2.13) and (2.14) is rewritten as

$$\Theta E_y = -\frac{d^2 E_y}{dx^2} + k_z^2 E_y = (\omega / c)^2 n^2(x) E_y \tag{C.6}$$

$$\Theta H_x = -\frac{d^2 H_x}{dx^2} + k_z^2 H_x = (\omega / c)^2 n^2(x) H_x \tag{C.7}$$

where Θ ($= -d^2/dx^2 + k_z^2$) is the Hermitian operator. The orthogonality of electric and magnetic modal fields and the normalized Bloch functions over a unit cell of length Λ are expressed by

$$\int_\Lambda E_y{}^*{}_{n'k'}(x) n^2(x) E_{y_{nk}}(x) dx = \int_\Lambda H_x{}^*{}_{n'k'}(x) n^2(x) H_{x_{nk}}(x) dx = \delta_{nn'}\delta(k-k') \tag{C.8}$$

$$\int_\Lambda u^*{}_{n'k}(x) n^2(x) u_{nk}(x) dx / \Lambda = \int_\Lambda v^*{}_{n'k}(x) n^2(x) v_{nk}(x) dx / \Lambda = \delta_{nn'} \tag{C.9}$$

where $E_y(x) = u_k(x)\exp(jkx)$ and $H_x(x) = v_k(x)\exp(jkx)$.

On the other hand, for the TM wave with off-plane propagation in the 1D PCs, the wave equation related to E_x and H_y of (2.13) and (2.14) is rewritten as

$$\Xi E_x = -\frac{d}{dx}\left[\frac{1}{n^2}\frac{d}{dx}\left(n^2 E_x\right)\right] + k_z^2 E_x = (\omega / c)^2 n^2 E_x \tag{C.10}$$

$$\Theta H_y = -\frac{d}{dx}\left[\frac{1}{n^2}\frac{dH_y}{dx}\right] + \frac{k_z^2}{n^2} H_y = (\omega / c)^2 H_y \tag{C.11}$$

where both Θ and Ξ are the Hermitian operators. The orthogonality of the electric and magnetic modal fields and the normalized Bloch functions over a unit cell of length Λ are expressed by

$$\int_\Lambda E_x{}^*{}_{n'k'}(x) n^2(x) E_{x_{nk}}(x) dx = \int_\Lambda H_y{}^*{}_{n'k'}(x) H_{y_{nk}}(x) dx = \delta_{nn'}\delta(k-k') \tag{C.12}$$

$$\int_\Lambda u^*{}_{n'k}(x) n^2(x) u_{nk}(x) dx / \Lambda = \int_\Lambda v^*{}_{n'k}(x) v_{nk}(x) dx / \Lambda = \delta_{nn'} \tag{C.13}$$

where $E_x(x) = u_k(x)\exp(jkx)$ and $H_y(x) = v_k(x)\exp(jkx)$. The orthogonality of electric and magnetic modal fields and the normalized Bloch functions over a unit cell of area S for the 2D PCs with off-plane propagation can be derived in a similar way.

C.3 Scaling Transformation

Due to the scaling nature of the Maxwell's equations, there is no fundamental length scale for the EM waves. Therefore, we can easily derive the scaling transformation of the modal properties such as the effective index and the modal field pattern with respect to the change of the pitch Λ and the refractive index $n(r)$ of the PCs and their related structures (e.g., PCWs and PCCs). For some given parameters, such as the pitch Λ_0, the field position r_0, and the frequency ω_0, the wave equation related to the magnetic field $\vec{H}(r)$ of (2.2) is rewritten as

$$\nabla\times[\frac{1}{n^2(r_0)}\nabla\times\vec{H}(r_0)]-(\frac{\omega_0}{c})^2\vec{H}(r_0)=0 \tag{C.14}$$

where ∇ is a linear operator. Now we change the pitch ratio M (i.e., Λ/Λ_0 or r/r_0) as the scale parameter of dimension of the PCs. So the index distribution of the PC is that $n'(r) = n(r/M)$. We change the variable r_0 of (C.14) by $r = Mr_0$. After some trivial derivations, (C.14) becomes

$$\nabla'\times[\frac{1}{n'^2(r)}\nabla'\times\vec{H}(r/M)]-(\frac{\omega_0}{Mc})^2\vec{H}(r/M)=0 \tag{C.15}$$

where $\nabla' = \nabla/M$ was used. As can be seen from (C.15), the new magnetic field pattern can be obtained through $\vec{H}'(r)=\vec{H}(r/M)$ with the frequency $\omega=\omega_0/M$. Similarly, the electric field pattern has the same scaling rule: $\vec{E}'(r)=\vec{E}(r/M)$. Therefore, the scaling transformations of the field pattern and the effective index ($n_{eff}=ck_z/\omega_0$) of the PC-based modes are obtained through scaling the position r and the frequency ω (or wavelength λ) by the same factor M, and given by

$$n_{eff}(\lambda, M)\,|_{fixed\ \mathrm{d/\Lambda}} = n_{eff}(\frac{\lambda}{M}) \tag{C.16}$$

$$\vec{E}(r, \lambda, M)\,|_{fixed\ \mathrm{d/\Lambda}} = \vec{E}(\frac{r}{M}, \frac{\lambda}{M}) \tag{C.17}$$

$$\vec{H}(r, \lambda, M)\,|_{fixed\ \mathrm{d/\Lambda}} = \vec{H}(\frac{r}{M}, \frac{\lambda}{M}) \tag{C.18}$$

where d/Λ is the air-hole size-to-pitch ratio of the PCs, λ is the operating wavelength, and M is the pitch ratio (i.e., Λ/Λ_0 with $\Lambda_0 = 2.3$ μm). Once the scaling transformations of the field pattern and the effective index are given, the scaling transformations related to other modal parameters defined in Appendix A such as the waveguide dispersion D_g, the mode effective area A_{eff}, the confinement loss Lc, and the confinement factor Γ, can be easily obtained:

$$D_g(\lambda, M)\,|_{fixed\ \mathrm{d/\Lambda}} = \frac{1}{M} D_g(\frac{\lambda}{M}) \tag{C.19}$$

$$A_{eff}(\lambda, M)\,|_{fixed\ \mathrm{d/\Lambda}} = M^2 A_{eff}(\frac{\lambda}{M}) \tag{C.20}$$

$$L_c(\lambda, M)\,|_{fixed\ \mathrm{d/\Lambda}} = \frac{1}{M} L_c(\frac{\lambda}{M}) \tag{C.21}$$

$$\Gamma(\lambda, M)\,|_{fixed\ \mathrm{d/\Lambda}} = \Gamma(\frac{\lambda}{M}) \tag{C.22}$$

where λ is the operating wavelength and M is the pitch ratio.

Bibliography

[1] G. P. Agrawel, *Fiber optic communication systems*. New York: John Wiley, 1997.

[2] A. W. Snyder and J. D. Love, *Optical waveguide theory*. London, U.K.: Chapman and Hall, 1995. ·

[3] K. Okamoto, *Fundamentals of optical waveguides*. New York: Academic Press, 2000.

[4] C. Vassallo, *Optical Waveguide Concepts*. Amsterdam, The Netherlands: Elsevier, 1991.

[5] E. Yablnovitch, "Inhibited spontaneous emission in solid-state physics and electronics," *Phys. Rev. Lett.*, vol. 58, no. 20, pp. 2059-2062, 1987.

[6] S. John, "Strong localization of photons in certain disordered dielectric superlattice," *Phys. Rev. Lett.*, vol. 58, pp. 2486-2489, 1987.

[7] J. D. Joannopoulos, R. D. Meade, and J. N. Winn, *Photonic crystals: molding the flow of light*. Princeton: Princeton University Press, 1995.

[8] K. Sakoda, *Optical properties of photonic crystals*. Berlin: Spinger-Verlag, 2001.

[9] C. M. Soukoulis, *Photonic band gap materials*. Boston: Kluwer Academic, 1996.

[10] E. Burstein and C. Weisbuch, *Confined electrons and photons*. New York: Plenum Press, 1995.

[11] C. M. Soukoulis, *Photonic band structure and localization*. New York: Plenum Press, 1993.

[12] K. M. Ho, C.T. Chan, and C. M. Soukoulis, "Existence of a photonic gap in periodic dielectric structures," *Phys. Rev. Lett.*, vol. 65, no. 25, pp. 3152-3155, 1990.

[13] S. L. Chuang, *Physics of optoelectronic devices*. New York: John Wiley, 1995.

[14] H. A. Macleod, *Thin-film optical filters*. Bristol: Adam Hilger, 1986.

[15] P. Yeh, *Optical waves in layered media*. New York: John Wiley, 1988.

[16] K. Tajima, J. Zhou, K. Nakajima, and K. Sato, "Ultra low loss and long length photonic crystal fibers," *Proc. Opt. Fiber Commun. Conf.*, PD1, 2003.

[17] N. Vekataraman, M. T. Gallagher, C. M. Smith, D. Muller, J. A. West, K.W. Koch, J. C. Fajardo, and S. Park, "Low loss (13 dB/km) air core photonic band-gap fibre," *Proc. ECOC'02*, PD1.1, 2002.

[18] F. Brechet, J. Marcou, D. Pagnoux, and P. Roy, "Complete analysis of the characteristics of propagation into photonic crystal fibers by the finite element method," *Opt. Fiber Technol.*, vol. 6, no. 2, pp. 181-191, 2000.

[19] A. K. Abeeluck, N. M. Litchinitser, C. Headley, and B. J. Eggleton, "Analysis of spectral characteristics of photonic bandgap waveguides," *Opt. Express*, Vol. 10, pp. 1320-1333, 2002.

[20] C. L. Xu, W. P. Huang, M. S. Stern, and S. K. Chaudhuri, "Full-vectorial mode calculations by finite difference method," *IEE Proc.-J*, vol. 141, no. 5, pp. 281-286, 1994.

[21] K. S. Chiang, "Review of numerical and approximate methods for the modal analysis of the general optical dielectric waveguides," *Opt. Quantum Electron.*, vol. 26, pp. S113–S133, 1994.

[22] W. P. Huang, *Methods for modelling and simulation of guided wave optoelectronics: Part1: modes and couplings*. Cambridge: EMW Publishing, PIER 10, 1995.

[23] W. P. Huang, *Methods for modelling and simulation of guided wave optoelectronics: Part2: waves and interactions*. Cambridge: EMW Publishing, PIER 11, 1995.

[24] M. S. Stern, "Semivectorial polarized finite difference method for optical waveguides with arbitrary index profiles," *IEE Proc.-J. Optoelectron.*, vol. 135, no. 5, pp. 56-63, 1988.

[25] Z. M. Zhu and T. G. Brown, "Full-vectorial finite-difference analysis of microstructured optical fibers," *Opt. Express*, vol. 10, no. 17, pp. 853-864, 2002.

[26] L. P. Shen, W.P. Huang, and S. S. Jian, "Design of photonic crystal fibers for dispersion-related applications," *J. Lightwave Technol.*, vol. 21, no. 7, pp. 1644-1651, 2003.

[27] M. Koshiba, *Optical waveguide analysis*. New York: McGraw-Hill, 1992.

[28] J. Katz, "Novel solution of 2D waveguides using the finite element method," *Appl. Opt.*, vol. 21, pp. 2747–2751, 1982.

[29] M. Koshiba, "Full vector analysis of photonic crystal fibers using the finite element method," *IEICE Electron*, vol. E85-C, no. 4, pp. 881-888, 2002.

[30] A. Cucinotta, S. Selleri, L. Vincetti, and M. Zoboli, "Holey fiber analysis through the finite-element method," *IEEE Photon. Technol. Lett.*, vol. 14, no. 11, pp. 1530-1532, 2002.

[31] C. L. Xu, W. P. Huang, and S. K. Chaudhuri, "Efficient and accurate vector mode calculations by beam propagation method," *IEEE J. Lightwave Technol.*, vol. 11, no. 7, pp. 1209-1215, 1993.

[32] S. S. A. Obayya, B. M. Azizur Rahman, K. T. V. Grattan, and H. A. El-Mikati, "Full vectorial finite-element-based imaginary distance beam propagation solution of complex modes in optical waveguides," *IEEE J. Lightwave Technol.*, vol. 20, no. 6, pp. 1054-1059, 2002.

[33] D. Zhou, L. P. Shen, and K. Ouelette, "Design and simulation of an InP spot size converter (SSC)," *18th Annual National Fiber Optic Engineers Conference (NFOEC),* PS. 2, Dallas, TX, Sept. 15-19, 2002.

[34] K. Saitoh and M. Koshiba, "Full-vectorial imaginary-distance beam propagation method based on a finite element scheme: Application to photonic crystal fibers," *IEEE J. Quantum Electron.*, vol. 38, pp. 927-933, 2002.

[35] N. N. Feng, G. R. Zhou, and W. P. Huang, "A scalar finite-difference time-domain method with cylindrical perfectly matched layers: Application to guided and leaky modes of optical waveguides," *IEEE J. Quantum Electron.,* vol. 39, no. 3, pp. 487-492, 2003.

[36] W.-P. Huang, D. Zhou, N. N. Feng, G. R. Zhou, L. P. Shen, and C. L. Xu, "FDTD method and its applications to simulation of photonic devices: An overview of recent development," Invited paper at *Asia Pacific Optical Communication Conference* (APOCC), 2002.

[37] M. Qiu, "Analysis of guided modes in photonic crystal fibers using the finite-difference time-domain method," *Microwave Optic. Technol. Lett.*, vol. 30, pp. 327-330, 2001.

[38] M. J. P. Berenger, "A perfectly matched layer for the adsorption of electromagnetic waves," *J. Comput. Phys.*, vol. 114, pp. 185-200, 1994.

[39] S. G. Johnson and J. D. Joannopoulos, "Block-iterative frequency-domain methods for Maxwell's equations in a planewave basis," *Opt. Express,* vol. 8, pp. 173-190, 2001.

[40] A. Ferrando, E. Silvestre, J. J. Miret, P. Andrés, and M. V. Andrés, "Full-vector analysis of a realistic photonic crystal fiber," *Opt. Lett.*, vol. 24, pp. 276–278, 1999.

[41] A. Ferrando, E. Silvestre, J. J. Miret, and P. Andres, "Donor and acceptor guided modes in photonic crystal fibers," *Opt. Lett.*, vol. 25, no. 18, pp. 1328–1330, 2000.

[42] A. Ferrando, E. Silvestre, J. J. Miret, P. Andrés, and M. V. Andrés, "Vector description of higher-order modes in photonic crystal fibers," *J. Opt. Soc. Am. A,* vol. 17, no. 7, pp. 1333-1340, 2000.

[43] D. Mogilevtsev, T. A. Birks, and P. St. J. Russell, "Localised function method for modelling defect modes in 2-D photonic crystals," *J. Lightwave Tech., vol.* 17, pp. 2078-2080,1999.

[44] T. M. Monro, D. J. Richardson, N. G. R. Broderick and P. J. Bennett, "Holey optical fibers: An efficient modal model," *J. Lightwave Technol.*, vol. 17, no. 6, pp. 1093-1102, 1999.

[45] T. M. Monro, D. J. Richardson, N. G. R. Broderick, and P. J. Bennet, "Modeling large air fraction holey optical fibers," *J. Lightwave Tecnol.*, vol. 18, pp. 50-56, 2000.

[46] M. J. Steel, T.P. White, C.M. de Sterke, R.C. McPhedran, and L.C. Botten, "Symmetry and degeneracy in microstructured optical fibers," *Opt. Lett.*, vol. 26, no. 8, pp. 488-490, 2001.

[47] T. P. White, B. T. Kuhlmey, R. C. McPhedran, D. Maystre, G. Renversez, C.M. de Sterke, and L. C. Botton, "Multipole method for microstructured optical fibers. I. formulation," *J. Opt. Soc. Am. B*, vol. 19, no. 10, pp. 2322-2330, 2002.

[48] B. T. Kuhlmey, T.P. White, G. Renversez, D. Maystre, L. C. Botton, C.M. de Sterke, and R. C. McPhedran, "Multipole method for microstructured optical fibers. II. Implementation and results," *J. Opt. Soc. Am. B*, vol. 19, pp. 2331-2340, 2002.

[49] T. A. Birks, J. C. Knight, and P. St. J. Russel, "Endlessly single-mode photonic crystal fiber," *Opt. Lett.*, vol. 22, pp. 961-963, 1997.

[50] M. C. -Lefort, E. Istrate, M. Allard, J. Poon, and E. H. Sargent, " Photonic crystal heterostructures: Waveguiding phenomena and methods of solution in an envelope function picture," *Phys. Rev. B*, vol. 65, no. 125318, 2002.

[51] E. Istrate, M. C. -Lefort, and E. H. Sargent, "Theory of photonic crystal heterostructures," *Phys. Rev.* B, vol. 66, pp. 075121, 2002.

[52] J. Poon, E. Istrate, M. Allard, and E. H. Sargent, "Multiple-scales analysis of photonic crystal waveguides," *IEEE J. Quantum Electron.*, vol. 39, pp. 778-786, 2003.

[53] T. Sørensen, J. Broeng, A. Bjarklev, E. Knudsen, and S. E. Barkou Libori, "Macro-bending loss properties of photonic crystal fibre," *Electron. Lett.*, vol. 37, pp. 287-289, 2001.

[54] M. Born and E. Wolf, *Principles of optics*. New York: Pergamon Press, 1970.

[55] T. Tamir, *Guided-Wave optoelectronics*. Berlin: Spinger-Verlag, 1990.

[56] W. P. Huang, R. M. Shubair, A. Nathan, and Y. L. Chow, "The modal characteristics of ARROW structures," *IEEE J. Lightwave Technol.*, vol. 10, no. 8, pp. 1015-1022, Aug. 1992.

[57] R. T. Bise, R. S. Windeler, K. S. Kranz, C. Kerbage, B. J. Eggleton, and D. J. Trevor, "Tunable photonic band gap fiber," *OSA Trends in Optics and Photonics (TOPS), Proc. OFC*'02, Postdeadline Ed., vol. 70, pp. 466-468, 2002.

[58] L. P. Shen, W. P. Huang, G. X. Chen, and S. S. Jian, "Design and optimization of photonic crystal fibers for broadband dispersion compensation," *IEEE Photon. Technol. Lett.*, vol. 15, pp. 540-542, 2003.

[59] W.-P. Huang, L. P. Shen, and S. S. Jian, "Design modeling and optimization of photonic crystal fibers for optical communication systems," Invited Paper at *the 8th China-Japan joint meeting on Optical Fiber Science and Electromagnetic Theory (OFSET)*, 2003.

[60] T. A. Birks, P. J. Roberts, P. St. J. Russell, D. M. Atkin, and T. J. Shepherd, "Full 2-D photonic band gaps in silica/air structures," *Electron. Lett.,* vol. 31, pp. 1941-1942, 1995.

[61] K. Saitoh and M. Koshiba, "Confinement losses in air-guiding photonic bandgap fibers," *IEEE Photon. Technol. Lett.*, vol. 15, pp. 236-238, 2003.

[62] R. F. Cregan, B. J. Mangan, J. C. Knight, T. A. Birks, P. St. J. Russel, P. Roberts, and D. C. Allan, "Single mode photonic band gap guidance of light in air," *Science*, vol. 285, pp. 1537-1539, 1999.

[63] J. C. Knight, T. A. Birks, P. St. J. Russell, and D. M. Atkin, "All-silica single-mode optical fiber with photonic crystal cladding," *Opt. Lett.*, vol. 21, pp. 1547-1549, 1996; Errata, *Opt. Lett.,* vol. 22, pp. 484–485, 1997.

[64] J. Broeng, D. Mogilevstev, S. E. Barkou, and A. Bjarklev, "Photonic crystal fibers: A new class of optical waveguides," *Opt. Fiber Technol.*, vol. 5, no. 3, pp. 305-330, 1999.

[65] T. M. Monro, "Holey optical fibers: Fundamentals and applications," in *Proc. OFC*'02, 2002, tutorial.

[66] J. Broeng, T. Søndergaard, S. E. Barkou, P.M. Barbeito, and A. Bjarklev, "Waveguidance by the photonic bandgap effect in optical fibres," *J. Opt. A: Pure App. Opt.,* vol. 1, pp. 477-482, 1999.

[67] J. B. Nielsen, T. Søndergaard, S. E. Barkou, A. Bjarklev, J. Broeng, and M. B. Nielsen, "Two-dimentional Kagome structure, fundamental hexagonal photonic crystal configuration," *Electron. Lett.*, vol. 35, no. 20, pp. 1736-1737, 1999.

[68] W. P. Huang, C. L. Xu, W. Lui, and K. Yokoyama, "Perfect matched layer boundary condition for modal analysis of optical waveguides: Leaky mode calculations", *IEEE Photon. Technol. Lett.*, vol. 8, pp. 652-654, 1996.

[69] G. Agrawal, *Nonlinear Fiber Optics*. New York: Academic, 1995.

[70] M. J. Gander, R. McBride, J. D. C. Jones, D. Mogilevtsev, T. A. Birks, J. C. Knight and P. St. J. Russell, "Experimental measurement of group velocity dispersion in photonic crystal fibre," *Electron. Lett.*, vol. 35, pp. 63-64, 1999.

[71] N. A. Mortensen, J. R. Folken, P. M. W. Skovgaard, and J. Broeng, "Numerical aperture of single-mode photonic crystal fibers," IEEE *Photon. Tech. Lett.*, vol. 14, pp. 1094 -1096, 2002.

[72] L. P. Shen, C. L. Xu, and W.-P. Huang, "Modal characteristics of index-guiding photonic crystal fibers: A comparison between scalar and vector analysis," internal reports.

[73] D. Ferrarini, L. Vincetti, M. Zoboli, A. Cucinotta, and S. Selleri, "Leakage properties of photonic crystal fibers," *Opt. Express*, vol. 10, pp. 1314–1319, 2002.

[74] T. P. White, R. C. McPhedran, and C. Martijn, "Multiport method for efficient microstructured optical fiber calculation," Conference on *Q.E.L.S.*, pp. 123-124, 2001.

[75] T. P. White, R. C. McPhedran, and C. M. de Sterke, "Confinement losses in microstructured optical fibers," *Opt. Lett.*, vol. 26, pp. 1660-1662, 2001.

[76] S. E. Miller and I. P. kaminov, *Optical fiber telecommunications II*. New York: Academic Press, 1988

[77] I. P. kaminov and T. L. Koch, *Optical fiber telecommunications IIIA*. New York: Academic Press, 1997.

[78] A. Ferrando, E. Silvestre, J. J. Miret, J. A. Monsoriu, M. V. Andrés and P. St. J. Russell, "Designing a photonic crystal fibre with flattened chromatic dispersion," *Electron. Lett., vol.* 35, pp. 325-327, 1999.

[79] A. Ferrando, E. Silvestre, J. J. Miret, and P. Andres, "Nearly zero ultraflattened dispersion in photonic crystal fibers," *Opt. Lett.*, vol. 25, pp. 790-792 , 2000.

[80] A. Ferrando, E. Silvestre, and P. Andres, "Designing the properties of dispersion-flattened photonic crystal fiber," *Opt. Express,* vol. 9, pp. 687-697, 2001.

[81] T. M. Monro, D. J. Richardson, N. G. R. Broderick, and P. J. Bennet, "Modeling large air fraction holey optical fibers," *J. Lightwave Tecnol.*, vol. 18, pp. 50-56, 2000.

[82] T. A. Birks, D. Mogilevtsev, J. C. Knight and P. St. J. Russell, "Dispersion compensation using single material fibres," *IEEE Photon. Technol. Lett.*, vol. 11, pp. 674-676, 1999.

[83] J. C. Knight, J. Arriaga, T. A. Birks, A. Ortigosa-Blanch, W. J. Wadsworth, and P. St. J. Russell, "Anomalous dispersion in photonic crystal fiber," *IEEE Photon. Technol. Lett.*, vol. 12, pp. 807-809, 2000.

[84] G. E. Town and J. T. Lizier, "Tapered holey fibers for spot-size and numerical-aperture conversion," *Opt. Lett.*, vol. 26, pp. 1042–1044 , 2001.

[85] W. H. Reeves, J. C. Knight, P. St. J. Russell, and P. J. Roberts, "Demonstration of ultra-flattened dispersion in photonic crystal fibers," *Opt. Express*, vol. 10, no. 14, pp. 609-613, 2001.

[86] Private communications from J. C. Knight and W. H. Reeves: Dept. of Physics, U. of Bath, UK, 2002.

[87] V. Srikant, "Broadband dispersion and dispersion slope compensation in high bit rate and ultra long haul systems", *Technical Digest of OFC 2001*, TuH1, 2001.

[88] J. Mathews and R. L. Walker, *Mathematical methods of physics.* New York: W. A. Benjamin, 1970.

Publications

The work carried out during this thesis has led to a number of publications in the international journals and conferences:

1. L. P. Shen, W.-P. Huang, G. X. Chen, and S. S. Jian, "Design and optimization of photonic crystal fibers for broadband dispersion compensation," *IEEE Photon. Technol. Lett.*, vol. 15, pp. 540-542, 2003.
2. L. P. Shen, W.-P. Huang, and S.S. Jian, "Design of photonic crystal fibers for dispersion-related applications," *J. Lightwave Technol.*, vol. 21, no. 7, pp. 1644-1651, 2003.
3. W.-P. Huang, L. P. Shen, and S. S. Jian, "Design modeling and optimization of photonic crystal fibers for optical communication systems," Invited Paper at *the 8th China-Japan joint meeting on Optical Fiber Science and Electromagnetic Theory* (*OFSET*), 2003.
4. W.-P. Huang, D. Zhou, N. N. Feng, G. R. Zhou, L. P. Shen, and C. L. Xu, "FDTD method and its applications to simulation of photonic devices: An overview of recent development," Invited paper at *Asia Pacific Optical Communication Conference* (APOCC), 2002.
5. D. Zhou, L. P. Shen, and K. Ouelette, "Design and simulation of an InP spot size converter (SSC)," *18th Annual National Fiber Optic Engineers Conference* (*NFOEC*), PS. 2, Dallas, TX, Sept. 15-19, 2002.